The Influence of Processing and Fluid Parameters on Injection Molding Flow

by

Thomas J. Bress

A dissertation submitted in partial fulfillment
of the requirements for the degree of
Doctor of Philosophy
(Mechanical Engineering)
in the University of Michigan
2009

Doctoral Committee:

Professor David R. Dowling, Chairperson
Professor Ellen M. Arruda
Professor Stephen L. Ceccio
Professor Volker Sick
Professor Alan S. Wineman
Associate Professor Michael J. Solomon

To my wife, Heather, for helping me chase my dream.

ACKNOWLEDGEMENTS

I would like to thank my committee members for their moral and material support. This was an unfunded project. I was given the opportunity to explore a topic that I was interested in solely because I was interested in it. There were no sponsors to please, there was no one to tell me what I should investigate. But such freedom comes at a price. Without a sponsor I had to rely on the generosity of others for the equipment that I used. With the exception of the injection molding machine, my entire experimental setup was pieced together from borrowed equipment.

First I would like to thank Prof. Dowling. This has been a long, difficult project that was uncertain even at the best of times. He never gave up on me and I thank him for it. I would like to thank Colonial Engineering for providing the initial seed money for this project. I would like to thank Professors Dowling, Ceccio and Arruda for investing in the injection molding machine. Prof. Ceccio deserves much thanks for the long-term loan of his laser, the heart of my experimental setup. I would like to thank Professors Ceccio and Dowling for allowing me to "borrow" the image acquisition equipment from another project. Prof. Sick loaned me a licensed copy of the PIV software that I used in this project, but more importantly he provided moral support and encouragement when I needed it most. Prof. Arruda kindly loaned me her polariscope and compensator and this formed the basis of entire chapter of this thesis. Prof. Wineman taught me the fundamentals of

continuum mechanics and viscoelasticity, without which the study of rheology is impossible. Prof. Solomon generously allowed me to use his cone-and-plate rheometer and asked his graduate students to provide me with technical assistance. I would also like to thank Kent Pruss for turning my mold drawings into reality. Thanks also to Jerry Polashak and Todd Wilber for always being there to repair load cell and thermocouple wires accidentally flattened by 30 metric tons of clamping force. I would also like to thank the late Prof. Filisko. He was generous with his time and assisted me with measurements on his ancient, pen-and-chart, non-computerized Instron capillary rheometer. Old-school but effective, he and that rheometer had much in common. He was one of the few people that I could turn to with practical polymer processing experience and I thank him for his advice.

But most of all I wish to thank my wife Heather for her continuing support. She always had faith that I would finish someday, and now that day has come. With her love, patience and support she has allowed me to chase a dream. It is a very rare privilege indeed, to have the freedom to chase a dream and to catch it. Finally, I would like to thank my sons Nathan and Zachary for their love and support. They have been very patient with me these past few weeks as I have brought this project to a close. Daddy's home!

TABLE OF CONTENTS

LIST OF FIGURES

Figure

LIST OF TABLES

Table

LIST OF APPENDICES

Appendix

CHAPTER 1

Introduction

Polymers are a broad range of organic substances that are made up of long, intertwined molecular chains. This structure gives polymers useful characteristics and they are an important engineering material. They are lightweight in comparison with steel and aluminum. Polymers have lower strength and stiffness than metals but their lower cost and weight make them more attractive than metals for many non-load bearing structural applications. They are also easily formed and shaped into complex geometries by injection molding, extrusion, thermoforming and other commonly used manufacturing processes.

Polymers play an ever increasing role in product design and manufacturing. In the year 2000 the average North American car contained 245.5 pounds of plastic, a weight percentage of 7.6% [1]. A total of 4.1 billion pounds of plastic were used by the auto industry in 2000, a 17% increase from 3.5 billion pounds used in 1996 [1]. This trend was indicative of polymer production as a whole. The total North American production of plastics in the year 2000 was 87 billion pounds, a 19% increase from 73 billion pounds in 1996 [1].

In the auto industry plastics were originally used almost exclusively in the vehicle's interior of automobiles but they now have a major presence in exterior compo-

nents (exterior trim and body panels) and underhood components (coolant bottles, anti-noise baffles and resonators, and intake manifolds) as well. With the current drive for fuel economy and recyclability the importance of plastics, particularly thermoplastics, will only increase.

Injection molding is one of the most common and most important methods of processing polymers. It provides a method for making geometrically complex parts with cycle times as low as those found in the die casting of metals. A modern injection molding machine is shown in Figure 1.1. Polymers generally have low thermal conductivity and are easily degraded by direct application of heat so they cannot be melted and formed in the same manner that metals are cast. Injection molding takes advantage of the high viscosity of polymer melts to generate and distribute heat through viscous dissipation and mixing. Solid pellets of a polymer are placed into the hopper of an injection molding machine and are carried through the barrel by the rotation of a large screw. Frictional heating softens the pellets until they begin to flow. The high viscosity and thorough mixing of the polymer melt by the screw gives a high temperature, evenly heated melt. As the liquid polymer collects at the end of the screw the pressure increases and forces the screw back. When the screw has moved back far enough to build up the amount of liquid plastic necessary to fill the mold the machine is ready to start an injection event.

The injection molding cycle consists of the following phases.

1. *Injection.* The screw moves forward like a ram and forces the plastic through the nozzle of the machine and into the mold. Once it enters the mold it passes through the sprue, into the runner(s) and through the gate(s) into the mold cavity.

Figure 1.1: The Vista-Sentry injection molding machine

2. *Packing and Holding.* Plastics shrink during solidification. This is undesirable since the goal of injection molding is to make parts that match the mold cavity shape. Plastics are also somewhat compressible. To combat shrinkage liquid plastic is packed into the mold after the filling phase is complete. The pressure in the mold rises rapidly during the packing stage. This high pressure is maintained in the holding phase. Fluid enters the mold slowly during this phase and it has long been known [2] that this flow influences the frozen-in molecular orientation of the solid plastic part. This in turn affects the residual stresses and strains in the final solid part.

3. *Sealed Cooling.* The gate is a very narrow opening into the mold. Since it is narrow it freezes off before the main body of the part solidifies. When the gate solidifies it isolates the contents of the mold from the machine and the part

cools and solidifies in a sealed state. Even though the part is sealed internal flow can still occur due to temperature gradients and solidification effects.

4. *Shot Buildup and Part Ejection.* Once the gate has frozen the part can no longer be affected by the screw. During this cooling period the screw rotates and builds up a new shot of liquid plastic. When the part has solidified the mold opens and the part is ejected. By this time a new shot of liquid plastic is waiting in the barrel of the molding machine. The mold closes and a new injection cycle starts. Typical cycle times range from one to several minutes.

1.1 Motivation

Engineers that design plastic parts are concerned with dimensional stability, mechanical properties, residual stresses, warpage and part-to-part consistency. The engineers that manufacture the parts are concerned with fill time, process variability, and the effects of processing parameters on part quality. All of these concerns are affected by the fluid mechanics of the mold filling process. The fluid mechanics affects the solid mechanics by influencing the molecular orientation within the solid part. The orientation of the molecules in the solid part plays a critical role in determining the properties of the part. This orientation is influenced by the fluid flow during the mold filling, packing, holding and cooling phases of the injection cycle. Thus the fluid mechanics of injection molding has a major impact on the final product.

As a result, engineers need to predict flow patterns in a mold. Easily controlled molding parameters such as melt temperature, melt pressure and injection rate greatly influence the melt flow and can be used to improve parts and processes. Unfortunately, polymer melt flow prediction is very difficult. Polymers are made up of long molecular chains. These chains move and orient themselves under ap-

plied shear stress, giving rise to non-Newtonian phenomena such as shear thinning, viscoelasticity, memory effects, and non-zero normal stress differences.

The mold flow problem consists of predicting the velocity field for the unsteady, non-isothermal flow of a non-Newtonian liquid that solidifies as it flows in a complex geometry. Add to this the fact that the constitutive relations for the fluid are complicated or largely unknown and it becomes obvious that predicting polymer flow is a task best suited for a computer.

Computational polymer fluid dynamics is an active area of research and commercial codes are available for predicting mold flow. The accuracy of these codes depends on the validity of the constitutive models they employ and on their inherent assumptions about the mold geometry and flow. It is difficult to judge the accuracy of the codes and the models on which they are based because of the lack of in-mold flow data with which to compare them. As discussed below, non-Newtonian flow research has focused on simplified processes such as steady capillary flow into cavities or on simplified non-Newtonian liquids such as Boger fluids. Real time velocity vector field data of commonly used polymers under actual molding conditions has not been reported in the archival literature at the present time.

Newtonian fluid researchers have captured velocity vector fields in high speed air and water flows using a laser-sheet particle-imaging technique known as Particle Image Velocimetry, or PIV. PIV has been extensively used to generate accurate flow velocity measurements in Newtonian flows. Newtonian fluids are constitutively well characterized but the high speeds typical to flows of engineering relevance leads to turbulence. The closure problem and the need for turbulence models makes the prediction of turbulent flow difficult. Experimentally obtained velocity vector field information is useful for developing and validating turbulence models and computer

codes.

The difficulties inherent in the use and validation of theoretical constitutive relations for non-Newtonian flows are similar to those in the use and validation of turbulence models in Newtonian flows, and the same benefits might be reaped from comparing computational predictions to velocity field data. PIV would be particularly well suited to polymer melt flows because such flows are much slower and much more viscous than typical Newtonian flows, leading to Reynolds numbers far below unity. The non-Newtonian research community has not yet embraced PIV techniques.

This thesis addresses this situation and provides the following unique contributions:

1. The direct study of commercially important non-Newtonian polymer liquids with current Newtonian flow techniques.

2. A quantitative study of the mold filling process based on a new and unique experimental data base. This data base can be used to evaluate polymer fluid constitutive models and computer codes.

3. The direct investigation of flow during the packing phase of injection molding.

4. The characterization of the residual stress field of the solidified parts using polarized light, along with a proposed computational method to allow the extraction of the same parameters from computed three-dimensional residual stress fields.

1.2 Previous Work in the Visualization of Non-Newtonian Flows

The use of in-mold flow visualization as a tool to study the flow of polymers in an injection molding machine was first reported by Gilmore and Spencer in 1951 [3]. A glass walled mold was used to qualitatively filling flow, weld line formation, and the undesirable jetting of polymer melt from the gate across the mold cavity. These researchers also used simple models of the flow to study the effects of injection pressure, temperature and packing time on the injection molding process [4]. Polarized light was used to study the impact of packing flow on the physical properties and molecular orientation of solid parts [2]. The results of these experimental and theoretical investigations were combined into an overview of the fluid mechanics of mold filling [5]. The present study extends this early work by providing quantitative results.

Kamal and Kenig [6, 7] combined flow visualization with a more sophisticated mathematical model to study the in-mold flow of partially crystalline polymers. Their model simulated the one dimensional radial creeping flow of a power law fluid of limited compressibilty in a semi-circular mold. High speed photography of a glass walled mold was used to track the flow front of polyethylene as it filled a semi-circular mold. This data was used to confirm the model predictions. The present study also provides qualitative front-tracking results in combination with the velocity vector field information of the polymer melt.

A remarkable aspect of the work of Gilmore and Spencer and Kamal and Kenig is that they used industrially relevant polymers in industrially relevant molding machines. In the 1970's the focus of research in modeling and visualization narrowed to studying the fundamentals of the non-Newtonian flow of polymers in idealized

geometries. Instead of using actual injection molding machines or extruders many researchers used capillary rheometers with glass dies to visually study polymer flow. An early example of the use of a glass die and a capillary rheometer is the melt fracture study of Tordella [8]. A popular technique, described by Schmidt [9], involved the preparation of special preformed polymer rods for the capillary rheometer. Colored pellets of the parent plastic were inserted into the solid polymer rod in specified locations. The rod was then fed into the machine. The resulting part would have bands of color that revealed the final location of the marker pellets. Although this technique actually measures gross displacements instead of velocities Schmidt was able to use it to demonstrate the fountain flow that results from the interacting extensional and shear flows at the melt front. White and Dee [10] combined this method with windowed molds to study mold filling phenomena. White [11] used this data for an analysis of isothermal and non-isothermal flow in rectangular molds. The transparent rheometer concept was also used by Oda [12] to study the effect of extrudate swell on jetting in mold filling, by Chan [13] to study the effects of glass fibers on the molding process, and by Lee [14] to study fiber orientation. A good summary of the results of this period relating flow effects to the characteristics of solid parts was given by White and Dietz [15]. A notable exception to the trend of using industrial polymers in simplified geometries is described by Anastas, Lynn and Brodkey [16]. This experiment used an extruder with a transparent barrel to process frozen pellets of plasticized polystyrene. In effect they used an idealized polymer to study an industrial machine. The investigation reported here differs from these studies in that it presents quantitative velocity information of the flow of an industrial polymer in an industrial injection molding machine.

In the late 1970's and 1980's the focus of research narrowed even further to the

study of idealized non-Newtonian liquids in idealized geometries. Well-characterized fluids and simple geometries allowed researchers to concentrate on fundamental rheological questions and on constitutive modeling. Coyle, Blake and Macosko [17] photographed fountain flow patterns in Newtonian and shear-thinning liquids and compared them to the results of Schmidt [9]. The simpler apparatus and idealized fluids gave better insight into the fountain flow process. Typical of this period was the large number of studies of the flow of non-shear thinning elastic liquids (the so-called Boger fluids) in abrupt contractions. These studies investigated the impact of elasticity on the flow of non-Newtonian liquids and have been well described by Boger [18]. Most of these studies involved visualization of the streamlines in a steady flow through the use of long exposure photography. Fluids with different viscoelastic properties showed very different streamline patterns. In contrast, the results presented here are quantitative measures of the unsteady flow of an industrial plastic flowing in a mold in an industrial molding machine.

From the early 50's until the late 70's most of the flow visualization experiments of polymers and polymeric liquids consisted of forensic studies on solid parts, observation of steady state streamlines through transparent molds and dies, observation of fluid stress patterns through flow birefringence, and front tracking. The forensic studies included the inspection of short shots to observe the flow of plastic in molds, the marker pellet method described above [9], and the use of birefringence on solid parts to observe the effects of flow parameters on the locked in strain orientation [2].

These studies had many inherent limitations. Visualization of streamlines could only provide quantitative information about the streamlines themselves, not the velocity field itself, and were limited to steady flows. Front tracking and flow birefringence could give some quantitative measure of the flow, but again the velocity field

could not be measured directly. The forensic studies were limited because they could not be used to study the polymer melt flow directly. Rather, the effects of the flow on the solid part were used to deduce facts about the flow itself.

Forensic methods are still being used today, often in conjunction with other methods of investigation. For example, Hobbs [19] used short shots to complement his investigation of weld line morphology using optical micrographs. Chen, Hsu and Jung [20] have used co-injection molding to mold parts from clear and colored polystyrene. The colored polymer was used late in the molding cycle during packing flow to highlight the packing flow penetration in the solid part. Yokoi, Kamata, and Kanematsu [21] used a coil to produce a magnetic field around the gate of an injection mold. A magnetic powder was mixed with the plastic. The coil was then energized at desired intervals, magnetically marking the polymer that flowed through the gates. The final location of these magnetically marked particles gave information about the flow field, but again in contrast to the current work detailed velocity field information could not be extracted.

Front tracking is also an active area of research. Yokoi, Watanabe and Oka [22] used a mold with a glass insert to study the formation of weld lines using front tracking methods. Weissenberger, Giacomin, Reuscher and Russell [23] have used neutron radiography to observe mold filling in an aluminum mold. No glass windows were required. In 2004 Özdemir et. al. [24] used front tracking in a glass-inserted mold to study melt-front advancement and compared experimental data to Moldflow simulations.

Melt flow visualization has been used to address other molding problems as well. Yokoi et al. [25] used a glass-inserted mold to study jetting during mold filling. Yokoi [26, 27] also used this mold to study the formation of surface defects known

as flow marks.

A major limitation of all of these methods is that point velocity data and velocity vector field data is difficult, if not impossible to obtain. This began to change in the mid 1970's. Experimenters in the field of Newtonian fluid mechanics had been using lasers to perform non-intrusive point velocity measurements since the mid 1960's. Laser doppler velocimetry (LDV) was used to measure velocities at discrete points in water and air flow fields. A good overview of the development of LDV has been given by Penner and Jerskey [28]. LDV has been used on non-Newtonian flows since the mid-70's. An early example is Ramamurthy's use of LDV to study die flow instabilities [29]. Mackley and Moore [30] used LDV to make velocity measurements of polyethylene flowing into a slit. A 1995 article by Ahmed and Mackley [31] describes the use of LDV and flow birefringence to study the flow of polyethylene in a glass walled slit die. Yalamanchili [32] used LDV to study the flow of dilute polymer solutions through corrugated channels in the same year.

This was a major step forward in the visual study of Newtonian and non-Newtonian flows. For the first time optically transparent molds could be used to generate detailed, quantitative measurements of melt flow velocities. LDV, though limited to point measurements in transparent fluids, gave accurate measurements of velocities as a function of time in unsteady flows. Even with these advances, though, there were still major limitations. Flow fields are more important in fluid mechanics than flow at a particular point. Shear stresses and velocity gradients are intimately linked, and measurement of velocity gradients requires planar measurements of velocity.

The use of lasers has also allowed vector field information to be obtained. Lasers can been used to produce thin sheets of light. Seed particles are used to track the flow dynamics. Prior to the development of lasers seed particle studies were full-field

for the most part. The advantage that the laser brought was the ability to selectively illuminate particles in specific planes.

The simplest way to extract velocity information from a laser and seed particle experiment is to simply use long exposures to capture the pathlines of a steady flow. This was done in 1991 by Tremblay [33] to study the flow of polyethylene blends in a capillary rheometer through sudden contractions. Individual particles were not tracked, but the superposed pathlines provided information about the nature of the flow. This technique has limitations in unsteady flows.

Short exposure photographs can also be taken to capture particle pathlines. If the exposure is long enough to capture portions of the particle pathlines and short enough that these pathline fragments are linear then the velocity vectors of the particles may be estimated from a single image. This technique was used successfully by Kröger and Rath [34] to study the flow field in a device designed to measure elongational viscosity using exposures of 0.5 seconds. If the exposure is shortened further and the seeding density is low enough that individual particles may be identified and tracked from image to image then a pair of consecutive images may be used to estimate the particle velocity vector. This technique is known as particle tracking velocimetry (PTV). Yokoi and Inagaki [35] used a video camera to get 30 ms exposures of the flow of polystyrene in the thickness direction of an injection mold. Tehrani [36] used PTV to study particle migration in pipe flows of non-Newtonian fluids.

PTV is the logical first step towards measuring velocities in a plane. PTV could be used to measure not only fluid velocities, but velocity gradients. This meant that quantities such as vorticity and strain rate could be measured experimentally.

The main difficulty with this method is its requirement for low seeding density. Data analysis of PTV images requires clear pathlines (as in [34]) or it requires track-

ing each particle from frame to frame (as in [35]). In either case the seeding density needs to be low, resulting in low spatial resolution of the measured velocity field.

The seeding density issue can be overcome by pulsing the laser light to produce multiple exposures of the flow field. The overlapping images produce a speckle pattern that cause Young's fringes when illuminated with an interrogation laser. The orientation and spacing of the fringes at each interrogation point can be used to determine the in-plane components of the velocity vector. For very high seeding densities this method is called laser speckle velocimetry (LSV). This technique has been used to study the steady flow of a Boger fluid through a glass tube with a contraction [37]. For medium seeding density it is called particle image velocimetry (PIV). A thorough overview of these techniques has been given by Adrian [38] and a recent comprehensive practical guide has been written by Raffel, Willert and Kompenhans [39]. For medium seeding densities digital photography can be used to capture the images and cross-correlation techniques can be used to estimate the velocity field. The resolution is not as fine as on chemical film but it bypasses the need to develop photographs and interrogate them point by point with a laser. This variation of PIV is called digital PIV (DPIV) and has been described by Willert and Gharib [40]. The studies described herein use DPIV.

DPIV was used by Baumert [41] in 1997 to study flow instabilities in Boger fluids. This is one of the few recent attempts at using DPIV in a non-Newtonian fluid. But in this work extremely low particle seeding densities were used in conjunction with exceedingly long (25 second) exposures. The resulting images were processed as described by Willert and Gharib [40]. While technically this can be called a DPIV experiment, its seeding density and exposure time set it outside the norm of standard PIV experiments. Pakdel and McKinley [42] performed a series of experiments on

non-Newtonian solutions and Boger fluids in various geometries. Their studies used a standard CCD camera and more typical particle seeding densities and were true DPIV experiments in non-Newtonian fluids.

The current state of the art in the field of polymer flow investigations is the use of PTV or LDV with model fluids in simplified geometries. For example, in 2002 Giri Kollo et. al. [43] used PTV to study the fountain flow effect of a single phase viscoelastic fluid (liquid soap) in a cylindrical geometry. In 2004 Michaeli and Blömer [44] used LDV to study the flow of a pumped model fluid in a model spiral die at room temperature. PIV has been used to study non-Newtonian fluids at room temperatures and pressures and in simple geometries [42]. At the present time true PIV has not been used to study polymer melts flowing under injection molding conditions.

1.3 Previous Work on the Visualization of Residual Stress

The photoelastic effect was first discovered by Sir David Brewster [45, 46] and has long been used to study stress distributions in transparent plastic parts. The molecular orientation of the part at any given point is a result of the residual strain at that point, and this orientation in turn determines the index of refraction tensor at that point. The residual strains in an elastic part determine the residual stresses as well, and measurements of the components of the index of refraction tensor at a point can be used to experimentally determine the residual strains and stresses at that point using the stress-optic rule.

Measurements of the index of refraction tensor components can be made with a polarimeter. The residual strain field in a plastic part causes fringe patterns to appear in the part when the part is placed in the polarimeter. Observations of the

fringes due to index of refraction differences can then be translated into observations about the residual strain and stress fields. The current study exploits prior work in this area to provide documentary information about residual stresses in injection molded parts.

This is a mature area of study and there are many introductory texts on the subject. Experimental stress analysis in general is well-presented by Dally [47] and by Hendry [48]. A classic two-volume text on photoelasticity was written in the 1940's by Frocht [49, 50]. The subject of three-dimensional photoelasticity was addressed by Aben [51] and a modern treatise on digital photelasticity was presented by Ramesh [52]. Polarization of light and its application to photoelastic studies is treated by Huard [53]. Matrix methods in photoelasticity are presented very practically by Gerrard and Burch [54] and with more theoretical details by Theocaris and Gdoutos [55].

Birefringence studies of polymers can be divided into two broad categories, flow birefringence in the molten state and residual stress birefringence in the solid state. Some researchers have combined the two, such as in a 1978 study by Han [56]. Han filmed the flow birefringence patterns of polystyrene during injection and then measured the residual stress after the part had solidified. Flow birefringence studies in themselves are not directly relevant to the present work, but they are interesting to note since they all involve visualization of the flow of non-Newtonian liquids.

Many researchers have used flow birefringence to study the flow of polymer melts and other non-Newtonian liquids. White and Baird [57] used flow birefringence to study planar entry flows of polymer melts. Subramanian [58] used a similar technique to test constitutive equations for polymer melts. A notable feature of these two works is that they use polymer melts in industrial equipment. Saito [59] built an elaborate

optical access mold designed for polarized light. He studied the flow birefringence during the shot to visualize stress gradients in a flow around an obstruction.

It is interesting to note that while the object of these flow birefringence studies is different than that of the present work (measurement of stress fields during flow as opposed to measurement of velocity fields during flow), they are much closer to the present work in spirit than the velocity field studies previously cited. Flow birefringence researchers have been more willing to study the flow of industrially relevant polymers in industrially relevant equipment than their flow velocity colleagues. Perhaps this is because the phenomena of flow birefringence is non-Newtonian in nature and has been developed by researchers interested in the flow of polymer melts and solutions. In contrast, PIV had its genesis in Newtonian flow studies and has not yet been fully embraced by the non-Newtonian flow community.

1.4 Summary

The goal of the present work has been to study the melt flow of an industrially relevant polymer in industrially relevant equipment using standard analysis techniques and techniques not yet adapted to this type of flow. This goal is reflected in the experimental design. The flow studies presented here are of a Dow STYRON 615 APR polystyrene melt flowing in a Cincinnati Milacron VS33 injection molding machine. True DPIV was used to study the flow, with seeding densities and frame rates typical of Newtonian DPIV studies. Information about the residual stresses was extracted using a standard polariscope. In this way modern experimental techniques have been used to provide quantitative results in an area of research that was qualitatively explored fifty years ago.

CHAPTER 2

Experimental Design and Setup

A general schematic of the experimental setup can be seen in Figure 2.1. First, the particles and plastic pellets were weighed and mixed together. Then the pellet and particle mixture was poured into the hopper of the injection molding machine and a shot was manually prepared in the barrel.

The CCD camera was then placed in a free running mode with an open shutter. The vertical sync signal was stripped from the camera and used to synchronize the pulsed laser to the camera frame rate. The lab was then darkened and a movie recording initiated on the the computer.

The injection molding machine cycle was then started. The laser illumination was manually controlled during the shot to offset illumination problems due to the motion of the flow front. At the end of the cycle the image acquisition was ended. The part was removed, labeled and stored for residual stress measurements with a polarimeter.

The experimental setup can be divided into these broad categories:

Polymer Melt and Particles Includes the particle and polymer selection and characterization of the polymer-particle melt

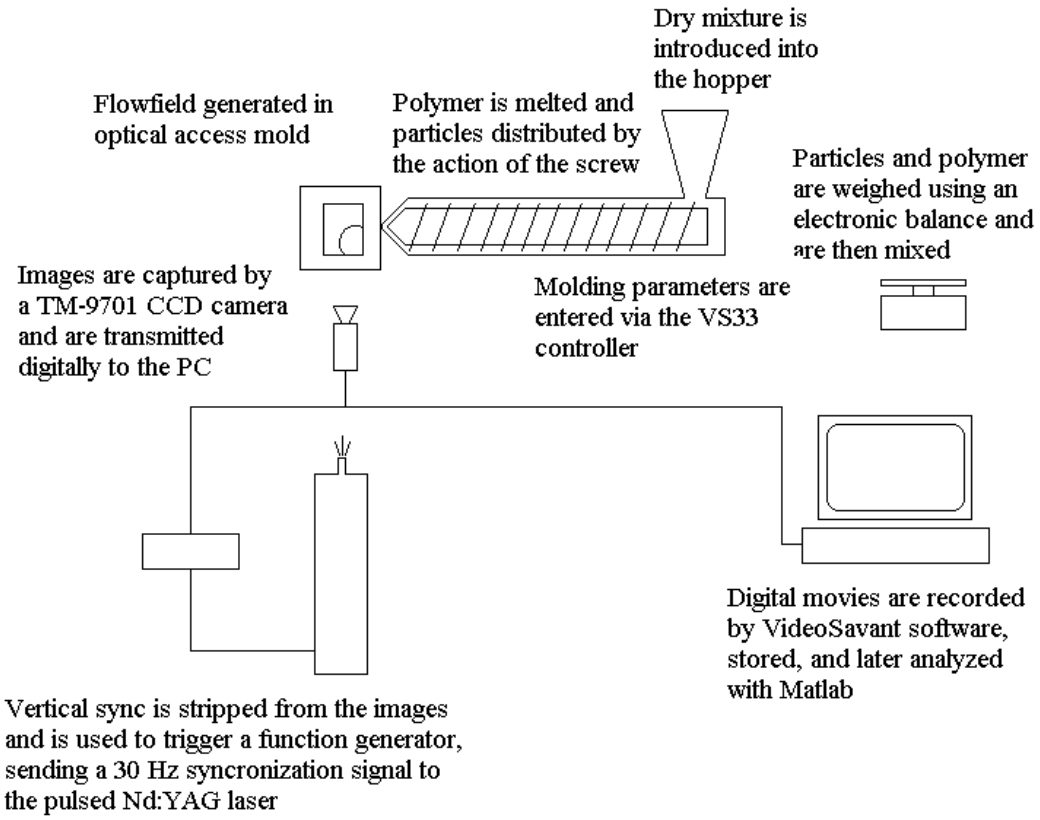

Figure 2.1: Schematic of the experimental setup

Flow Generation Includes the injection molding machine, the optical access mold and the auxiliary melt pressure and mold temperature measurements

Image Capture Includes the laser, sheet-producing optics, CCD camera, frame-grabber and image recording software

Residual Stress Measurements Includes birefringence measurements with a polarimeter and null-balance compensator

Each of these categories will be discussed separately below. First, a comment about variable naming conventions. This chapter deals with rheology and polarimetry and both fields often have different meanings attached to common variable names. For instance, λ typically stands for wavelength in polarimetry and time constants in rheology. In this chapter λ will refer to wavelengths, τ will be used for time constants, and σ will be used for stresses.

2.1 The VS33 Injection Molding Machine

The Vista-Sentry VS33 is an injection molding machine capable of generating 30 metric tons of clamp force and a 100 gram shot capacity. Machines this size are commonly used in industry to make small plastic parts. The specifications of the Vista-Sentry VS33 injection molding machine are listed in Table 2.1 [60]. The machine itself is shown in Figure 1.1.

2.2 PIV Particles

Many types of particles were tried during the course of this experiment, as discussed in Section 3.2. The particle that was finally chosen for this work is manufactured under the trade name Alu*flake by the Glitterex corporation. These particles

Table 2.1: Specifications of the Cincinnati Milacron VS33 injection molding machine

Specification	English	Metric
Max. Displacement	6.83 in^3	111.96 cm^3
Max. Injection Pressure	18,156 psi	1252 bar
Max. Injection Rate	5.71 in^3/sec	93.68 cm^3/s
Injection Screw Stroke	4.33 in	110 mm
Screw Diameter	1.42 in	36 mm
Screw L/D Ratio	17.7:1	17.7:1
Max. Screw Speed	205 RPM	205 RPM
Torque at Screw	4800 in-lb	542 Nm
	@ 2475 psi	@ 170 bar
Number of Barrel Pyrometers	4	4
Total Heat Capacity	5.36 kW	5.36 kW
Max. Clamp Force	33 tons	30 tons
Max. Clamp Stroke	9.84 in	250 mm
Max. Ejector Stroke	3.15 in	80 mm
Max. Ejector Force	1.9 tons	1.7 tons

are highly reflective clear-coated aluminum flakes. These flakes are precision-cut squares that measure 0.004"$\pm$0.001" on a side with a thickness of 0.0005". As discussed in Section 3.2.3, the particles have an equivalent spherical diameter of 60μm. The a detailed analysis of the ability of these particles to track the non-Newtonian flow is discussed in Chapter 3.

2.3 STYRON 615APR

STYRON 615APR is a high flow, FDA compliant all-purpose resin typically used in medical, pharmaceutical, and packaging applications. It was chosen for this project because it is easy to mold, has excellent transparency, is used in industry, and is readily available. The physical properties of this material are shown in Table 2.2 [61].The injection molded mechanical properties of this material are shown in Table 2.3 [61].

One of the goals of this work is to provide benchmark data for those seeking to

Table 2.2: Physical, optical and thermal properties of STYRON 615APR as provided by Dow. The middle column designates the relevant ASTM standard governing the test method.

Physical Properties		
Melt flow rate (200° C/5 kg)	D 1238	14.0 g/10 min
Specific Gravity	D 792	1.04
Linear Thermal Expansion (10^{-5})	D 696	9.0 cm/cm/° C
Mold Shrinkage	D 955	.003-.007 cm/cm

Optical Properties		
Transmittance	D 1003	90%
Haze	D 1003	1%
Refractive Index	D 542	1.59

Thermal Properties		
Vicat Softening Temperature (120° C/hr, 1 kg)	D 1525-B	101° C
Deflection Temperature Under Load	D 648	
@ 0.45 MPa, Unannealed		88° C
@ 1.8 MPa, Unannealed		76° C

Table 2.3: Injection molded mechanical properties of STYRON 615APR as provided by Dow. The middle column designates the relevant ASTM standard governing the test method.

Impact Strength (12.7× 3.2 mm specimen)		
Notched Izod @23° C	D 256	16.0 J/m
Gardner Impact @23° C	D 3029	0.113 J

Tensile Strength (12.7× 3.2 mm specimen, 5 mm/min rate)		
Yield Tensile Strength	D 638	44 MPa
Ultimate Tensile Strength	D 638	44 MPa
Ultimate Elongation	D 638	1.5%
Tensile Modulus	D 638	2868 MPa

Flexural Properties (1.3 mm/min rate)		
Flexural Strength (3 point)	D 790	83 MPa
Flexural Modulus (3 point)	D 790	3130 MPa

model the flow of polymers during injection molding. Data will be presented related to the residual stresses in the form of birefringence measurements of the solid part, as described in Chapter 8. In order for this data to be useful to a modeler the stress-optic coefficient of the polymer must be known.

The stress-optic coefficient relates the difference in principal stresses at a point to the difference in index of refraction along the principal directions. In practice the difference in index of refraction is measured as a fringe order using a polariscope and a null-balance compensator as described in Section 2.9. The fringe order f is given by:

$$f = \frac{hc}{\lambda}(\sigma_1 - \sigma_2) \tag{2.1}$$

where h is the thickness of the specimen at the point of interest, c is the stress-optic coefficient for the polymer, λ is the wavelength of light used in the polarimeter, and σ_1 and σ_2 are the principle stresses at the point of interest. The stress-optic coefficient c is a material property of the polymer and is measured in Brewsters (Br), with one Brewster equal to 10^{-12} Pa^{-1}. The details of the measurement of c are given in Section 2.9. The value of c for the polymer used in this study was determined to be 8.0 $\pm$ 0.6 Br.

2.4 Characterizing the Polymer and Particle Mixture

Samples of the polymer and particle mixture were sent to DatapointLabs (`www.datapointlabs.com`) for material testing. Viscosity measurements were performed on a Goettfert Rheograph 2003 capillary rheometer using a representative mixture of STYRON615 APR pellets and Alu*flake particles. Dynamic tests were performed on a Rheometrics ARES cone and plate rheometer using 1" diameter disks cut from the center of plaques molded at 230° C at an injection rate of 23.0 cm^3/s. All tests

were performed at a temperature of 230° C. The full report from DatapointLabs can be found in Appendix A.

2.4.1 Shear-rate Dependent Viscosity of the Polymer and Particle Mixture

Viscosity data at high shear rates is best obtained with a capillary rheometer, while data at low shear rates more easily obtained with a cone and plate rheometer. For an oscillatory shear test the shear strain is given by

$$\gamma(t) = \gamma_0 \sin \omega t \tag{2.2}$$

where γ_0 is the strain amplitude and ω is the frequency. The resulting shear stress can be expressed as

$$\sigma_{12}(t) = \gamma_0 \omega \left[\eta'(\omega) \cos \omega t + \eta''(\omega) \sin \omega t\right] \tag{2.3}$$

where η' and η'' are material functions with the units of viscosity. A complex viscosity can then be defined as

$$\eta^*(\omega) \equiv \eta'(\omega) - i\eta''(\omega) \tag{2.4}$$

The magnitude of the complex viscosity as a function of frequency of the polymer and particle blend used in the present work is plotted in Figure 2.2.

The Cox-Merz Rule [62] predicts that the magnitude of the complex viscosity is equal to the viscosity measured at corresponding values of frequency and shear rate:

$$\eta(\dot{\gamma}) = |\eta^*(\omega)|, \quad \omega = \dot{\gamma} \tag{2.5}$$

This rule was used to superpose the low frequency complex viscosity data ($\omega < 1$ rad/s) with the viscosity data obtained by the capillary rheometer. The resulting viscosity curve is shown in Figure 2.3.

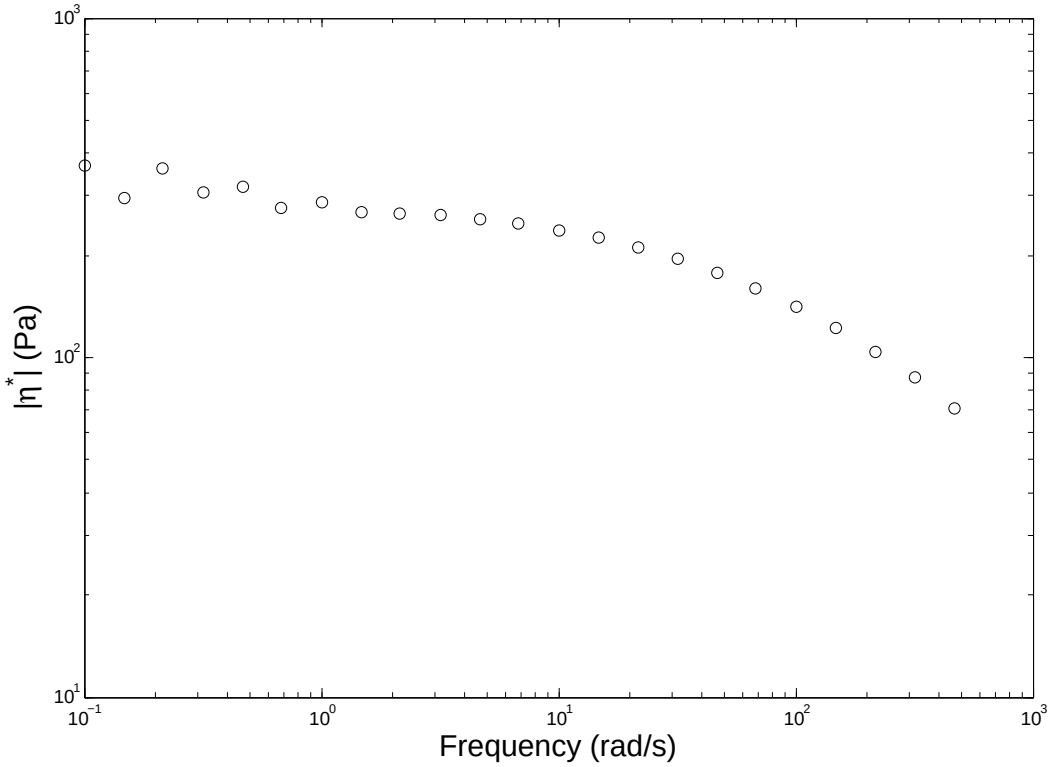

Figure 2.2: Complex viscosity data for STYRON 615APR with 0.02% (by weight) loading of aluminum flakes at a temperature of 245° C obtained by an ARES cone and plate rheometer (viscosity error ±1.17%).

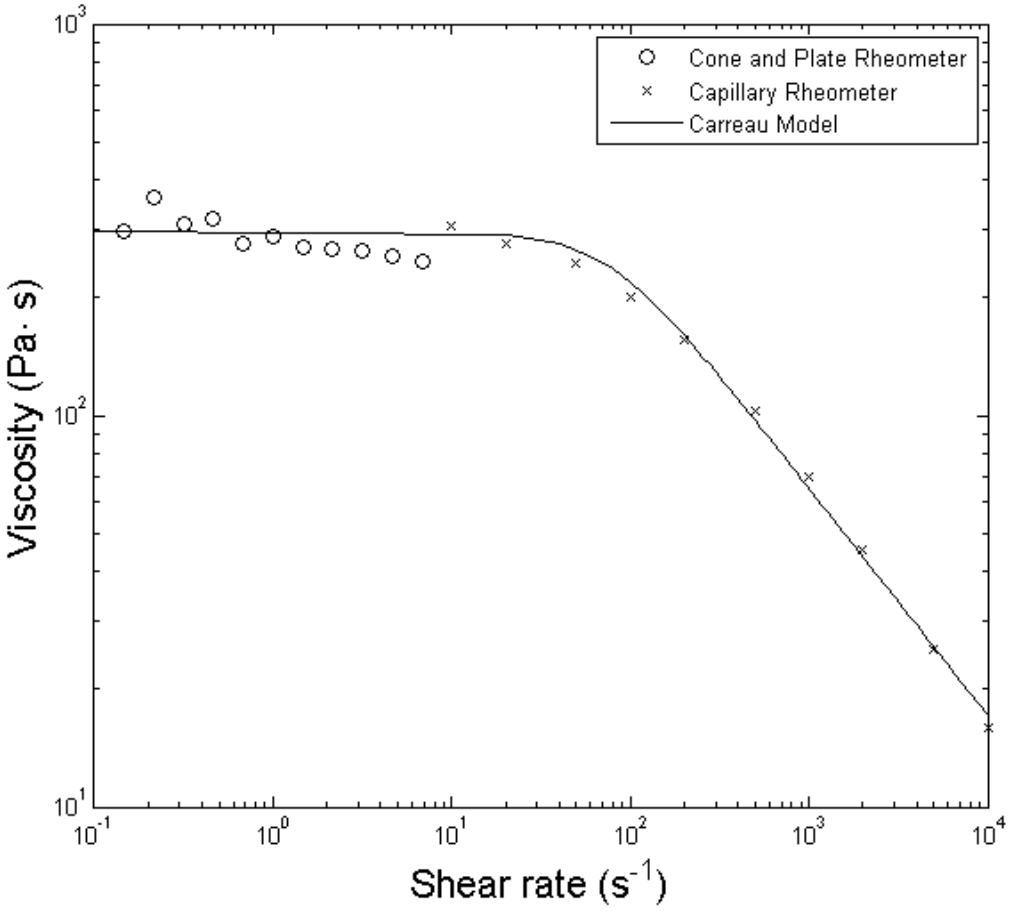

Figure 2.3: Viscosity data for STYRON 615APR with 0.02% (by weight) loading of aluminum flakes at a temperature of 245° C. The circles represent the magnitude of the complex viscosities determined by an ARES cone and plate rheometer (viscosity error ±1.17%). The squares represent data taken with a Goettfert Rheograph 2003 capillary rheometer (viscosity error ±2.49%). The Cox-Merz rule was used to combine the two data sets. The solid line represents a best-fit of the Carreau model with constants $\eta_0 = 295.43$ Pa·s , $\tau = 0.0193$ s, and $n = 0.4179$.

This viscosity curve can be fitted using the Carreau model [63]

$$\eta = \eta_0[1 + (\tau\dot{\gamma})^2]^{\frac{n-1}{2}} \tag{2.6}$$

where η_0 is the zero-shear viscosity, λ is a time constant, and n is the power-law exponent. MATLAB was used to fit the Carreau model to the combined viscosity data shown in Figure 2.3. The best-fit Carreau parameters are $\eta_0 = 295.43$ Pa·s , $\tau = 0.0193$ s, and $n = 0.4179$.

At high strain rates the Carreau model reduces to the power law model

$$\eta = m\dot{\gamma}^{n-1} \tag{2.7}$$

with n=0.4179 and $m = \eta_0\tau^{n-1} = 2940.6$ Pa·s ^{n}.

2.4.2 Impact of PIV Particles and Molding History on the Shear-rate Dependent Viscosity

Chapter 3 addressed the question of how well the PIV particles track the polymer melt flow. Another question of interest relates to the effect of the particles on the properties of the base polymer. Do the particles change the flow behavior of the polymer? Yet another question relates to the shear history of the polymer. Computer simulations usually use the properties of virgin material when calculating the melt flow even though the material has undergone significant shearing in the barrel of the injection molding machine and during its passage through the runners and gate of the mold. Is this a valid assumption?

To address these questions several tests were made using an Instron 1611 capillary rheometer at the University of Michigan shown in Figure 2.4. Viscosity curves were generated using virgin STYRON 615APR pellets with and without particles. In addition, several molded specimens were made with and without particles. These specimens were sawed into pellet-sized pieces and were also tested in the capillary

Figure 2.4: Instron 1116 Capillary Rheometer

rheometer. The data was reduced using the Rabinowitch correction as described by Brodkey [64]. The results are shown in Figure 2.5. This figure shows data from four different materials: virgin polymer pellets, virgin polymer pellets with 0.02% by weight PIV particles, molded polymer without particles, and polymer molded with 0.02% by weight PIV particles. All tests were performed at 230° C using a capillary with 1.0035"±0.001" length and 0.0501"±0.5% diameter.

The superposition of the curves in Figure 2.5 shows that the presence of particles and the molding history do not affect the shear-thinning viscosity of the base polymer.

2.4.3 Linear Viscoelastic Properties of the Polymer and Particle Mixture

The linear viscoelastic properties of a polymer can be characterized by the relaxation modulus $G(t)$[63]. The most popular way represent the shear relaxation modulus in functional form is through the use of the generalized Maxwell model [62].

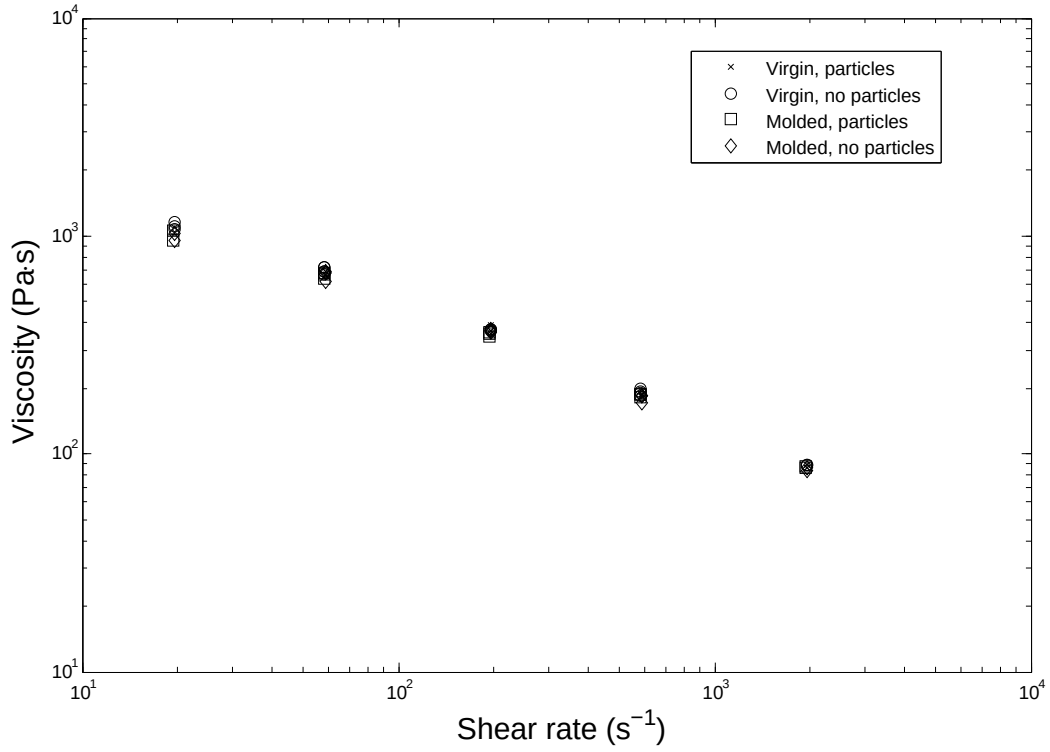

Figure 2.5: Viscosity data for virgin and molded STYRON 615APR with and without 0.02% (by weight) loading of aluminum flakes at a temperature of 230° C (viscosity error ±4%). The superposition of the curves indicates that the molding history and presence of particles do not affect the shear-thinning viscosity of the base polymer.

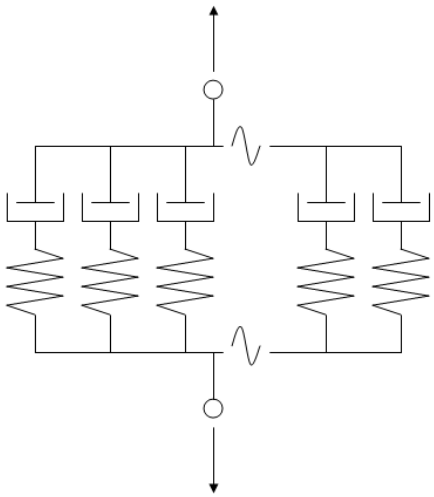

Figure 2.6: Mechanical analog for the generalized Maxwell model.

In this model the rheological constitutive equation is analogous to a parallel assembly of N Maxwell elements as shown in Figure 2.6. Each Maxwell element consists of a spring and dashpot in series. The shear relaxation modulus of a single Maxwell element is given by

$$G(t) = G_i e^{-t/\tau_i} \tag{2.8}$$

where G_i and τ_i are the relaxation strength and relaxation time of the Maxwell element. In the generalized Maxwell model the elements are additive and the overall relaxation modulus is given by

$$G(t) = \sum_{i=1}^{N} G_i e^{-t/\tau_i} \tag{2.9}$$

As the number of Maxwell elements approaches infinity the collection of relaxation times and strengths can be replaced by a continuous relaxation spectrum H [65]:

$$G(t) = \int_{-\infty}^{+\infty} e^{-t/\tau} H(\ln \tau) d(\ln \tau) \tag{2.10}$$

The relaxation spectrum is also related to the storage modulus G' and loss mod-

ulus G" [65]:

$$G'(\omega) = \int_{-\infty}^{\infty} \frac{H(\ln\tau)\omega^2\tau^2}{1+\omega^2\tau^2} d(\ln\tau) \tag{2.11}$$

$$G''(\omega) = \int_{-\infty}^{\infty} \frac{H(\ln\tau)\omega\tau}{1+\omega^2\tau^2} d(\ln\tau) \tag{2.12}$$

The storage and loss moduli are measures of the amount of energy stored and dissipated during an oscillatory shear test. The measured shear stress in such a test can be expressed as

$$\sigma_{12}(t) = \gamma_0 \left[G'(\omega)\sin\omega t + G''(\omega)\cos\omega t\right] \tag{2.13}$$

Comparison with Equation 2.3 shows that $G' = \omega\eta''$ and $G'' = \omega\eta'$.

In the present work the relaxation modulus of the polymer-particle mixture was not measured directly. The storage and loss moduli were measured directly, though, so in principle Equations 2.11 and 2.12 can be used to determine the relaxation spectrum H. Once the spectrum is known Equation 2.10 can be used to calculate the relaxation modulus.

In practice this is difficult for a number of reasons. First, as Dealy [62] points out, rheometers are limited to a range of a few decades of frequency and the reliability of the inferred H curve decreases rapidly as $\tau \to \omega_{min}^{-1}$ and $\tau \to \omega_{max}^{-1}$, where ω_{max} and ω_{min} are the largest and smallest frequencies at which experiments were possible. A second difficulty arises from the form of Equations 2.11 and 2.12. These equations are Fredholm equations of the first kind and inverting them is an ill-posed problem. Any approximation of H from these equations will be non-unique. Honerkamp and Weese [66] have shown that the use of a mathematical technique known as classical Tikhonov regularization can be used to calculate a discrete spectrum from experimental data that converges to the continuous spectrum as the number of Maxwell elements is increased.

Honerkamp [66] used a FORTRAN program called FTIKREG (Fast TIKhonov REGularization) [67] to extract relaxation spectra from rheometer data. As an example of how FTIKREG works, assume that it is desired to find the spectrum H from measurements of the storage modulus G'. Given a set of n data points g'_i with experimental errors σ_i and a trial spectrum H, the trial spectrum can be used to make estimates of the storage modulus G'_i using Equation 2.11. A relative error estimate ε is given by

$$\varepsilon = \sum_{i=1}^{n} \frac{1}{\sigma_i^2} \left(g'_i - G'_i\right)^2 \tag{2.14}$$

The program FTIKREG minimizes the expression

$$V(\Lambda) = \varepsilon + \Lambda \|LH\|^2 \tag{2.15}$$

where L is an operator and Λ is a the regularization parameter. The first term of this expression forces the trial function to approximate the experimental data. The second term leads to a smooth estimate of the spectrum H [67].

FTIKREG was used in the present work to extract the relaxation spectrum from the cone and plate rheometer data provided by DatapointLabs. The program solved Equations 2.11 and 2.12 simultaneously. The second derivative was chosen for the operator L and an additional constraint was imposed that the spectrum vanish smoothly at the upper and lower boundaries of the frequency range. The spectrum was calculated over the interval of 10^{-4} seconds to 10 seconds, the interval being dictated by the range of frequency of the rheometer data. The resulting spectrum is shown in Figure 2.7. The spectrum has six distinct peaks corresponding to six predominant relaxation times.

The spectrum was then used to generate the parameters of the generalized Maxwell model. The spectrum H in Figure 2.7 was first approximated as a set of six delta

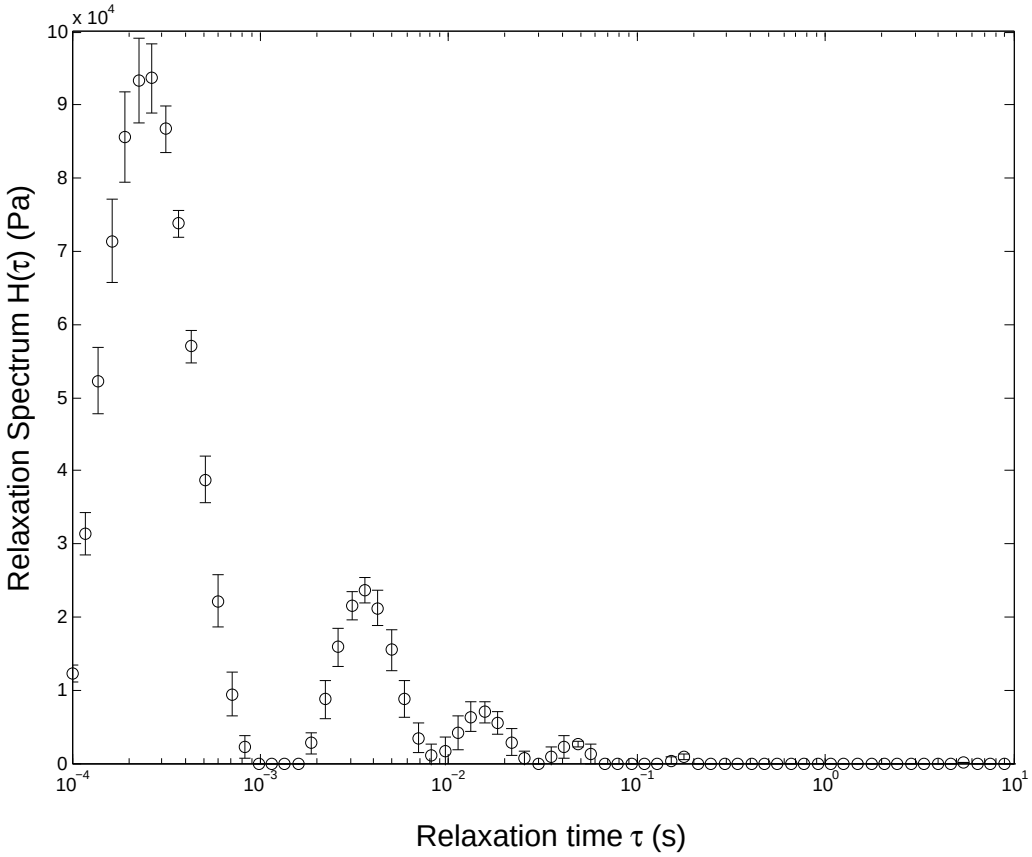

Figure 2.7: Relaxation spectrum of the polymer-particle mixture calculated by the program FTIKREG. The peaks of this spectrum were used to generate the relaxation times and moduli of the generalized Maxwell model used in Figure 2.8.

Table 2.4: Relaxation times τ_i and strengths G_i for a six-element generalized Maxwell model of the polystyrene-particle blend.

τ_i (s)	G_i (Pa)
2.66×10^{-4}	118872
3.59×10^{-3}	19881
1.56×10^{-2}	4653
4.86×10^{-2}	1146
1.79×10^{-1}	193
5.46	18

functions with each delta function centered at a peak of H. The coefficient of each delta function was set equal to the area under the corresponding peak of the spectrum. This resulted in a discrete spectrum $\hat{H}$ with the following form:

$$\hat{H} = \sum_{i=1}^{n} G_i \delta(\ln\tau - \ln\tau_i), \qquad G_i = \int_{peak} H d(\ln\tau) \tag{2.16}$$

where n is the number of peaks and τ_i are the times at which the peaks occur. Substituting $\hat{H}$ into Equation 2.10 gives

$$G(t) = \int_{-\infty}^{+\infty} e^{-t/\tau} \left(\sum_{i=1}^{n} G_i \delta(\ln\tau - \ln\tau_i) \right) d(\ln\tau) \tag{2.17}$$

$$= \sum_{i=1}^{n} G_i e^{-t/\tau_i} \tag{2.18}$$

which is the definition of the generalized Maxwell model given in Equation 2.9. The values of the relaxation times and of the corresponding relaxation strengths calculated by this process are shown in Table 2.4.

The magnitudes of the last two peaks in Table 2.4 are considerably smaller than the first four. Is it necessary to include them in the generalized Maxwell model? To answer this question the generalized Maxwell model parameters were evaluated by using them to calculate curves for G' and G'' using the following equations [62]

$$G'(\omega) = \sum_{i=1}^{i=N} \frac{G_i \omega^2 \tau_i^2}{1 + \omega^2 \tau_i^2} \tag{2.19}$$

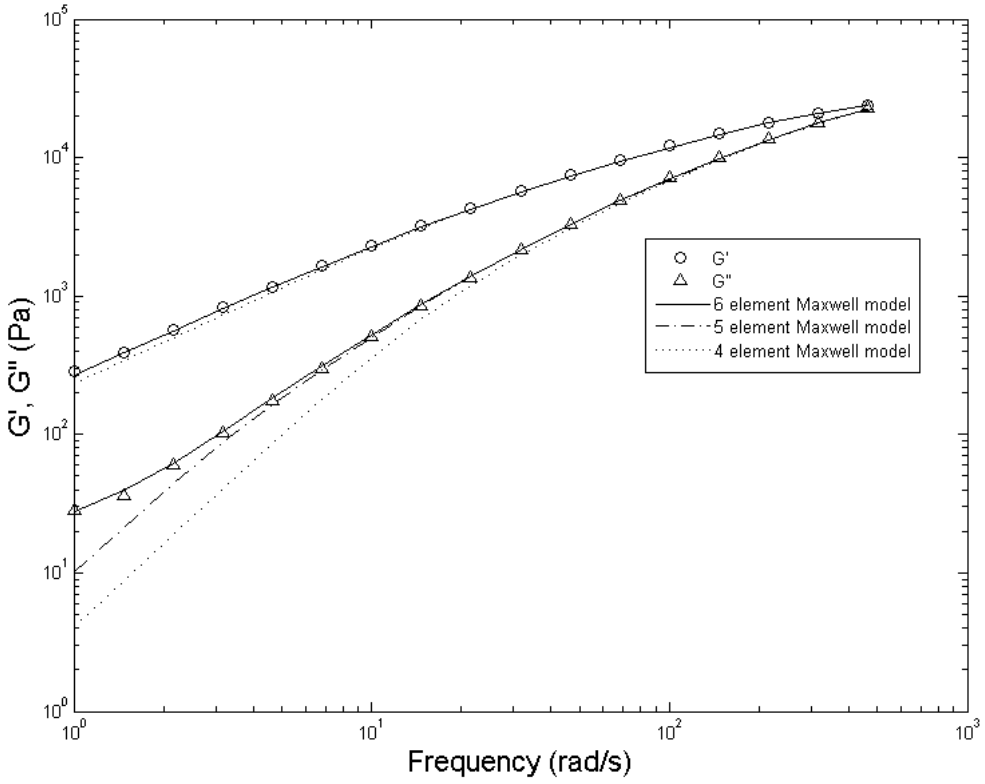

Figure 2.8: Storage and loss moduli for STYRON 615APR with 0.02% (by weight) loading of aluminum flakes at a temperature of 245° C, (error ±1.17%). The curves are the predicted values of G' and G" using four, five and six element generalized Maxwell models.

$$G''(\omega) = \sum_{i=1}^{i=N} \frac{G_i \omega \tau_i}{1 + \omega^2 \tau_i^2} \tag{2.20}$$

Three different n-element Maxwell models were compared, with each model using the first n entries of Table 2.4. The results of using a four-element, five-element and six-element model are plotted in Figure 2.8. From the figure it is evident that the G'' curve is well represented by the four-element Maxwell model. The number of Maxwell elements has a much greater impact on the G' curve. Figure 2.8 shows that only the six-element model adequately represents the G' data.

The relaxation modulus was then calculated from the six element Maxwell model using Equation 2.9. The result is shown in Figure 2.9.

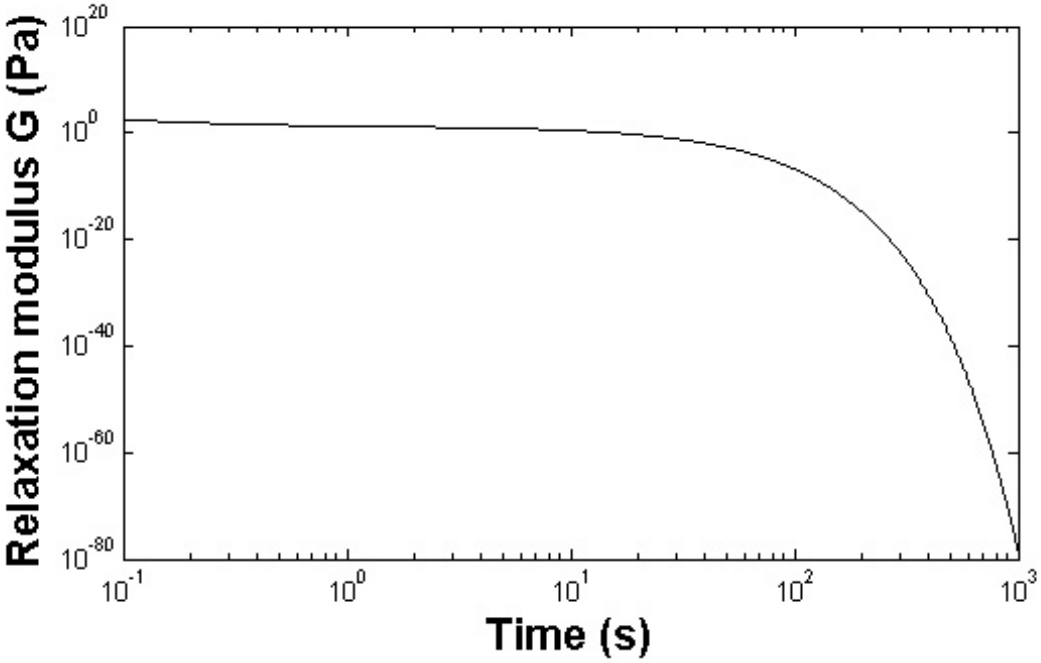

Figure 2.9: Relaxation modulus of STYRON 615APR with 0.02% (by weight) loading of aluminum flakes at a temperature of 245° C. The modulus was calculated using the six element generalized Maxwell model described in Table 2.4.

The relaxation modulus shown in Figure 2.9 can be used to cross-check the viscosity curve shown in Figure 2.3. In Figure 2.3 the low shear-rate data was calculated from the cone-and-plate rheometer data using the Cox-Merz rule since the capillary rheometer data did not extend below a shear rate of 1 s^s. This resulted in a zero-shear viscosity η_0 equal to 295 Pa·s . The theory of linear viscoelasticity can be used [63] to show that

$$\eta_0 = \int_0^\infty G(s)ds = \sum_i G_i \tau_i \tag{2.21}$$

Performing this calculation with the values shown in Table 2.4 gives $\eta_0 = 364$ Pa·s .

2.4.4 Nonlinear Viscoelastic Properties of the Polymer and Particle Mixture

The relaxation modulus discussed above is a linear viscoelastic property. Polymers also exhibit nonlinear viscoelastic effects, chief of which is the presence of normal stress differences under shear flow [63]. The first normal stress difference N_1 was measured by Datapoint Labs as a function of shear rate $\dot{\gamma}$ for the polymer-particle mixture. The quantity N_1 was calculated from the normal force F on the plate of radius R using the following formula [68]:

$$N_1 = \tau_{11} - \tau_{22} = \frac{2F}{\pi R^2} \tag{2.22}$$

From this data the first normal stress coefficient may be calculated [63]:

$$\Psi_1 = \frac{N_1}{\dot{\gamma}^2} \tag{2.23}$$

The resulting curve of Ψ_1 versus shear rate is shown in Figure 2.10.

2.4.5 The Deborah Number

The fundamental nondimensional group in non-Newtonian fluid mechanics is the Deborah number, *De* [69]. The Deborah number is defined as the ratio of the char-

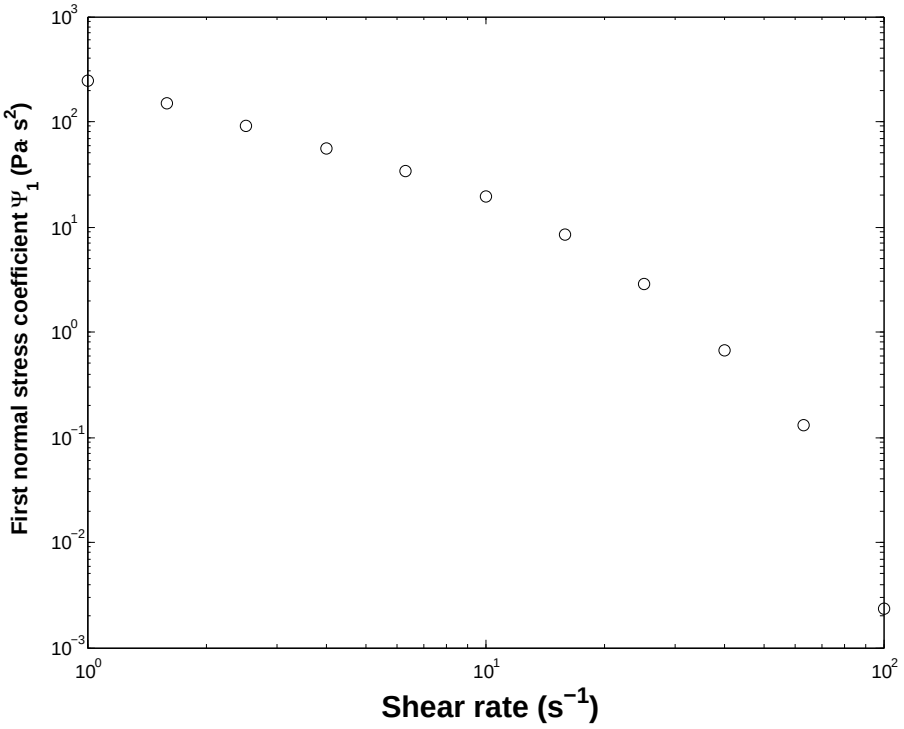

Figure 2.10: First normal stress coefficient Ψ_1 for STYRON 615APR with 0.02% (by weight) loading of aluminum flakes at a temperature of 245° C, (error $\pm 1.17\%$).

acteristic time of the fluid to the characteristic time of the flow. Solid-like behavior is observed for $De \gg 1$ and fluid-like behavior is observed for $De \ll 1$. Viscoelastic behavior is observed for $De \sim O(1)$.

The characteristic time of the flow may be taken to be the duration of the experimental observation [63], but there is no universally accepted way to calculate the characteristic time of the flow for any given situation. A variety of methods will be employed here and the results tabulated.

One approach is to use the time constant λ from the Carreau model, Equation 2.6 [70]. Using this method, the characteristic time of STYRON 615 APR is 0.0193 s.

Another method is to use the first normal stress coefficient, Ψ_1, to create a characteristic time linked to the elasticity of the flow [70]:

$$\lambda_T = \frac{\tau_{11} - \tau_{22}}{\tau_{12}\dot{\gamma}} = \frac{\Psi_1}{\eta} \tag{2.24}$$

In this formulation the characteristic time is a function of strain rate. Figure 2.11 was constructed using Equation 2.24 and the data provided by Datapoint Labs found in Appendix A. The characteristic time λ_T ranges from 0.86 seconds at a strain rate of 1 s^{-1} to 1.6×10^{-5} seconds at a strain rate of 100 s^{-1}, a strain rate typical of injection molding.

A characteristic time of the fluid can also be extracted from the $G(t)$ curve. Bird [63] shows that the ratio of integrals $\int_0^\infty sG(s)ds / \int_0^\infty G(s)ds$ appears in the solution of many linear viscoelastic problems, where G is the relaxation modulus and s is the elapsed time from a reference time t', $s = t - t'$. This integral has the units of time and Bird [63] points out that it is often used as the characteristic time of the fluid in the construction of the Deborah number.

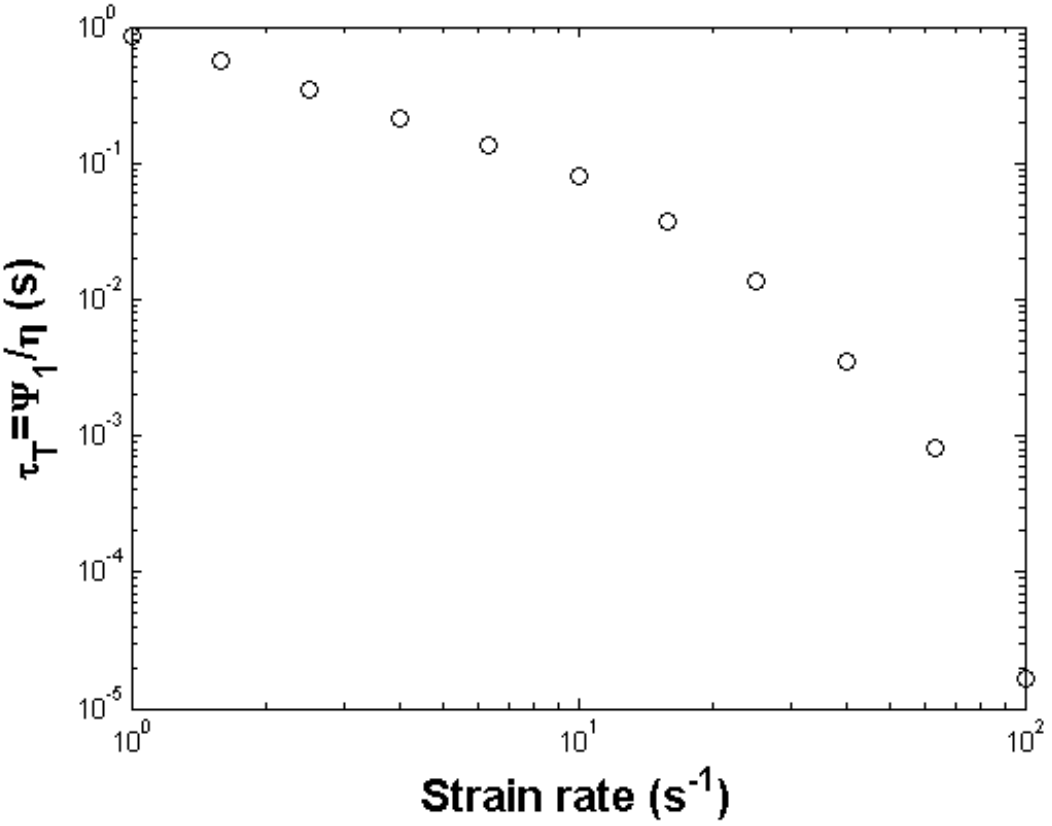

Figure 2.11: Characteristic time of the fluid based on the first normal stress coefficient Ψ_1 for STYRON 615APR with 0.02% (by weight) loading of aluminum flakes at a temperature of 245° C.

Carrying out these integrations using the generalized Maxwell model leads to the following expression for the characteristic time of the fluid τ_c:

$$\tau_c = \frac{\int_0^\infty sG(s)ds}{\int_0^\infty G(s)ds} = \frac{\sum_{i=1}^{N} G_i\tau_i^2}{\sum_{i=1}^{N} G_i\tau_i} \tag{2.25}$$

Substitution of the discrete Maxwell model parameters from Table 2.4 into Equation 2.25 gives a characteristic time of the fluid equal to 2.4 seconds.

It is curious that this last estimate of the characteristic time is orders of magnitude larger than the others described. The difficulty arises from the fact that a real polymer has a spectrum of relaxation times and each method weighs the individual relaxation times differently to calculate a single characteristic time of the fluid. This is well illustrated by a final calculation of the relaxation time recommended by Shenoy [70]. Shenoy [70] points out that the characteristic time for any material can be defined as the time required for a material to reach 63.2% or 1-1/e of its ultimate retarded elastic response to a step change.

Bird [63] shows that the stress growth at the inception of steady state shear flow in a linear viscoelastic fluid is given by

$$\tau_{xy} = \dot{\gamma}_0 \int_0^t G(t-t')dt' = \dot{\gamma}_0 \int_0^t G(s)ds = \eta^+\dot{\gamma} \tag{2.26}$$

where $\dot{\gamma}_0$ is the magnitude of the step change in the strain rate at time $t = 0$ with the restriction that the product of $\dot{\gamma}_0$ and the maximum relaxation time be much less than unity. The viscosity function η^+ can be calculated using the generalized Maxwell model parameters shown in Table 2.4. The result is shown in Figure 2.12, where it has been scaled by the zero-shear viscosity η_0.

The difficulty in choosing a characteristic time is immediately apparent. The viscosity curve climbs sharply, and then slows over a long period of time. The

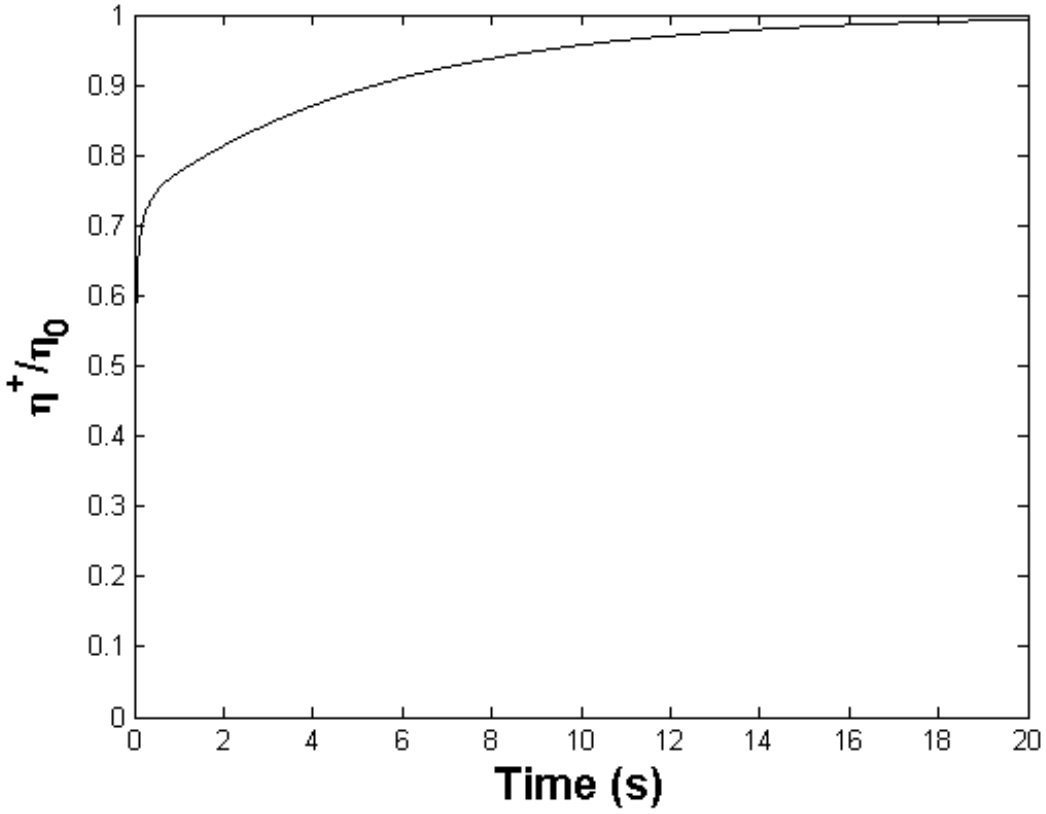

Figure 2.12: Stress growth function of an initially quiescent linear viscoelastic fluid that experiences a step change in strain rate.

viscosity curve reaches 63.2% of its final value in 0.07 seconds, but it takes 18 seconds to reach 99% of its final value. So using the 63% rule would give a time constant of 0.07. Using the rule of thumb that it takes four time constants to reach the final value would give a time constant of 4.5 seconds. This explains the time constants calculated above that range from 0.019 seconds to 2.4 seconds.

In addition to the difficulty in establishing a characteristic time of the fluid, the characteristic time of the flow varies with injection rate. In the present work the fastest mold fill time was 1.3 seconds, and the slowest was 4 seconds. The range of Deborah numbers corresponding to the different estimates of the characteristic time discussed above are shown in Table 2.5.

Table 2.5: Deborah numbers based on varied calculations of the characteristic time of the fluid. The "Reference" column gives the Figure or Equation that the estimate was based upon. The minimum and maximum Deborah numbers are based on fill times of 4 seconds and 1.3 seconds, respectively.

τ (s)	Reference	Min.	Max.
1.66×10^{-5}	Equation 2.24	4.15×10^{-6}	1.28×10^{-5}
0.019	Equation 2.6	0.00475	0.0146
0.07	Figure 2.12	0.018	0.054
2.4	Equation 2.25	0.6	1.8

Most of the estimates of the Deborah number shown in Table 2.5 are much less than unity. This would suggest that viscoelasticity would play little or no role in the flow studied in the present work. This suggestion was found to be accurate, as will be discussed in Chapter 5.

2.5 The Optical Access Mold

The heart of the flow field generation system is the optical access mold, specially designed for this experiment and described previously by Bress [71]. An isometric view of the closed mold can be seen in Figure 2.13. An exploded view of the mold components can be seen in Figure 2.14. See Appendix B for detailed drawings of the mold components and a brief explanation of their function.

A schematic of the mold cavity, windows, and cavity orientation with respect to the parting plane can be seen in Figure 2.15. The mold has a cavity that produces plaques with dimensions of 109.5 mm × 66.7 mm × 6.3 mm (4.3125" × 2.625" × 0.25"). The mold has three windows: two along the small faces at the top and bottom of the cavity (66.7 mm × 6.3 mm), and one along the largest face (109.5 mm × 66.7 mm). There is $\frac{1}{2}^\circ$ of draft along the top and bottom windowed faces as well as on the steel face opposite the large window to facilitate ejection of the molded

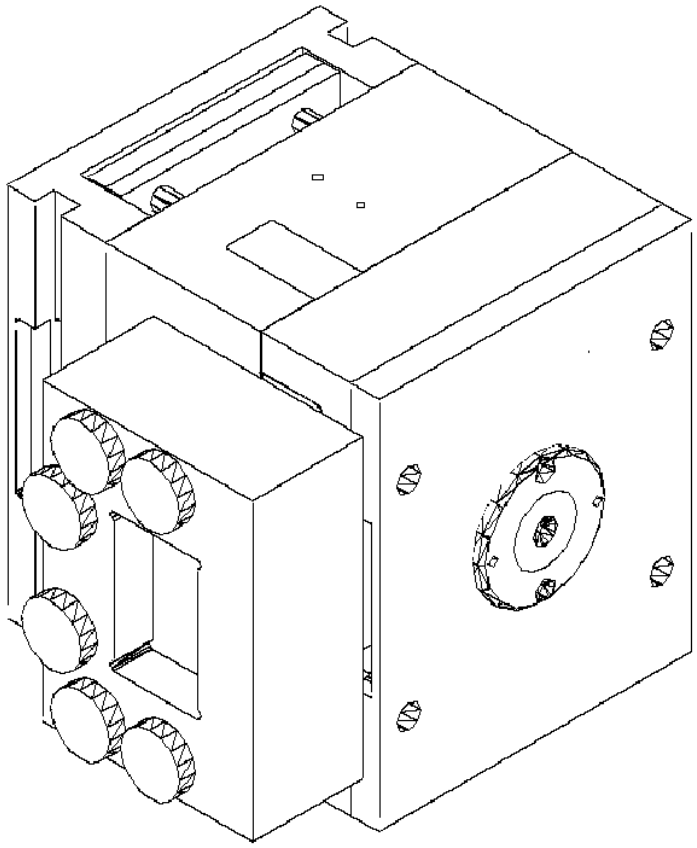

Figure 2.13: Isometric view of the optical access mold

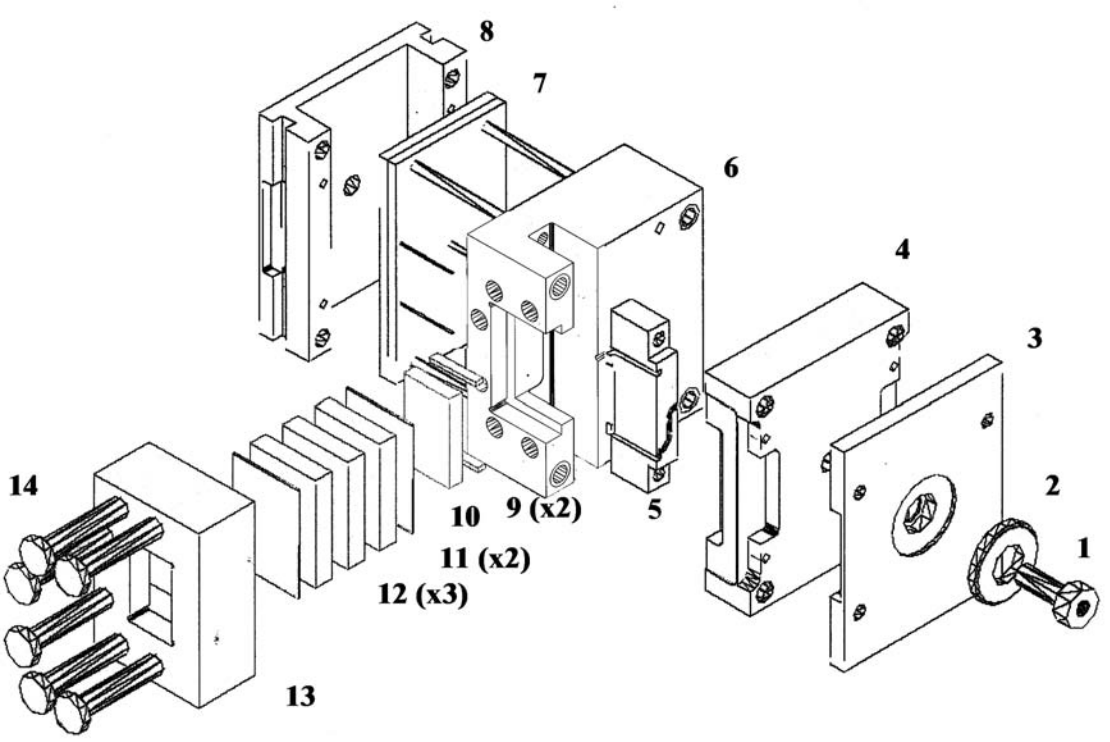

Figure 2.14: Exploded view of the optical access mold. 1. Sprue bushing 2. Guide ring 3. Top clamping plate 4. "A" plate 5. Cavity block 6. "B" plate 7. Front and rear ejector plates with ejector pins and return pins 8. Rear clamping plate 9. Acrylic entrance and exit windows 10. 0.75" thick quartz window 11. 0.125" thick polycarbonate shields 12. Three 1" thick glass plates 13. Steel window brace 14. Six 1" diameter hardened steel bolts

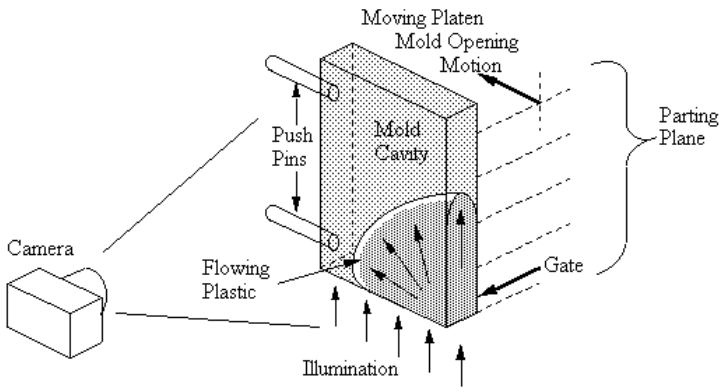

Figure 2.15: Melt flow visualization schematic. The liquid plastic enters the rectangular mold at the lower right corner. The mold cavity is contained within the portion of the mold base attached to the moving platen. The flowing plastic is viewed through a window over the planform area of the part. Light enters and exits the mold through the windows on its top and bottom.

parts. The mold cavity may be illuminated from either the top or bottom windows. In Bress [71] both approaches were used with a halogen source, in the current work a laser sheet entering from the bottom of the mold was used. The rectangular shape was chosen to allow planar windows for undistorted viewing and for ease of meshing in computational mold-filling studies.

Typically parts such as these would be made with one of the large 109.5 mm $\times$ 66.7 mm faces on the parting plane for easy part ejection. But as shown in Figure 2.15, the parts were made with one of the 109.5 mm $\times$ 6.3 mm faces on the parting plane. This unusual orientation allows full visualization of the mold cavity from the side of the mold facing the operator of the machine, and also extends the machine's clamping capability to parts with larger planform area. By placing a small edge in contact with the stationary half of the mold higher packing pressures can be used without flashing than would be possible in the more typical orientation.

This unusual choice of orientation comes at a price. The main disadvantage is

difficulty of part ejection. In the more typical orientation the only faces in frictional contact with the mold would be the four small edges. In the orientation necessary for visualization two of those small edges are substituted with the largest faces on the part. This necessitates longer cooling times to promote shrinkage, and at times loosening or removal of the window to remove the part. Another restriction resulting from this orientation is that the gate must be placed along the face that is in contact with the stationary mold platen. The gate may be placed anywhere on this face. In this study the gate is a semi-circular channel 3.125 mm in diameter that is centered 5 mm above the lower right corner of the part. See Figures 2.23 for more details.

An exploded view of the mold can be seen in Figure 2.14. The mold was designed as a solid model using AutoCAD. The main challenge was to design a window that could withstand the extremely high melt pressures found in the packing phase of a typical injection molding cycle. Finite element analysis was used to create a design capable of withstanding a 69 MPa melt pressure. The portion of the window in contact with the melt is a quartz block 19 mm thick. Quartz was chosen for its capability of withstanding significant temperature gradients. A 3 mm thickness of polycarbonate acts as a buffer between the quartz and three 25 mm thick pieces of plate glass. These are followed by another 3 mm thick layer of polycarbonate and the whole assembly is held in place by a steel brace and six hardened grade-eight 25 mm diameter bolts. The top and bottom walls of the cavity are also transparent. They can be formed by rectangular blocks of either quartz or acrylic and are held in place by slots machined into a steel block inserted into the mold base.

This steel insert is another notable feature of the mold design. The insert holds the quartz pieces that form the top and bottom of the mold, and forms the rear face and left side wall of the mold cavity. The thickness, length and width of the final

part are all determined by the steel insert. The number, type and location of the gates are also determined by the insert. Transducers of various types can be placed on the rear wall of the cavity by modifying the insert. The draft angles on all faces (except for that of the large quartz face, which has no draft) are also determined by the insert. The insert makes the optical access mold a modular design that can easily be adapted for different melt flow experiments. The insert was steam treated to give it a uniform blue-black finish, improving the image contrast of the PIV digital movies.

The mold was constructed from a DME mild tool steel mold base.

2.6 Image Capture

The imaging system consists of the following elements:

- Pulnix TM-9701 CCD camera
- PC with a Coreco Dig-SE frame grabber running Io Industries VideoSavant v3.0 software
- HP8116A Pulse/Function Generator
- Spectra-Physics Quanta-Ray Nd:YAG laser with sheet-producing optics

2.6.1 The Pulnix TM-9701 CCD camera

The Pulnix camera has a 30 Hz frame rate and was run in non-interlace mode to better freeze the particle motion. The camera provides 8 bit gray scale 640 pixels by 480 pixels images which are transmitted to the PC by a digital cable. The camera specifications can be found in Table 2.6.

The camera was modified to output a vertical sync signal through one of the pins on its power connection. This signal is used to trigger the HP pulse generator. The

Table 2.6: Specifications of the Pulnix TM-9701 progressive scanning full frame shutter camera

Imager	2/3" progressive scanning interline transfer CCD
Pixels	768 (H) × 484 (V)
Cell size	11.6μm × 13.6μm
Scanning	525 lines 30 Hz or 60 Hz 2:1 interlace
Resolution	8 bits (256 gray levels)
S/N ratio	50 dB min.
Min. illumination	1.0 lux, f=1.4
Gamma	1.0

pulse generator then sends a pulse train to the Spectra-Physics laser, specifically tailored to the laser's input sync requirements.

The camera was set to free-running mode with an open shutter. During an experiment the room lights are extinguished. Each time a new image frame was started the vertical sync pulse triggered the laser to fire. The laser fired in a quick burst, freezing the particle motion without need of shuttering the camera. Each image frame corresponded to a single pulse of laser light.

2.6.2 Calibration of the Pulnix-TM9701 Camera

All image systems suffer from distortion of one form or another. The distortion inherent in the digital images taken by the TM-9701 camera was compensated using a MATLAB software package written by Jean-Yves Bouguet [72].

A checkerboard pattern image target was used to calibrate the camera. The target consisted of alternating black and white 5mm squares. It was placed in the mold cavity in six different orientations as shown in Figure 2.16.

When the target was in place the mold was closed and a halogen lamp placed atop the mold directly above the light path. The safety gate was then closed and an image taken with the TM-9701 camera. Note that since the window is present

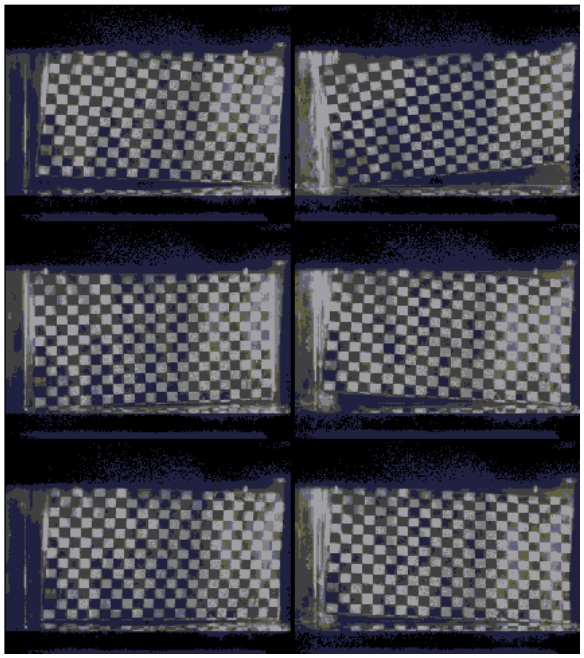

Figure 2.16: Calibrating the Pulnix-TM9701 camera with a checkerboard target.

and the safety gate is shut that all of the light-transmitting elements used to make digital movies of the melt flow are in place during the calibration.

The images were then processed by the Matlab calibration package. The calibration program located the corners of each square in the checkerboard pattern of the calibration images. The orientation of the checkerboards was then calculated and a sixth-order image distortion model was created. An example of the complete distortion model of the TM-9701 camera is shown in Figure 2.17. The radial component of the distortion model is shown in Figure 2.18 and the tangential component of the distortion model is shown in Figure 2.19.

Once the distortion model was calculated it was used to undistort the individual frames of the melt-flow movies. This step was performed prior to any other image processing. The distortion model did not correct for non-square pixels but it did provide a measurement of the pixel aspect ratio. That measurement was used to correct for non-square pixels after the PIV and melt front image processing had been

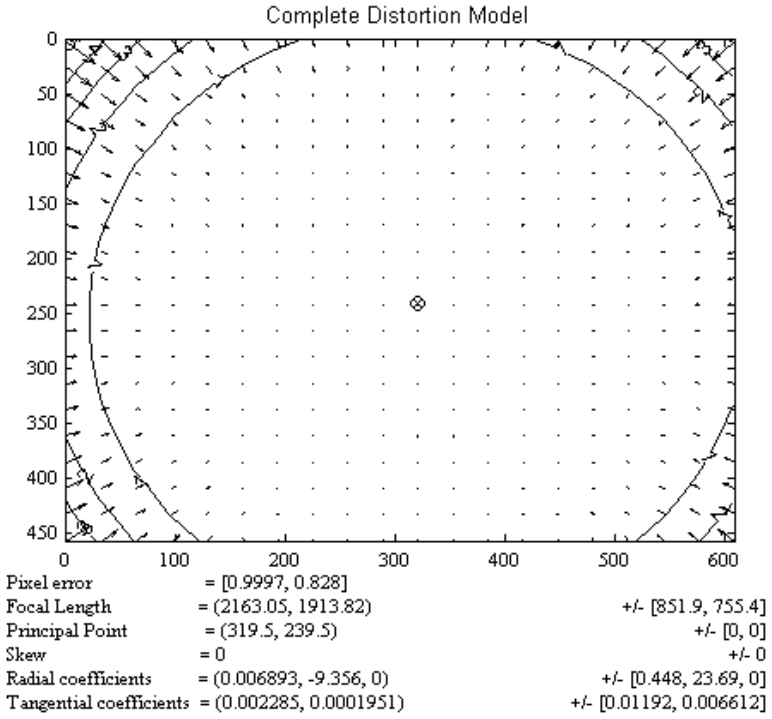

Figure 2.17: The complete distortion field of the Pulnix 9701 CCD camera

completed.

As an example, a raw image frame is shown in Figure 2.20. The result of running the undistortion program on this image is shown in Figure 2.21. These two images are hard to distinguish with the naked eye, but there are differences. These differences are illustrated in Figure 2.22, which shows the result of subtracting the undistorted image in Figure 2.21 from the raw image shown in Figure 2.20.

2.6.3 The Spectra-Physics Nd:YAG laser

A Spectra-Physics GCR-130-030 Nd:YAG laser was used. The laser produced a 2.8W beam of 532 nm coherent light. As described below, the laser was pulsed at the Pulnix TM-9701's frame rate of 30 Hz resulting in an energy discharge of 93 mJ/pulse. The laser was positioned on the floor in front of the injection molding machine at right angles to it. The laser was targeted at the open area underneath the

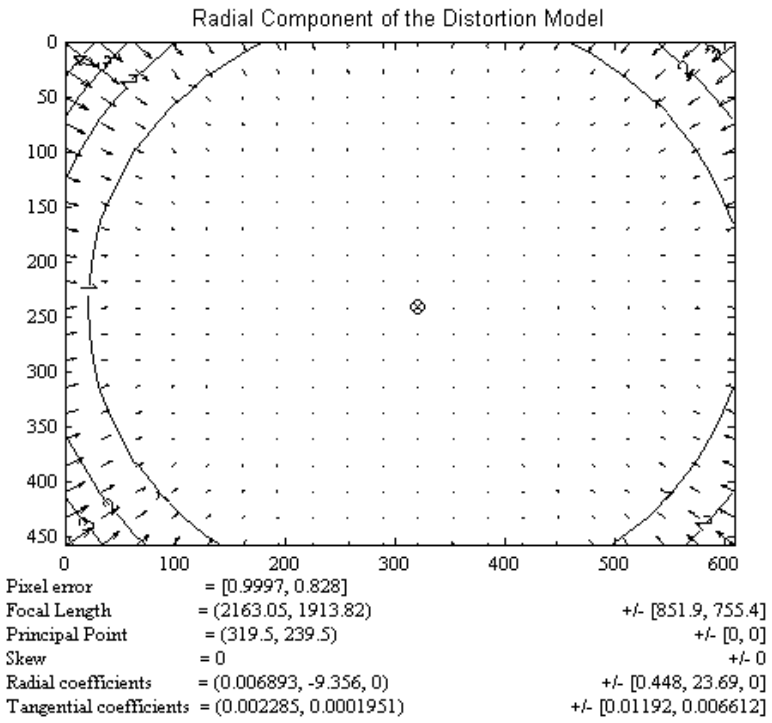

Figure 2.18: The radial component of the distortion field of the Pulnix 9701 CCD camera

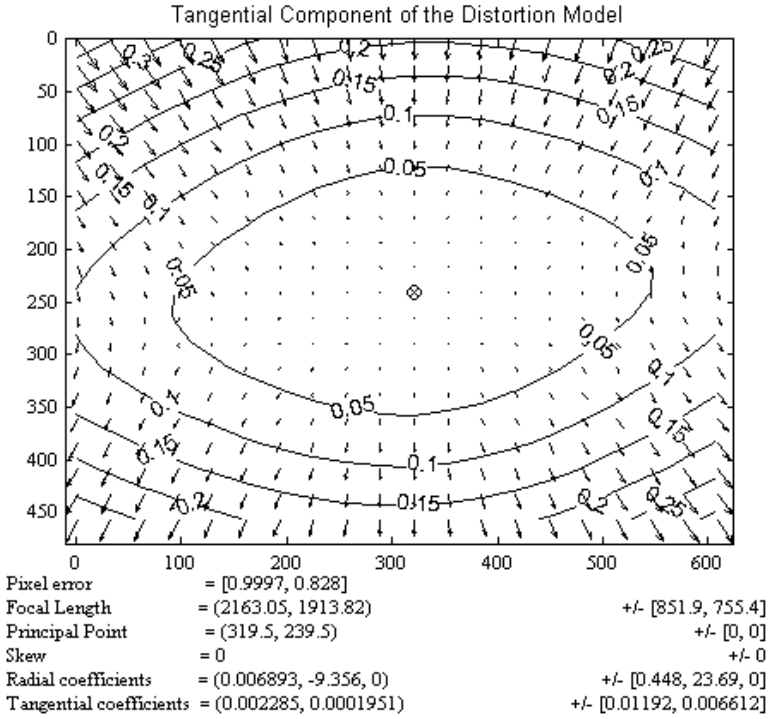

Figure 2.19: The tangential component of the distortion field of the Pulnix 9701 CCD camera

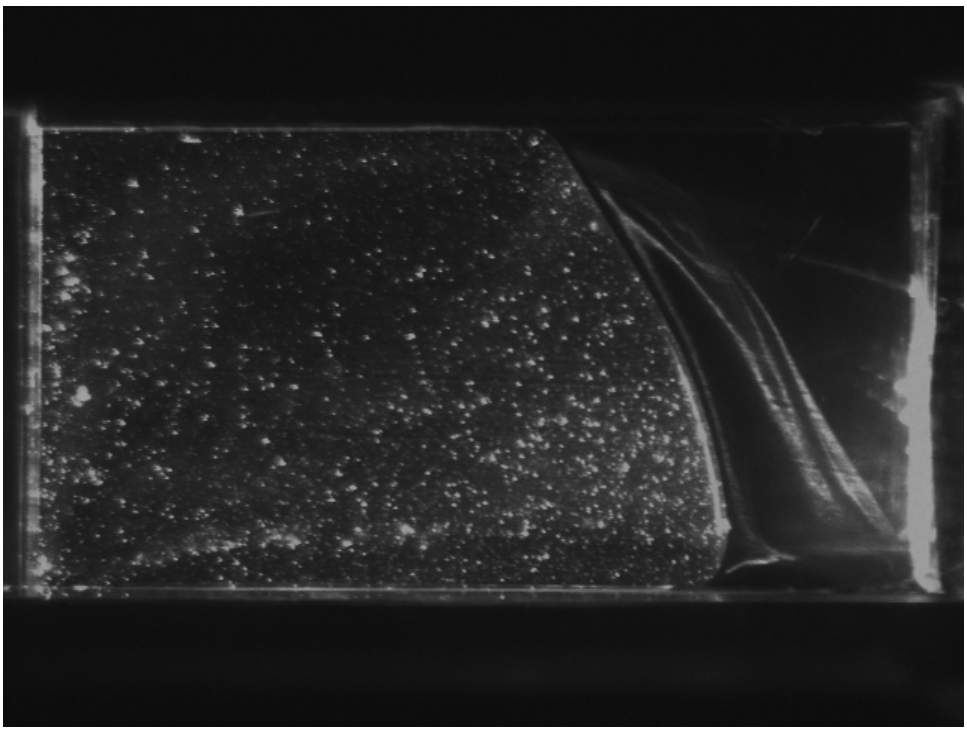

Figure 2.20: A typical raw image frame taken by the Pulnix 9701 CCD camera

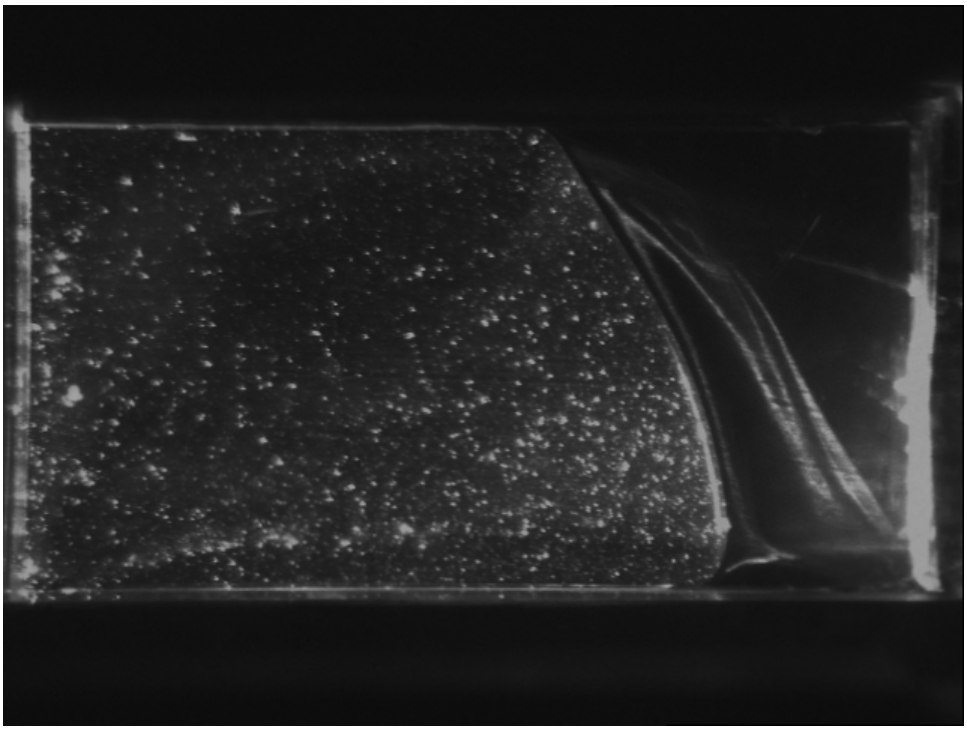

Figure 2.21: The result of running the undistortion program on the image in Figure 2.20

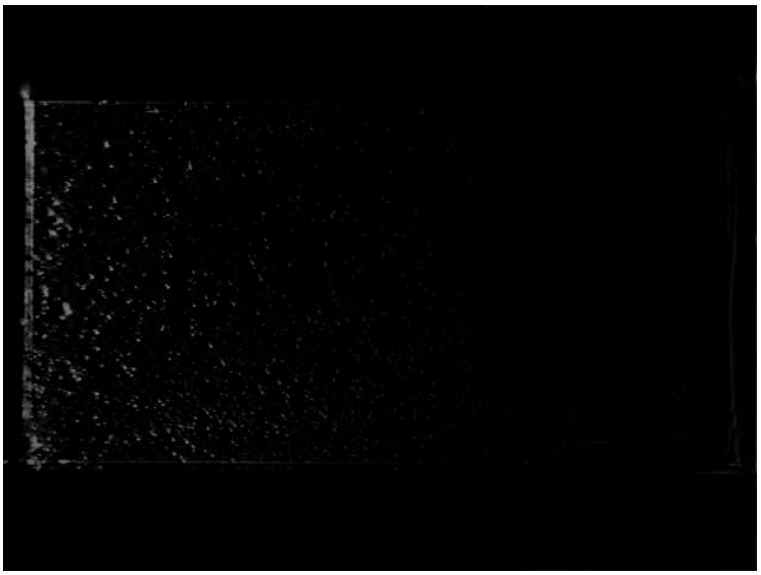

Figure 2.22: The result of subtracting the undistorted image shown in Figure 2.21 from the raw image shown in Figure 2.20

mold. The beam was redirected upward by a right-angle prism and was then focused by a convex lens fixed to a translation stage, allowing the beam to be steered as well as focused. The beam was then intercepted by a plano-concave lens, spreading the beam into a 1 mm thick sheet. The sheet entered the bottom of the optical access mold and exited through the top, illuminating the mold cavity. The sheet-forming optics were all mounted to an optical rail which was supported by a post fixed to a heavy base. The base was not in contact with the injection molding machine, and the molding machine was mounted on isolation pads. This minimized the transmission of vibrations to the sheet-producing optics.

The camera was mounted on a tripod placed between the laser and the injection molding machine. The camera was fixed to a two-axis tilt table, allowing for fine correction of the camera angle with respect to the mold cavity. A 28mm Nikon lens is used, to which is attached an adjustable red gel filter. The filter extended only part way into the field of view and could be rotated freely with respect to the camera. This allowed the filter to be used as a user-controlled glare shield that could be targeted at any of the cavity edges simply by rotating the filter.

The images were transmitted digitally to the frame grabber and were captured and displayed using the VideoSavant software. The images are then stored to the hard drive for subsequent analysis.

2.7 In-Mold Pressure Measurements

The melt pressure in the cavity was measured at the gate on the 109.5 mm $\times$ 6.3 mm face of the part formed by the stationary half of the mold. A D-M-E SS-405C 500 lb. slide sensor was used in conjunction with a D-M-E IPC-01-01 Pressure Control Unit. The load cell was mounted beneath a 3.175 mm diameter pin. The recorded

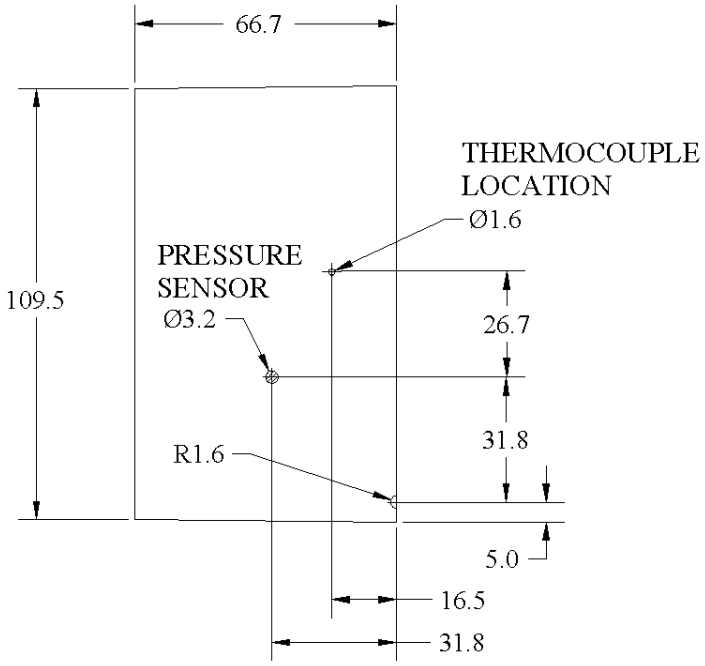

Figure 2.23: Schematic of the steel face of the mold cavity showing the in-mold sensors. One pressure sensor is located at the gate on a perpendicular wall and the other is located as shown here. The in-mold thermocouple is located as shown. The thermocouple is 6mm below the cavity surface. All dimensions are in millimeters.

load was divided by the area of the pin face to get the melt pressure.

The pin face was flush with the mold surface to avoid the hole pressure effect [73]. The placement of the sensor on the side face of the part keeps the sensor from being directly impacted by the plastic as it exits the gate.

An Omega LCGC series 1 kg load cell was located on the large face of the mold cavity as shown in Figure 2.23. This load cell was also located beneath a 3.175 mm pin whose face was flush with the mold surface. The sensor was mounted in the removable mold insert and was powered by an HP E3611A DC Power Supply.

The signals from both load cells were conditioned and amplified by a Krohn-Hite Model 3362 low-pass/high-pass 4-pole Butterworth/Bessel filter. The Model 3362

was configured as a low-pass Butterworth filter with a 20 Hz frequency cut-off and provided the D-M-E sensor with 20 dB of input gain and the Omega sensor with 40 dB of input gain.

The conditioned and amplified signals were then routed to a Data Translation DT301 data acquisition board. This board was chosen for its compatibility with VideoSavant. VideoSavant recorded the pressure signals simultaneously with the melt flow images, sychronizing the pressure data to the image data.

A calibration curve of the system consisting of the Omega LCGC load cell, the Krohn-Hite filter and the DT301 data acquisition board is shown in Figure 2.24.

The sensor near the gate produced readings during the filling stage that were suspiciously low compared to values predicted by Moldflow. Since this sensor has a maximum pressure input of 61 MPa and the pressures recorded during the filling stage are on the order of 0.5 MPa it was possible that the sensor was not accurate in this range. To test this theory the mold was pressure tested. Aluminum blocks replaced the glass in the windows. A pressure line was tapped into the cavity and the line was connected to a cylinder of compressed nitrogen. The mold cavity was filled with a viscous grease and the mold was then sealed with RTV. The tank pressure regulator was used to vary the pressure from 0-0.6 MPa and the output of the sensor was recorded.

The result of this experiment is shown in Figure 2.25. The sensor is inaccurate at pressures below 0.6 MPa. This could be due to a number of factors. The pressure test of the mold was designed to mimic actual operating conditions. The sensor is housed in a slot in the stationary half of the mold. The sensor sits beneath the head of a mold pin, with the other end of the pin flush to the mold surface. When the mold closes the area around the sensor is subjected to clamp forces, and these forces

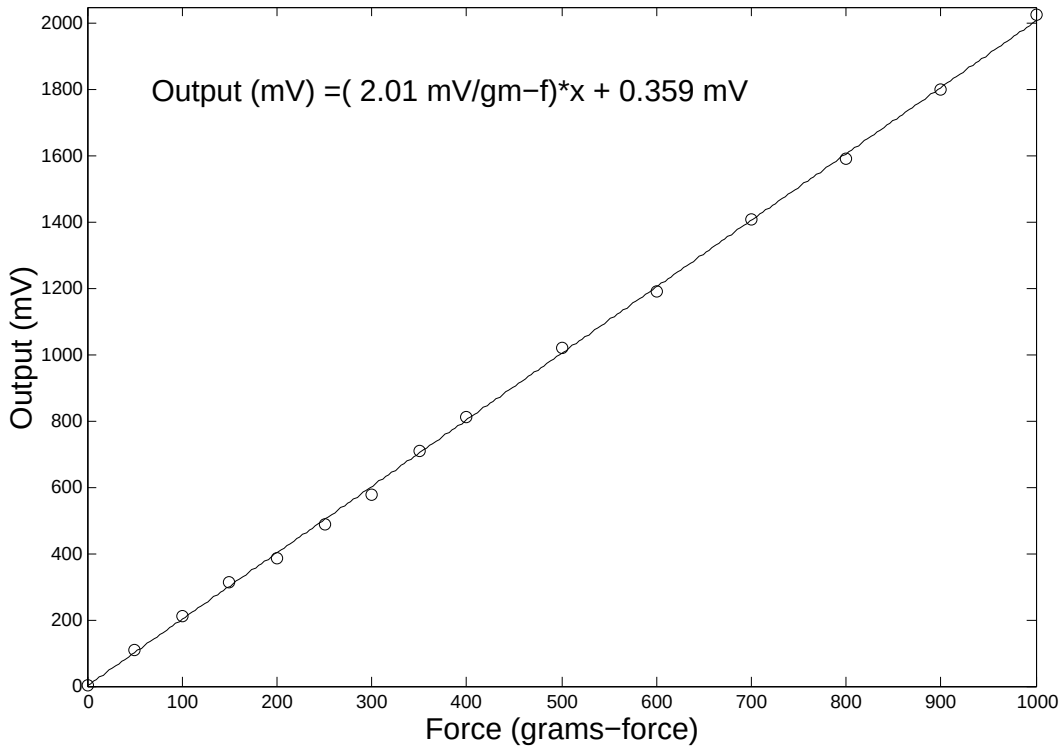

Figure 2.24: Calibration curve of the system consisting of the Omega LCGC load cell, the Krohn-Hite filter and the DT301 data acquisition card. The error on the output voltage is ± 3mV.

may interfere with the sensor reading. The hole around the mold pin may also distort slightly, causing the pin to bind, or perhaps Coulomb friction is a factor. Sensitivity and dynamic range may have also played a role. The sensor was designed to read pressures as high as 61 MPa, and the filling pressures were under 1 MPa.

A correction factor was calculated, defined as the ratio of the imposed pressure to the pressure recorded by the sensor at the gate. The sensor was found to be inaccurate at low pressures, with the correction factor approaching a plateau of 1.6. This scaling factor curve was applied to measurements made during the filling stage. The sensor proved accurate at high pressures, and so no scaling factor was applied during the packing phase.

2.8 Mold Temperature Measurement

The mold temperature was monitored with an insulated T-type thermocouple. The thermocouple was mounted 6 mm below the surface of the large mold face formed by the mold insert. The thermocouple mounting hole was in the insert. A second thermocouple was used to monitor the ambient air temperature.

2.9 Residual Strain Measurements

Birefringence measurements were made using a Vishay Model 080 Polariscope as shown in Figure 2.27. The polariscope uses white light that can be transformed into either plane or circularly polarized light. The circular polarizers are designed for a wavelength of 575 nm, producing a sharp red-purple tint of passage at the first fringe order. The polariscope was outfitted with an optional Vishay Model 084A monochramator as shown in Figure 2.28. The monochramator is a narrow-band interferential filter with a 10 nm bandpass at the same 575 nm tint of passage

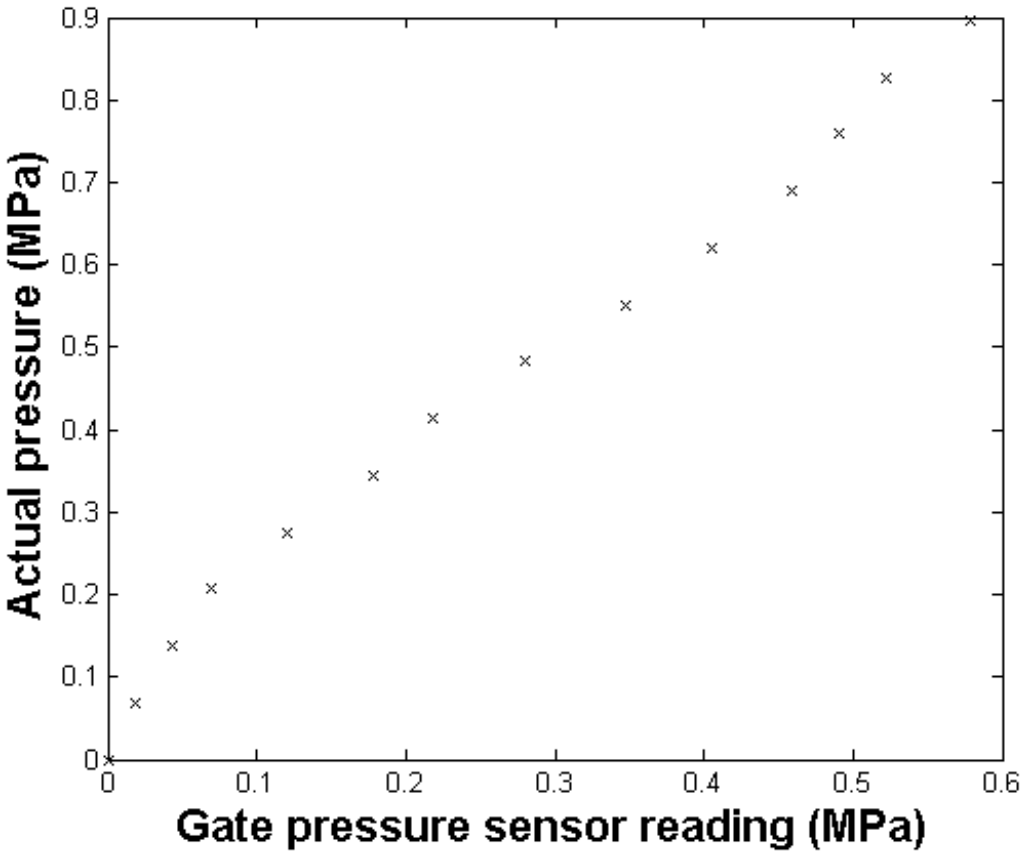

Figure 2.25: Calibration of the gate pressure sensor at a low pressure range. The calibration curve shows that the sensor is inaccurate at low pressures.

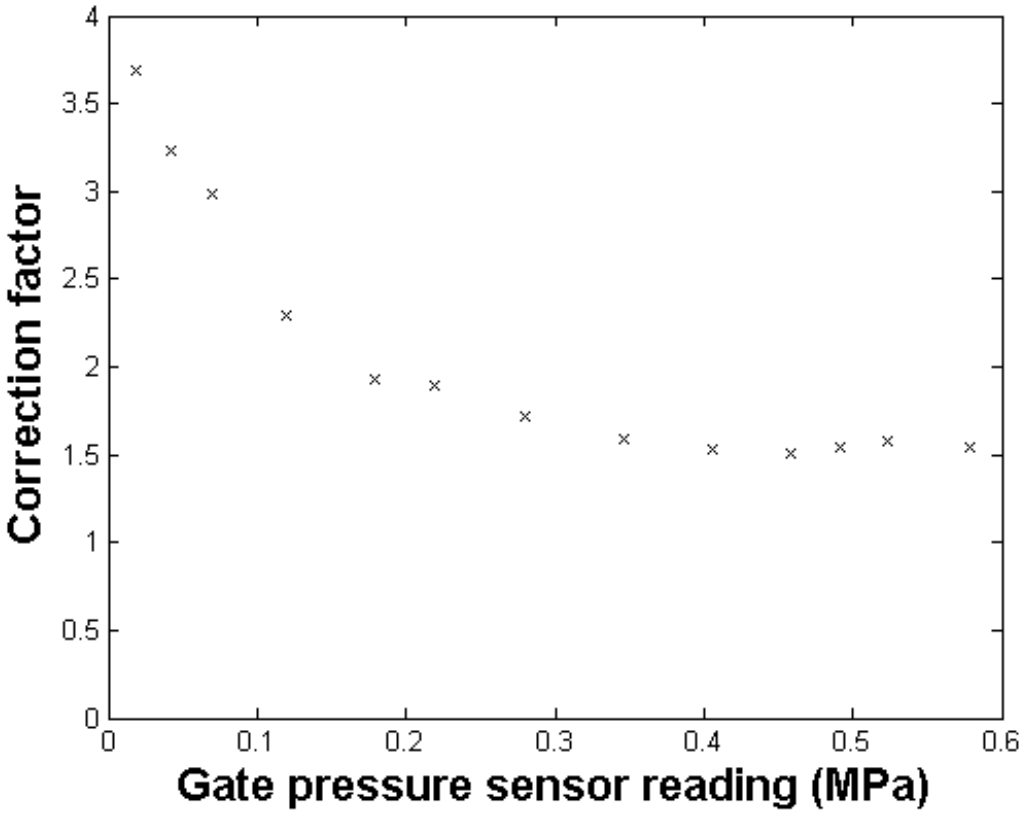

Figure 2.26: Correction factor for the gate pressure sensor at a low pressure range. The correction factor was defined as the imposed pressure divided by the pressure sensor reading. The scaling factor reaches a plateau value of 1.6.

Figure 2.27: The Vishay Model 080 Teaching Polariscope. The polariscope uses an overhead projector as a white light source.

wavelength. When in use it converts the multicolored fringes into monochromatic ones, the same that you would see if a monochromatic 575 nm light source was used in the polariscope instead of white light. Specimens rested on a Vishay Model 083 stress-free transparent support stage and fringe measurements were made using a Vishay Model 285 manual null balance compensator. The stress-free support stage and the compensator are also shown in Figure 2.28. All residual strain measurements were made following the procedure described in ASTM 4093 [74].

A plane polarized strain viewer was also used for calibration purposes. The circular polarizers were removed from the Vishay Model 080 Polariscope and were mounted in the proper orientations and positions on the plane polarized strain viewer. This created a circularly polarized strain viewer that could easily be placed on its

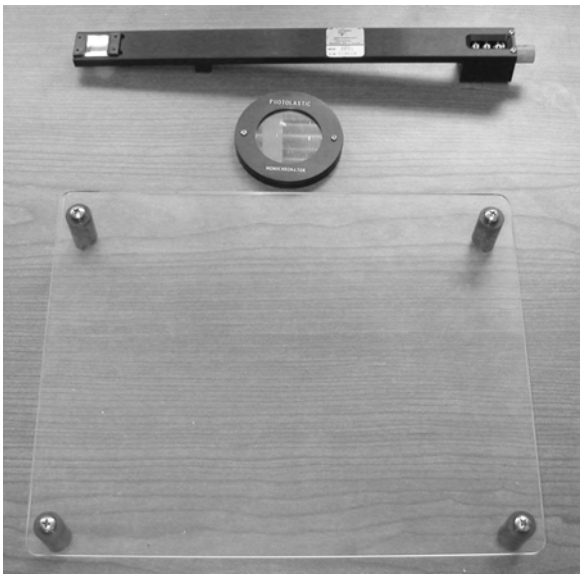

Figure 2.28: Auxiliary test equipment for the Vishay Model 080 polariscope. From top to bottom: Vishay Model 285 null-balance compensator, Vishay Model 84A monochromator, Vishay Model 083 stress-free support stage.

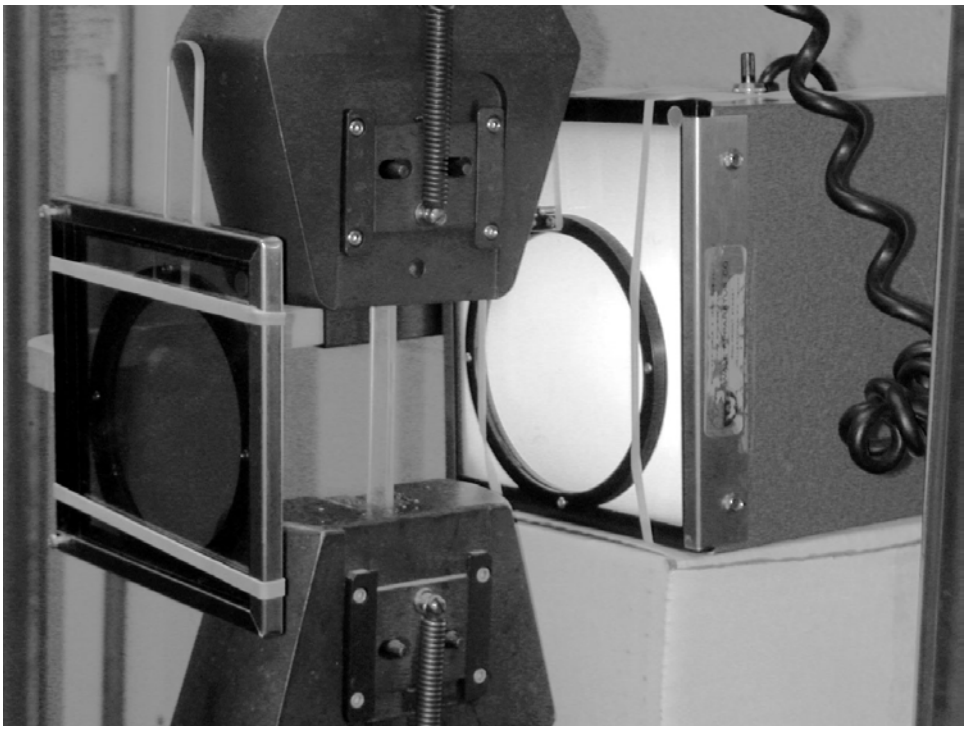

Figure 2.29: Measuring the stress-optic coefficient of Styron 615APR. The specimen is placed in an Instron 8516 tensile test machine and is viewed with a circularly polarized stress viewer. The fringe order is measured using a Vishay Model 285 null balance compensator (not shown).

side for calibration purposes.

The stress-optic coefficient for Styron 615APR was measured using this circularly polarized strain viewer and an Instron 8516 tensile test machine. Rectangular test specimens were molded on an Arburg M60 All-Rounder injection molding machine. The specimens were then annealed in a Stabil-Therm constant temperature cabinet for 24 hours at 90° C. The specimen width and thickness were constrained in the cabinet. The length was left unconstrained, allowing the parts to shrink with the annealing process but preventing them from warping.

The specimen cross-section dimensions were then measured with calipers and the specimen was then mounted in the Instron 8516. The circularly polarized strain viewer was then placed on its side with the circular polarizers on either side of the specimen as shown in Figure 2.29. A preload was placed on the specimen until the gage length appeared black in the strain viewer. This preload was recorded as a load offset to be subtracted from subsequent load readings. The load was then increased incrementally and the Vishay 285 null balance compensator was used to measure the fringe order at each load.

In this test the specimen experienced uniaxial tension along its length, making that direction a principal direction. The stress in the perpendicular direction was zero, making the measured uniaxial stress equal to the principal stress difference.

The results of these tests were then plotted as fringe order vs. stress. An example curve is given in Figure 2.30, where it is evident that the assumption of a linear relationship between applied stress and measured fringe order is valid. The slope of the best fit line, call it m, is equal to the ratio of the fringe order to the principal stress difference. Equation 2.1 can then be rewritten as:

$$c = \frac{\lambda}{h} m \tag{2.27}$$

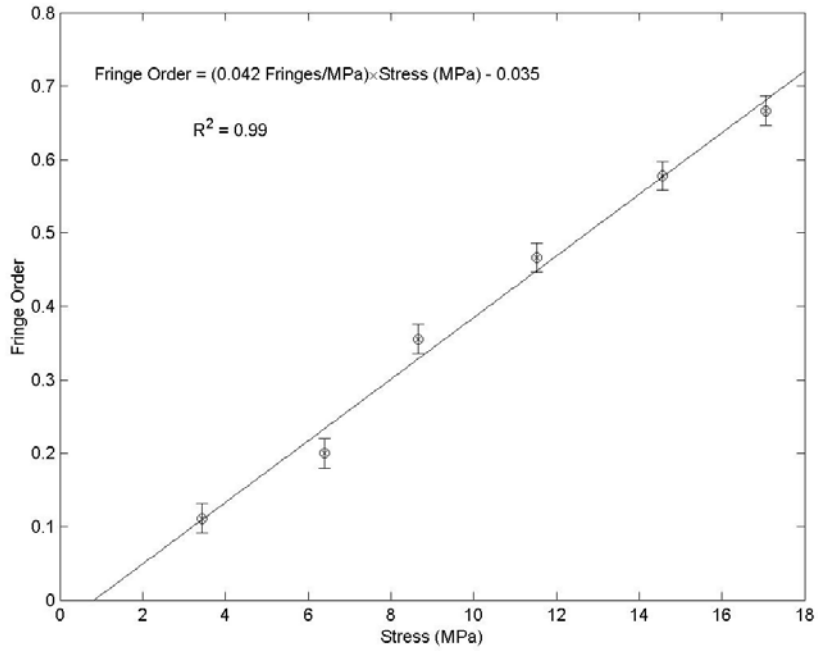

Figure 2.30: Plot of the results of one of the birefringence calibration tests. Known stresses are placed on the sample and the resulting fringe order is measured with a null balance compensator. The thickness of the specimen was 3.5 mm and the fringe order was based on a reference wavelength of 575 nm.

where c is the stress-optic coefficient, h is the part thickness, λ is the design wavelength of the polariscope and m is the slope of the fringe order vs. stress curve. The design wavelength of the Model 080 polariscope is 575 nm.

This test was repeated eleven times using specimens that were molded at the high and low values of the melt temperatures and injection rates used to make the plaques in the optical access mold. The results of each test were plotted and the slope of the best-fit line was calculated. The stress-optic coefficient was then calculated for each sample using Equation 2.27 and the resulting distribution was used to estimate c. The value of c was found to be 8.0 ± 0.6 Br.

Tabulated values of the stress-optic coefficient c are difficult to find. Tabulated values of c for STYRON 615 APR at a wavelength of 575 nm are even more elusive.

A comparison to tabulated values of c can only be made in a general sense since tabulated values are typically listed only for generic polystyrene in the glassy state with no mention of the wavelength of light used to make the measurement. Tabulated values of c for solid polystyrene range from 5 Br [75] to 10.7 Br [76]. Wimberger [77] collected previously published results and gave c a range from 6-10 Br. The mean measured value of 8.0 Br falls comfortably within these tabulated values.

CHAPTER 3

On the use of PIV in Polymer Melts

Injection molding involves the unsteady, non-isothermal flow of a shear-thinning, viscoelastic liquid under high temperatures and pressures. In the current study the nominal melt pressures in the barrel of the molding machine are as high as 10,000 psi, and as high as 3000 psi in the mold cavity during packing. Nominal temperatures were as high as 245° C. The fluid has a free surface and is solidifying as it flows. This poses technical challenges to experimentalists interested in the application of PIV to the flow of polymer melts, and poses analytical challenges to theoreticians and programmers interested in modelling such a flow. Fortunately, some of the aspects of polymer melt flow offer benefits not enjoyed by Newtonian PIV researchers, and some of the difficulties they face do not apply to PIV in polymer melts. The purpose of this chapter is to examine both the positive and negative factors involved in applying PIV to polymer melt flows.

3.1 Injection Molding Flow Characteristics

Injection molding flow has distinguishing characteristics that are common to nearly all molding flows. The characteristics that will be considered here were chosen because they all affect the design and setup of a PIV experiment in a polymer melt.

3.1.1 High Viscosity

A major benefit of PIV in polymer melts is the fact that polymers are orders of magnitude more viscous than typical Newtonian liquids such as air, water and lubricating oils. The Reynolds number of a polymer melt flow is be many orders of magnitude smaller than typically encountered in Newtonian PIV experiments.

To estimate a typical Reynolds number for the polymer melt flow in the present work, take a reference length equal to the cavity thickness h and define a characteristic velocity using the cavity length and the fill time T_f. This gives the following expression for the Reynolds number:

$$\mathrm{Re} = \frac{\rho h^2}{\eta T_f} \tag{3.1}$$

Using h = 6.4 mm, T_f= 1 s, ρ = 1050 kg/m^3 and η = 300 Pa·s gives a Reynolds number of 1.4×10^{-4}.

Many of the spatial and temporal resolution issues that face Newtonian PIV experimenters are avoided because of the extremely low Reynolds number of polymer melt flows. For example, the flow is smooth, turbulence is not an issue, and large dense particles can be used without loss of tracking accuracy. This makes the flow of polymer melts particularly well-suited to digital implementations of PIV. As Willert and Gharib [40] point out, the current technological limitations on the image size and frame rate of CCD cameras limits the application of DPIV to moderate speed flows. But this statement is somewhat biased towards low-viscosity Newtonian fluids. It would be better to say that technological limitations currently limit DPIV to low Reynolds number flows. The viscosity of polymer melts is so high that higher velocities can be tolerated without transitioning into turbulence.

The high viscosity of polymers has its disadvantages as well. It takes large pres-

sure differences to pump highly viscous fluids and the melt pressure in the cavity is on the order of tens of megapascals during the packing phase. Since injection molds are not typically transparent a window system must be designed that can withstand these high pressures if it is to be used to study mold packing as well as mold filling.

3.1.2 Flat Velocity Profile

Polymer melts are typically shear-thinning liquids. Their viscosity as a function of strain rate can be described by a number of constitutive models. The simplest is the power law model:

$$\eta = m\dot{\gamma}^{n-1} \tag{3.2}$$

where η is the viscosity, n is the power-law exponent, m is the power-law coefficient, and $\dot{\gamma}$ is the shear rate. For a Newtonian liquid, $n = 1$ and m is the viscosity. Departures from Newtonian behavior can be gauged by n. If $n < 1$, the fluid is shear-thinning. The shear-thinning index of the polystyrene used in this study is 0.42.

A more accurate model of polymer behavior is the Carreau model, a good description of which can be found in Bird [63]. This model includes a zero-shear viscosity and represents the low shear-rate behavior of polymer melts more accurately than the power law model:

$$\eta = \eta_0[1 + (\tau\dot{\gamma})^2]^{\frac{n-1}{2}} \tag{3.3}$$

where η_0 is the zero-shear viscosity, τ is a time constant, n is the power law exponent and $\dot{\gamma}$ is the shear rate. For high shear rates $(\tau\dot{\gamma})^2 \gg 1$ and the Carreau model reduces to the power law model.

Injection molded parts are typically designed with the thinnest possible thicknesses, on the order of a few millimeters. This means that injection molding flow is

a pressure-driven flow that takes place in a thin channel. Given the high viscosity of polymer melts large pressure drops are needed to produce this flow. The regions of the flow near the cavity walls experience the highest shear stress while the region near the midplane experiences very little shear. For shear-thinning polymers this creates zones of low-viscosity melt near the walls and a zone of high viscosity melt in the center, leading to a plug-flow velocity profile instead of the parabolic profile expected with a Newtonian flow.

The velocity profile of the Poiseuille flow of a power-law fluid in a channel of width $2B$ is derived in Section C.1. The profile is given by:

$$u = u_{max}\left(1 - \left|\frac{y}{B}\right|^{\frac{n+1}{n}}\right) \tag{3.4}$$

This profile is plotted in Figure 3.1 for a polystyrene with an index of 0.42 and for a Newtonian fluid with an index of 1.0. The profile of the channel flow using a Carreau model of polystyrene is also superposed. This profile was calculated using Carreau model curve fit shown in Figure 2.3. The pressure gradient for the flow was -8.0 MPa/m, a gradient that gives centerline velocities comparable to those observed in the optical access mold with a volume flow rate of 34.0 cm^3/s.

This broad, flat velocity profile is a boon for PIV work in polymer melts. The goal of the work presented here was to measure the velocities at the midplane of the mold cavity. The plug-flow velocity profile is much more forgiving to errors in laser sheet thickness and centering than a parabolic profile would be. The flow velocity is nearly uniform over a broad region at the center of the mold.

An estimate of velocity bias errors due to sheet thickness and sheet offset can be calculated using the velocity profile given by Equation 3.4. Given a laser sheet with width $2h$ in a channel of width $2B$ and walls at $y = \pm B$. The sheet is parallel to the

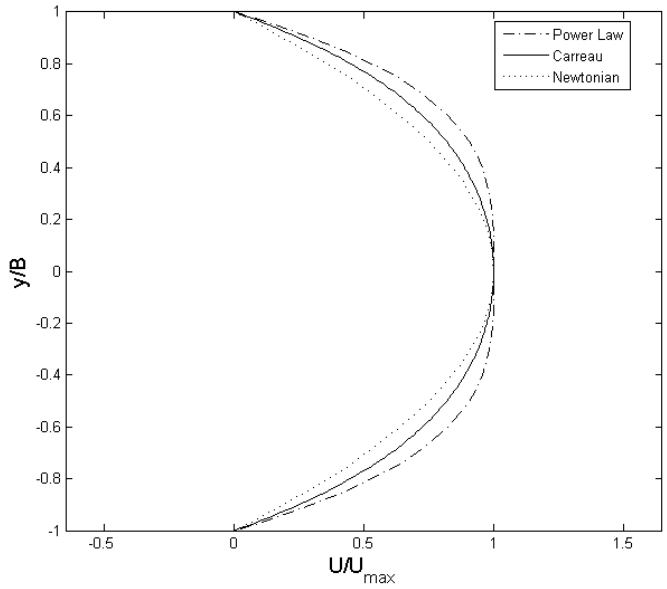

Figure 3.1: Fully developed non-dimensionalized velocity profiles for a shear-thinning liquid and a Newtonian liquid in a channel of width $2B$. The Carreau model parameters are $\eta_0 = 295.43$ Pa·s , $\lambda = 0.0193$ s, and $n = 0.42$. The power law exponent is $n = 0.42$.

walls and has a centerline at $y = y_0$. The average velocity encompassed by the sheet is given by:

$$\bar{u} = \frac{u_{max}}{2h} \int_{y_0-h}^{y_0+h} \left(1 - \left|\frac{y}{B}\right|^{\frac{n+1}{n}}\right) dy \tag{3.5}$$

Since the flow front is symmetric we can assume that the offset error is positive without loss of generality. The analysis will also be limited to those laser sheets that encompass the cavity centerline. These two conditions can be expressed as:

$$y_0 > 0 \tag{3.6}$$

$$y_0 - h < 0 \tag{3.7}$$

Care must be taken when carrying out the integration in Equation 3.5 because of the absolute values involved. Due to the conditions listed above the limits of integration bracket zero and the argument of the absolute value will change sign

during the integration. The integral must be done in pieces:

$$\begin{aligned}
\frac{\bar{u}}{u_{max}} &= \frac{1}{2h}\int_{y_0-h}^{0}\left(1-\left|\frac{y}{B}\right|^{\frac{n+1}{n}}\right)dy+\frac{1}{2h}\int_{0}^{y_0+h}\left(1-\left|\frac{y}{B}\right|^{\frac{n+1}{n}}\right)dy \\
&= \frac{1}{2h}\int_{0}^{h-y_0}\left(1-\left|\frac{y}{B}\right|^{\frac{n+1}{n}}\right)dy+\frac{1}{2h}\int_{0}^{y_0+h}\left(1-\left|\frac{y}{B}\right|^{\frac{n+1}{n}}\right)dy \qquad (3.8) \\
&= 1-\frac{n}{2n+1}\frac{B}{2h}\left(\left(\frac{h-y_0}{B}\right)^{\frac{2n+1}{n}}+\left(\frac{y_0+h}{B}\right)^{\frac{2n+1}{n}}\right) \qquad (3.9)
\end{aligned}$$

Let ϵ_0^* be the offset error normalized by the channel half-thickness B, and let h^* be the sheet thickness normalized by the cavity thickness. Then:

$$\frac{\bar{u}}{u_{max}} = 1-\frac{n}{2n+1}\frac{B}{2h}\left[(h^*-\epsilon_0^*)^{\frac{2n+1}{n}}+(\epsilon_0^*+h^*)^{\frac{2n+1}{n}}\right] \qquad (3.10)$$

Define a measure of the velocity bias error u_{err}^* as the negative of the percentage difference between u_{max} and $\bar{u}$:

$$\begin{aligned}
u_{err}^*(\%) &= 100\times\frac{u_{max}-\bar{u}}{u_{max}} \\
&= 100\times\frac{n}{2n+1}\frac{B}{2h}\left[(h^*-\epsilon_0^*)^{\frac{2n+1}{n}}+(\epsilon_0^*+h^*)^{\frac{2n+1}{n}}\right] \qquad (3.11)
\end{aligned}$$

Figure 3.2 shows superposed contour plots of Equation 3.11 for polystyrene with $n = 0.42$ and a Newtonian fluid with $n = 1$. The shear-thinning fluid is much less sensitive than the Newtonian fluid to sheet thickness and offset errors. Combinations of laser sheet thickness and offset that would lead to 5% velocity bias errors in a Newtonian fluid give less than an 1.6% velocity bias error in the polystyrene.

These bias errors can be considered as upper and lower bounds on the bias errors in the present work. As shown in Figure 3.1, the Carreau model predicts a velocity profile that falls between the Newtonian and power-law profiles. Unlike the Newtonian and power-law profiles, the shape of the Carreau profile is not self-similar at different flow rates. High pressure gradients push the profile toward the power-law limit and low flow rates push the profile toward the Newtonain limit. Therefore the

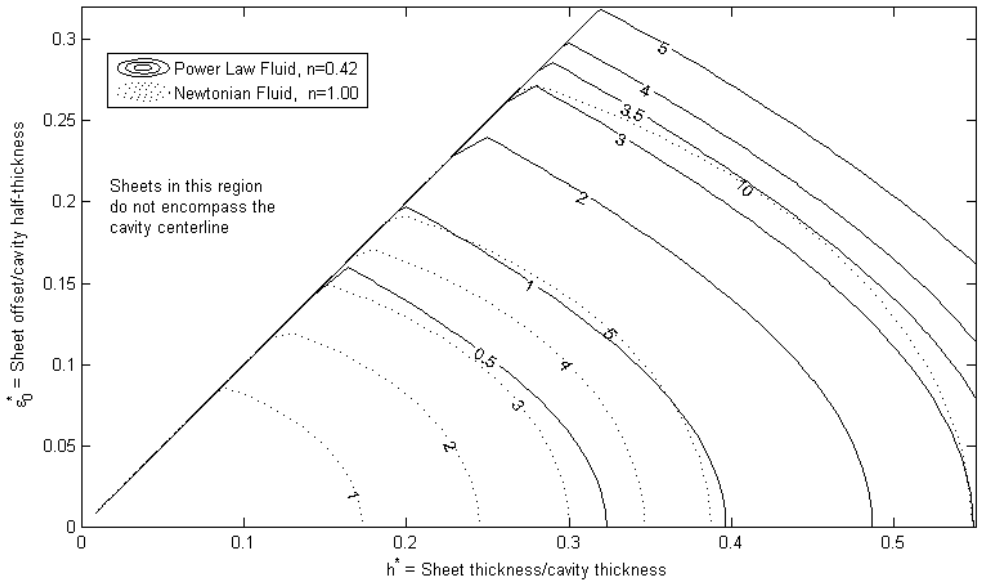

Figure 3.2: Contours of percent velocity bias error as a function of sheet thickness/cavity thickness and sheet offset/cavity half-thickness for a shear-thinning fluid with power law exponent of 0.42–+ and a Newtonian fluid. A sheet in a Newtonian fluid with a velocity bias error of 5% has an error of only 1% in the shear-thinning fluid. A sheet in a Newtonian fluid with a velocity bias error of 10% has less than a 3.5% velocity bias error in the shear-thinning fluid.

actual bias error will be a function of the flow rate for Carreau model fluids. A practical result of this observation for PIV experimentation is that the bias error becomes smaller at higher flow rates.

3.1.3 Fountain Flow

The flow of a polymer melt into a cavity is essentially a fountain flow, see Figure 3.3. As the mold fills there must be a flow front, a boundary between the polymer melt and the air in the cavity. The polymer melt flows from the gate toward the

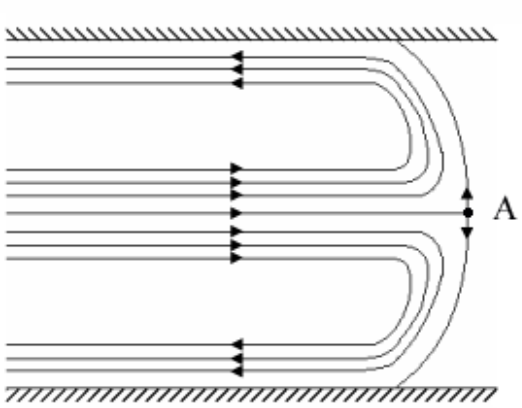

Figure 3.3: Streamlines for fountain flow in a frame of reference traveling with the stagnation point 'A'. The flow in the center of the channel reaches a stagnation point at the front and is redirected to the walls, causing out-of-plane motion near the front.

front in the middle portion of the cavity, the velocity vectors remaining parallel to the cavity walls. As the flow reaches the front it is redirected like a fountain toward the cavity walls. The polymer solidifies rapidly once it has made contact with the wall

The fountain flow effect has an impact on PIV in polymer melts. In the neighborhood of the front it cannot be guaranteed that the particles are moving in the midplane of the mold. Therefore PIV results very close to the front are suspect.

The fountain flow causes other problems as well. The strong curvature of the flow front through the thickness direction acts as a lens and can cause glare at the flow front. Fortunately these two problems, out-of-plane motion and glare, are confined to the same region of the image.

3.1.4 Moving Flow Front

Injection molding flows have a moving flow front during the filling stage. The front not only moves but it also changes shape as the polymer melt fills the cavity.

The flow front is a polymer-air interface whose curvature affects the transmission

of light. Transparent polymers have indices of refraction ranging from 1.495-1.60[78]. The polystyrene used in this work has an index of 1.59. This means the polystyrene-air interface has a critical angle θ_c of 38.97° [79]. Total internal reflection occurs if the incident angle of the laser sheet on the interface is greater that θ_c and partial reflection occurs for angles less than θ_c. This leads to uneven illumination of the polymer melt.

Total internal reflection can occur when the laser sheet impinges on the interface from the air or from the polymer melt. Figure 3.4 illustrates both problems. In the region labeled A the curvature of the flow front prevents the penetration of the laser sheet. This creates a dead zone in which the particles are under-illuminated. In the region labeled B the curvature of the front reflects the laser light back into the polymer melt, creating a saturated zone in which the particles are over-illuminated. This over-illumination places a limit on the laser power during this portion of the mold filling. If the laser power is too high this region oversaturates. If the laser power is set low enough to avoid oversaturation in this region then the rest of the polymer melt will be under-illuminated.

When the polymer melt contacts the far wall the dead zone issue disappears, but the internal reflection problem due to the flow front intensifies. During the transition from radial flow to channel flow the flow front changes shape rapidly and the reflected laser light sweeps through the area behind the front like a searchlight, see Figure 3.5. This means that illumination of individual particles in this region may change radically from movie frame to movie frame, causing problems for the PIV cross-correlation. The rapid transition from radial flow to channel flow may also cause the non-spherical aluminum flakes to rotate, changing their illumination and also causing potential PIV problems.

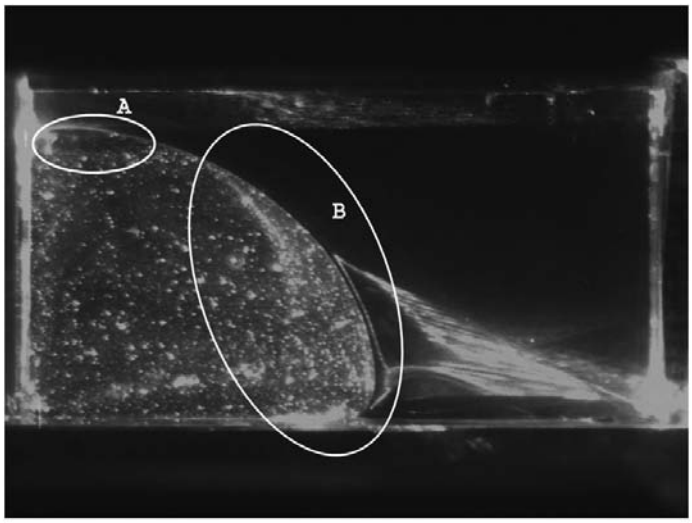

Figure 3.4: Uneven illumination due to total internal reflection. In the portion of the image labeled A the laser sheet is reflected from the interface and fails to illuminate particles in the polymer melt. In the portion of the image labeled B the laser sheet is reflected back into the polymer melt causing the region behind the front to be over-illuminated.

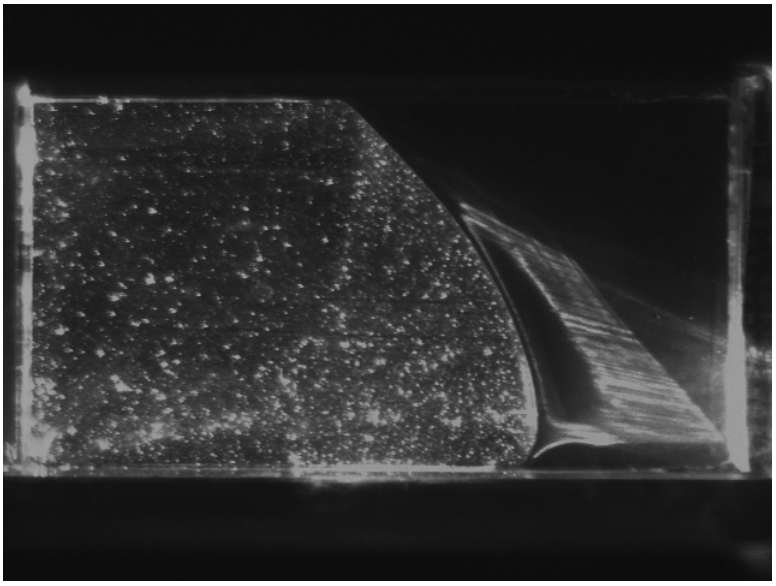

Figure 3.5: Uneven illumination due to total internal reflection. In this portion of the mold filling the front changes shape rapidly and the reflected laser light sweeps through the area behind the front like a searchlight.

3.1.5 Effects of Strong Radial Flow

Cross-correlation is the heart of PIV analysis. An interrogation window is placed on an image and is cross-correlated with a window on the succeeding image. The second window is moved about systematically and a cross-correlation is performed at each new location. The correlation will have a local maximum when particles in the first window match particles in the second. The amount of displacement $\vec{d}$ between the two windows and the time difference between the two frames are used to determine the local velocity at the location of the first window:

$$\vec{u} = \frac{\vec{d}}{M\Delta t} \tag{3.12}$$

where M is a scale factor with units of pixels/length.

If the particles from the first window cannot be found in the second window, or if the particles from the first window correlate with the wrong particles in the second window the method will fail. This leads to difficulties if the underlying flow field has a strong radial character.

Raffel [39] points out that the cross-correlation analysis assumes that all the particles in an interrogation window experience a constant displacement $\vec{d}$. Particles with initial positions $\vec{x_i}$ in the first image will be found at $\vec{x_i} + \vec{d}$ in the second. This maximizes the correlation peak. Small variations in the velocity vector among particles in the same interrogation window will lead to a lower, but still identifiable, cross-correlation peak. This leads to a trade-off in window size selection. Large windows contain more particles to correlate, small windows have particles with more uniform velocities.

In a radial flow, though, none of the particles in an interrogation window have identical velocity vectors no matter how small the window. Each particle has a

velocity component that causes it to separate from its neighbors. This velocity component gets stronger the closer the particles are to the origin of the radial flow. Since the displacement of particles is not constant for any interrogation window near the gate, there will be a zone around the gate in which PIV will fail. Techniques such as super-resolution PIV [80] might succeed if the individual particles can be tracked, but standard PIV methods will fail.

To estimate the severity of this problem assume that two particles of diameter d_p in a radial flow are separated by a distance x as shown in Figure 3.6. The particles are both at a distance R from a volume source Q in a channel of width $2B$. The particles subtend an angle 2θ from the source. The velocity of the particles is given by:

$$u_r = \frac{Q}{4\pi RB}\hat{e}_r \tag{3.13}$$

During the time Δt the particle separation increases to $x + \Delta x$ but the angle θ stays constant:

$$\sin\theta = \frac{x}{2R} = \frac{x + \Delta x}{2(R + u_r \Delta t)} \tag{3.14}$$

Solving for Δx gives

$$\Delta x = \frac{Q\Delta t}{4\pi R^2 B}x \tag{3.15}$$

Imagine that a cross-correlation is performed with the original particles separated by x in the first frame and the with the particles separated by $x + \Delta x$ in the second frame. The cross-correlation will fail when the the increased separation Δx is greater than or equal to the particle diameter d_p. This will happen at a critical radius R_c:

$$R_c \leq \sqrt{\frac{Qx\Delta t}{4\pi d_p B}} \tag{3.16}$$

To estimate R_c take the average initial particle separation to be equal to half the length of the interrogation window. Given an interrogation window of $N \times N$

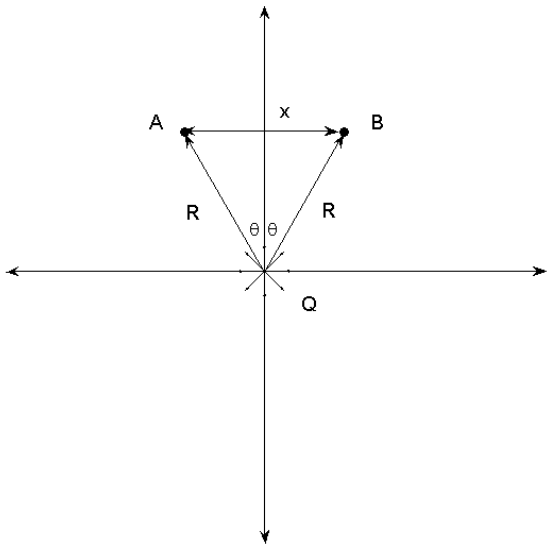

Figure 3.6: Particles in a radial flow with source strength Q and initial separation x. The particles are at a distance R from Q and subtend an angle of 2θ.

pixels and a magnification factor of M pixels per unit of length the average initial separation is equal to $N/2M$:

$$R_c \leq \sqrt{\frac{QN\Delta t}{8M\pi d_p B}} \tag{3.17}$$

For the present work the maximum flow rate is 34.5 cm^3/s, the particle equivalent spherical diameter is 60μm(see Section 3.2.3), Δt is 1/30 second, w is 6.3 mm and the magnification factor M is 5.2 pixels/mm. This gives a maximum critical radius of 38.6 mm. Particles within this radius will separate from each other by a distance greater than the particle diameter between movie frames. Standard PIV techniques will be unreliable or fail altogether in this region. Table 3.1 lists the critical radii for the flow rates and geometry used in the present work.

3.1.6 Effects of Extensional Flow

The present work did not involve an extensional flow, but extensional flows are often studied by non-Newtonian flow researchers. The argument of Section 3.1.5

Table 3.1: Critical radius R_c for the flow rates and geometry used in the present work. PIV will fail at points whose radial distance from the gate is less than R_c.

Flow rate (cm^3/s)	R_c (mm)
11.5	22.3
17.3	27.3
23.0	31.5
34.5	38.6

can also be applied to the use of PIV in extensional flows. The basic argument of Section 3.1.5 is that PIV will fail if particles in the interrogation volume separate from each other more than a particle diameter between image frames. In such a case the cross-correlation will fail. In an extensional flow the effect would be much more severe. Two particles separated by a distance x_0 in the direction of the extensional flow will separate exponentially fast [63]:

$$x = x_0 e^{\dot{\varepsilon}\Delta t} \tag{3.18}$$

where x is the new particle separation and $\dot{\varepsilon}$ is the extensional strain rate of the flow.

The particles separate much faster than in a radial flow and, even worse, the effect is uniform over the entire flow field. The change in particle separation over the time Δt is given by

$$\Delta x = x_0(e^{\dot{\varepsilon}\Delta t} - 1) \tag{3.19}$$

PIV will fail when $\Delta x > d$. This means that instead of a critical radius as was seen radial flow, there is a critical particle separation. For PIV to succeed we must have

$$x_0 < \frac{d}{e^{\dot{\varepsilon}\Delta t} - 1} \tag{3.20}$$

This analysis can be taken further. The minimum particle separation, assuming

no overlap in the images, is d itself. Setting x_0 equal to d results in

$$\dot{\varepsilon}\Delta t \leq \ln 2 \tag{3.21}$$

This can be used to calculate the maximum strain rate that can be resolved for a given camera frame rate f. Taking $f = 1/\Delta t$:

$$\dot{\varepsilon}_{max} = f \ln 2 \tag{3.22}$$

This is a much more severe condition than that imposed by radial flow. Radial flow imposes a dead-zone radius around the source that is dependent on the flow rate and the frame rate of the camera. Extensional flow imposes a restriction on the entire field, and the maximum extension rate of the experiment as a whole is dictated by the frame rate of the camera.

3.1.7 Non-Isothermal Flow

Polymer melt flow is non-isothermal by its very nature. This causes unavoidable problems for PIV analysis because the index of refraction of a polymer is a function of its temperature. That means that the sheet thickness can vary with position in the melt. This is mitigated by the broad, flat velocity profile of the shear-thinning melt as shown in Figure 3.1.

3.2 Particle Selection

PIV calculates the Lagrangian velocity of particles at a point and equates it to the Eulerian velocity of the fluid at that point. The only way this can produce accurate results is if the particle motion tracks the fluid motion. The particles also need to be well mixed in the fluid and easily visible.

3.2.1 Practical Issues

There are many practical issues in particle selection for polymer melt PIV that are not found in standard PIV experiments. Most of these issues stem from the fact that the PIV particles are introduced to the polymer while it is in the solid state.

The solid polymer pellets and the PIV particles are weighed separately and are coarsely mixed together outside of the molding machine. Then the mixture is poured into the hopper. The screw then plasticizes the pellets and simultaneously mixes the PIV particles with the melt. Fortunately most injection screws are designed to promote good mixing. There were no issues in the present work with poor particle distribution in the melt. The difficulty lies in the fact that melting the polymer pellets through screw action is a high shear operation. Many of the particles typically used in PIV experiments will not survive the polymer melting process.

Many sizes and types of particles were tried and discarded. The first particles tried were those used in conventional Newtonian PIV work. Hollow glass spheres ranging from 50 μm to 100 μm were tested first, both silvered and not silvered. These particles were bright enough, but tended to be pulverized by the mixing action of the screw. Fluorescent particles were tried as well, with the same result. Glitter flakes were also tried, but they also failed to survive the passage through the screw.

The high viscosity of polymer melts allows heavy particles to be used without sacrificing tracking accuracy, as described in Section 2.2. Various metal particles were tried. Aluminum flakes were tried first. These survived the passage through the screw and were bright enough, but they were not symmetric and the literature on the dynamics of their interaction with the surrounding polymer is scanty. Aluminum oxide powder was then tried, but the diameter control, general shape and reflectance were not satisfactory.

Atomized copper spheres were then tried. These particles did not have the orientation problems experienced by the aluminum flakes, but the reflectance from the copper surface was mediocre. Atomized aluminum spheres were tried next. These particles also survived the passage through the screw and had higher reflectance than the copper particles, but were still not reflective enough to give good PIV images.

In the end the aluminum flakes were selected for their superior reflectance. Even though spherical particles would have been preferred the flakes were the only particles that resulted in adequate PIV images. The flakes used were precision-cut squares 0.004" on a side with a thickness of 0.0005". Further details about the specifications of these particles can be found in Section 2.2.

3.2.2 Particle Interactions

Particle suspensions in Newtonian fluids can behave like non-Newtonian fluids. As Kamal [81] points out, suspensions of particles in Newtonian fluids can exhibit yield stresses, time and/or strain dependent properties, shear thinning or thickening, and normal stresses. These phenomenon are due to structures generated by particle-particle interactions. The interaction of these structures with the surrounding flow leads to non-Newtonian effects. Polymer PIV experiments should be designed to reduce these non-Newtonian effects so that they will not be intertwined with genuine non-Newtonian effects of the base fluid.

Fortunately, this is easily done in a polymer melt PIV experiment. The seeding density is quite low, typically 0.02% by weight. The strength and amount of particle interaction increase with the seeding density, so low seeding densities minimize these effects. The high viscosity of polymer melts also helps achieve this goal. As pointed out by Metzner [82], when fluid phase viscosity exceeds about 100 Pa·s there is usually

no evidence of interparticle effects. The polystyrene melts in this work had zero-shear viscosities of near 300 Pa·s , so particle interactions are likely to be inhibited.

3.2.3 The Equivalent Spherical Diameter

In order to speculate on the ability of the particles to track the non-Newtonian flow an equivalent spherical diameter must be chosen. Two choices of equivalent spherical diameters that are applicable have been described by Jennings [83]. One choice of equivalent spherical diameter is obtained by calculating the diameter of a sphere with a volume equal that of the square flake. For a square flake with side s and thickness t the equivalent volume diameter d_v is given by:

$$d_v = \left(\frac{6s^2t}{\pi}\right)^{\frac{1}{3}} \tag{3.23}$$

For the particles used in this work d_v= 63μm.

Another choice of equivalent spherical diameter is the Stokes diameter. The Stokes diameter is the diameter of a sphere that sediments at the same rate as the non-spherical particle. This choice of diameter seems particularly appropriate for a discussion of PIV analysis. For a disc-like particle with diameter δ and diameter-to-thickness ratio ρ Jennings [83] gives the following expression for the Stokes diameter d_s:

$$d_s = \delta\sqrt{\frac{3}{2\rho}\tan^{-1}\rho} \tag{3.24}$$

Using the planiform area of the square particle to calculate an equivalent disk diameter δ gives d_s=60 μm.

These two equivalent diameters are in good agreement. For the purposes of this chapter d_s will be used as an equivalent spherical diameter.

3.2.4 Flow Tracking Accuracy

The standard measure of the ability of a particle to assume the velocity of the local flow field is that the Stokes number St be much less than unity [84]:

$$\mathrm{St} = \frac{\tau_v}{\tau_f} \ll 1 \tag{3.25}$$

where τ_f is a characteristic time of the fluid and τ_v is the momentum response time defined as:

$$\tau_v = \frac{d_p^2 \rho_p}{18\mu_f} \tag{3.26}$$

Taking the fill time T_f as a characteristic time of the flow gives the following expression for the Stokes number:

$$\mathrm{St} = \frac{d_p^2 \rho_p}{18\mu_f T_f} \tag{3.27}$$

where d_p is the particle diameter, ρ_p is the particle density, and μ_f is the dynamic viscosity of the fluid. The density of aluminum is 2700 kg/m^3 and the density of polystyrene is 1050 kg/m^3[85]. Using the polymer viscosity of 295.4 Pa·s and a fill time of 1 s gives a Stokes number of 2×10^{-9}. This is much lower than Stokes numbers found in typical Newtonian PIV experiments. Melling [86] collected data on the particles used by numerous Newtonian flow PIV studies. The Stokes numbers of the particles used in these studies ranged from $O(10^{-2})$ to $O(10^{-1})$.

Another tracking issue to consider, especially with heavy particles, is the effect of gravity on particle motion. Raffel et. al. [39] give the following expression for the slip velocity of a spherical PIV particle:

$$V_{slip} = d^2 \frac{(\rho_p - \rho)|\dot{V}|}{18\eta} \tag{3.28}$$

where $\dot{V}$ is the particle acceleration and ρ and η are the fluid density and viscosity. Replacing $\dot{V}$ with the gravitational acceleration g gives a slip velocity on the order of 10^{-8} m/s. Gravitational effects on the particles are negligible.

These calculations show that metallic particles are quite suitable for PIV in polymer melts. Caution must be used, however, since these calculations are based on the assumption that the particle experiences Stokes drag in a Newtonian fluid. In polymer melts these assumptions may not apply. The impact of non-Newtonian effects on the particle drag are explored in the following sections.

3.3 Particle Drag in Non-Newtonian Fluids

To estimate how well the spherical particles track the flow the drag on the particle from the surrounding liquid must be known. There is a large body of literature studying drag on spheres in creeping non-Newtonian fluids. Chhabra [87] has published an excellent compendium of the relevant research on this topic. He devotes separate chapters of his book to the drag experienced by a sphere moving in a generalized Newtonian (time-independent) fluid and in a viscoelastic fluid. The same will be done here. Unfortunately, as Chhabra [87] notes, there is a dearth of experimental data relating to the non-spherical particle dynamics in non-Newtonian fluids. An equivalent spherical diameter must be chosen in order to use the current literature to speculate on the impact of non-Newtonian fluid parameters on PIV analysis.

3.3.1 Particle Drag in Shear-Thinning Fluids

Chhabra [87] claims that the general consensus of available research is that shear-thinning effects enhance the drag on spherical particles. This is good for PIV in polymer melts because it decreases the Stokes number. Bush and Phan-Tien [88] did computational studies of the drag coefficient for spheres in Carreau model fluids and compared them to the results of Chhabra and Uhlherr [89]. They presented the

following Stokes drag relation:

$$F_D = 6\pi\eta_0 r V X \tag{3.29}$$

where F_D is the drag force on on a particle of radius r moving with velocity V relative to a Carreau model fluid with zero-shear viscosity η_0. X is a correction factor equal to the ratio of the actual drag to the drag that would be experienced by a particle in a Newtonian fluid of viscosity η_0:

$$X = \frac{C_D \mathrm{Re}_0}{24} \tag{3.30}$$

where Re_0 is the Reynolds number based on the particle diameter and velocity and the zero-shear viscosity of the fluid:

$$\mathrm{Re}_0 = \frac{Vd}{\eta_0} \tag{3.31}$$

They then presented the following functional form of X:

$$X = (1 + k^2\Lambda^2)^{\frac{n-1}{2}} \tag{3.32}$$

where k is a fit parameter. Bush and Phan-Tien [88] present a table of k for various values of n, but showed that setting $k = 0.275$ matched a wide range of experimental data within $\pm 10\%$. The other parameter in Equation 3.32, Λ, is a dimensionless time scale known as the Carreau number:

$$\Lambda = \frac{2\tau V_{slip}}{d_p} \tag{3.33}$$

where τ is the time constant of the Carreau model of a generalized Newtonian liquid, d_p is the particle diameter and V is the particle velocity relative to the fluid.

To calculate the value of Λ for the present work the velocity V_{slip} must be estimated. In PIV both the particle and the fluid are moving, so V is the slip velocity

between the two. By design this slip velocity must be small if the PIV results are to be accurate. Equation 3.28 can be used to estimate this slip velocity. The shear rate in the region illuminated by the laser sheet should be very low, and is theoretically zero at the midplane, so the zero-shear rate viscosity can be used in Equation 3.28.

In order to calculate the slip velocity an estimate of the particle acceleration must be made. Mass conservation leads us to expect that the radial velocity in the region of the gate should be inversely proportional to r, and thus the acceleration should be inversely proportional to r^2:

$$\frac{dV}{dt} \propto r^{-2}\frac{dr}{dt} = \frac{V}{r^2} \tag{3.34}$$

Examination of the PIV results at the 34.0 cm^3/s show velocities of approximately 20 cm/s at a distance of 3 cm from the gate, giving an estimated acceleration of 22 m/s^2. Using these values and the Stokes diameter d_s in Equation 3.28 gives an estimated slip velocity on the order of 2.5×10^{-8} m/s. Using this value of the slip velocity, the particle diameter and the Carreau parameter $\lambda = 0.0193$ s in Equation 3.33 give an estimate of $\Lambda = 1.6\times10^{-5}$. Using this value in Equation 3.32 with $n = 0.42$ gives a correction factor of X=0.999.

This means that the drag experienced by the particle is equal to the drag experienced by a particle in a Newtonian fluid with viscosity equal to the zero-shear viscosity. This justifies the use of the zero-shear viscosity in calculating the Stokes number in Section 2.2.

This result is in accord with the general consensus reported by Chhabra [87] that shear thinning effects are neutral, or somewhat enhance the Stokes drag. For studies of power law fluids, the value of X is referenced to the particle drag for a Newtonian

fluid at the same effective Reynolds number $\mathrm{Re}_{\mathrm{PL}}$:

$$\mathrm{Re}_{\mathrm{PL}} = \frac{\rho V_{slip}^{2-n} d^n}{m} \tag{3.35}$$

where n and m are the power-law parameters. Bush and Phan-Tien [88] claim that X is approximately 1.4 for fluids with power-law exponents of 0.2-0.5, representing a drag enhancement over the Newtonian drag at the same effective Reynolds number. For the flows in the present work the effective power-law Reynolds number is on the order of 10^{-14}.

3.3.2 Particle Drag in Viscoelastic Fluids

Viscoelasticity can also affect particle drag. The general consensus as reported by Chhabra [87] is that viscoelasticity reduces particle drag, but that its effects are completely overshadowed by shear-thinning effects at low Reynolds numbers. At high Reynolds numbers the viscoelastic effects can be appreciable. This is apparent in the following empirical relation by Acharya et. al. [90]:

$$C_{De} = C_D \left[1 - 0.18(\mathrm{Re}_{\mathrm{PL}}\mathrm{We})^{0.19}\right] \tag{3.36}$$

where C_{De} is the drag coefficient in elastic liquids and C_D is the drag experienced by a particle in a Newtonian flow at the effective power-law Reynolds number defined in Equation 3.35. The Weissenberg number, W_e, is a measure of the importance of elastic effects:

$$W_e = \frac{\tau V}{r} \tag{3.37}$$

where τ is a characteristic relaxation time, V is the slip velocity and r is the particle radius. For the present work the Weissenberg number based on the particle size and slip velocity is on the order of 10^{-6}.

This relation shows that even at small Weissenberg numbers there will be a slight reduction in particle drag compared to a strictly shear-thinning, non-elastic power-law fluid. But since Re_{PL} is so small for the slipping flow of a polymer melt past a PIV particle the effect is negligible. The drag experienced by a particle in a creeping shear-thinning viscoelastic flow is effectively the same as that of a comparably shear-thinning non-elastic flow. This general result is confirmed by Chhabra and Uhlherr [89] and Bush and Phan-Tien [88] who found that the measured values of drag coefficients in highly viscoelastic fluids were in excellent agreement with purely viscous theories [87].

Based on the power-law model, then, shear-thinning enhances particle drag while viscoelasticity decreases particle drag. Overall, the particle drag is enhanced since the shear-thinning effects overshadow the viscoelastic effects. These conclusions are reflected in Table 3.2.

In some cases drag may be enhanced by viscoelasticity. Solomon and Muller [91] and Chmielewski et. al. [92] have found that drag can be enhanced in certain Boger fluids when referenced to particle drag in Newtonian fluids of the same viscosity. The drag enhancement occured at Weissenberg numbers greater than 0.1.

The determination of whether particle drag is enhanced or decreased by elastic effects in STYRON 615APR is beyond the scope of this project, although it is likely that drag enhancement does not occur since the particle Weissenberg number is an order of magnitude lower than the drag enhancement threshold found in the above-mentioned studies. In any case, drag enhancement would be positive for PIV in polymer melts. Since there is a strong possibility that drag is slightly reduced, however, the effect is listed as negative in Table 3.2.

3.4 Particle Migration Across Shear Planes

Gauthier [93, 94] showed that particles in non-Newtonian flows tend to migrate across planes of shear. In a series of tubular Couette and Poiseuille flows of shear-thinning and viscoelastic fluids he demonstrated that neutrally bouyant rigid spherical particles moved laterally, a phenomenon that would not be observed in Newtonian flows. For shear thinning fluids particles tended to move in the direction of the shear stress gradient, from the center toward the outer wall. The migration velocity dropped with increasing distance from the tube axis. For viscoelastic fluids the behavior was reversed. Particles moved in the direction of decreasing shear stress gradient, from the walls toward the tube axis. The migration velocity dropped with decreasing distance from the tube axis. In both cases the migration velocities increased with increasing flow rate.

This phenomena raises concerns for those attempting to use PIV in a polymer melt. Particle migration can cause a number of problems. The most pressing concern relates to particle migration in the plane of the image. If the particles do not follow the fluid flow then the PIV data will not be representative of the actual flow field. Luckily this concern is the most easily dismissed. The shear gradients in the midplane of the cavity are small, so any particle migration effects should also be small.

Another possible problem, though less pressing, is harder to dismiss. In an injection molding flow the shear gradient through the cavity thickness can be quite high. This means that particle migration into and out of the illuminated midplane is likely to happen.

Particle migration perpendicular to but within the illuminated plane poses no issue in this work. The PIV analysis is strictly two-dimensional, so lateral velocity

components are of no concern if the particle stays within the laser sheet. This is because, as mentioned previously, the velocity profile of a shear thinning fluid in a cavity flow is very flat at the midplane. Lateral motion within the sheet has very little effect on the in-plane velocity components. If three-dimensional PIV were employed or if a more weakly shear-thinning fluid were used then lateral migration perpendicular to but within the sheet would be more problematic than it is in this work.

Particle migration into the illuminated sheet due to viscoelastic effects is problematic, but not insurmountably so. Particles that are present only in the second image of a PIV pair raise the background noise level of the cross-correlation due to false positive matchups with the migrating particles. But if the particles in the first frame are still present in the second frame and if the illumination is good then the true correlation peak should still be found and the correct velocity vector calculated.

The most problematic effect of particle migration is the loss of illuminated particles as they migrate out of the laser sheet toward the cavity walls due to shear-thinning effects. Lost particles cause failures in the cross-correlation which lead to errors in the calculated velocities.

3.4.1 Particle Migration in Shear-thinning Fluids

Emerman [95] used dimensional analysis and curve-fitting of Gauthier's [94] shear-thinning fluid test data to produce an analytic expression relating the particle migration velocity U_r to the tube radius R, particle radius a, volume flow rate V and the power-law index n of the fluid. He produced the following model that fit the observed behavior in Gauthier's [94] experiments:

$$U_r = \frac{1}{50}(1-n)\frac{V}{R^2}\left(\frac{a}{R}\right)^n\left(\frac{r}{R}\right)^{2(n-1)} \tag{3.38}$$

Emerman recognized, however, that injection molding flow is more closely approximated by a two-dimensional Poiseuille flow rather than by a circular Poiseuille flow. In the absence of experimental data he created the following two-dimensional equivalent of Equation 3.38:

$$U_y = \frac{2^{3n}}{50}(1-n)\frac{Q}{h}\left(\frac{a}{h}\right)^n\left(\frac{y}{h}\right)^{2n-1} \tag{3.39}$$

where U_y is the lateral migration velocity, Q is the volume flux per unit width, h is the channel width, and y is the particle position with the cavity midplane at $y = 0$ and the walls at $y = \pm h/2$.

Emerman then made the broad claim that Equation 3.39 "gives the lateral migration rate in the y-direction of a spherical particle during injection molding due to the shear thinning of the polymer melt" [95]. He placed no qualifications on any of the variables appearing in the equation.

An attempt was made to use Equation 3.39 in the present work to estimate the severity of particle migration out of the midplane. It became apparent, however, that Equation 3.39 is not as applicable as Emerman claimed.

The problem lies in the $(y/h)^{2n-1}$ factor of Equation 3.39. Given that Gauthier's [94] fluid had a shear-thinning index of $n = 0.77$, Equation 3.39 predicts that the migration velocity *increases* with increasing distance from the center-plane. This contradicts Gauthier's observation that the migration velocity decreased as particles moved away from the center line.

Even worse, this behavior is dependent on the the value of n in Emerman's model. If $n = 0.5$ the y dependence of U_y disappears entirely. For fluids with $n < 0.5$, such as the polystyrene used in the present work, the exponent of y becomes negative. In this case the migration velocity does indeed decrease with increasing y, but tends to

infinity for particles near the midplane of the cavity. When applied to the present work this gives unreasonably large estimates of the migration velocity for particles in the laser sheet.

In the absence of experimental data and of reliable models of particle migration in two-dimensional Poiseuille fluids, no direct estimate of the particle migration velocity can be made in the present work.

3.4.2 Particle Migration in Viscoelastic Fluids

Emerman [95] also considered the effect of normal stress differences on particle migration, basing his analysis on the work of Brunn [96] and Chan and Leal [97]. These researchers calculated the lateral migration rate of a rigid sphere in an an unbounded second-order fluid, assuming low particle Reynolds number and low Weissenberg number. Applying their results to a two-dimensional Poiseuille flow Emerman [95] gave the following relation:

$$U_y = -\frac{482}{25}\frac{\psi_1}{\eta}\left(1+\frac{259}{241}\alpha\right)\left(\frac{a}{h}\right)^2\frac{Q^2}{h^4}y \tag{3.40}$$

where a is the radius of the sphere, h is the channel width, ψ_1 is the first normal stress difference, η is the viscosity and α is the negative of the ratio of the first and second normal stress differences.

Several observations can be made from this relation:

1. U_y/y is negative for polymer melts because $\psi_1 > 0$ [63] and α typically ranges from 0-0.4 [98] for these fluids. This means that particles will migrate toward the midplane. Therefore the viscoelastic effect and the shear-thinning effect on particle migration will tend to cancel each other out, with the caveat of Gauthier's [94] observation that particle migration outward due to shear-thinning seemed somewhat stronger than inward migration due to viscoelasticity.

2. U_y is zero at $y = 0$. Particles on the midplane do not migrate.

3. The ratio a/h will be small by design in any PIV experiment, leading to small values of U_y.

4. The viscoelastic U_y is linearly proportional to Q^2 and a^2, while the shear-thinning U_y is linearly proportional to Q and a^n. Particle migration due to normal stress differences is more sensitive to high flow rates than migration due to shear-thinning, but the effect is mitigated for PIV particles by the increased sensitivity to particle radius.

The viscosity and the first normal stress difference were measured for STYRON 615APR with a rheometer, see Section 2.4. It was found that $\eta = 295.4$ Pa·s and $\psi_1 = 1000$ Pa. The second normal stress difference could not be measured with the rheometer, but to be conservative it can estimated as 0.4α [98]. Taking the highest value of the volume flow rate used in this work (34.0 cm^3/s) and dividing it by the specimen width of 66.7 mm gives $Q = 5.25$ cm^2/s. Taking $y = 0.5$ mm to be the edge of the laser sheet and using these values in Equation 3.40 gives a worst-case estimate of the particle migration velocity U_y = -0.17 mm/s. For the conditions described above typical PIV velocities were on the order of 10 cm/s, indicating that particle migration due to viscoelastic effects will be negligible.

Finally, returning to Gauthier's [94] observation that migration due to shear-thinning was only slightly stronger than that due to viscoelasticity, it may be hoped that particle migration due to shear-thinning will also be negligible.

Table 3.2: Comparison of factors unique to PIV in polymer melts with Newtonian PIV experiments. A "+" in the center column means that this factor is favorable to PIV in polymer melts, a "-" means that the factor is unfavorable.

High viscosity	+	Reduces particle-particle interactions
	+	Increases Stokes drag, allows the use of larger and heavier particles
	+	Smooth flow due to low Reynolds number
	-	High pressures, large loads on window
Fountain flow	-	Causes out-of-plane particle motion near the melt front
Moving flow front	-	Reflection from front causes uneven illumination
Strong radial flow	-	Cross-correlation fails near gate
Non-isothermal flow	-	Laser sheet thickness is not constant
Particle mixing in the solid state	-	Particles are mixed with the melt in a high-shear environment. Standard PIV particles do not survive the process.
	+	Injection screws are designed to promote good mixing
Shear thinning	+	Increases Stokes drag at low Re
	+	Flattens the velocity profile in thickness direction
	-	Causes particle migration away from midplane
Viscoelasticity	-	Slightly decreases Stokes drag at low Re
	-	Causes particle migration toward midplane

3.5 Summary

A summary of the factors discussed in this chapter is given in Table 3.2. The technical challenges of setting up a PIV experiment in a polymer melt are exotic and formidable. But once the experiment is set up the high viscosity and shear-thinning nature of the flow eliminate many of the challenges faced by experimenters studying higher Reynolds number flows of Newtonian liquids.

CHAPTER 4

Image Analysis

The preparation and analysis of the digital images was a multi-step process that may be summarized as:

1. The Pulnix-9701 camera was calibrated as described in Section 2.6.2
2. Digital movies were made of the injection molding process
3. The images were corrected using the camera calibration
4. The flow front was manually extracted from the corrected images
5. Flow front propagation velocities were calculated from the extracted flow front images
6. The flow fronts and cavity walls were then used to create image masks, and the masks were used to extract the polymer melt images from the mold cavity
7. PIV analysis was performed on the masked, undistorted images of the flow
8. Median velocity fields were calculated from repeated trials for continuity analysis

The first three steps were discussed in Section 2.6.2. The rest of the steps will be explained and illustrated in the following sections.

4.1 Extracting the Flow Front Geometry

The flow front is the boundary between the illuminated midplane of the melt and the dark mold cavity. In a given digital image the flow front is a region where the intensity and the intensity gradient change sharply. Determining the location and shape of a region such as this is typically done using edge detection algorithms.

Edge detection is a very common image processing task and many algorithms have been developed to perform this task. Algorithms include Gaussian, Sobel, Prewitt, and Canny edge detection routines. Each one of these standard routines extracts edges by looking for steep intensity gradients. The details and effectiveness of the routines vary, but they all operate on this key principle.

Edge detection algorithms would normally be the best approach for extracting a boundary such as the melt flow front. PIV images of melt fronts, though, present some particular challenges to successful implementation of standard edge detection routines.

The first challenge to edge detection algorithms is that PIV images are speckled by nature. Images that are to be analyzed by a PIV program must consist of particle images that move with the local flow velocity. These particle images are small and bright, leading to an overall image that is filled with sharp changes in intensity over small length scales. These sharp changes in intensity are found by edge detection algorithms and result in a very high number of spurious edges that are not related to the flow front. The number of edges found depends on the algorithm used, but even the most sophisticated methods give practically unusable results. The edges found along the flow front are also typically unconnected, leading to more difficulties. In order for the results to be usable a human being would have to sort through the

edges, discarding those that are spurious and connecting those that lie on the front. As an example of this a typical image frame is shown in Figure 4.1. The result of using Matlab's implementation of Canny edge detection on this image is shown in Figure 4.2.

The second challenge to edge detection algorithms is related to the polymer melt itself. Stray reflections from the flow front onto the cavity wall can confuse edge detection algorithms. The presence of precursor gas in the mold can also increase the general level of illumination in the cavity near the front, reducing the contrast between the front and the cavity. Areas of high front curvature near the walls can lead to a lens effect, making that region of the image brighter than other regions. This increased brightness near the walls makes edge detection more difficult because it also reduces contrast.

After numerous failed attempts with the various edge detection routines available in the MATLAB Image Processing Toolbox it became obvious that a different approach was called for.

The binary morphological approach has many advantages, most prominently the fact that it can be automated to a significant degree. When the flow front is sharply defined in the image this method works well. Unfortunately the flow front is *not* always sharply defined in the digital image.

Fortunately human beings are better than computers at pattern recognition in cases like this. When all else fails the flow front can be traced by hand. This can be done at a computer but it is difficult. A mouse is not an ideal tool for this type of operation. It is difficult to create free curves by clicking and dragging a mouse. The proper tool for this type of work is a stylus, allowing the user to "draw" on the screen.

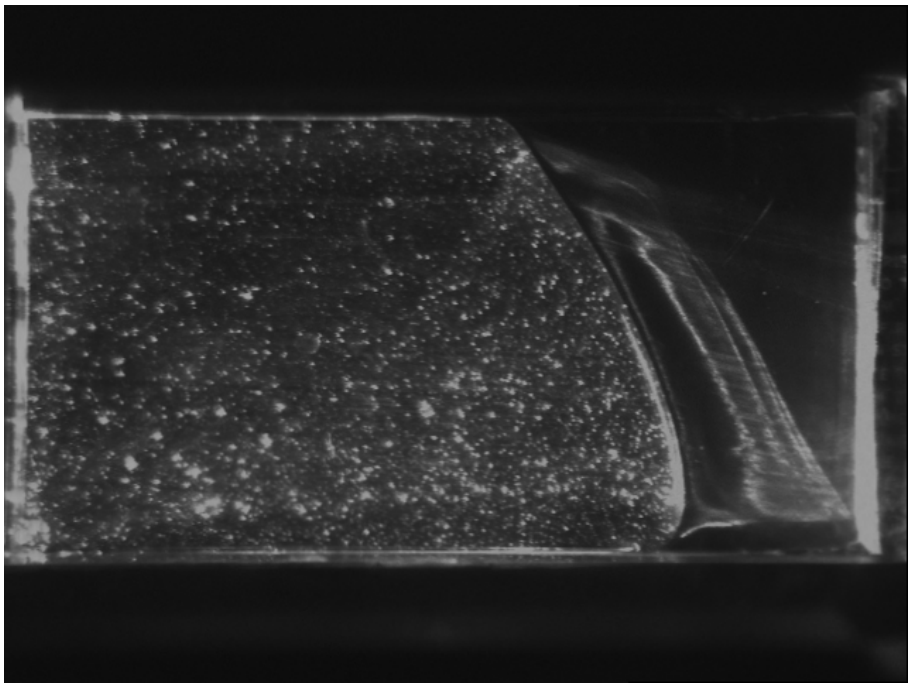

Figure 4.1: Typical frame from an injection molding movie.

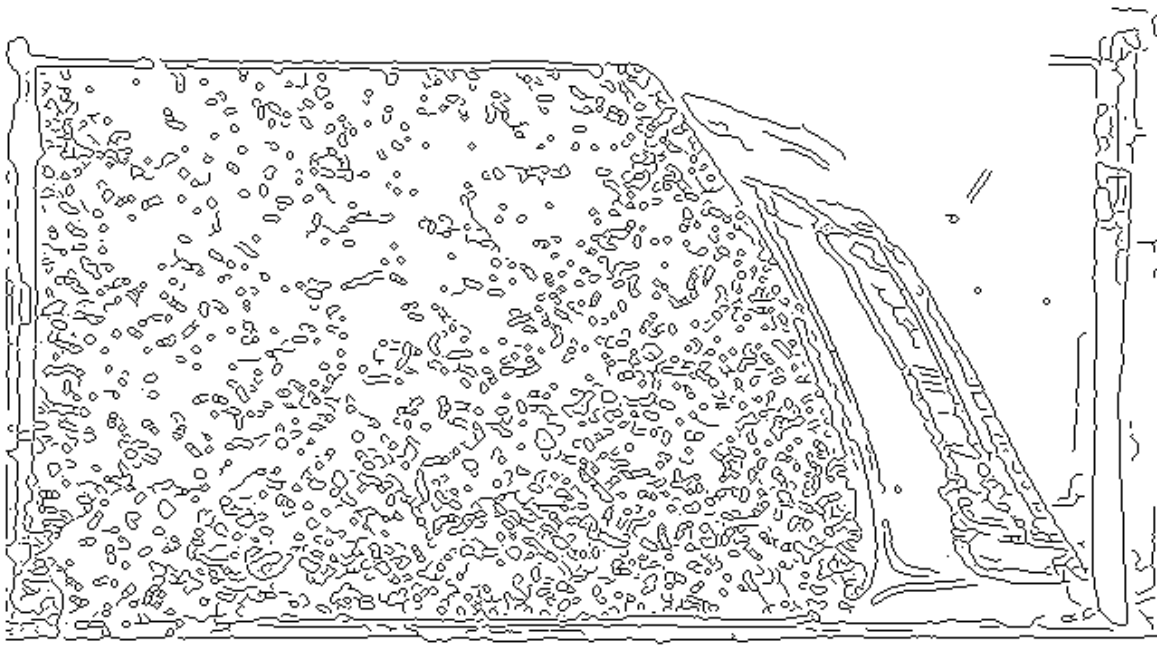

Figure 4.2: Results of using Matlab's implementation of Canny edge detection on the image shown in Figure 4.1

This can be done using a personal digital assistant (PDA). For this project a Tungsten TX PDA was used. A program called TealPaint v6.43 was used to manually extract the flow fronts when needed. The digital images were loaded on the PDA and read by TealPaint. The images were then magnified by a factor of eight, making the individual pixels large enough to be seen conveniently. The melt front was then positioned on the screen by dragging the PDA stylus. Once a portion of the front was centered on the screen the curve draw tool was used to trace the front. The curve draw tool allows the user to drag the stylus across the screen leaving a line in its wake. The motion of the stylus is averaged, creating a smooth line that follows the front without being overly jittery. The front was then traced in a piecewise fashion, moving the image around on the screen as necessary until the entire front was traced. The original image was then deleted, leaving only the tracing of the front. This image was then exported to a file and then loaded onto the computer that was used to perform the image analysis.

As an illustration of this process the result of manually extracting the flow front from the sample image shown in Figure 4.1 is shown in Figure 4.4.

4.2 Calculating the Velocity of the Flow Front

When the geometry of the flow front has been established it is possible to calculate the normal component of the front velocity at any point. The procedure is as follows:

1. Represent the flow front as a polynomial. The form and degree of the polynomial will depend on whether the flow has contacted the wall opposite the gate.

2. Select points along the flow front and calculate the normal vectors to the front. This gives the direction of the front velocity.

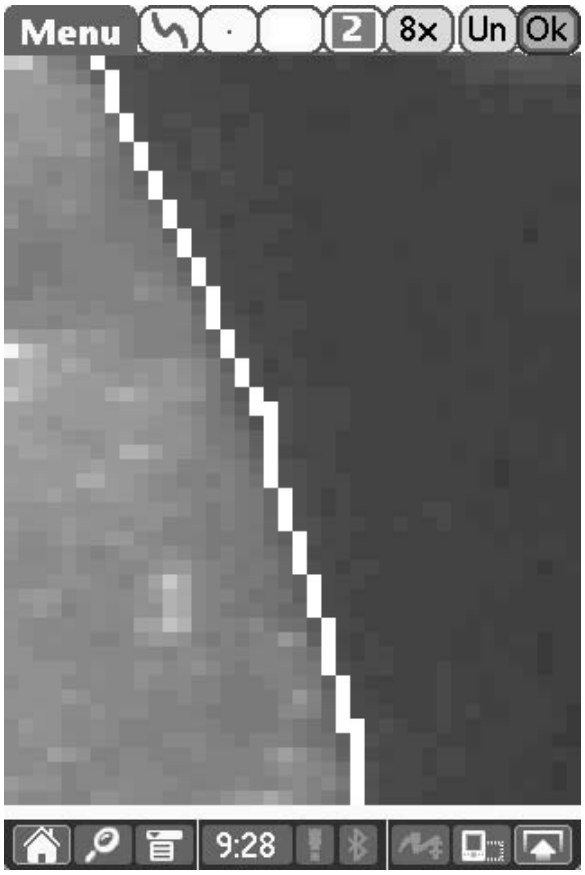

Figure 4.3: Manual extraction of the flowfront using TealPaint on a Tungsten TX PDA. The tracing was done directly on the PDA screen using a stylus with the image at 8x magnification.

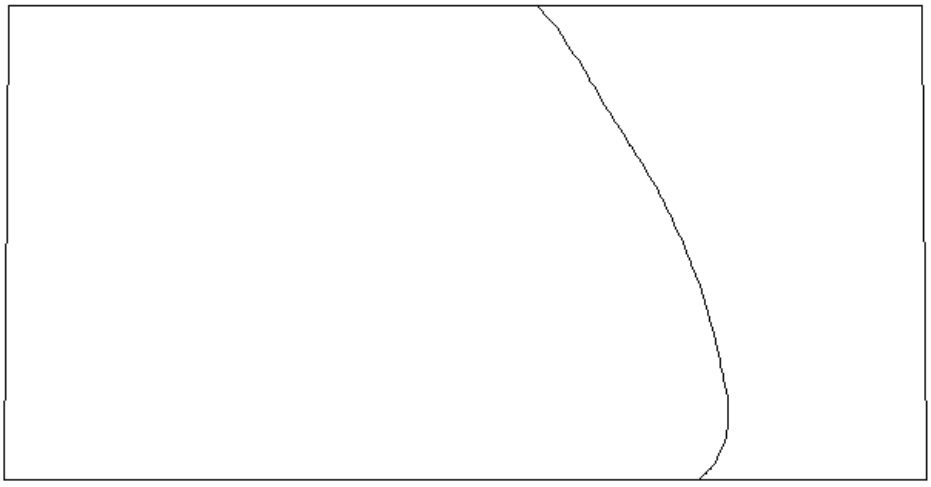

Figure 4.4: The result of manually extracting the flow front from Figure 4.1

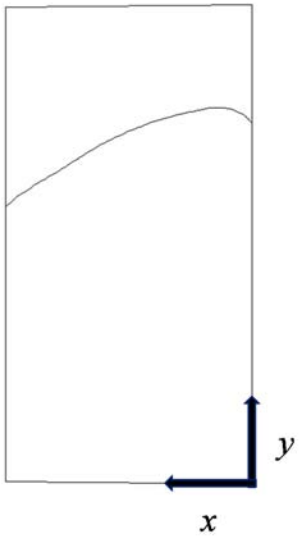

Figure 4.5: Coordinate system for fitting a polynomial to the extracted flow front for the channel flow regime. The origin is at the corner near the gate.

3. Superpose the front from the next frame of the digital movie. Propagate outward along the normal direction until the second front is intersected. This gives the magnitude of the front velocity.

4.2.1 Calculating the Flow Front Velocity in the Channel Flow Regime

This step is critical to calculating the front velocity. The approach taken depends on the flow front geometry. For fronts in the radial flow regime it is necessary to use polar coordinates in the calculations. This is not necessary for the channel flow regime, simplifying the calculations.

For the channel flow regime, rotate the flow field 90° counterclockwise about the lower left corner as shown in Figure 4.5. The flow front can now be represented by a function since each point on the front has a unique x coordinate. MATLAB was used to fit a tenth order polynomial to the flow front.

Once the polynomial has been fitted its derivative is easily calculated at any given point. This information is used to construct a unit vector tangent to the front at the

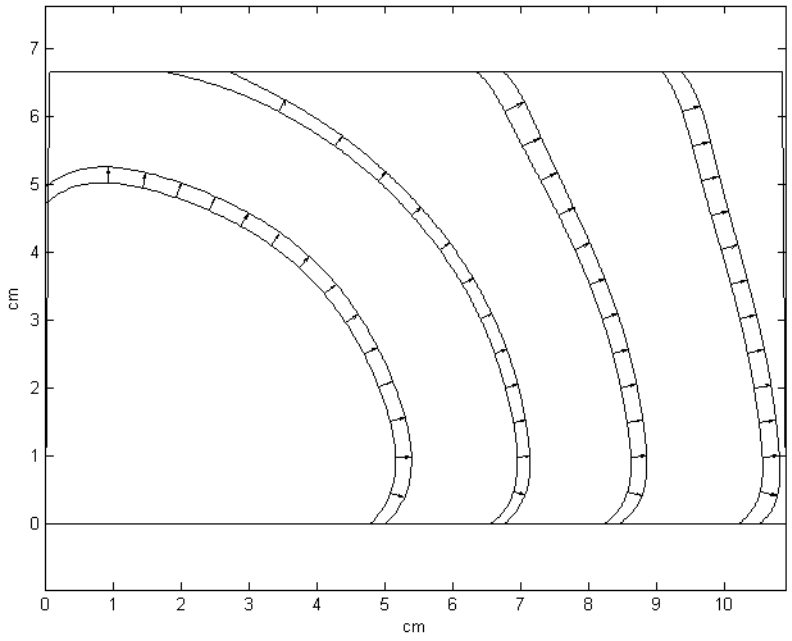

Figure 4.6: This figure shows flow fronts manually extracted at times equal to 30%, 50%, 70% and 90% of the overall fill time. Each front is also paired with the front taken from the movie frame immediately following. The velocity vectors show the front propagation displacements calculated using the methods described in Section 4.2.1 and Section 4.2.2.

point of interest. Once this vector has been determined a unit vector perpendicular to it (and thus to the front) is constructed, taking care to insure that this vector points away from the gate. This unit vector points in the direction of the perpendicular velocity component of the flow front.

The flow front from the next frame of the digital movie is then used. The front is fitted by a polynomial in the same manner described above. The point of interest on the first front is then used as a starting point. A test point is propagated along the normal direction until it intersects the polynomial representation of the second front. The propagation distance divided by the time between frames is equal to the magnitude of the flow front propagation velocity.

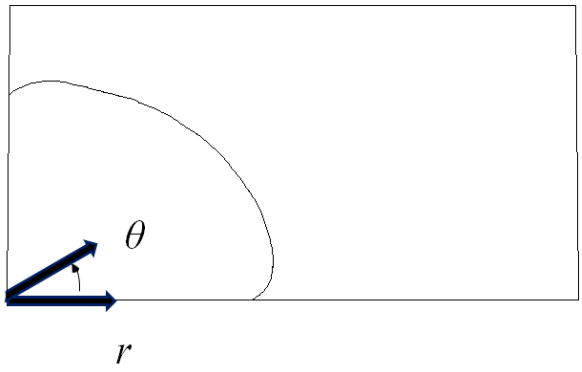

Figure 4.7: Coordinate system for fitting a polar polynomial to the extracted flow front for the radial flow regime. The origin is at the corner near the gate.

4.2.2 Calculating the Flow Front Velocity in the Radial Flow Regime

The procedure described above must be modified for flow fronts in the radial flow regime. The difficulty lies in the fact that the points on the flow front no longer have unique x coordinates, which means that the front cannot be described by a function using Cartesian coordinates. Rotation of the front will not resolve this difficulty.

Polar coordinates can be used to sidestep this problem. If the points on the flow front are represented with polar coordinates as shown in Figure 4.7 then the points will all have unique θ components. This means that a polynomial of the form $r = r(\theta)$ can be constructed. The r coordinates of the flow fronts in the radial flow regime are well-represented by sixth-order polynomials in θ.

Care must be taken when calculating the derivative of this polynomial. The derivative of $r(\theta)$ is not equal to the slope of the tangent vector of the front. Using the relations $x = r\cos\theta$ and $y = r\sin\theta$ and letting $r' = dr/d\theta$ it can be shown using

the chain rule that

$$\frac{dx}{d\theta} = -r\sin\theta + r'\cos\theta \tag{4.1}$$

$$\frac{dy}{d\theta} = r\cos\theta + r'\sin\theta \tag{4.2}$$

The ratio of these equations can be used to get the slope of the vector tangent to the front:

$$\frac{dy}{dx} = \frac{r\cos\theta + r'\sin\theta}{-r\sin\theta + r'\cos\theta} \tag{4.3}$$

Once the normal directions have been determined the procedure is the same as for the channel flow regime with modifications for using polar coordinates. The point of interest on the front is propagated along the normal directions in Cartesian coordinates. At each new position of the point along the normal the Cartesian coordinates are transformed into polar coordinates. The polar polynomial of the next sequential front is then used to check whether the point has been propagated far enough to intersect the second front.

4.3 Calculating the Velocity Field of the Polymer Melt

The flow fronts and cavity outlines were then used to create image masks. The flow front and cavity outline were used to create a binary image mask, as illustrated in Figure 4.8. The mask was created by inverting the image shown in Figure 4.4 and using the binary morphology functions in the MATLAB Image Processing Toolbox to fill in the portion of the image representing the polymer melt. The cavity edges were then removed to create a mask in which pixels representing the polymer melt have a value of “1” and all other pixels have a value of “0”.

This image was used to mask the undistorted movie image, leaving only the portion of the image occupied by the molten polymer as illustrated in Figure 4.9.

Figure 4.8: The binary mask created from Figure 4.4

These images were then used as the inputs for the PIV analysis.

The PIV analysis was accomplished using DaVis 6.2.2 software. The PIV analysis was performed using cross-correlation on consecutive images from the mold-filling movies. Adaptive multipass with decreasingly smaller window size was used. The first three passes used 64 pixel $\times$ 64 pixel windows followed by two passes with 32 pixel $\times$ 32 pixel windows. The highest injection rate runs required initial passes at 128 pixels $\times$ 128 pixels followed by passes at 32 pixels $\times$ 32 pixels. The windows had a 50% overlap, resulting in a grid spacing of sixteen pixels. The resulting data was filtered using a median filter. The data was smoothed using a 3 $\times$ 3 Gaussian filter.

The PIV output was then processed as follows. First, the data was scaled to real world coordinates. The lower corner of the cavity near the gate was used as the origin of the coordinate system. The data and coordinates were then scaled to correct for the non-square pixels of the Pulnix camera and the image size of the cavity was used to calculate the magnification factor of the image. Once the points were in real-world coordinates the PIV displacements were divided by the camera

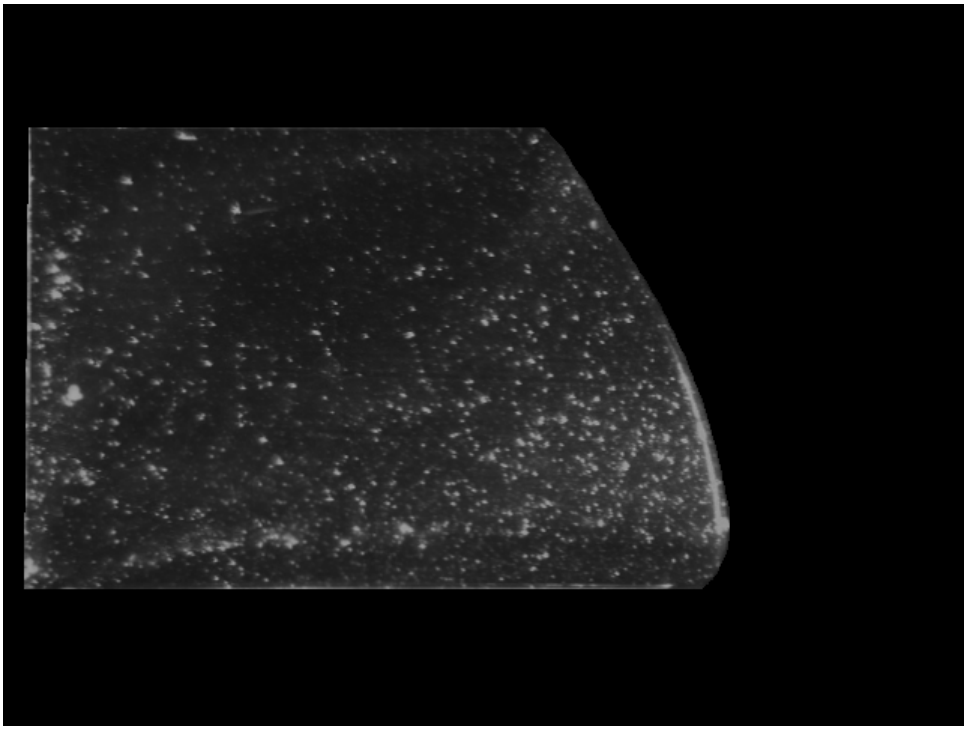

Figure 4.9: The masked version of Figure 2.21 created using the mask shown in Figure 4.8

frame rate to calculate local velocities in real-world coordinates.

4.4 Combining Multiple Data Sets with Median Filtering

One of the drawbacks of performing PIV experiments in a polymer melts is the difficulty in obtaining an even distribution of particles throughout the flowfield. As discussed in Chapter 3, the mixing of particles and polymer first takes place in the solid state. Particles and pellets are mixed together and are introduced into the hopper of the injection molding machine. The mixing of particles into the liquid plastic occurs in the barrel of the injection molding machine and is outside of the experimenter's control. There is no way to check the particle distribution before a shot is made, and once the shot is underway the laminar nature of the flow ensures that regions of the fluid that are particle-poor remain particle-poor throughout the

shot.

This led to difficulties in the PIV analysis in the present work. The resulting velocity vector fields had large gaps in them due to uneven particle distribution in the melt. The locations and number of these gaps would vary unpredictably from shot to shot. The low-particle areas would lead to obviously erroneous velocity vectors or would lead to areas with no velocity vectors at all. Figure 4.10 shows two PIV fields calculated at the 90% fill time for two different specimens made under the same molding conditions during the same run of parts. Velocity vector drop-outs are evident in both fields, but in different locations.

The solution to this problem hinges on the fact that the overall flowfield was very repeatable and very smooth. The velocity at a given point and a given time was very consistent from shot to shot, even if the particle density was inconsistent. This consistency suggested that the results of different movies made under the same conditions could be pooled to overcome the random defects in particle density.

For each set of processing parameters a number of movies were be made under identical conditions. The digital movies were then processed, typically yielding a set of 6-8 sets of velocity vector fields and their corresponding flow fronts for a particular time of interest.

The PIV vector fields were then superposed for each time of interest. Since most of the data sets were taken from a series of sequential runs the camera location and calibration were constant over a given set. This meant that the PIV grid points also tended to be constant for a given data set. The data sets were examined manually to ensure that the grid coordinates were identical. If they were not identical the non-conforming data sets would be interpolated onto the grid used by the other members of its set.

For each grid point there was a set of velocity vectors, one vector for PIV field in the set. A median filter was implemented for each component of the velocity vector, and the median velocity components were selected at each grid point.

Since the location of the bad vectors varied from shot to shot there were only a few bad vector components at any given point in the flow field. The median was chosen rather than the average at each point since the median is more robust and is less likely to be affected by bad vectors. The effect of taking the median at each point was to eliminate the gaps due to variations in particle density in the images. An example of the outcome after median filtering is shown in Figure 4.11.

The flow fronts from the superposed PIV images were also superposed on each other and the entire set used as an input to the polynomial fitting scheme described in Section 4.2. The flow front positions were very consistent, falling in a range of ± 0.25 cm around the best fit front. An example of this consistency is shown in Figure 4.12. This figure shows a superposition of flow fronts from six data sets and the best fit curves calculated from them.

4.5 Estimating the Error of the Median Velocity Fields

The following procedure was used to estimate the error in the median velocity fields. Eight movies were made under identical conditions and were processed as described above. The movies were then divided into two sets of four movies each and the median filter was applied to each set at the point of 90% fill. Let the resulting median fields be $\vec{v}_1$ and $\vec{v}_2$. A difference field $\Delta\vec{v}$ was then calculated, with $\Delta\vec{v} = v_1 - v_2$. An error estimate ε was then calculated as

$$\varepsilon = \sqrt{\frac{\sum |\Delta\vec{v}|^2}{\sum |\vec{v_1}|^2}} \tag{4.4}$$

The error ε can be interpreted as the mean magnitude of the difference field

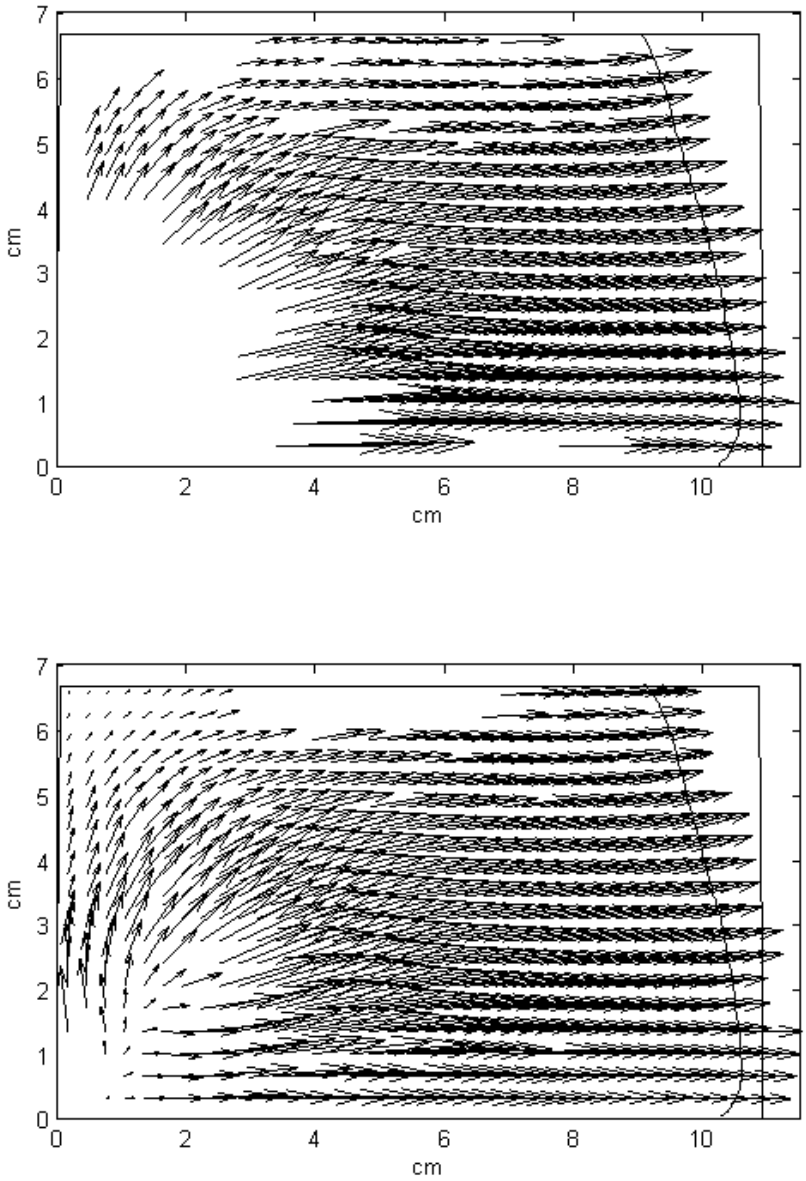

Figure 4.10: PIV vector fields computed at the 90% fill time for two different specimens molded under the same conditions during the same run of parts. The PIV fields have missing vectors in different places of the flow field. This problem is corrected with median filtering as described in Section 4.4. The PIV fields also show the failure of the PIV software to resolve the correct vectors near the gate.

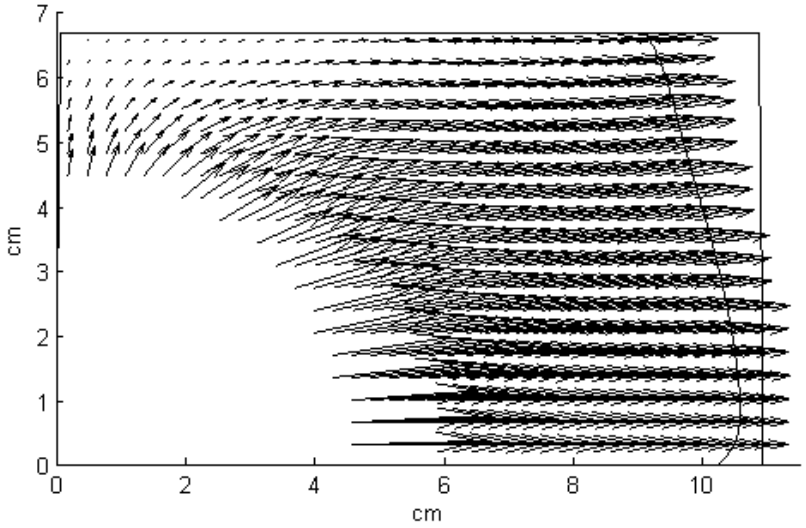

Figure 4.11: This figure shows the result of median filtering a set of seven PIV fields calculated at the same point of fill from specimens molded at identical conditions. Two of the PIV fields used in the set are shown in Figure 4.10. A dead-zone radius was applied around the gate to eliminate vectors from the region where the PIV analysis fails.

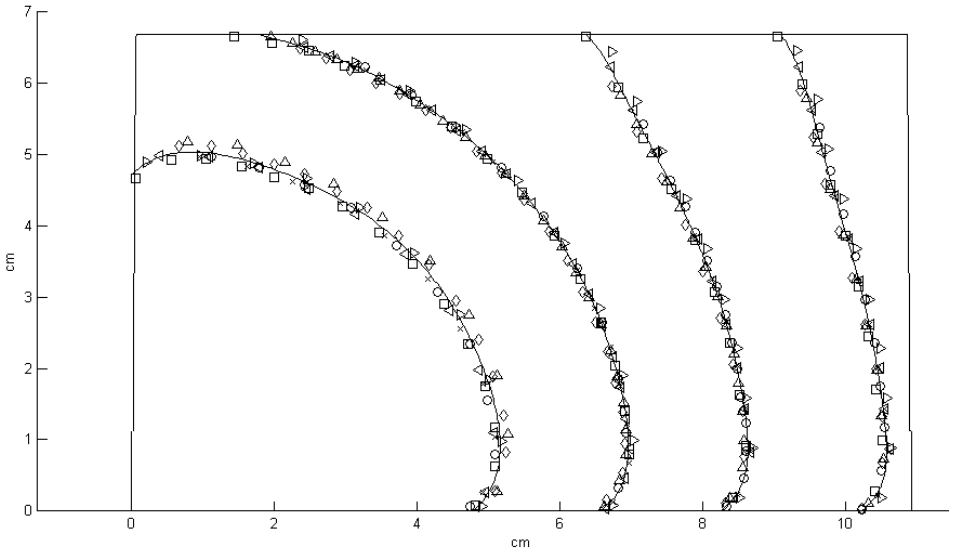

Figure 4.12: Flow fronts extracted from data sets molded at identical conditions. The data points shown are subsets of the actual data for clarity of plotting. The best-fit fronts calculated from these fronts are also displayed.

normalized by the mean magnitude of the vectors in the median field. This process was then repeated for every possible way of dividing the original set of vector fields into two equal subsets. The resulting distribution of ε had a mean of 8.2%, leading to an upper bound error estimate on the median velocities of $\pm$8.2%; medians from eight samples should be more accurate.

4.5.1 Nondimensionalizing the Continuity Equation

The continuity equation in Cartesian coordinates for the flow of an incompressible fluid is given by Equation 4.5. This equation is true regardless of the Newtonian or non-Newtonian nature of the fluid.

$$\nabla \cdot \vec{v} = 0 \tag{4.5}$$

The polymer flow in this study is incompressible during the filling process. Also, the flow at the center plane of the cavity can be considered two-dimensional except near the gate and near the front. At the gate the flow is still developing into a smooth laminar flow and two-dimensionality cannot be guaranteed. At the front the fountain flow effect shown in Figure 3.3 creates a three-dimensional region of flow. But for region in between the gate and the front, the flow at the midplane should be two-dimensional and incompressible. Thus Equation 4.5 can be expressed in this region as:

$$\frac{\partial u}{\partial x} + \frac{\partial v}{\partial y} = 0 \tag{4.6}$$

Since the PIV vector data is taken at discrete time intervals Δt and on a regularly spaced grid of points with separations Δx and Δy the continuity equation can also be discretized:

$$\frac{\Delta u}{\Delta x} + \frac{\Delta v}{\Delta y} = \varepsilon(x, y) \tag{4.7}$$

where ε is an error term with units of inverse time. The error will be a function of position for any given PIV vector field. The error arises from inaccuracies in the PIV data itself and from the inherent numerical error arising from approximating derivatives on a discrete grid.

Ideally ε would be zero at all points in the flow field during mold filling except for at the gate. But PIV analysis delivers only an uncertian measurement of the velocity vector field and so ε will not be identically zero at each point in the flow field. But as the quality and resolution of the PIV data increase the magnitude of ε should decrease.

It is desirable to nondimensionalize Equation 4.7 and in particular to nondimensionalize ε. A nondimensionalized ε would become a measure of the quality of the PIV data. The nondimensionalization used in this work developed from consideration of the nature of the error term ε and of the basic nature of PIV analysis.

The error ε can be interpreted as a field of volume sources and sinks, depending on the sign of the error at any given point. By the nature of PIV analysis the velocity vector at a given point in the flow field must be considered constant over the interrogation volume V_I used to to generate that velocity vector [40]. Consequently the velocity gradients must also be considered constant within V_I. Since ε is the sum of two velocity gradients it must also be constant within V_I. Thus Equation 4.7 may be integrated over a given interrogation volume as follows:

$$\iiint_{V_I} \varepsilon \mid_{(x,y)} dV = V_I \; \varepsilon \mid_{(x,y)} \tag{4.8}$$

The error term now has the units of volume flow rate. For an injection molding flow it is natural to nondimensionalize the result of Equation 4.8 using the injection flow

rate Q. This leads to a nondimensionalized continuity equation:

$$(\nabla \cdot \vec{v})^* = \varepsilon^* \tag{4.9}$$

with

$$(\nabla \cdot \vec{v})^* = \frac{V_I}{Q} \nabla \cdot \vec{v} \tag{4.10}$$

$$\varepsilon^* = \frac{V_I \varepsilon}{Q} \tag{4.11}$$

The term $(\nabla \cdot \vec{v})^*$ is the nondimensionalized flow divergence. The variable ε^* can be interpreted as the local spurious source strength scaled by the global injection rate. If $\varepsilon^* = 0$ at a point then the continuity equation is satisfied at that point. As the magnitude of ε^* at a point approaches unity the magnitude of the erroneous source strength at that point approaches that of the injection flow rate itself.

4.5.2 Calculating the Flow Divergence

The previous sections described how the flow front was extracted and how the velocity vector field was generated. With this data in hand the velocity gradients at each point can be calculated, and thus the flow divergence.

A Matlab program was written to process the velocity data. The cavity outline and flow front were used to delineate the time-varying boundary of the flow. The PIV grid points within the flow domain were then classified by their distance from the boundary. Points that were more than one full grid spacing from the boundary were classified as interior points and points that were less than one full grid spacing from the boundary were classified as boundary points. The x and y distances from the physical boundaries (cavity walls and flow front) were then calculated for each boundary point.

The boundary points then needed further classification. If a grid point was within one grid spacing of a cavity wall it was considered a cavity boundary point, and if it was within one grid spacing of the flow front it was considered a flow front boundary point. Note that the classification of a given point can differ for the x and y directions. For example, a point near the top wall could be a boundary point in the y direction and an interior point in the x direction. A point near the intersection of the front and a wall could be a flow front boundary point in the x direction and a cavity boundary point in the y direction.

Once the points were classified the velocity gradients could be calculated. The velocity gradients of the interior points were calculated using a standard central differencing scheme as described by Gerald [99]:

$$\frac{\partial u}{\partial x} = \frac{u_{i+1} - u_{i-1}}{2h_i} + O(h_i^2) \tag{4.12}$$

$$\frac{\partial v}{\partial y} = \frac{v_{j+1} - v_{j-1}}{2h_j} + O(h_j^2) \tag{4.13}$$

where i is a counter that increases in the positive x direction and j is a counter that increases in the positive y direction. The variables h_i and h_j are the grid spacings in the x and y directions respectively.

In order to maintain the second order accuracy of the gradient approximations special care was needed at the boundary points. Cavity boundary points used a variation of the central differencing scheme formulated for non-uniform grid spacing. Flow front boundary points required a three-point one-sided differencing scheme.

A cavity boundary point has two neighboring points in the direction perpendicular to the cavity wall. One point is an interior point that has a known velocity and is separated from the cavity boundary point by a full grid spacing. The other neighboring point is on the cavity wall itself. This point is less than a full grid spacing away

and is assumed to have zero velocity (the no-slip condition). The gradient was then calculated using a non-uniform grid spacing central differencing scheme described by Gerald [99].

Given a function $f(x)$ known at discrete points with non-uniform spacing let $f_0 = f(x_0)$, $f_+ = f(x_0 + h_+)$, and $f_- = f(x_0 - h_-)$ with $h_+ \neq h_-$. Manipulating the Taylor expansions of f_+ and f_- results in:

$$\frac{\partial f}{\partial x} = \left(\frac{f_+}{h_+^2} - \frac{f_-}{h_-^2}\right)\left(\frac{1}{h_+} + \frac{1}{h_-}\right)^{-1} - f_0\left(\frac{1}{h_+} - \frac{1}{h_-}\right) + O(h_+ h_-) \tag{4.14}$$

Note that this formula reduces to Equation 4.12 for the case $h_+ = h_-$, as it should.

A flow front boundary point also has two nearest neighbors, an interior point and a point on the front. The problem here is that the midplane velocity of the the point on the front is unknown due to the fountain flow effect. This precludes the use of a central differencing scheme. In order to maintain second-order accuracy a three-point one-sided differencing scheme was used as described by Gerald [99]. The two nearest interior points in the desired direction were used with the boundary point to approximate the gradient in that direction.

Given a function $f(x)$ known at discrete points with uniform spacing h let $f_0 = f(x_0)$, $f_1 = f(x_0 + h)$, and $f_2 = f(x_0 + 2h)$. Then:

$$\frac{\partial f}{\partial x} = \frac{-f_2 + 4f_1 - 3f_0}{2h} + O(h^2) \tag{4.15}$$

After the velocity gradients $\partial u/\partial x$ and $\partial v/\partial y$ were calculated for all internal and boundary points the nondimensional divergence error ε^* was calculated using Equation 4.10. The value of ε^* was then superimposed on the PIV graph as a pseudocolor field using the Matlab "Jet" colormap. Figure 4.13 shows the result of applying the scaled continuity equation to the median-field PIV data shown in Figure 4.11.

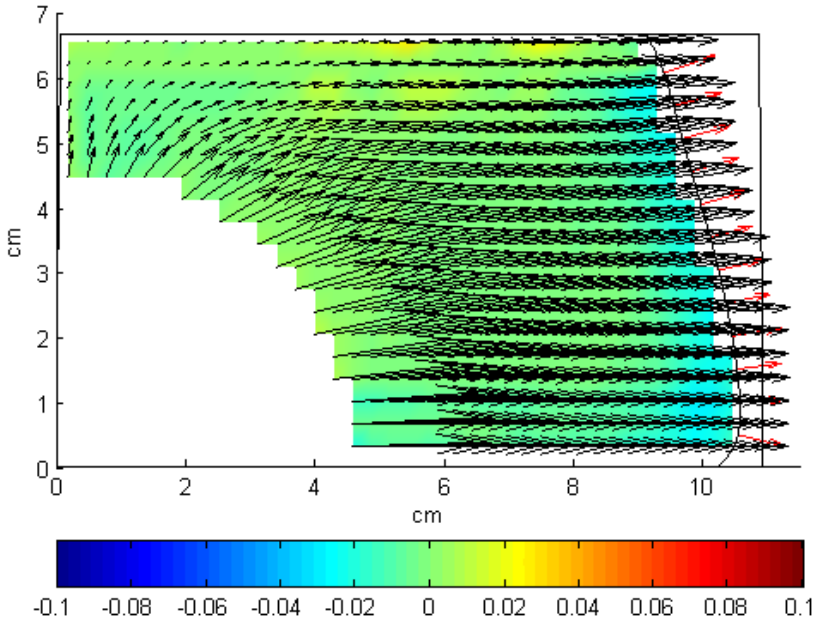

Figure 4.13: Application of the scaled continuity equation described in Section 4.5.1 to the median-field PIV data shown in Figure 4.11. The front propagation velocity vectors are also shown.

CHAPTER 5

Parameter Study of the Effects of Injection Rate and Melt Temperature on Mold Filling

A parameter study of the mold filling process was performed using the experimental setup described in the previous chapters. The goal of the study was to examine the effects of injection rate and melt temperature on the flow kinematics of the filling of the optical access mold.

5.1 Molding Conditions

An initial parameter study was performed using melt temperature and injection rate as the input parameters. The values chosen for this study are listed in Table 5.1. The parameter values were chosen to represent the widest practical range for the experimental setup. At temperatures and speeds lower than this range the flow would not fill the mold smoothly and short shots would often result. The injection molding machine labored excessively at speeds higher than this range, and at temperatures exceeding this range the melt viscosity would be low enough to cause difficulties in building up the shot.

Eight digital videos were made for each set of molding conditions and the results were processed according to the procedure described in Chapter 4.

Table 5.1: Molding conditions used in the parameter study

Injection rate (cm^3/s)	Melt temperature ($^\circ$ C)
11.5	230
23.0	230
34.5	230
11.5	245
17.3	245
34.5	245

5.2 PIV Results

The resulting PIV fields are shown in Figures 5.1 through 5.12. The vector fields shown correspond to values of t^* equal to 0.3, 0.5, 0.7 and 0.9 where t^* is time normalized by the fill time of the optical access mold. Note that the cavity and vector fields in these figures have been rotated clockwise by 90° for convenience in plotting.

The black vectors show the velocity field of the polymer melt along the midplane during mold filling and the red vectors show the melt front propagation velocity. The melt velocity and melt front vectors have been scaled down by a factor of ten for convenience in plotting. The figures also show the shape of the flow front and the surrounding cavity. The pseudocolor field superposed on the flow shows the nondimensionalized continuity error as described in Equation 4.10. Green represents areas of the flow where continuity was satisfied to a high degree of accuracy. Red represents areas of the flow where the PIV analysis yields spurious volume sources, and blue represents areas of the flow where the PIV analysis yields spurious volume sinks. The range of errors covered by the color range is ±10% of the gate flow source.

The size of the dead zone around the gate was chosen to match the predictions found in Table 3.1. Errors around the periphery of the dead zone may be attributed to

the difficulty of using standard PIV to measure radial flow, as described in Chapter 3. Errors near the flow front may be attributed to the fountain flow effect also described in Chapter 3. Notice that the region near the front is consistently colored light blue, meaning that volume is disappearing near the front. The fountain flow effect is a three-dimensional phenomena that carries the fluid away from the center plane of the mold and deposits it on the side walls of the mold. This would explain the errors seen in the continuity equation near the front. Another factor contributing to continuity errors near the front is the fact the front has curvature in the thickness direction as well as in the midplane. This could lead to optical distortion near the front.

5.3 Calculating the Volume Flow Rate from the PIV Data

The volume flow rate can be calculated from the PIV fields and then compared to the injection rate to test the integrated accuracy of the data. This test was performed using the t^*=0.9 data at all molding conditions.

Taking the cavity in the orientation shown in Figures 5.1 through 5.12, call the long cavity dimension x and the short cavity dimension y. A set of control volumes was constructed using the walls of the cavity and a control surface S perpendicular to the x-axis as shown in Figure 5.13. Each control volume had a different x-coordinate for the surface S. The range of the location of S was chosen to be larger than the critical radius at which the PIV analysis failed and smaller than the flow front location to avoid the fountain flow effect.

Applying the mass conservation equation, the volume flux through S was calculated as follows:

$$Q = \int_S [u(y) \pm u_\varepsilon(y)] w(y) F dy \tag{5.1}$$

where u is the component of the fluid velocity in the x-direction, u_ε is the velocity

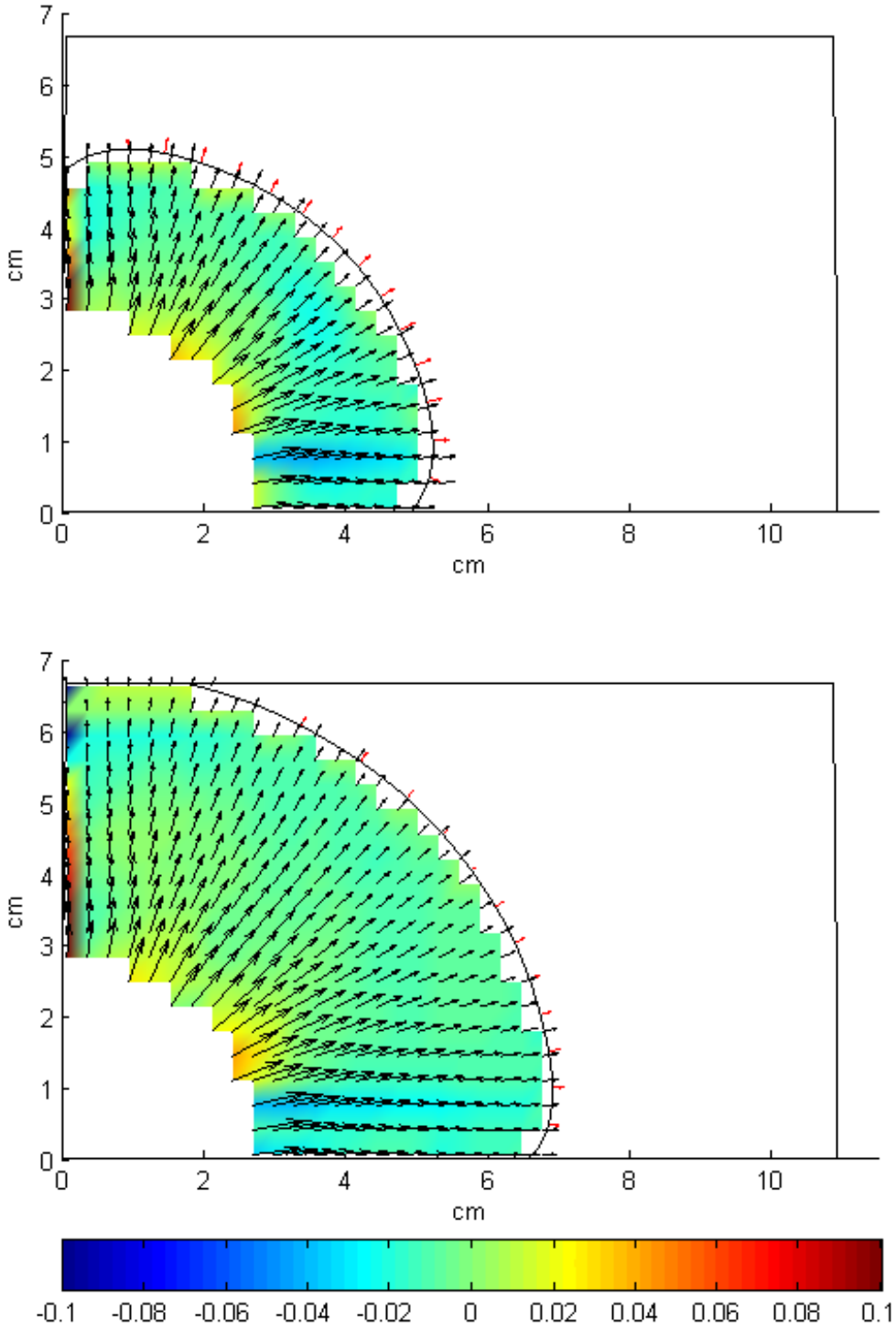

Figure 5.1: 230° C, 11.5 cm^3/s, t^*=0.3 (top) and t^*=0.5 (bottom)

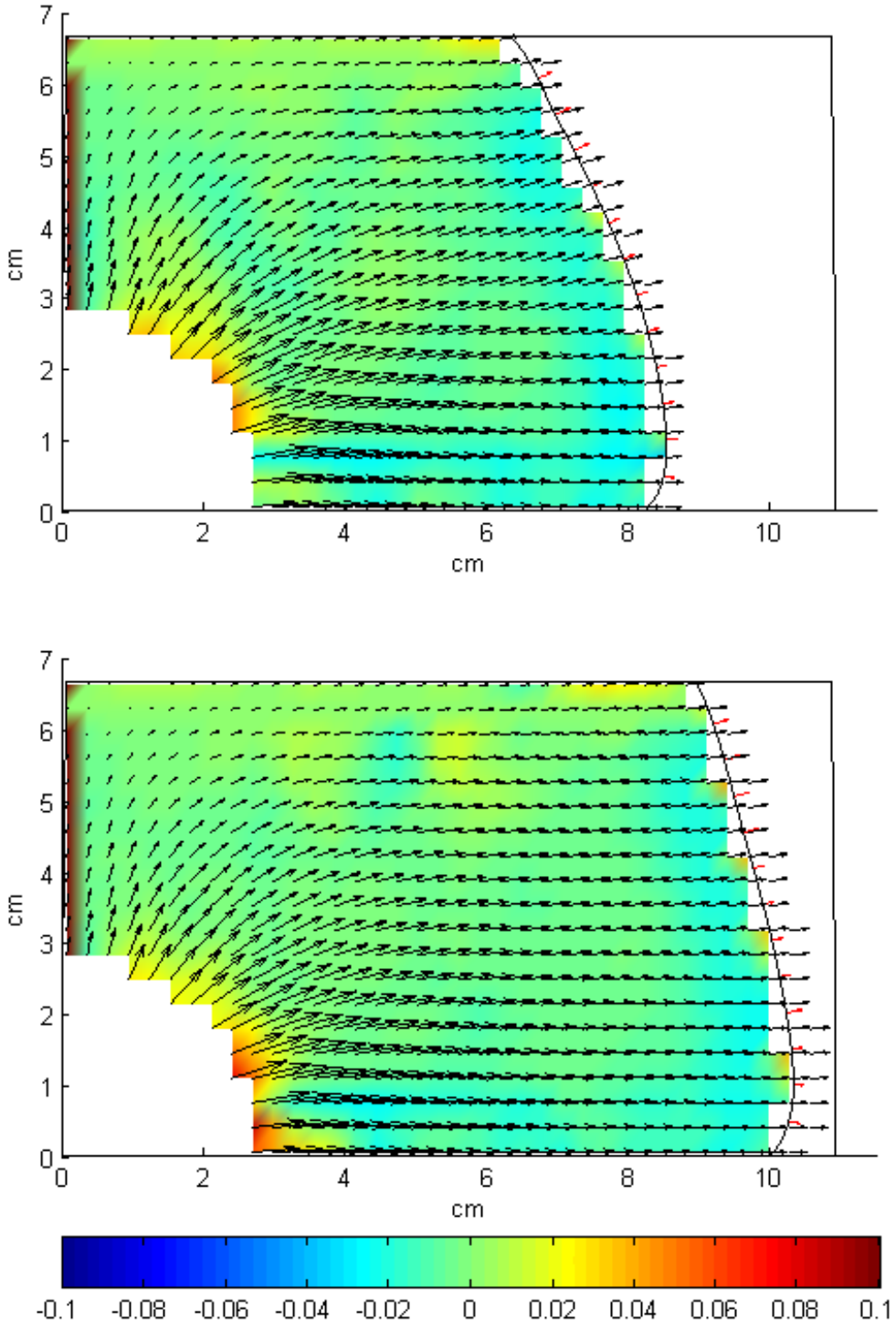

Figure 5.2: 230° C, 11.5 cm^3/s, t^*=0.7 (top) and t^*=0.9 (bottom)

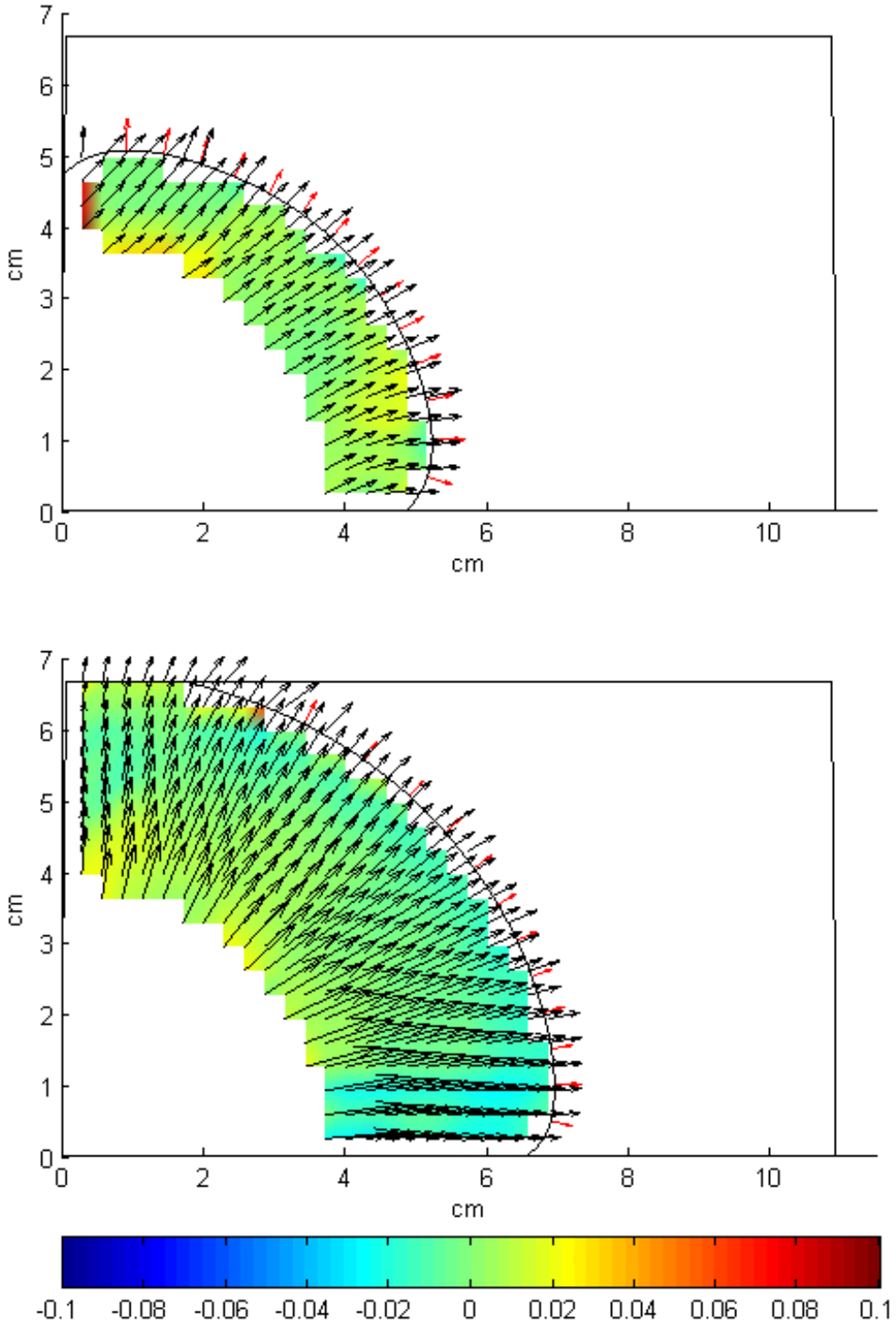

Figure 5.3: 230° C, 23.0 cm^3/s, t^*=0.3 (top) and t^*=0.5 (bottom)

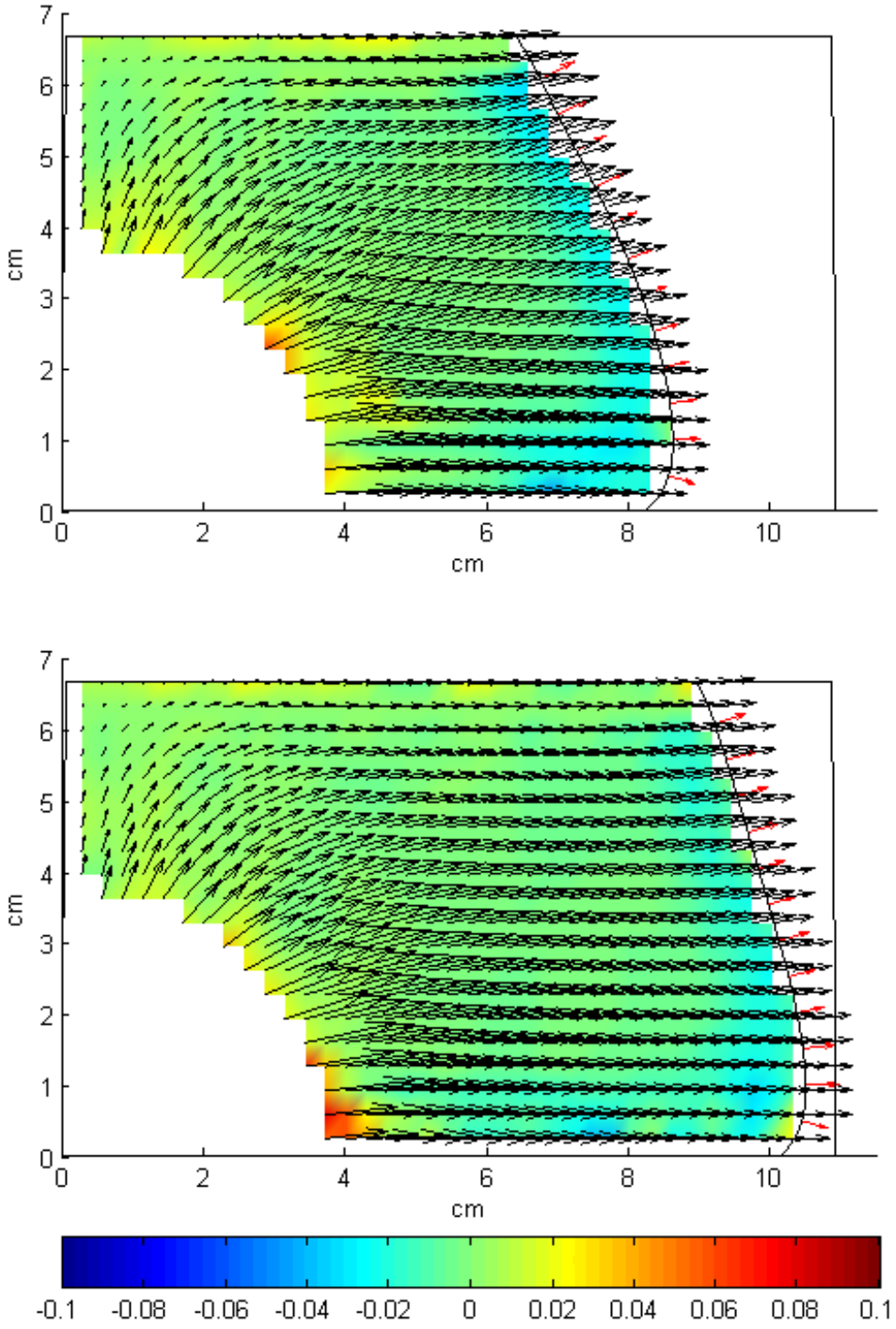

Figure 5.4: 230° C, 23.0 cm^3/s, t^*=0.7 (top) and t^*=0.9 (bottom)

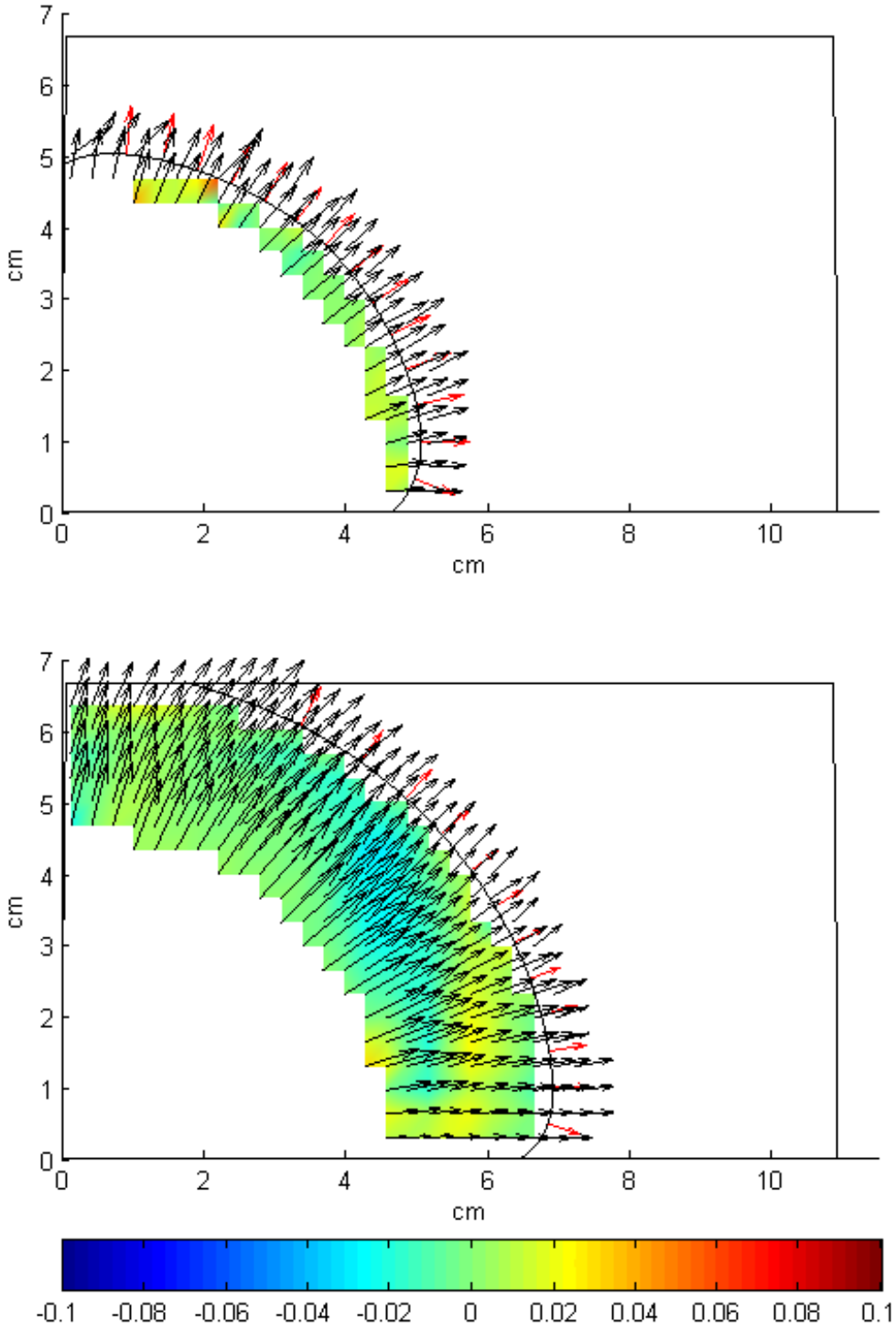

Figure 5.5: 230° C, 27 cm^3/s, t^*=0.3 (top) and t^*=0.5 (bottom)

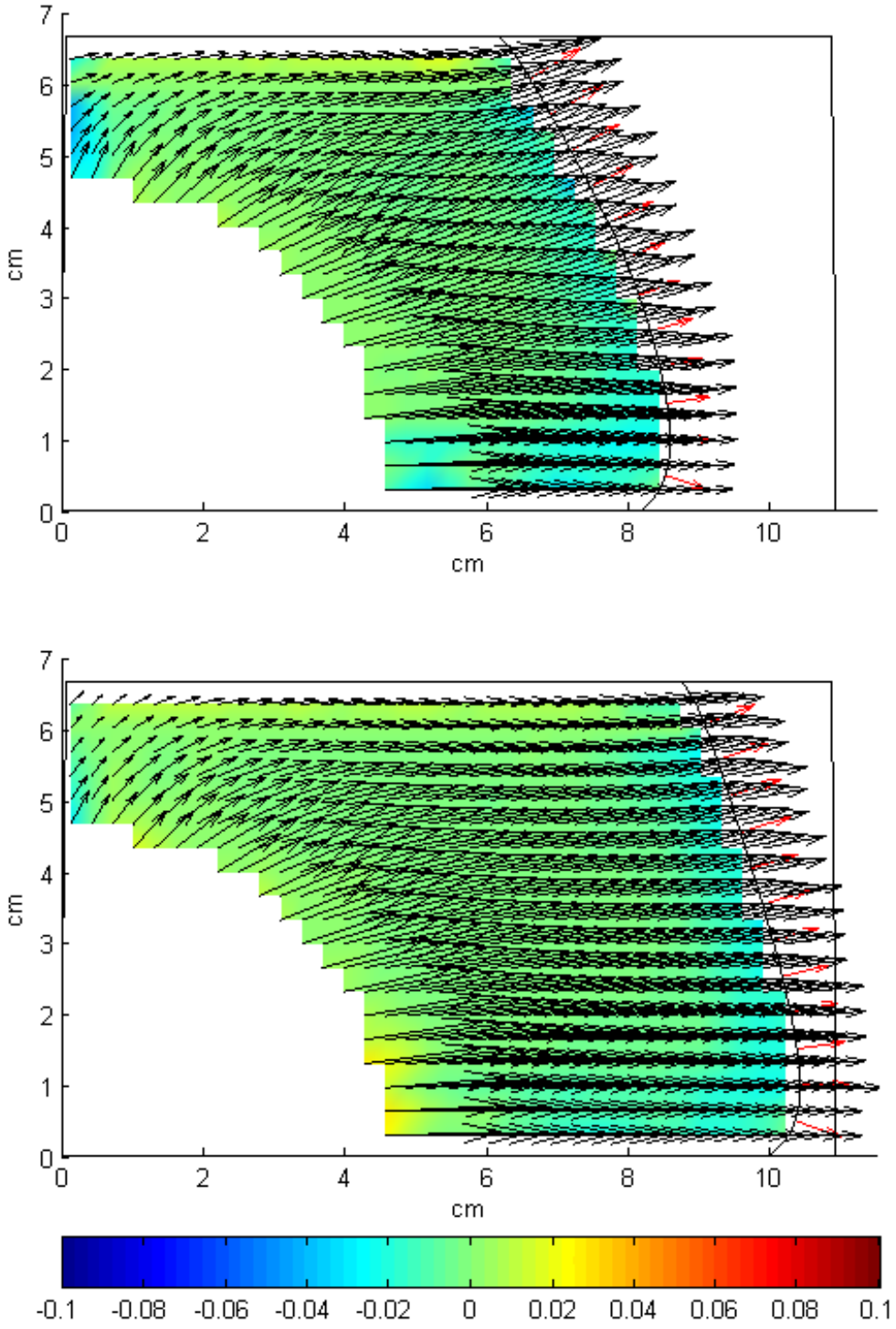

Figure 5.6: 230° C, 27 cm^3/s, t^*=0.7 (top) and t^*=0.9 (bottom)

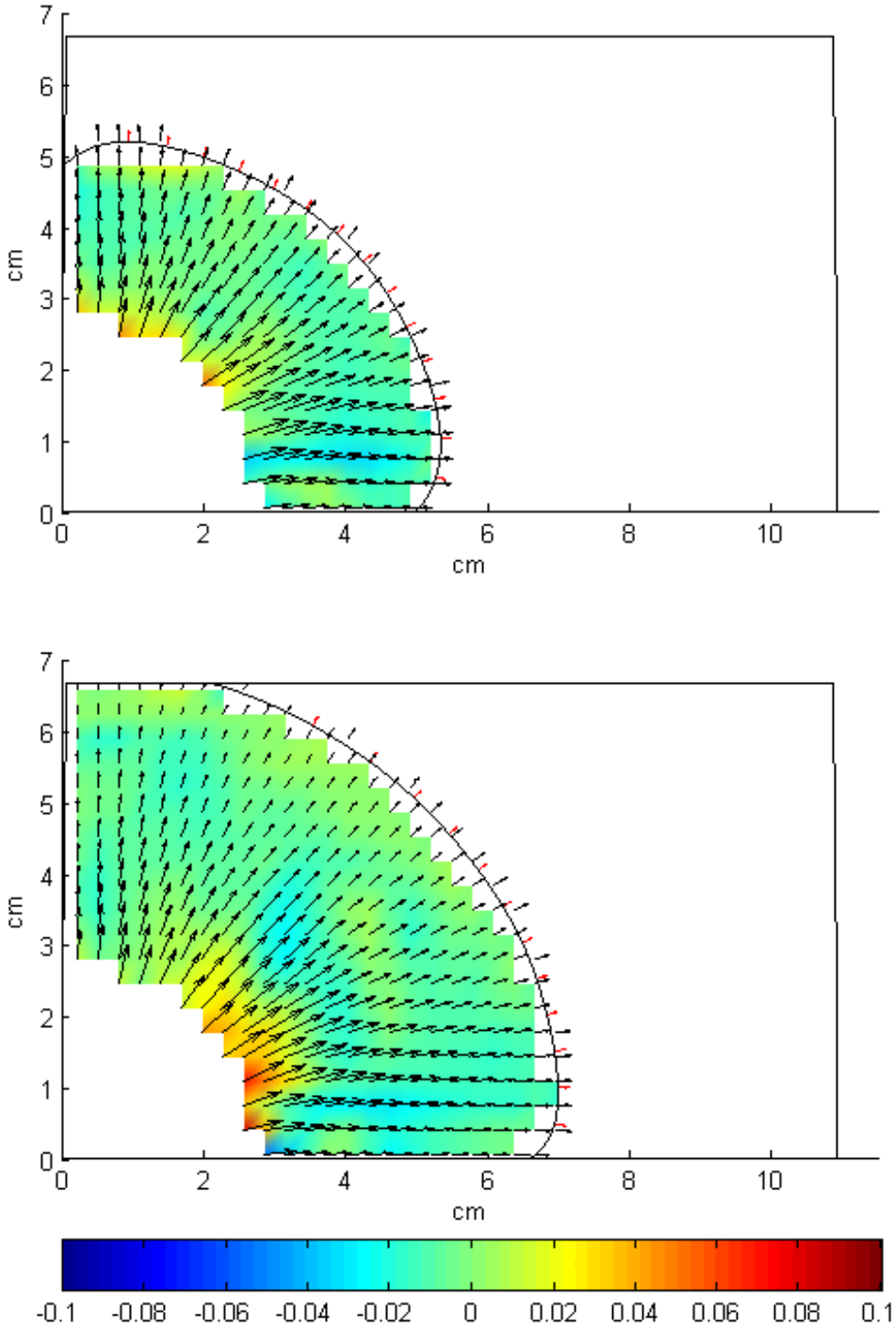

Figure 5.7: 245° C, 11.5 cm^3/s, t^*=0.3 (top) and t^*=0.5 (bottom)

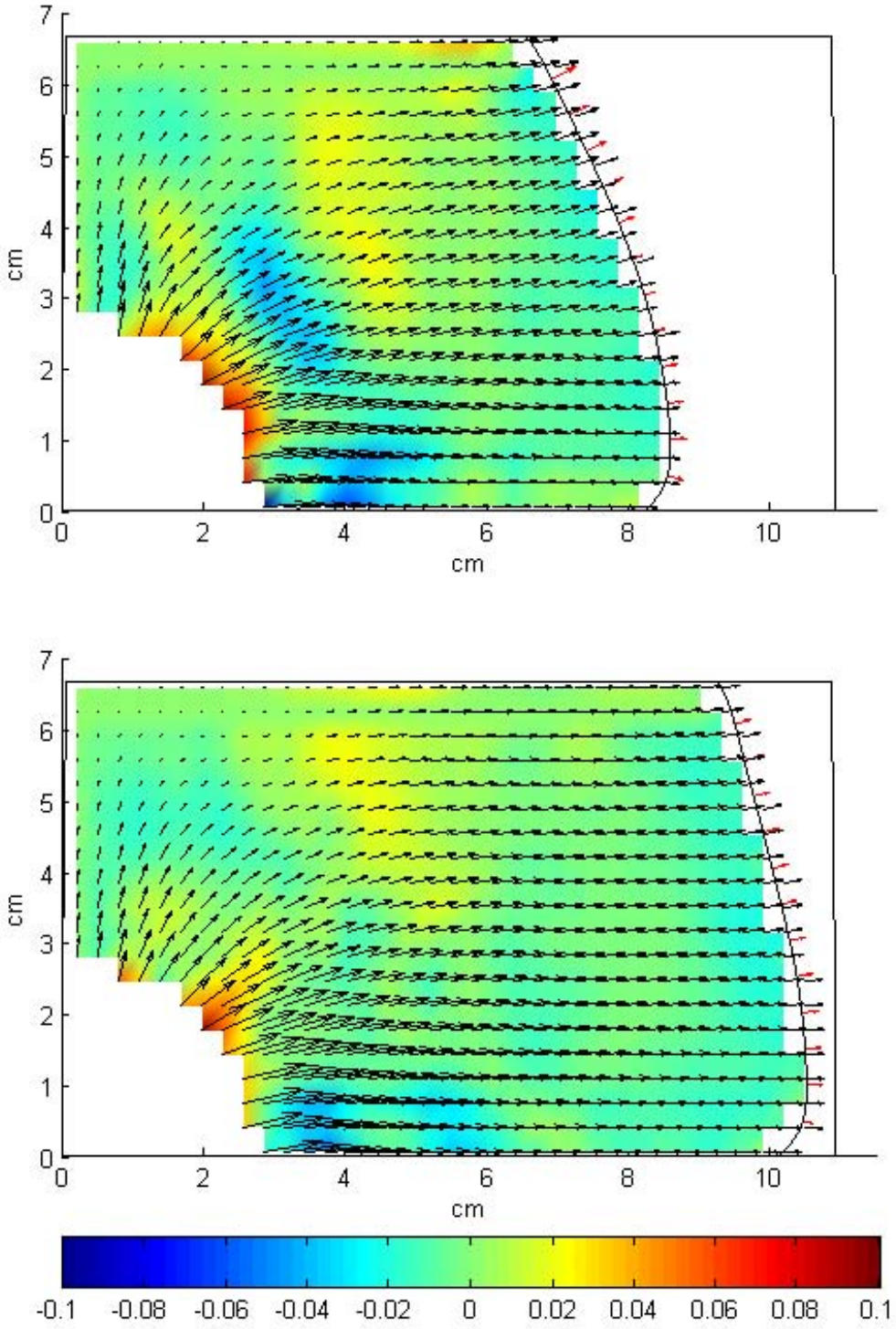

Figure 5.8: 245° C, 11.5 cm^3/s, t^*=0.7 (top) and t^*=0.9 (bottom)

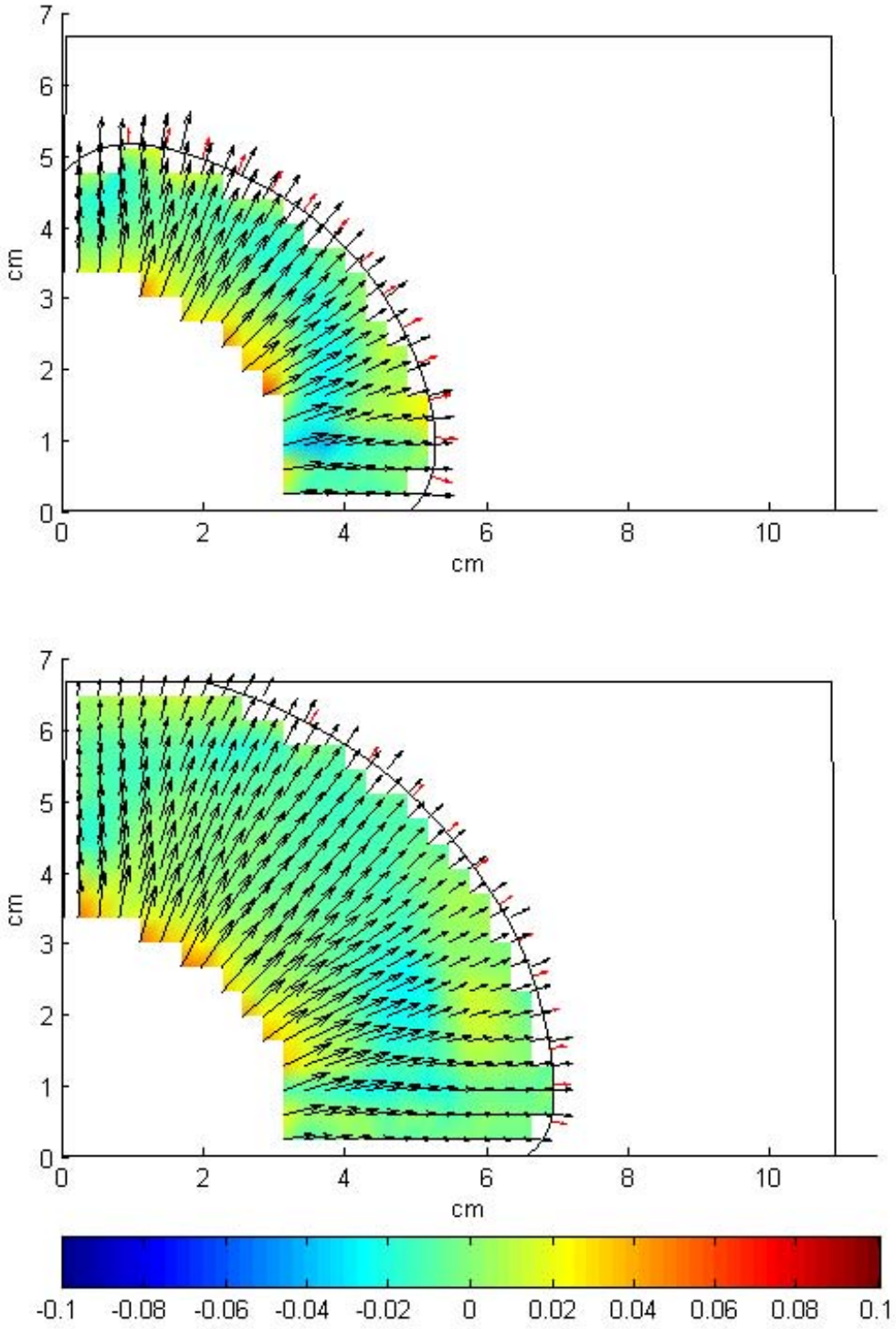

Figure 5.9: 245° C, 17.3 cm^3/s, t^*=0.3 (top) and t^*=0.5 (bottom)

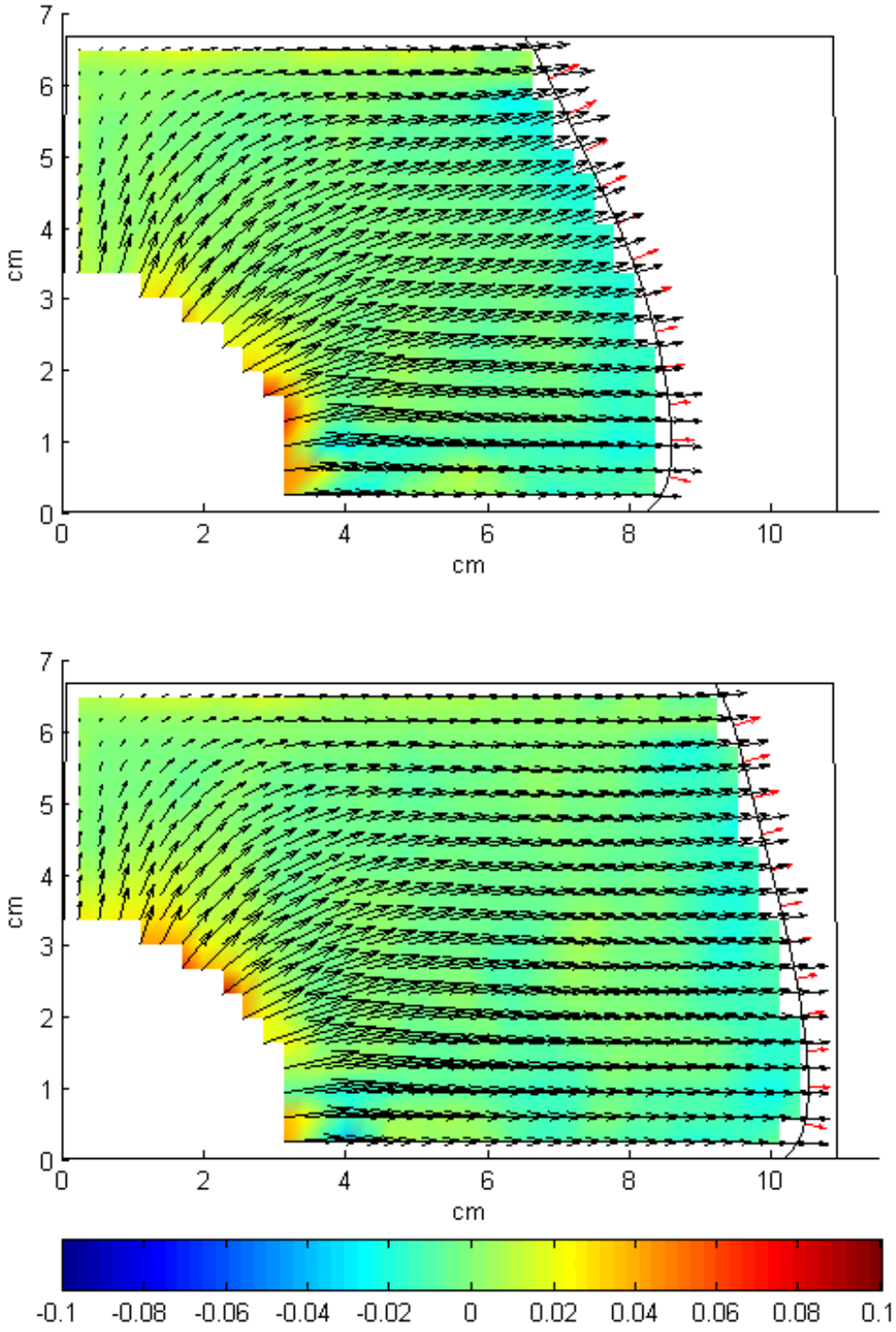

Figure 5.10: 245° C, 17.3 cm^3/s, t^*=0.7 (top) and t^*=0.9 (bottom)

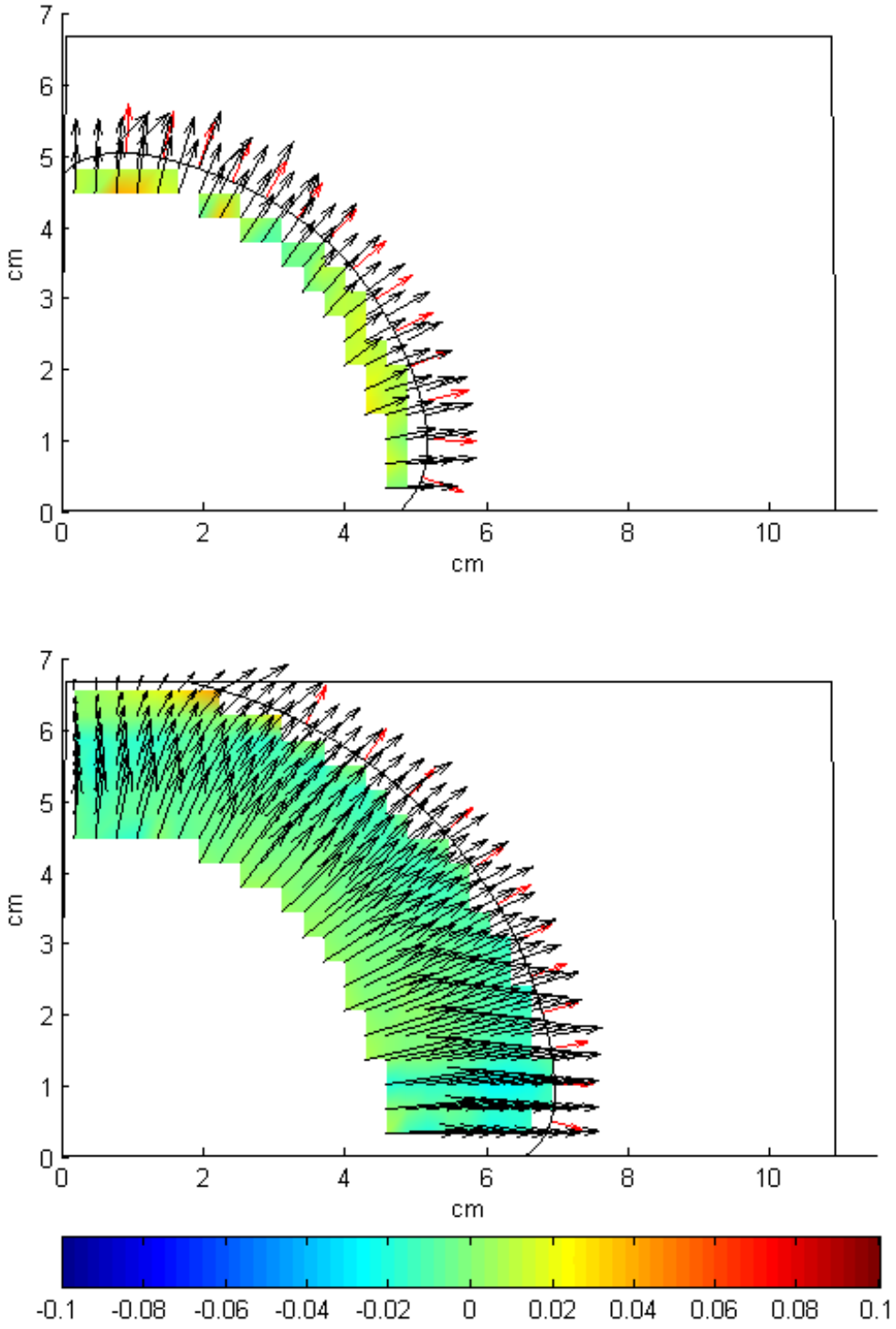

Figure 5.11: 245° C, 27 cm^3/s, t^*=0.3 (top) and t^*=0.5 (bottom)

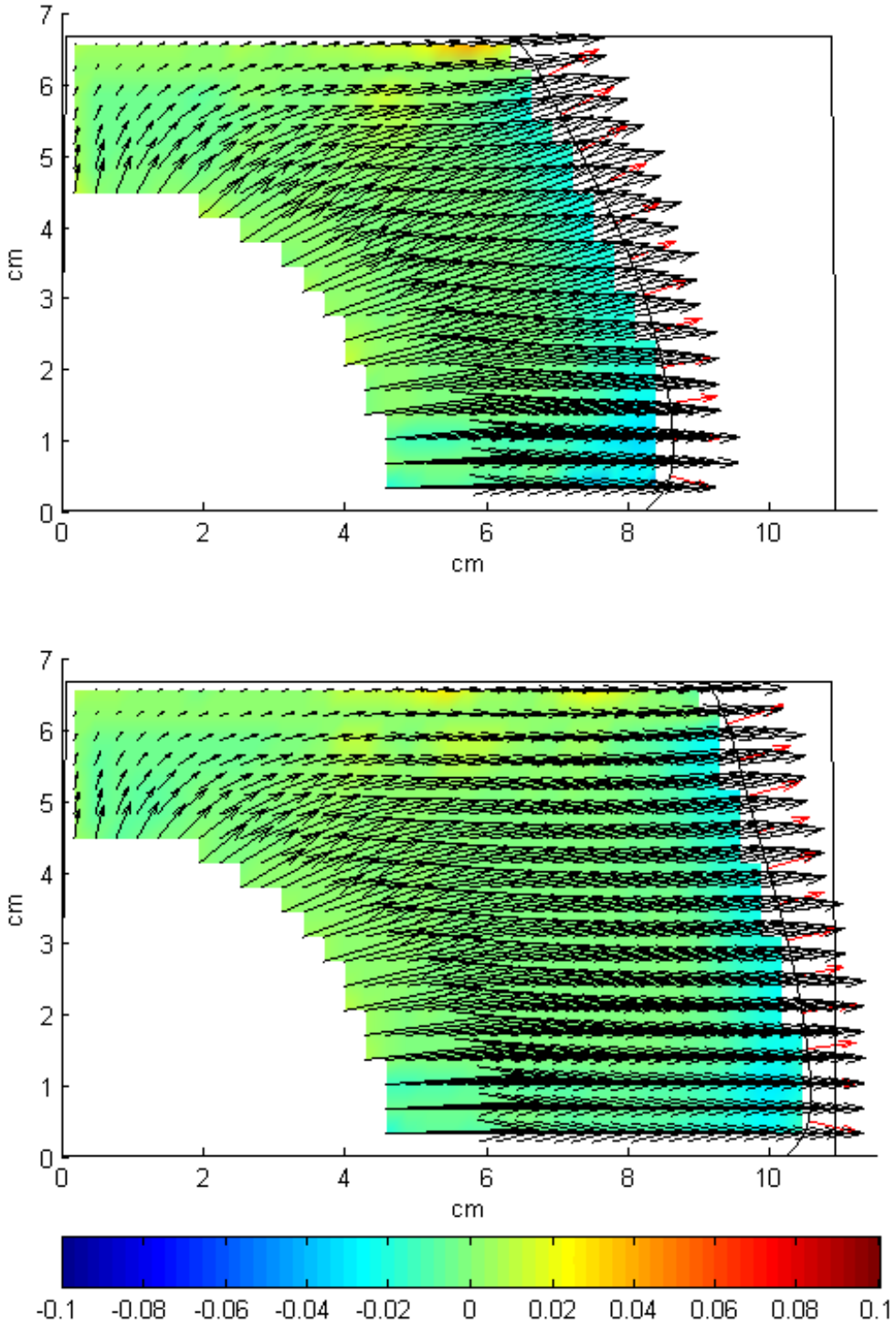

Figure 5.12: 245° C, 27 cm^3/s, t^*=0.7 (top) and t^*=0.9 (bottom)

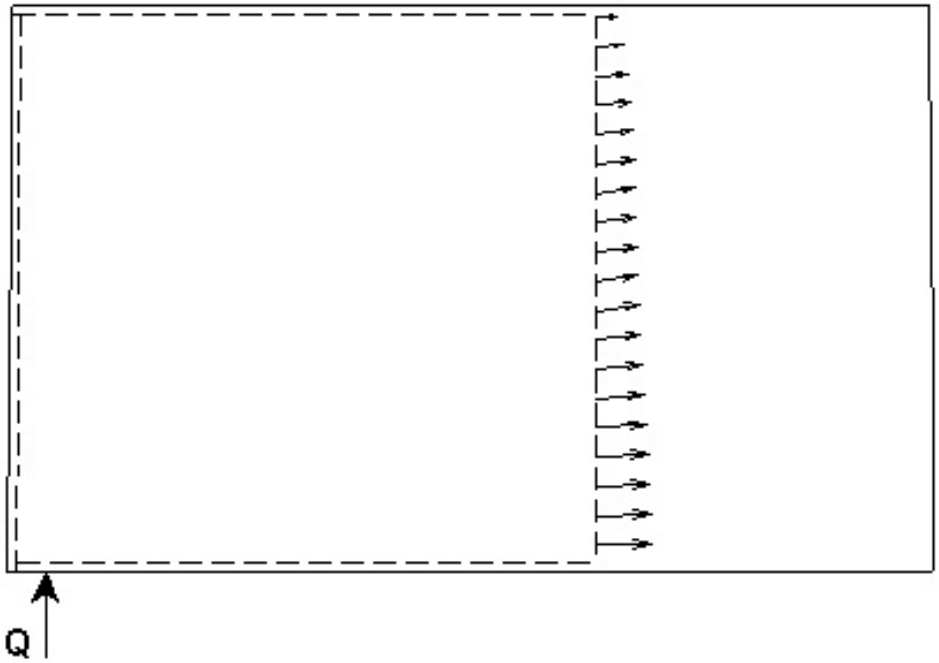

Figure 5.13: Illustration of the control volume used for the volume flux and profile factor calculations shown in Figure 5.14 and Figure 5.15. The x-coordinate of the right-hand surface ranges from 2 cm to 8 cm in these figures, in this example it is at 7 cm.

error, $w(y)$ is the cavity thickness taking draft into account, and F is a profile factor. The velocity error u_ε at each point was set to twice the standard deviation of the velocity vectors making up the median field at that point.

The profile factor F is a function of the velocity profile through the cavity thickness. Since this profile was not measured the value of F is unknown. In order to circumvent this difficulty a normalized flow rate was calculated. The 11.5 cm^3/s, 230° C run was chosen as a baseline and its flow rate was calculated at a number of x coordinates using a profile factor of unity. The mean of these flow rates was designated as Q_0. A scaling factor f_Q was also defined as the injection rate of a given run normalized by 11.5 cm^3/s. These factors were used to calculate a normalized flow rate for every data set for various control volumes.

$$Q^* = \frac{Q}{Q_0 f_Q} \tag{5.2}$$

If it is assumed that the value of the profile factor F is constant over the range of flow rates studied and that it is not a function of y then both Q and Q_0 are linearly dependent on F and the normalized volume flux Q^* in independent of F.

Ideally the value of Q^* should be close to unity for every injection rate and for any location of the control surface S. Figure 5.14 shows that the PIV data does indeed predict volume fluxes that scale linearly with the nominal injection rates.

Calculating absolute values of the volume flow rate directly from the PIV vector fields is not possible because the velocity profile through the thickness of the mold cavity was not measured. However, an estimate of the profile can be made and compared to that of a comparable power-law fluid.

Appendix C gives a derivation of the velocity profile of a power-law fluid flowing

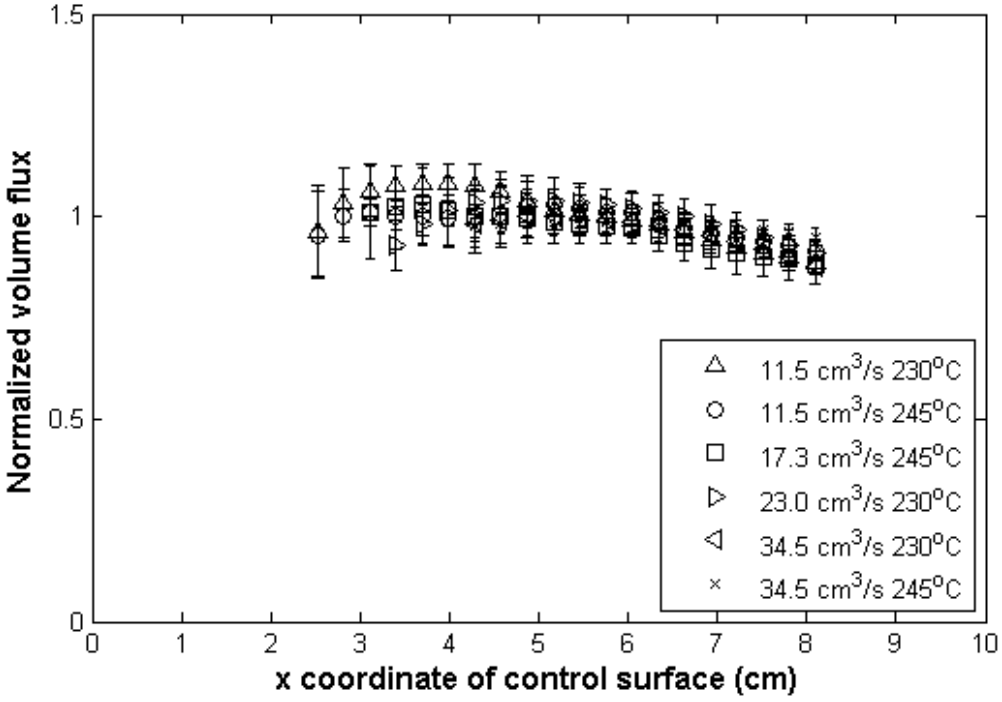

Figure 5.14: Normalized volume flux vs. normalized x-coordinate. The volume flux was normalized by the mean flux of the 11.5 cm^3/s, 230° C test and by ratio of the nominal flow rate and 11.5 cm^3/s. The x-coordinate is normalized by the length of the mold cavity.

through a channel. The volume flow rate of such a flow is

$$Q = 2WB\bar{u} = 2WB\frac{n+1}{2n+1}u_{max} = 2WBFu_{max} \tag{5.3}$$

where F is a profile factor equal to $(n+1)/(2n+1)$, with n being the shear-thinning exponent of the power-law fluid.

Equation 5.1 can be used to estimate the profile factor F if it is assumed that F is constant:

$$F = \frac{Q_0}{\int_S u(y)w(y)dy} \tag{5.4}$$

where Q_0 is the imposed volume flow rate of the injection molding machine and $w(y)$ is the cavity thickness accounting for draft.

In Chapter 2 the shear-thinning of exponent of polymer-particle mixture was found to be equal to 0.42. This gives a profile factor $F = 0.77$.Figure 5.15 shows the result of using Equation 5.4 to estimate the profile factor at various x-coordinates at t^*=0.9 for all six sets of molding conditions studied. At small values of x, closer to the gate, the flow is more radial and the value of F is less than 0.77. But as the flow moves further from the gate it develops into a channel flow. The further the flow is from the gate, the more fully-developed the channel flow becomes and the profile factor approaches the power-law value of 0.77. The mean of the values shown in Figure 5.15 is 0.7±0.1.

So, even though the absolute flow rate cannot be measured, the congruence of the estimated profile factor with that of a power-law fluid with the same shear-thinning exponent suggests that the volume flow rates of the PIV vector fields match those imposed by the injection molding machine.

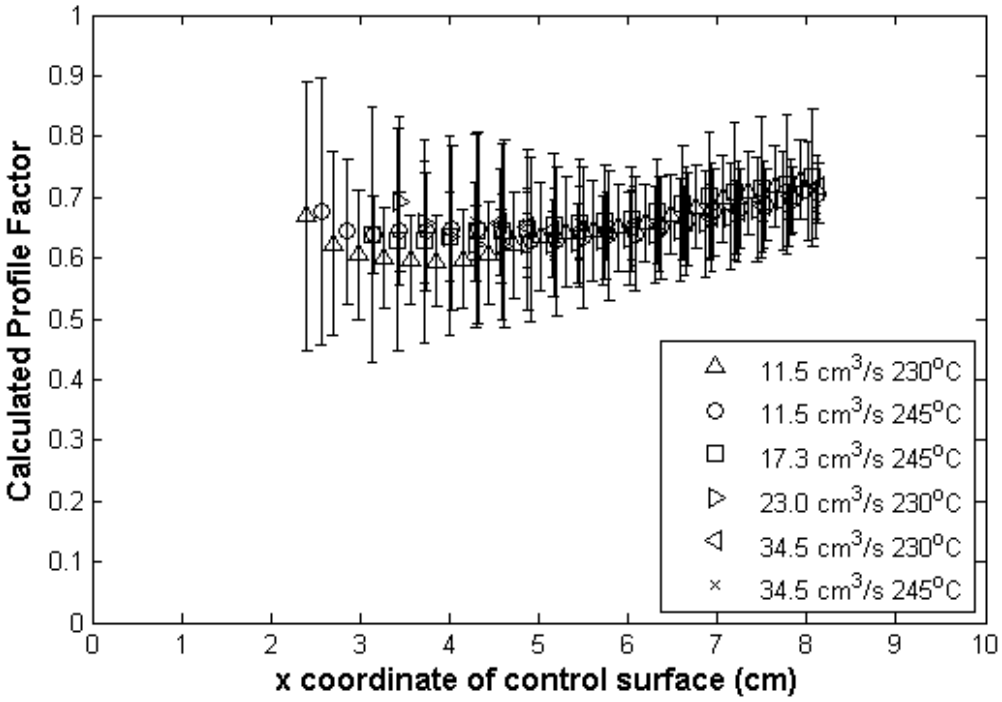

Figure 5.15: The calculated velocity profile factor through the thickness of the mold cavity for the six sets of molding conditions studied. The profiles were calculated at various x coordinates using the PIV fields at t^*=0.9. The profile factor for a power-law fluid with n=0.39 in a one-dimensional channel flow is 0.78. The mean of the data shown here is 0.7±0.1.

5.4 Flow Kinematics of the Filling of the Optical Access Mold

Do the injection parameters have a statistically significant impact on the observed PIV flow fields? Certainly the injection rate has a significant effect on the observed magnitudes of the PIV fields. Faster injection rates lead to higher velocities. The question needs to be rephrased to eliminate this trivial answer.

To compare flow fields with different injection rates we can first find a scaling factor that best eliminates the effect of the flow rate difference. One way to do this is to examine the residual field $\vec{r}$

$$\vec{r} = \vec{v}_1 - \alpha\vec{v}_2 \tag{5.5}$$

where $\vec{v}_1$ and $\vec{v}_2$ are two velocity fields under consideration. By convention we will take $\vec{v}_1$ to be the field with the higher injection rate. The constant α is a scaling factor that is chosen minimize the scalar R where

$$R = \sum |\vec{r}\,| = \sum |(\vec{v}_1 - \alpha\vec{v}_2)| \tag{5.6}$$

The scalar R is the magnitude of the vector sum of all the vectors in the residual field.

Choosing α to minimize R gives a scaling factor α that best approximates the equation

$$\langle\vec{v}_1\rangle = \alpha\langle\vec{v}_2\rangle \tag{5.7}$$

where $\langle\vec{v}_1\rangle$ and $\langle\vec{v}_2\rangle$ are the average velocities of the PIV fields. To see this, let N be the number of PIV vectors in the given velocity fields. Divide both sides of

Equation 5.6 by N and assume that the residual term R/N is small:

$$\left| \frac{\sum \vec{v}_1}{N} - \alpha \frac{\sum \vec{v}_2}{N} \right| = \frac{R}{N} \tag{5.8}$$

$$\approx 0 \tag{5.9}$$

$$\langle \vec{v}_1 \rangle \approx \alpha \langle \vec{v}_2 \rangle \tag{5.10}$$

where $\langle \vec{v}_1 \rangle = \sum \vec{v}_1/N$ and $\langle \vec{v}_2 \rangle = \sum \vec{v}_2/N$. Since the polymer melt flow during the mold filling phase is incompressible and since the cavity volume remains constant the average velocities should scale linearly with injection rate. The factor α should be approximately equal the ratio of injection rates for any vector fields $\vec{v}_1$ and $\vec{v}_2$.

In order to calculate α the PIV velocity vector fields must be resolved to exactly the same grid points. This was not possible to enforce experimentally since the grid point positions are functions of camera placement and calibration, and these varied slightly from data set to data set. A reference grid was chosen for the purpose of this analysis and all of the PIV vector fields were resolved to this reference grid using linear interpolation. Zero-magnitude velocity vectors were placed at the cavity walls to aid in the interpolation of PIV vectors at the periphery of the field.

Once all of the data sets were resolved to the same grid a critical radius needed to be chosen to eliminate the region near the gate where PIV analysis failed. MATLAB was used to perform unconstrained nonlinear optimization to determine the value of α for every pair of median data sets for a range of critical radii from 2 cm to 6.5 cm. The critical radius was varied to ensure that the choice of dead-zone radius did not influence the final result.

The result can be seen in Figure 5.16. In this plot the deviation of α from the injection rate ratio Q_{12} is plotted versus the critical radius. Here $Q_{12} = Q_1/Q_2$, the ratio of the injection rates set on the injection molding machine. The deviations

Table 5.2: Legend for Figures 5.16, 5.19, 5.29, and 5.30.

	$\vec{v}_1$		$\vec{v}_2$	
Symbol	Q (cm^3/s)	T (° C)	Q (cm^3/s)	T (° C)
○	34.5	245	11.5	245
●	34.5	230	11.5	230
▽	23.0	230	11.5	230
▼	34.5	245	17.3	245
◊	17.3	245	11.5	245
♦	34.5	230	23.0	230
□	34.5	245	23.0	230
■	34.5	245	11.5	230
▷	34.5	230	17.3	230
▶	34.5	230	11.5	245
◁	17.3	245	11.5	230
◀	23.0	230	11.5	245
×	23.0	230	17.3	245
△	34.5	245	34.5	230
▲	11.5	245	11.5	230

plateau and remain fairly constant for radii of 4 cm or more. In the plateau region the mean deviation is 3.3%. The values of α closely approximated the ratio of injection rates for any given pair of data sets.

Do the injection parameters have a statistically significant effect on the deviation of α from the injection rate ratio? This question can be addressed using Analysis of Variance (ANOVA) [100]. The variation of the deviation of α from Q_{12} was examined as a function of two variables. The first variable, Q_{12}, was defined as the ratio of nominal injection rates of the faster flow to the slower. All of the PIV field pairings had values of Q_{12} equal to 1, 1.33, 1.5, 2 or 3. The second variable was a two-level variable relating to temperature. This variable, T_{12}, had a value of zero if the melt temperatures were identical between two vector fields and had a value of one if the temperatures were different.The residual metric data was collected from the 90% fill data of the median vector fields. Data less than 4.5 cm from the gate was ignored to

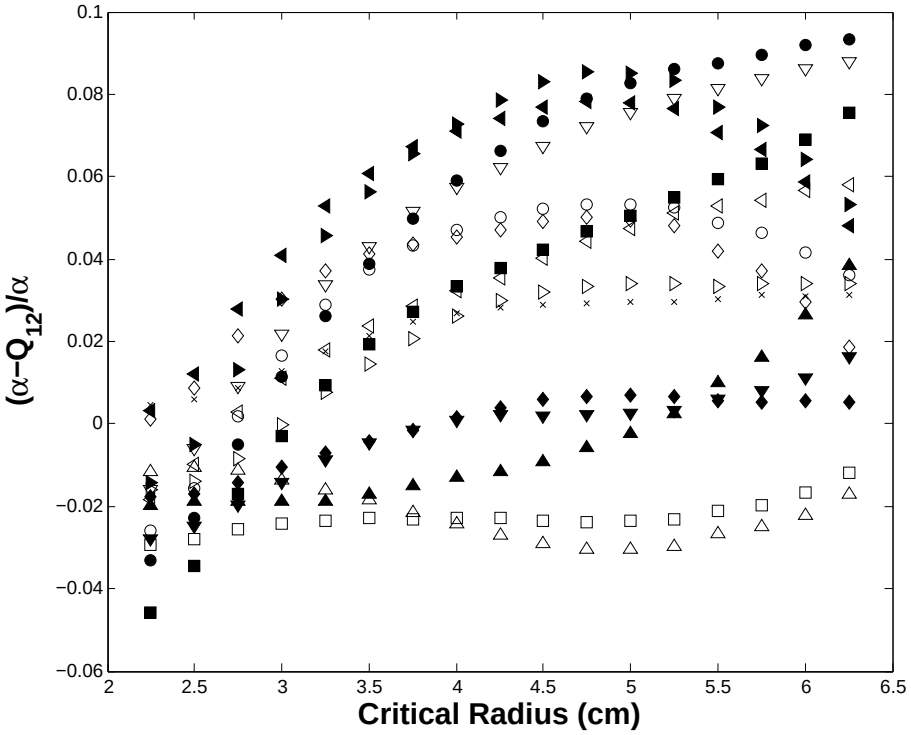

Figure 5.16: Deviation of the calculated scaling factor α from the ratio of injection rates Q_{12} as a function of critical radius for all possible median field comparisons. The legend for the symbols is found in Table 5.2.

Table 5.3: Statistical significance levels as functions of p-value

$p > 0.10$	Not significant
$0.10 \geq p > 0.05$	Mildly significant
$0.05 \geq p > .01$	Significant
$p \leq .01$	Highly significant

remove any influence of the critical radius below which PIV analysis failed.

The null hypothesis of the ANOVA analysis was that the variables Q_{12} and T_{12} had no effect on the deviation of α from Q_{12}. MATLAB was used to perform the analysis. The outcome of the ANOVA analyses are a set of p-values gauging the significance of the given factors in accounting for the observed variation in the data. The statistical significance as a function of p-value used in the present work follows that described by Koopmans [100] and is shown in Table 5.3.

The resulting p-value for the Q_{12} variable was 0.1017 and the p-value for the T_{12} variable was 0.9908. This means that the null hypotheses cannot be rejected at the 90% significance level. The injection parameters do not have a statistically significant effect on the deviation of α from the incompressible scaling factor Q_{12}.

This can be illustrated by the use of notched box plots, as described by McGill [101]. A box plot is a means of graphically displaying relevant statistics of a data set. A typical box plot is shown in Figure 5.17. The center line of the box represents the median of the data set. The top and bottom of the box are the upper and lower quartiles of the data, thus the box itself contains the middle 50% of the data set. The whiskers extending above and below the box extend to the most extreme non-outlier data points, defined as points that lie within ± 1.5 inter-quartile ranges of the edges of the box. Individual outliers are indicated by '+' symbols. If the data set has a normal distribution with standard deviation σ, Koopmans [100] shows that the

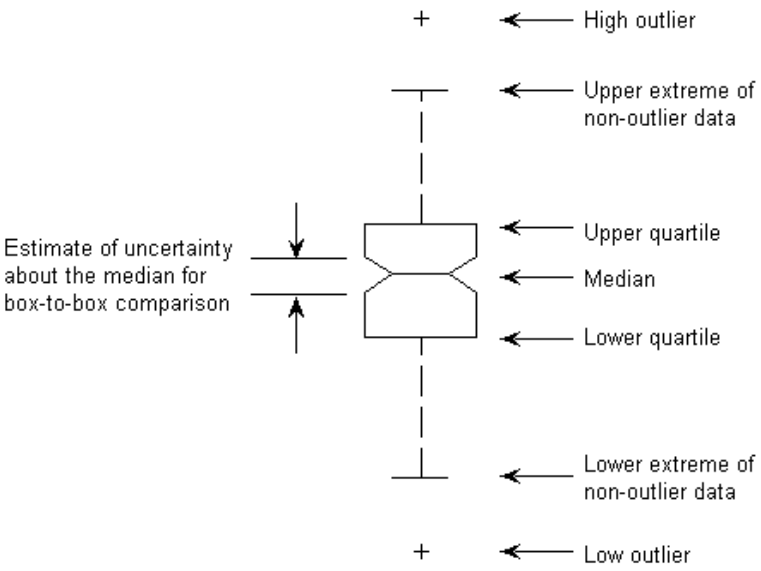

Figure 5.17: Schematic of a typical boxplot. Box plots graphically represent relevant statistics of a data set.

upper and lower limits of the box are at $\pm 1.348\sigma$ and the ends of the whiskers are at $\pm 2.696\sigma$.

The notches in the box represent a robust estimate of the uncertainty about the median for box-to-box comparisons. Boxes whose notches do not overlap have medians that are significantly different at the 95% confidence level [101].

Figure 5.18 shows boxplots of the deviation of the calculated scaling factors α from the nominal injection rate ratios as a function of injection rate ratio and temperature. The figure shows that there is no statistically significant difference in the deviations when sorted by the temperature variable. The figure shows that there seems to be an upward trend of the error as the injection rate ratio increases, but the confidence intervals (as shown by the notch widths) are also large.

The slight increase in the deviation of α from the injection rate ratio can possibly

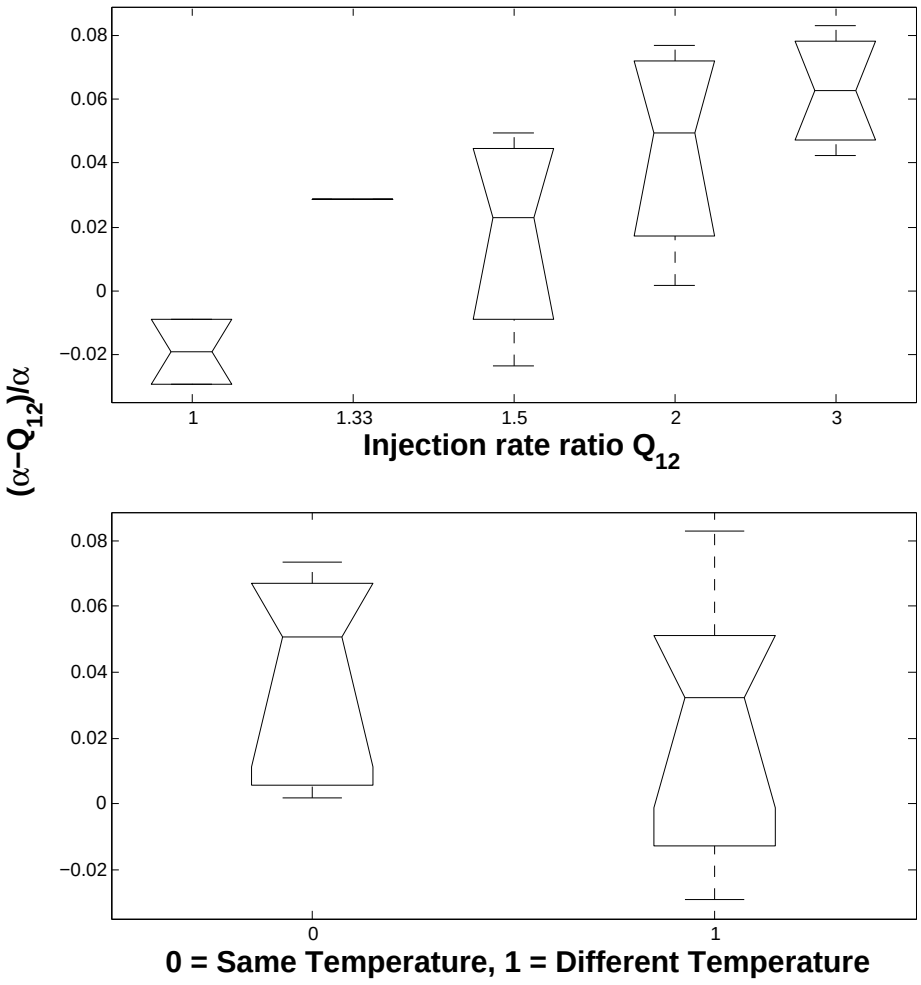

Figure 5.18: Boxplot of the deviation of the calculated incompressible scaling factors α from the nominal injection rate ratios as a function of injection rate ratio and temperature difference.

be explained by the fact that the digital movies were all taken with the same frame rate. As the injection rate increases the amount of change in the flow field that takes place between frames also increases. This could lead to an inherent increase in the error associated with the velocity fields, and this could in turn lead to larger deviations in α from the nominal injection rate ratios.

Once α has been determined a nondimensional error metric ε_R can be defined :

$$\varepsilon_R = \sqrt{\frac{\sum_{i,j} |\vec{r}(i,j)|^2}{\sum_{i,j} |\vec{v}_1(i,j)|^2}} \tag{5.11}$$

This metric can be interpreted as the mean residual vector magnitude normalized by the mean magnitude of the higher injection rate field. A plot of the residual metric for all possible median field comparisons vs. critical radius is shown in Figure 5.19.

As in Figure 5.16, Figure 5.19 shows that the residual metric plateaus as the critical radius increases. For consistency, a critical radius of 4.5 cm was chosen for the following analysis.

If the residual metric ε_R is high, it is an indication that there is a significant difference in the flow fields that cannot be accounted for by a simple scaling of injection rates. Since a laminar Newtonian flow would scale linearly with the injection rate this would suggest a non-Newtonian fluid effect.

The metric ε_R can now be used to rephrase the question asked at the beginning of this section: Do the injection parameters have a statistically significant impact on the residual PIV vector fields? In other words, do the injection parameters have a statistically significant impact on the injection molding flow that cannot be accounted for by a simple incompressible viscous Newtonian scaling?

MATLAB was used to perform a 2-way ANOVA on the residual metric results using a 95% significance level.

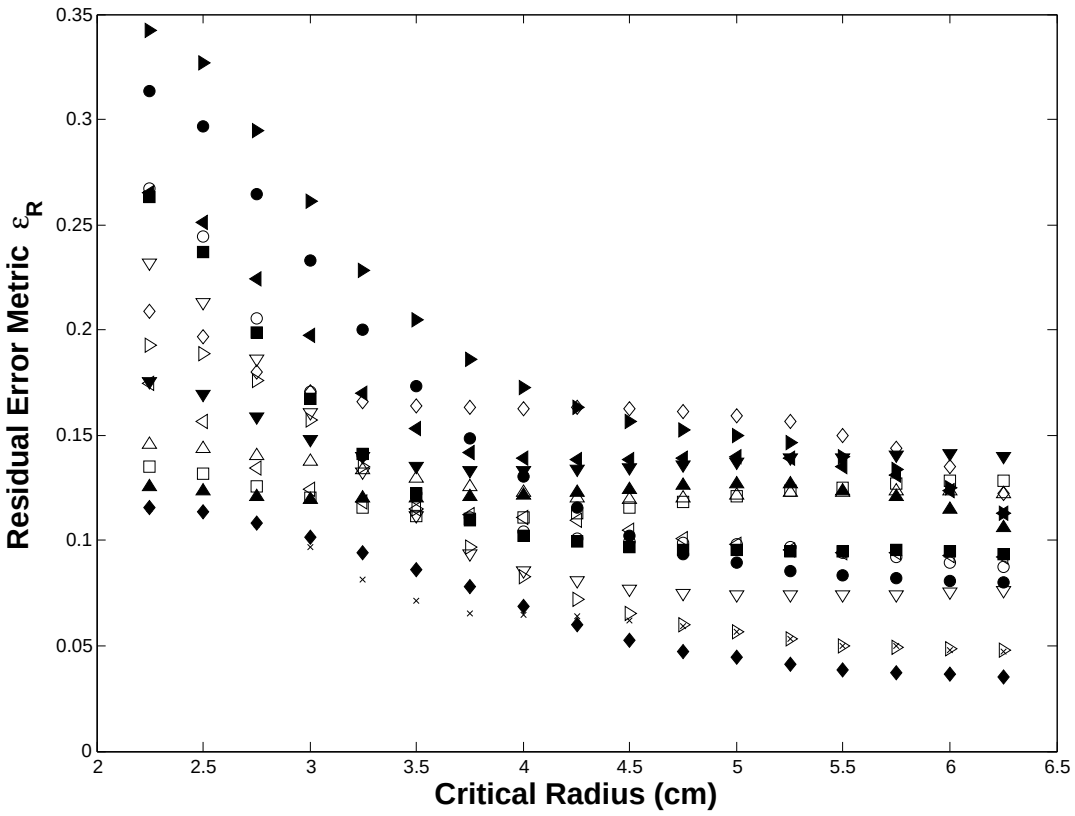

Figure 5.19: Residual metric ε_R as a function of critical radius for all possible median field comparisons. The legend for the symbols is found in Table 5.2.

The null hypotheses were that the injection rate ratio and temperature difference had no effect on the residual metric ε_R. The resulting p-value for the injection rate ratio was 0.7377 and the resulting p-value for the temperature difference was 0.7168. Thus the null hypotheses could not be rejected. The injection rate ratio and the temperature difference had no statistically significant impact on the residual metric ε_R. Within the bounds of this parameter study, the injection parameters had no significant impact on the flow kinematics that could not be explained using a simple Newtonian scaling factor.

There was only one PIV field pairing with an injection ratio of 1.33, leading to a perhaps unnecessary extra level of Q_{12}. The ANOVA analysis was carried out a second time, assigning the residual metric of the Q_{12}=1.33 run to the Q_{12}=1.5 group to reduce the number of levels of Q_{12}. The resulting p-value for the new Q_{12} was 0.8923 and the p-value for T_{12} was 0.9352, leading to the same conclusion that the injection parameters have no statistically significant effect on the residual metric.

Figure 5.20 shows boxplots of the residual metric sorted by the variables Q_{12} and T_{12}. There was only one pairing with a ratio of 1.33, leading to a degenerate boxplot for that injection ratio. The position of the notches indicate that the means of the different groups are not statistically distinguishable from each other.

Note that this conclusion does not mean that the polymer flow is Newtonian. The flow profile through the thickness of the cavity is non-Newtonian, but was not measured in this work. But this conclusion does not claim that the in-plane flow is Newtonian either. The underlying flow may have non-Newtonian characteristics, but in this study those characteristics scale with a simple Newtonian scaling factor.

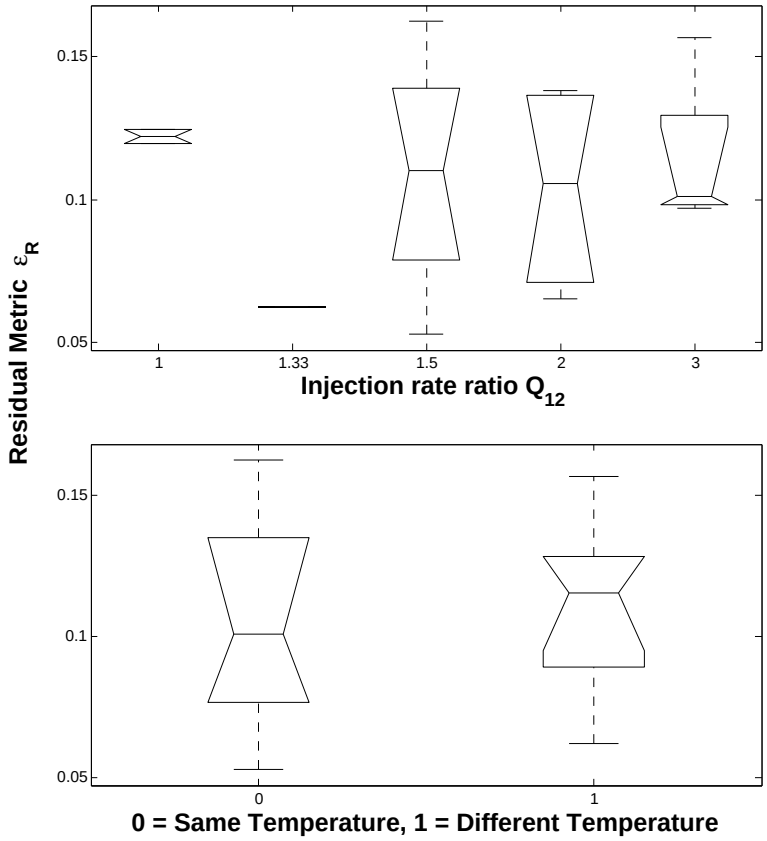

Figure 5.20: Boxplots of the residual metric as a function of injection rate ratio and melt temperature difference. The molding parameters have no statistically significant effect on the residual metric.

5.5 Examining the Structure of the Residual Velocity Fields

The previous analysis examined the global effect of the molding parameters on the velocity fields. Although no statistically significant effect was found, there might still be interesting effects found at the local level. In order to examine this possibility the residual fields were compared with each other to see if any structural similarities were present.

This analysis was carried out using cross-correlations. Given two residual vector fields a correlation coefficient Φ may be defined as:

$$\Phi = \frac{\sum \vec{r}_1 \cdot \vec{r}_2}{\sqrt{\sum |\vec{r}_1|^2 \sum |\vec{r}_2|^2}} \tag{5.12}$$

where $\vec{r}_1$ and $\vec{r}_2$ are residual fields (including scaling factors) as defined in Equation 5.5.

If two residual fields are well-correlated then the value of Φ would approach unity. If the two fields were uncorrelated the value of Φ would approach zero.

The correlations were carried out for every pair of residual fields and the results were tabulated and explored. A histogram of the correlation coefficients is shown in Figure 5.21. The values are distributed fairly evenly across the interval (-1,1) with a mean of 0.0651. No discernable effect of molding parameters on the correlations was found.

To confirm this statistically, a Kolmogorov-Smirnov test was performed [102]. The Kolmogorov-Smirnov test compares the empirically determined cumulative distribution function (CDF) of a given random variable to the known CDF of a particular distribution. The null hypothesis is that the two distributions are the same.

MATLAB was used to perform a Kolmogorov-Smirnov test comparing the distri-

bution of Φ to a uniform distribution. The resulting p-value was 0.0724, leading to the conclusion that the null hypothesis could not be rejected at the 5% significance level. The correlations of the residual fields have a distribution statistically indistinguishable from a uniform distribution. This can be seen graphically in Figure 5.22.

The residual fields show no meaningful correlation. The molding parameters do not cause meaningful structure in the residual fields that persists from one case to another.

5.6 Simulating the Mold Filling Flow with Moldflow

As described in Section 1.1, one of the motivations of this research was to provide data that could be used to benchmark existing polymer-flow simulation codes. To accomplish this Moldflow 6.1 was used to simulate the flow studied in the present work.

A midplane mesh model of the cavity of the optical access mold was constructed and is shown in Figure 5.23. Summary statistics of the mesh can be found in Table 5.4. A midplane mesh is two-dimensional, but the assigned thickness of the elements can vary to reflect changes in the cavity thickness. In the optical access mold, draft on the large steel surface opposite the main window causes the cavity thickness to vary. This was reflected in the midplane mesh and is illustrated in Figure 5.23. The assigned element thicknesses varies across the shaded regions and are listed in Table 5.4.

Simulations were run for the same set of molding conditions used in the PIV experiments. The Moldflow results were then exported to Matlab for further analysis. This process involved a number of steps. The average velocities and the nodal fill times were exported to XML files, and XML parsing routines were written in Matlab

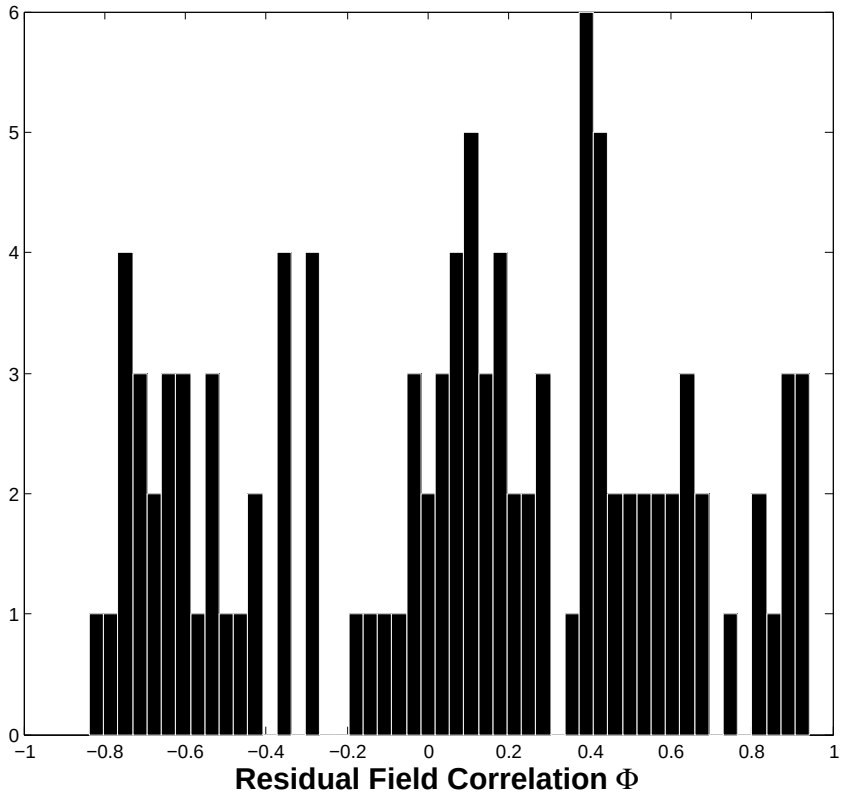

Figure 5.21: Histogram of the correlations between median field residuals. The correlations show no trend that can be linked to molding conditions.

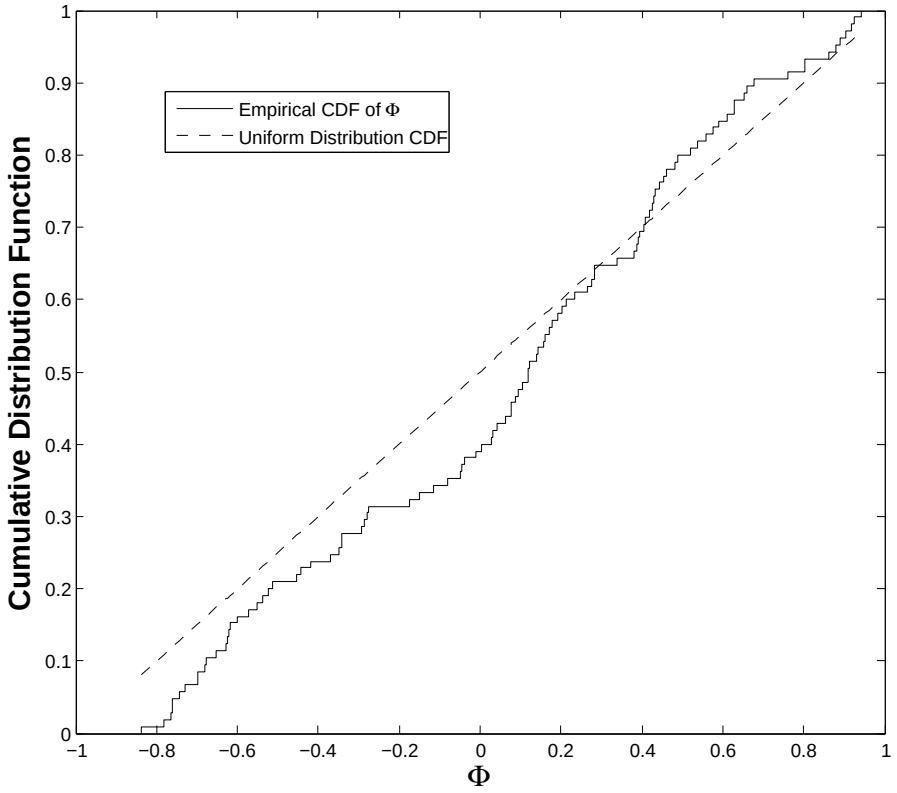

Figure 5.22: Cumulative distribution functions of Φ and of a uniform distribution. The two functions are not statistically distinguishable at the 5% significance level

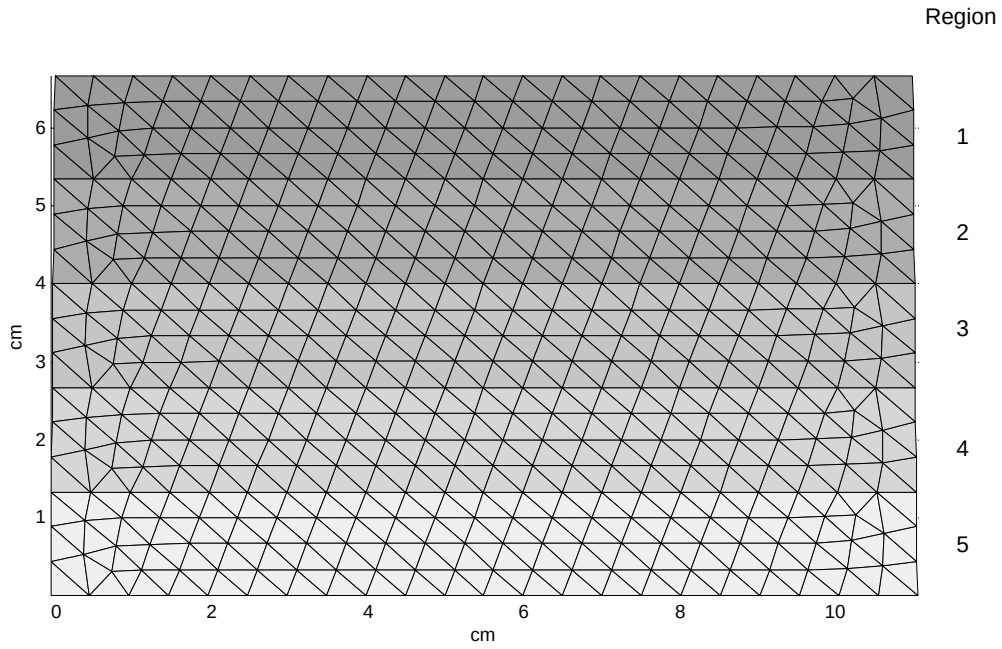

Figure 5.23: Mesh used in the Moldflow simulation of the mold filling process. The mesh is in the same orientation as the cavities shown in Figures 5.1-5.12. The shaded regions denote elements with constant assigned thickness. The thickness varies to account for draft in the mold cavity. The assigned element thicknesses are found in Table 5.4.

Table 5.4: Statistics for the Moldflow mesh used to simulate the flow in the mold filling phase.

Entity Counts	
Surface triangles	880
Nodes	478
Mesh volume	48.9511 cm^3/s
Mesh area	73.7051 cm^2

Surface triangle aspect ratio	
Minimum aspect ratio	1.233
Maximum aspect ratio	2.033
Average aspect ratio	1.535

Assigned element thicknesses	
Region 1	6.408 mm
Region 2	6.641 mm
Region 3	6.525 mm
Region 4	6.757 mm
Region 5	6.874 mm

to extract the necessary information from the tagged XML files. Moldflow calculates one average velocity per mesh element per time step and locates the average velocity vector at the centroid of each element. The velocities can be saved to a file, but they are referenced to element number only, not to specific centroid coordinates. The situation is similar for the nodal fill times. The fill times are referenced to node numbers, but the node coordinates are not given.

In order to perform post-processing on the Moldflow results the node coordinates were needed, as well as a list of which nodes bound each element. This information was obtained by exporting the mesh information to an ASCII file. Another parsing routine was written to extract the necessary node and element information from the file. A linked list of element boundary nodes and nodal coordinates was created, and this information was then used to calculate the centroid coordinates of each

element. These coordinates were then matched to the average velocity data through the element number. The final result was an array of velocity data with linked centroid coordinates, allowing the data to be plotted outside of Moldflow as shown in Figure 5.24.

Extracting the flow front information from the Moldflow results presented similar difficulties. Moldflow does not report flow front information *per se*, it instead calculates the time it takes for melt to reach each node of the mesh. This results in a spatial distribution of fill times. A contour plot can then be made for any desired fill time, with the contour denoting the boundary of the melt at that given time. This boundary can be thought of as the flow front.

In order to calculate the flow front position outside of Moldflow the array of nodal fill times was exported to an XML file. A parsing routine was written that extracted the fill times and corresponding node numbers and imported them into Matlab. The node coordinates were extracted from the ASCII mesh file and were linked to the corresponding fill times. This resulted in a non-uniform spatial distribution of fill times since the node coordinates do not fall on a regular grid. This spatial distribution was then interpolated onto a regular grid to enable the use of Matlab's `contour` function. The `contour` function was then used to plot contours at desired fill times. The coordinates of the contour points were then used to plot the simulated flow fronts, as shown in Figure 5.25.

Further post-processing was needed to perform a direct comparison of the Moldflow simulation with the experimentally measured PIV results. The goal of the post-processing was to plot the Moldflow results with the same grid spacing, flow front velocity vectors, and overlaid continuity scaling that were used on the PIV data shown in Figures 5.1- 5.12. The Moldflow velocity vectors were reported at

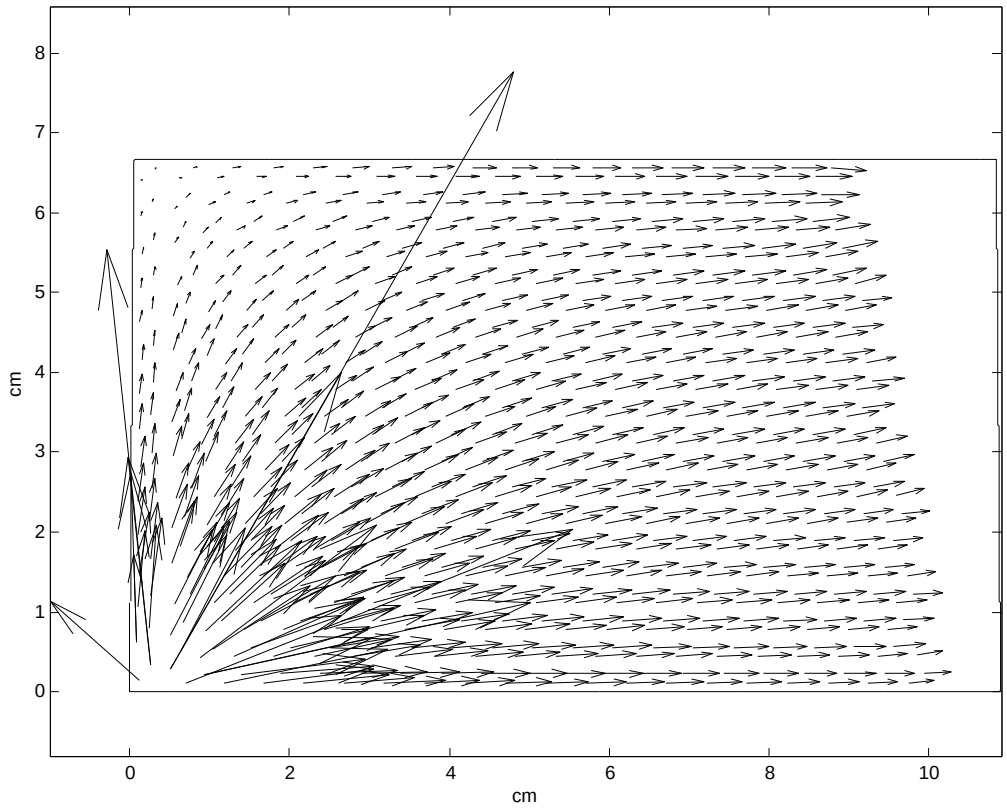

Figure 5.24: Example of Moldflow simulation data prior to post-processing. The velocity vectors are placed at the centroids of the triangular mesh elements shown in Figure 5.23. The flow front is a contour of nodal fill times matching the point of time at which the velocity field was calculated.

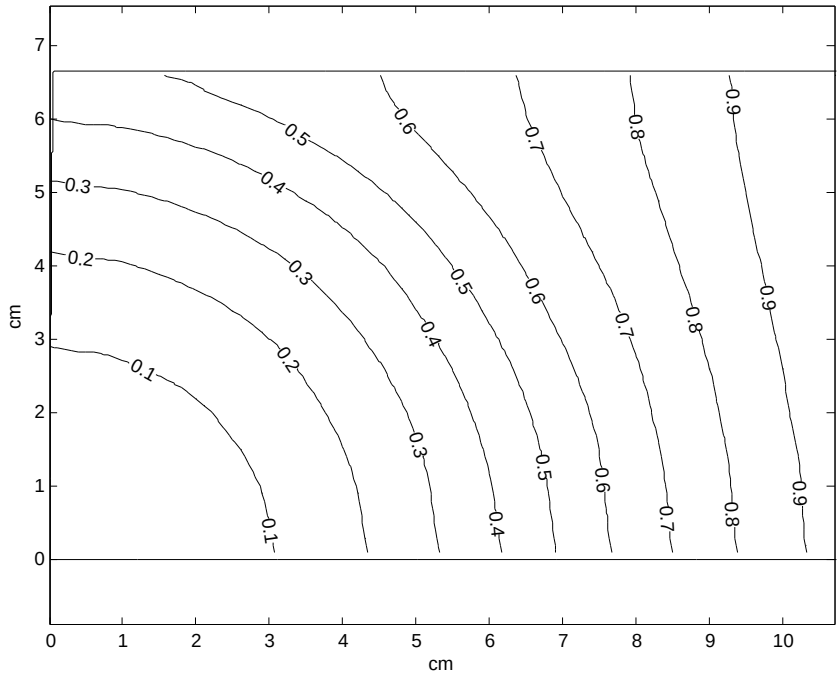

Figure 5.25: Contour plots of Moldflow nodal fill time results. The contours are of the nondimensionalized fill time t^*, the ratio of the local fill time to the total fill time.

the centroids of the mesh elements, forming an irregular array of velocity vectors. These vectors were then resolved onto the same grid produced by the DaVis PIV processing software. The corresponding flow front contour was then calculated for the same point in time. An example is shown in Figure 5.26.

A second flow front contour was then calculated at a time $1/30^{th}$ of a second later to allow calculation of the front propagation velocity with the same time resolution as was used with the hand-traced flow fronts from the digital mold-filling movies. The melt velocity and flow front contour data were then put into exactly the same format as the DaVis PIV results and the hand-traced flow front coordinate data.

In order to facilitate comparison between the experimental data and simulation results the PIV dead zone radii were also applied to the simulation results. As seen in Figure 5.24 there is no dead zone near the gate in the simulation results, but applying a dead zone to the simulation has two positive effects. First, it allows a direct comparison between the data and the simulation. Vectors that appear in the simulation results will always have corresponding vectors in the experimental data plots. Second, it makes it easier to plot the simulation results on the same scale as the experimental data. The velocity vectors near the gate are quite large and dominate the images when plotted at the same scale as the experimental data.

The result of this post-processing effort was a set of Moldflow simulation data that was indistinguishable in format from the experimental PIV and flow front data. This allowed the same processing and plotting routines to be used for both the experimental data and the simulation results. For example, the same scaled continuity pseudo-color plot could be superposed on the simulation results that was used in the PIV analysis.

The final result of this post-processing can be seen in Figure 5.27 and Figure 5.28.

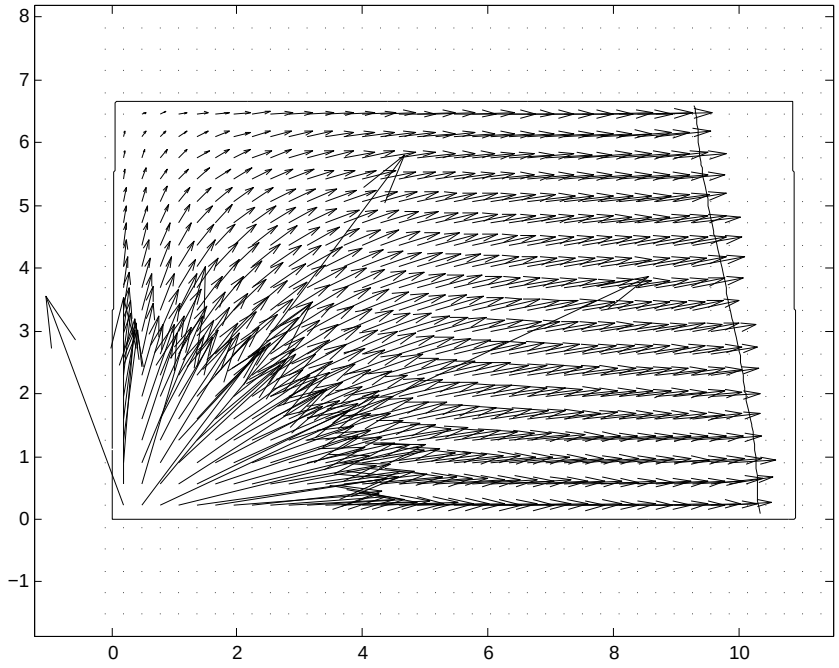

Figure 5.26: Result of interpolating the Moldflow velocity results onto a grid with the same density as the PIV results shown in Figures 5.1- 5.12. The Moldflow flow front has also been superposed on the data.

These are the results of the Moldflow simulation of the melt flow resulting from a 245° C melt injected at a rate of 34.5 cm^3/s.

5.7 Examination of the Structure of the Simulated Velocity Fields

In Section 5.4 and Section 5.5 it was found that the PIV velocity fields scaled linearly with volume flow rate and that the residual fields that remained after accounting for this scaling were uncorrelated and uniformly distributed. These same analyses were then performed on the simulation data to see if the same results would be obtained.

First the simulation fields were compared to each other and a best-fit scaling factor α was calculated for each pair of simulation fields using Equation 5.5. As with the PIV results the calculations were repeated for various critical radii to ensure that the final result was not a function of critical radius.

The deviation of the best-fit scaling factor α from the injection rate ratio was then plotted against the critical radius. The result of this is shown in Figure 5.29. The legend for the symbols is found in Table 5.2.

This figure is directly comparable to the analysis of the PIV vector fields shown in Figure 5.16. A comparison of the two shows that the deviation from Newtonian scaling for the simulation results is a factor of ten smaller than that of the PIV results. This indicates that the simulation results are even more strongly scalable with injection rate than the PIV results.

The residual fields were then created for the simulation results using Equation 5.5 and the residual metrics calculated using Equation 5.11. The residual metrics were calculated using several values of critical radii to ensure that the results did not

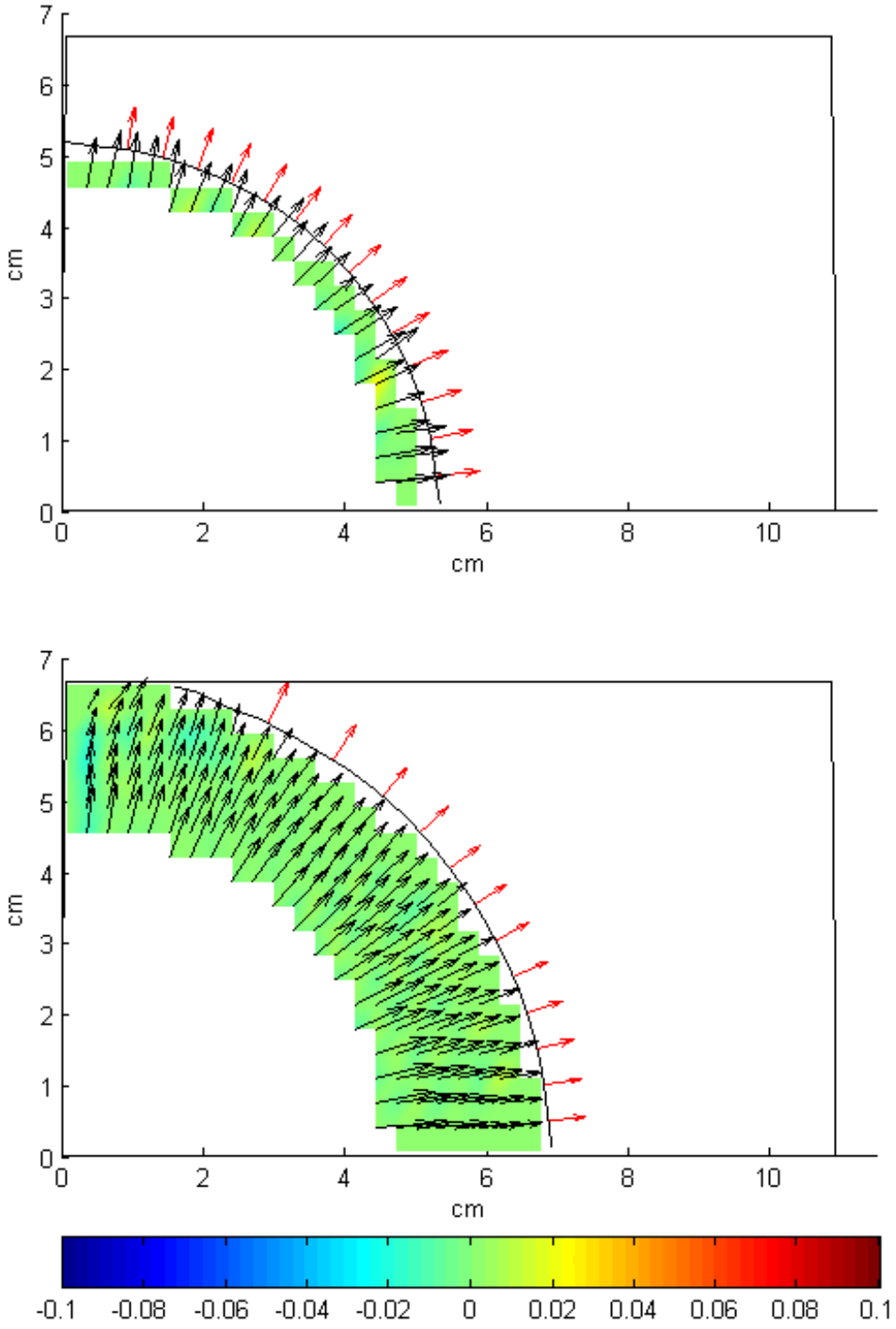

Figure 5.27: Moldflow simulation: 245° C, 34.5 cm^3/s, t^*=0.3 (top) and t^*=0.5 (bottom)

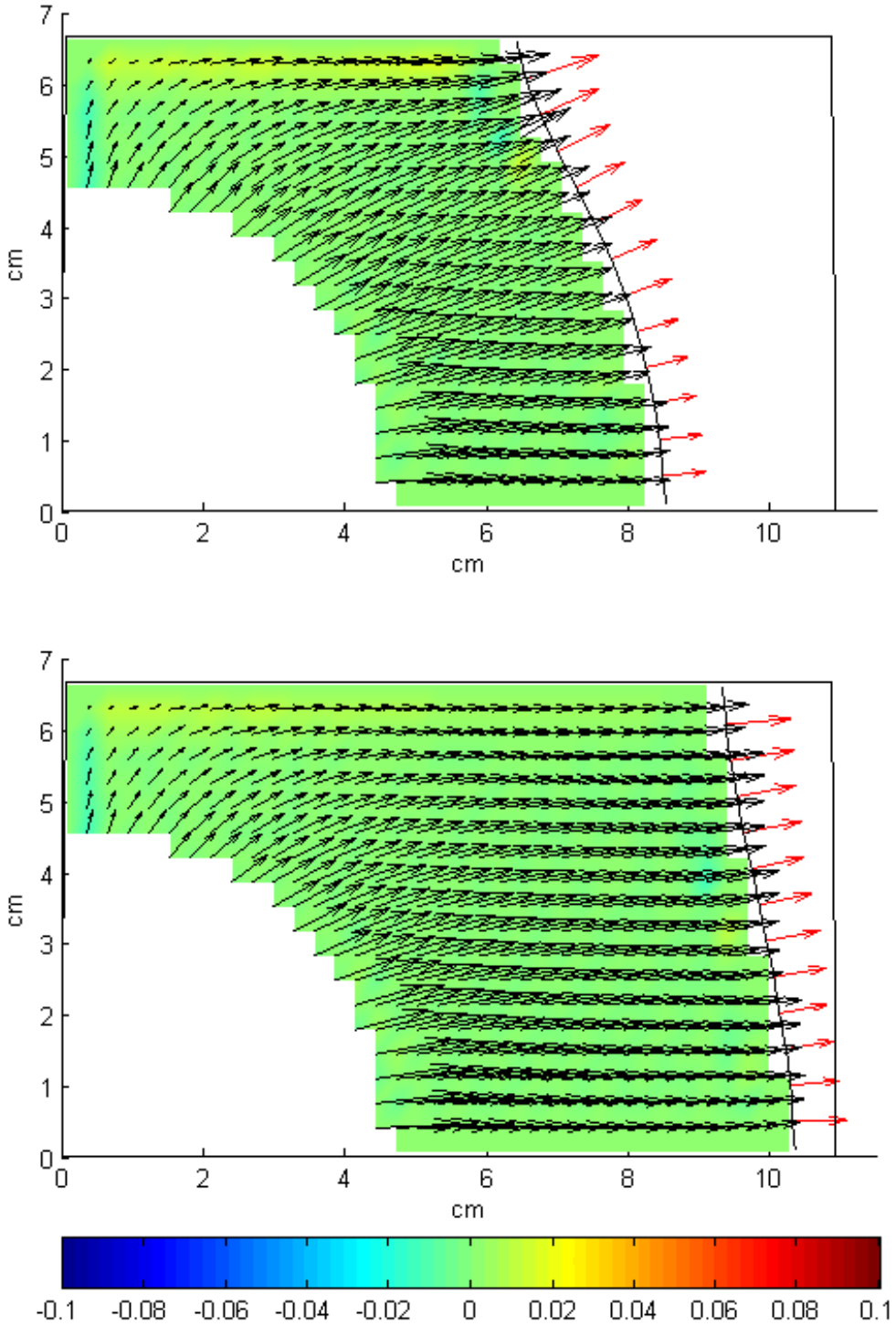

Figure 5.28: Moldflow simulation: 245° C, 34.5 cm^3/s, t^*=0.7 (top) and t^*=0.9 (bottom)

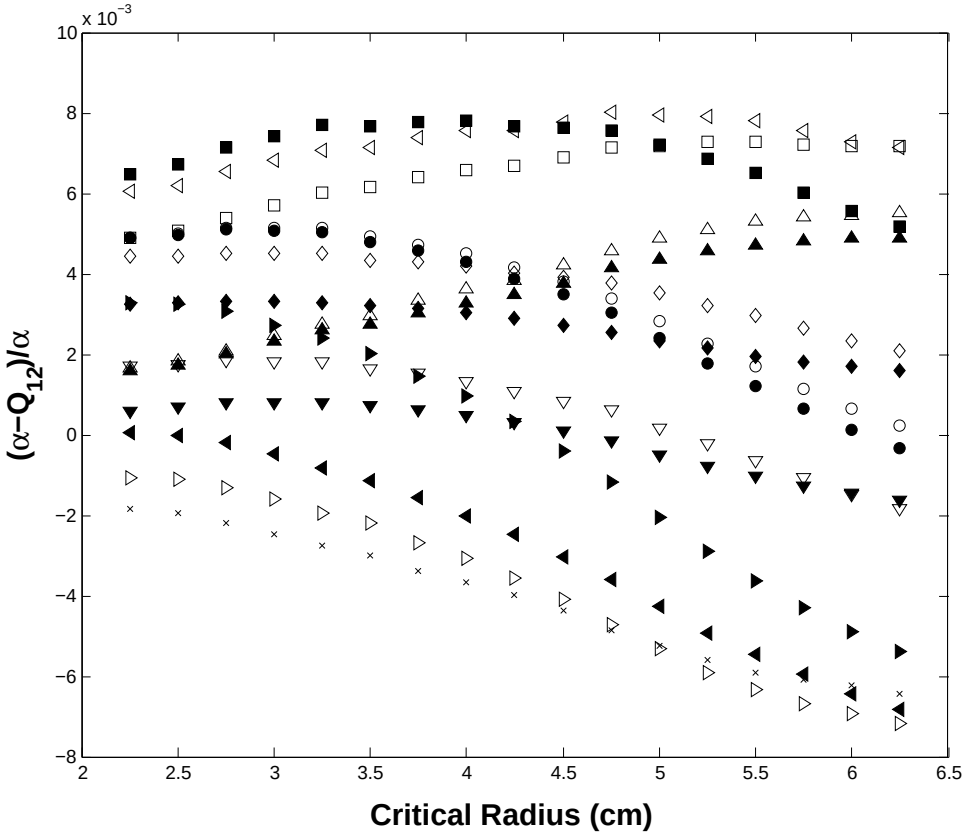

Figure 5.29: Deviation of the calculated scaling factor α from the ratio of injection rates Q_{12} as a function of critical radius for all possible comparisons of the Moldflow simulation results. The legend for the symbols is found in Table 5.2. The deviations for the simulations are a factor of ten smaller than those calculated from the PIV results as shown in Figure 5.16.

Table 5.5: Summary of the statistics used to describe the experimental PIV results and the Moldflow simulation results. These results show that both the experimental and simulation velocity fields scale in a Newtonian fashion with the injection rate ratio.

Experimental Results	
$(\alpha - Q_{12})/\alpha$	0.03±.07
Residual metric ε_R	0.11±0.07

Simulation Results	
$(\alpha - Q_{12})/\alpha$	0.003±.008
Residual metric ε_R	0.03±0.07

depend on the choice of critical radius. The resulting residual metrics were then plotted against critical radius in Figure 5.30. The legend for the symbols can be found in Table 5.2.

Comparing Figure 5.30 to the corresponding figure for the PIV data, Figure 5.19, it can be seen that the relative error metric for the simulation is on the order of three times smaller than that found in the PIV data. In combination with Figure 5.29 this shows that the simulation results scale linearly with injection rate. When this scaling is accounted for between two fields the residual field is much smaller than that found in the PIV velocity fields. The summary statistics of the scaling factor and residual metric calculations for both the PIV data and the Moldflow simulations can be found in Table 5.5.

The effect of injection rate and temperature on the scaling factor α and on the residual metric for the simulated velocity fields was then studied. ANOVA analyses identical to those carried out on the PIV data and described in Section 5.4. The results of these analyses on the simulation results, as well as those on the PIV data, are shown in Table 5.6 and Table 5.7.

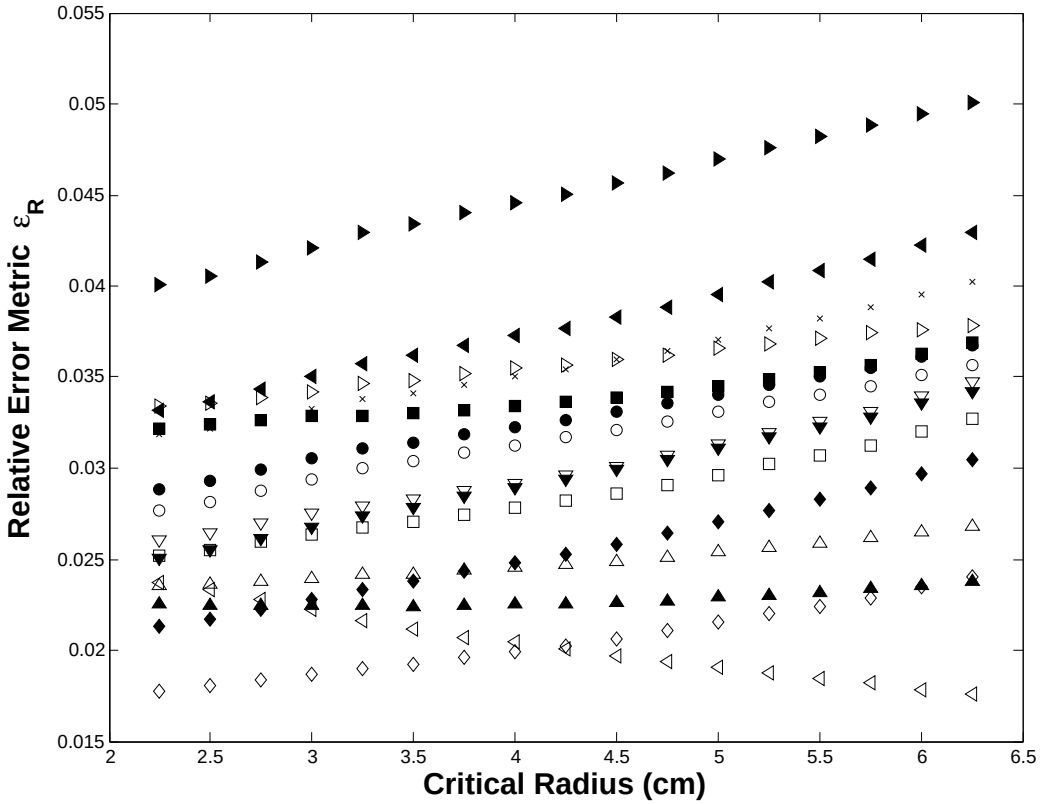

Figure 5.30: Residual metric ε_R as a function of critical radius for all possible median field comparisons. The legend for the symbols is found in Table 5.2. The residual metrics for the simulations are a factor of three smaller than those calculated from the PIV results as shown in Figure 5.19.

Table 5.6: Summary of the results of the statistical tests used to analyze the deviation of the velocity field scaling from Newtonian scaling summarized in Table 5.5. The ANOVA analyses tested the null hypotheses that the injection rate ratio and melt temperature were not significant factors of the observed variations of the best calculated scaling factor from the Newtonian scaling factor. The analyses were carried out at the 5% significance level.

Experimental Results

Factor	p-value	Significance
Injection rate ratio	0.1017	Not significant
Temperature	0.9908	Not significant

Simulation Results

Factor	p-value	Significance
Injection rate ratio	0.0084	Highly significant
Temperature	0.9979	Not significant

It was found that temperature was not a statistically significant factor for the deviation of the scaling factors from the injection rate ratio, with a p-value of 0.9979. This agrees with the analysis on the PIV data. However, the injection rate ratio was a highly significant factor with a p-value of 0.0084. These results are illustrated graphically with boxplots in Figure 5.31. This is in contrast with the analysis on the PIV results which showed that injection rate ratio was not significant. These results are illustrated graphically with boxplots in Figure 5.31.

Melt temperature was a mildly significant factor in explaining the variation found in the residual metric with a p-value of 0.0632. Injection rate ratio was a highly significant factor with a p-value of 0.0061. These results are illustrated graphically with boxplots in Figure 5.32. This again is in contrast with the analysis on the PIV results, which showed that neither melt temperature nor injection rate ratio were significant factors.

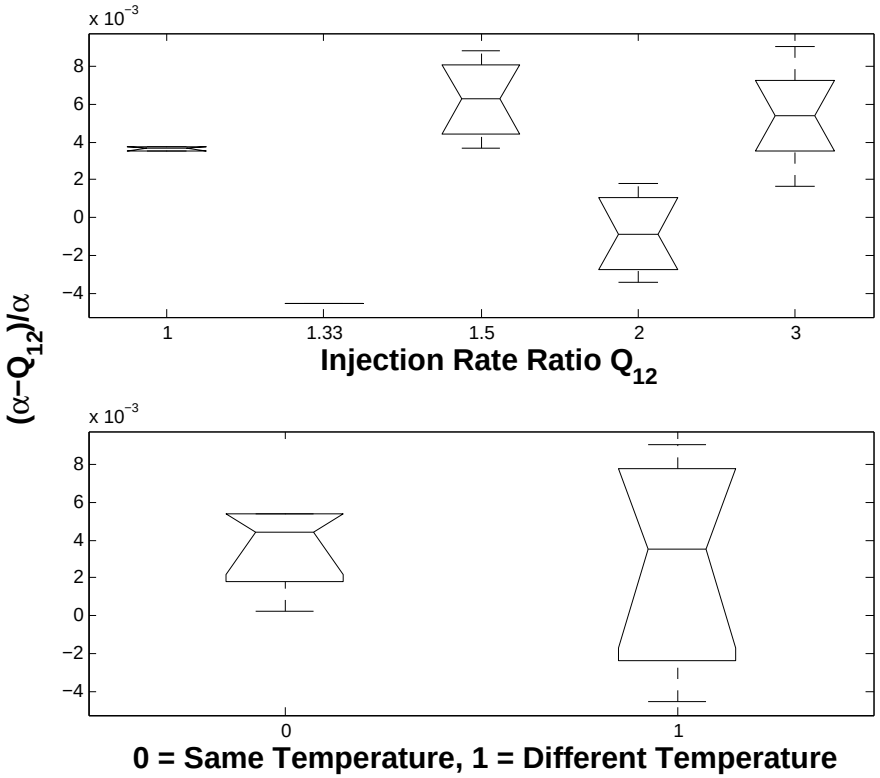

Figure 5.31: Boxplot of the deviation of the incompressible scaling factors α from the nominal injection rate ratios for the Moldflow simulation results as a function of injection rate ratio and temperature difference.

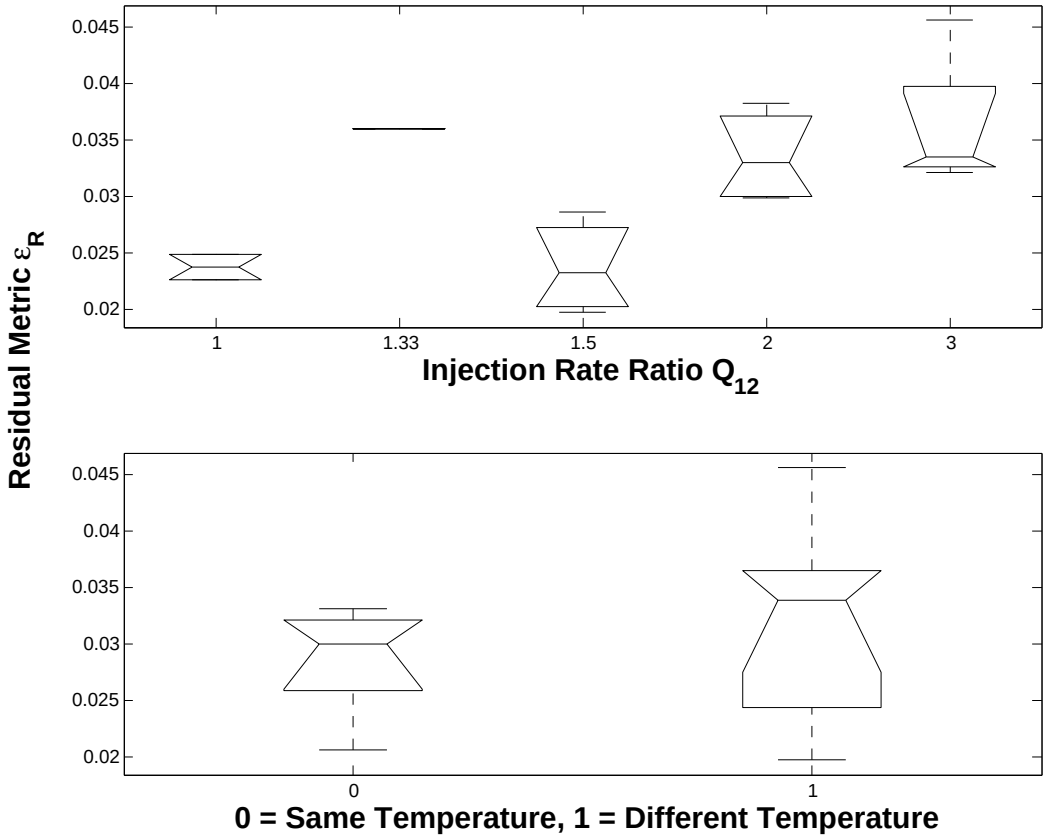

Figure 5.32: Boxplots of the residual metric for the Moldflow simulation results as a function of injection rate ratio and melt temperature difference. The molding parameters have no statistically significant effect on the residual metric.

Table 5.7: Summary of the results of the statistical tests used to analyze the residual velocity fields after accounting for the Newtonian scaling with injection rate summarized in Table 5.5. The ANOVA analyses tested the null hypotheses that the injection rate ratio and melt temperature were not significant factors of the observed variations of the residual metric.

Experimental Results

Factor	p-value	Significance
Injection rate ratio	0.7377	Not significant
Temperature	0.7168	Not significant

Simulation Results

Factor	p-value	Significance
Injection rate ratio	0.0061	Highly significant
Temperature	0.0632	Mildly significant

It must be kept in mind that even though there are discrepancies between the ANOVA analyses on the PIV and simulation scaling factors and residual metrics, these results are secondary. The primary result of comparing the PIV and simulation scaling factors is that both deviate only slightly from the injection rate ratios, with the deviation in the simulation results a factor ten smaller than that of the PIV results. Similarly, the residual metrics of both are small, with the simulation residual a factor of three smaller than that of the PIV results. When the much smaller scaling deviations and residual metrics of the simulations were examined more closely it was found that injection rate ratio was a significant factor. This was not the case for the PIV data.

The residual fields of all possible pairings of the simulation results were then cross-correlated as they were for the PIV results using Equation 5.12. The goal of this analysis was to see if there were any significant, persistent structures remaining in the residual fields after the injection rate scaling had been accounted for. A

Table 5.8: Summary of the results of the Komolgorov-Smirnov tests used to analyze the correlations of the residual experimental PIV fields with each other and of the correlations of the Moldflow simulation residual fields with each other. The null hypotheses of the tests were that the distributions of the correlations were uniform. The tests were carried out at a 5% significance level.

Data Source	p-value	Conclusion
Experiment	0.0724	Uniform distribution
Simulation	2.4863×10^{-4}	Non-uniform distribution

histogram of the correlations is shown in Figure 5.33.

The cumulative distribution function of these correlations is shown in Figure 5.34 along with the CDF of a uniform distribution. Unlike the corresponding figure for the PIV results, Figure 5.22, the CDF of the simulation correlations seems to differ significantly from that of a uniform distribution. This conclusion was confirmed by a Komolgorov-Smirnov test. This test resulted in a p-value of 2.4863×10^{-4}, rejecting the null hypothesis that the correlation distribution was taken from a population with a uniform distribution. This result is in contrast to the corresponding test on the PIV data, as shown in Table 5.8.

5.8 Simulating Polymer Melt flow with the Hele-Shaw Approximation

Before comparing the experimental and simulated results a brief overview of Moldflow's solver is in order. Moldflow uses a Hele-Shaw model to model the fluid flow in the mold cavity. The Hele-Shaw model assumes that the pressure gradients in the cavity thickness direction are negligible, $\partial p/\partial z \ll \partial p/\partial x$ and $\partial p/\partial z \ll \partial p/\partial y$, and that flow in the cavity thickness direction is negligible, $v_z \ll v_x$ and $v_z \ll v_y$.

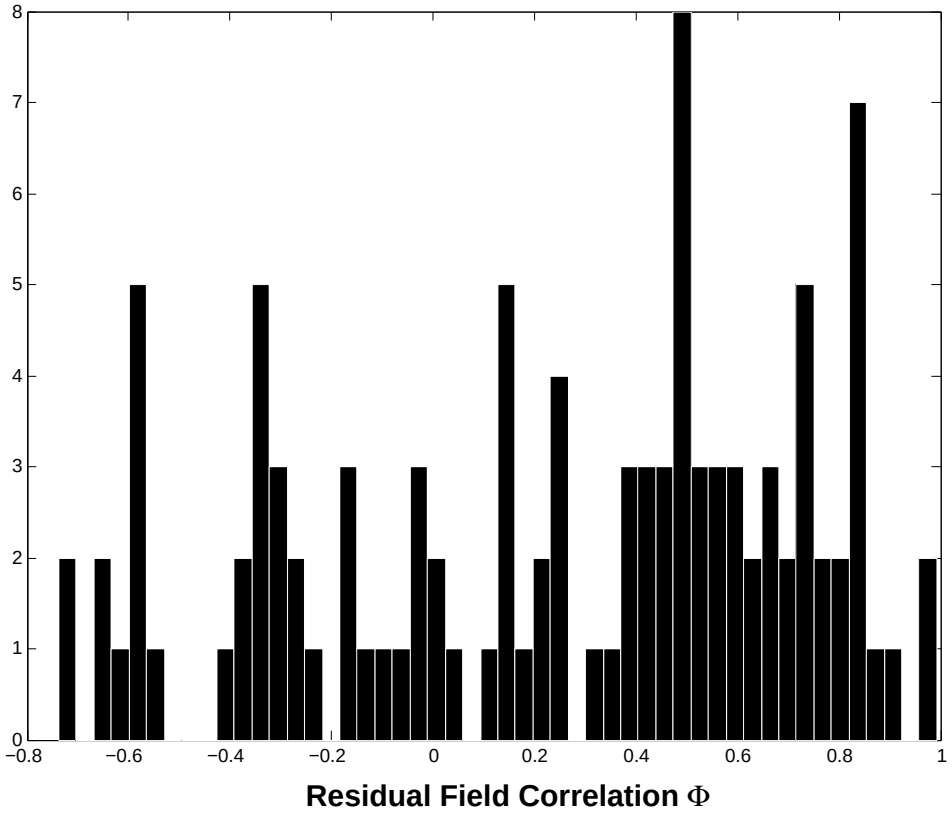

Figure 5.33: Histogram of the correlations between Moldflow simulation residuals created in the same manner as Figure 5.21.

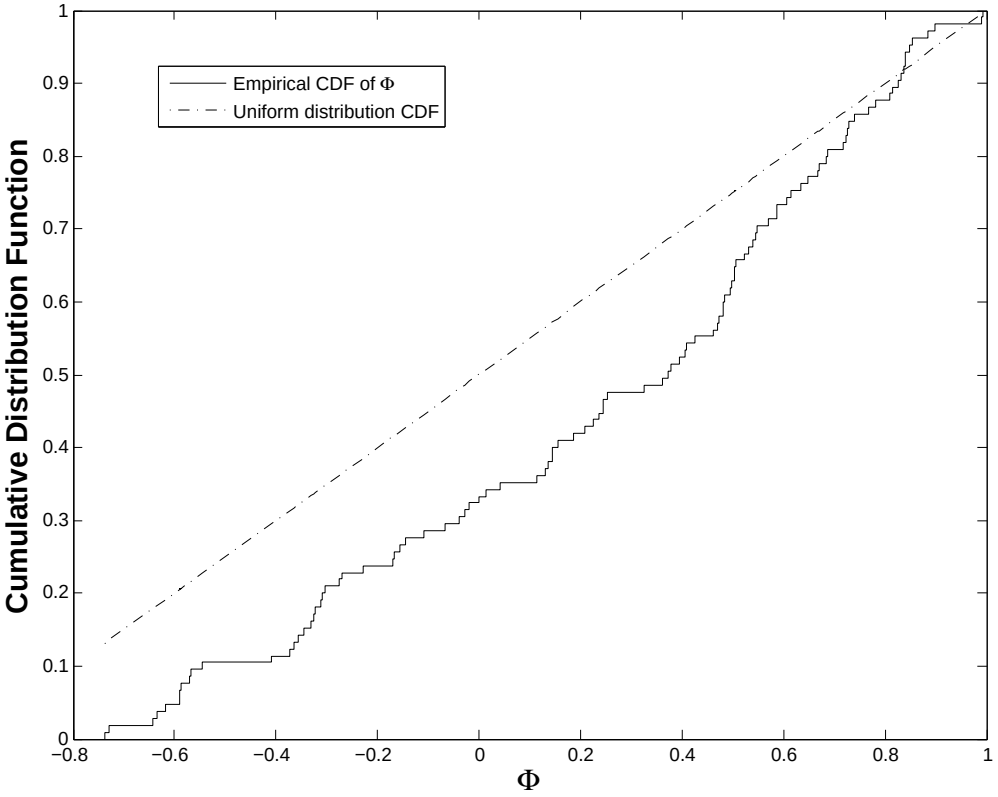

Figure 5.34: Cumulative distribution functions of Φ, based on Moldflow results, and of a uniform distribution.

Dantzig and Tucker[103] give a good summary of the use of the Hele-Shaw equation in the modeling of polymer flow. Following their derivation, the Hele-Shaw model equation is given by:

$$\nabla \cdot (S \nabla p) = 0 \tag{5.13}$$

where S is the flow conductance and is given by:

$$S(x, y) = \int_0^B \frac{z^2 dz}{\eta(x, y, z)} \tag{5.14}$$

and η is the local viscosity and B is the cavity half-thickness.

Once Equation 5.13 has been used to determine the pressure distribution the gap-wise average velocities are given by

$$\bar{u} = -\frac{S}{B} \nabla p \tag{5.15}$$

The full velocity distributions can be calculated using

$$\vec{u} = -\left(\int_z^h \frac{z' dz'}{\eta(z')} \right) \nabla p \tag{5.16}$$

where z' is a dummy variable of integration.

The Hele-Shaw approximation does not satisfy the full continuity equation $\nabla \cdot u = 0$. It instead satisfies an integrated continuity equation, a weaker requirement. This can be seen by combining Equations 5.13 and 5.15:

$$\nabla \cdot (B \bar{u}) = 0 \tag{5.17}$$

Equations 5.13 and 5.15 have important ramifications for any simulation employing the Hele-Shaw model. First, only average velocities are calculated. It is possible to calculate velocity variations in the thickness direction using Equation 5.16, but this velocity profile only affects the magnitude of the velocity as a function of thickness. The velocity vector orientations are constant throughout the thickness of the

part. Equation 5.17 also shows that velocity profiles calculated from the flow conductance are not guaranteed to satisfy the continuity equation since only the average velocity used in the mass conservation equation.

Another important ramification arises from consideration of the boundary conditions of Equation 5.13. Dirichlet boundary conditions are typically imposed at the front, where $p = 0$, and at the injection location where an injection pressure may be specified. At the solid boundaries of the mold cavity Neumann boundary conditions are imposed with $\partial p/\partial n = 0$. Equation 5.15 show that this is equivalent to imposing a no-penetration boundary condition at the walls. These boundary conditions completely specify the solution of Equation 5.13, so a no-slip boundary condition cannot be imposed on a flow when using the Hele-Shaw model. In fact, Dantzig [103] points out that there will always be a pressure gradient parallel to the wetted surface of the mold. Since the velocity is parallel to the pressure gradient, this means that there will always be a non-zero tangential velocity at the walls of the mold when using the Hele-Shaw model.

Another ramification of the Hele-Shaw model concerns its prediction of flow fronts. Programs such as Moldflow use the calculated pressure distribution to generate average velocities, and then uses these velocities to move the polymer in the cavity. But along the cavity walls the imposed boundary condition is $\partial p/\partial n = 0$. This means that isobars will always be perpendicular to the cavity walls at the point of intersection with the wall. Since the flow front is also an isobar with $p = 0$, this means that the flow fronts will also be perpendicular to the cavity walls.

One last ramification of the Hele-Shaw model is its assumption of negligible velocity in the thickness direction. This is a good approximation for polymer melt flows in most areas of the mold cavity, but it does not hold true near the flow front due to the

fountain flow effect. To summarize, then, the Hele-Shaw model has limitations that can be expected to cause deviations between simulation results and experimental data:

- Only the average velocities are calculated. Midplane velocities may be calculated by assuming a constitutive relation, but they are not guaranteed to satisfy continuity.
- The no-slip boundary condition cannot be imposed, and slip velocities should be expected along the walls.
- Flow fronts will tend to be perpendicular to the cavity walls.
- Fountain flow effects near the front cannot be captured by the Hele-Shaw model.

5.9 Comparison of the Simulated Flow Fronts with the Experimental Data

Figure 5.35 shows a comparison between the manually extracted flow fronts and the Moldflow simulation fronts at t^*=0.1, 0.3, 0.5, 0.7 and 0.9 for specimens molded at 245°C and 11.5 cm^3/s. The striking feature of this figure is the difference between the data and the simulation near the cavity walls. This is due to the Hele-Shaw approximation. As discussed in Section 5.8, the Hele-Shaw approximation enforces the no-penetration boundary condition but not the no-slip boundary condition. Since the velocity is proportional to the pressure gradient, the no-penetration condition forces the component of the pressure gradient perpendicular to the cavity walls to be zero at the walls. This in turn forces the pressure isobars to be perpendicular to the cavity walls. The flow front coincides with the $p = 0$ isobar, so the simulated flow

fronts based on this isobar will tend to be perpendicular to the walls when using the Hele-Shaw approximation. This is not what actually happens in the mold cavity. In the flow fronts extracted from the digital movies the fronts always curve toward the wall due to the no-slip boundary condition.

Another feature of Figure 5.35 is that the actual fronts always lead the simulated fronts. This is due to the fountain flow effect. The actual fronts have curvature through the thickness of the cavity. Examination of a short shot would show that the flow front has a somewhat parabolic shape when viewed from the side. The manually extracted flow fronts trace out the tip of this profile. The simulation calculates an average velocity, which is constant through the thickness of the part. This means that the experimentally determined fronts will lead the simulated fronts, even if the two fronts enclose equal polymer volumes.

The differences between the measured and the simulated fronts are shown in Figure 5.36 and Figure 5.37. Figure 5.36 compares the flow fronts at t^*=0.1 and t^*=0.3. At these two times the flow is primarily radial. The coordinates of the points on the fronts were converted into polar coordinates using the reference frame illustrated in Figure 4.7. The normalized residuals of the r-components of the points on the fronts were calculated for values of θ ranging from 0° to 90°. The figure shows that the simulated fronts are most accurate in the middle of the cavity and have high residuals near the walls.

Figure 5.37 compares the flow fronts at t^*=0.5, t^*=0.7 and t^*=0.9. At these times the flow is primarily a channel flow. The coordinates of the points on the fronts were transformed to the reference frame illustrated in Figure 4.5 and the normalized residuals of the y coordinates were calculated for values of x ranging from 0 to 6.7 cm. Again, the simulated fronts are most accurate near the middle of the cavity but

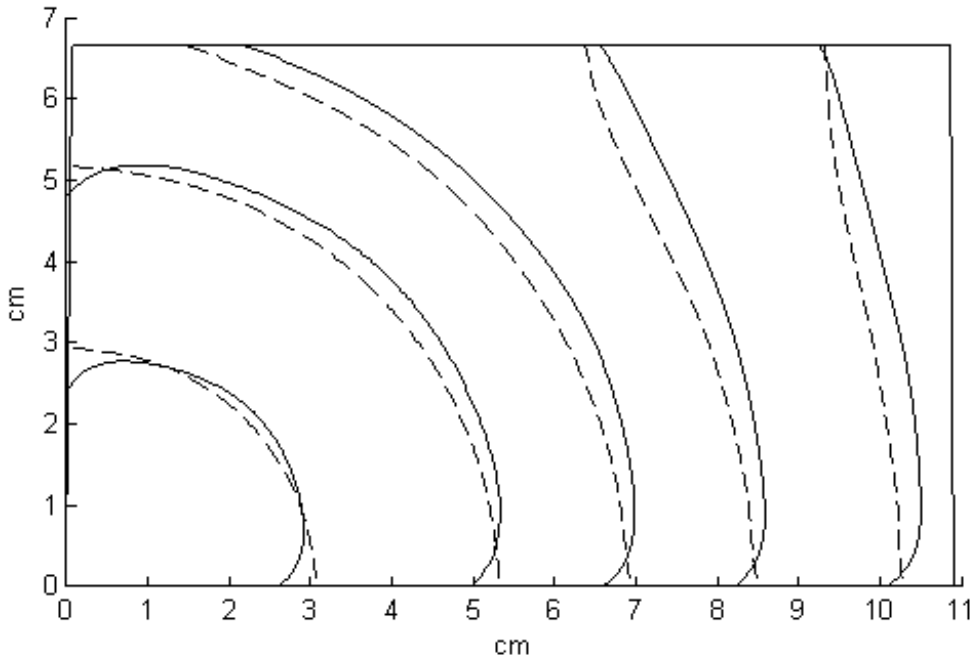

Figure 5.35: Comparison of the simulation flow fronts (dashed lines) with those extracted manually from the digital movies of the mold filling (solid lines).

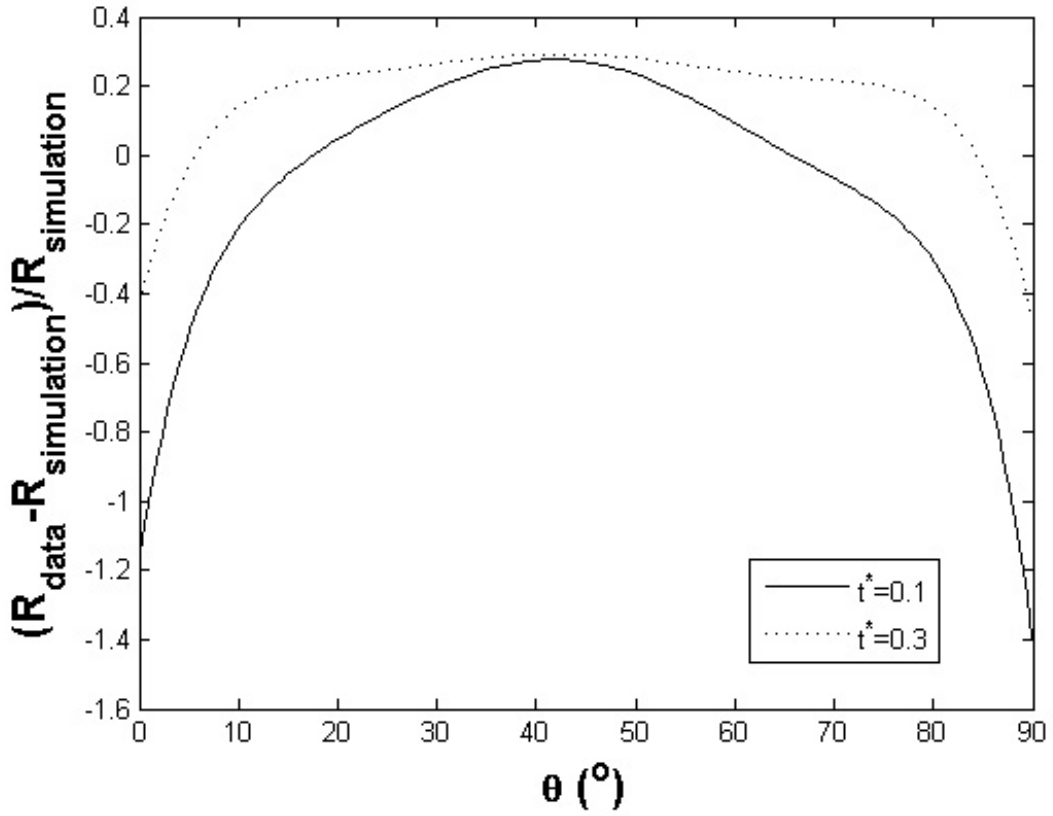

Figure 5.36: Comparison of the simulation flow fronts with those extracted manually from the digital movies of the mold filling for the radial flow regime.

have significant residuals near the walls.

5.10 Comparison of the Simulated Velocity Fields with the Experimental PIV Data

In Section 5.5 it was shown that the simulation results scale with the injection rate. That being the case, the results for the 245°, 34.5cm^3/s conditions shown in Figure 5.27 and Figure 5.28 can be taken as typical of the simulation results and will be compared with the experimental results at the same molding conditions shown in Figure 5.11 and Figure 5.12.

Direct comparison of the experimental and simulated flow fields is complicated by the fact the Hele-Shaw analysis calculates average flow velocities, not midplane

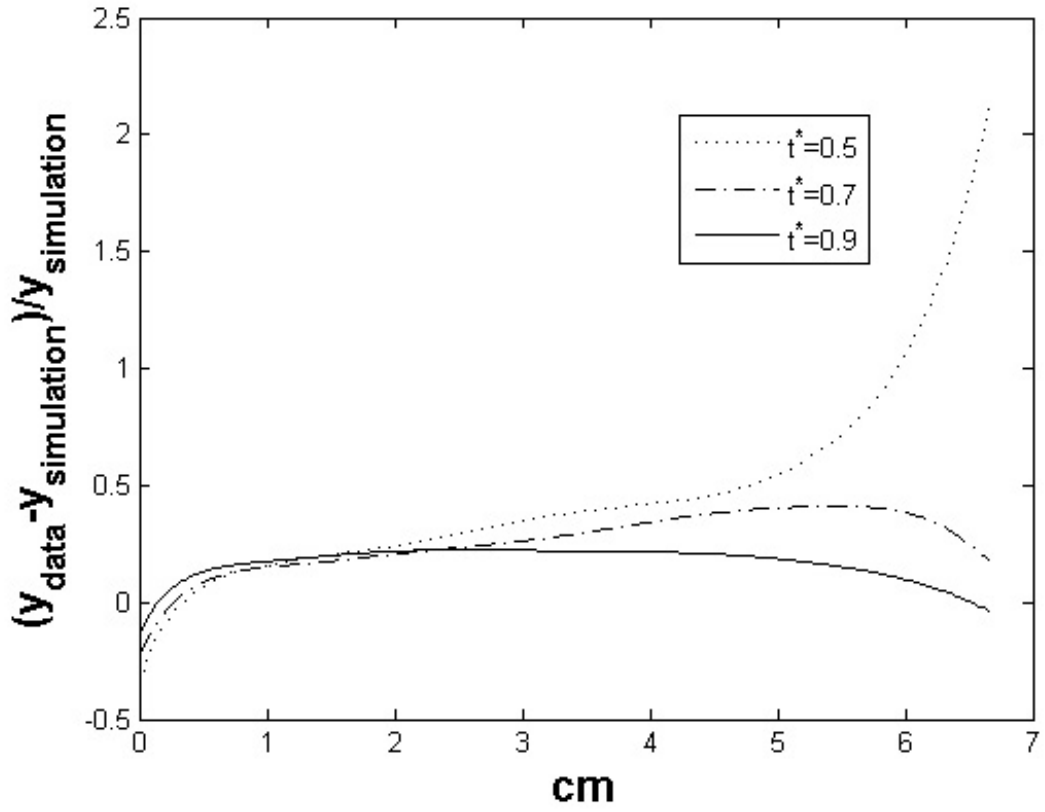

Figure 5.37: Comparison of the simulation flow fronts with those extracted manually from the digital movies of the mold filling for the channel flow regime.

velocities. But, since for the bulk of the flow the Hele-Shaw assumptions hold true for polymer melts, a Hele-Shaw analysis should deliver accurate streamlines and thus accurate velocity vector orientations. This suggests that the best approach to comparing the experimental results with simulations would be to examine the velocity vector orientations and magnitudes separately.

In order to compare velocity vector orientations the vector angles were calculated at each point in the t^*=0.9 field and in the corresponding PIV vector field. A scalar field was created by subtracting the simulation orientations from the PIV orientations at ecah point in the field. A pseudo-color overlay was then used to superpose this scalar field on top of the simulated vector field. The result of this operation is shown in Figure 5.38. This figure shows that the predicted orientations are quite good, with a mean angular difference of 1.7°. The standard deviation of the orientations was 1.4°.

Direct comparison of the PIV midplane velocity vectors to the Moldflow results is not possible since Moldflow calculates average velocities, not midplane velocities. An intermediate step must be taken to make a comparison. Two such steps are considered here. The first is to use the PIV data to calculate average velocities. The second is to use the Moldflow simulation to calculate midplane vectors.

In Figure 5.15 it was shown that in the channel-flow region of the mold filling process the average profile factor F was 0.7. If this factor is applied to the entire field an estimated average velocity field can be calculated as $\bar{u} = Fu$. Figure 5.39 shows the result of this comparison. The pseudo-color overlay represents the ratio of the PIV vectors to the simulated vectors and is overlaid on the simulated vector field. In general the comparison is quite good, with the mean ratio of magnitudes equal to 0.998 and a standard deviation of 0.25. The main areas of difference are

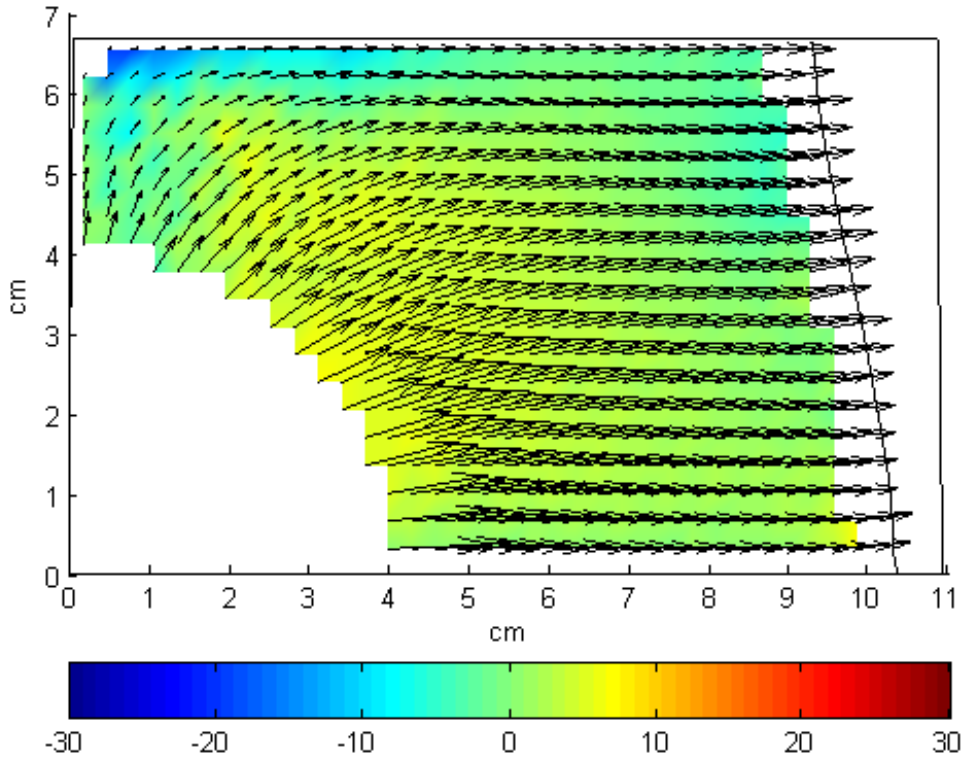

Figure 5.38: Pseudocolor overlay represents the difference in angles between the PIV vectors and the Moldflow simulation vectors in degrees. The mean angular difference is 1.7°.

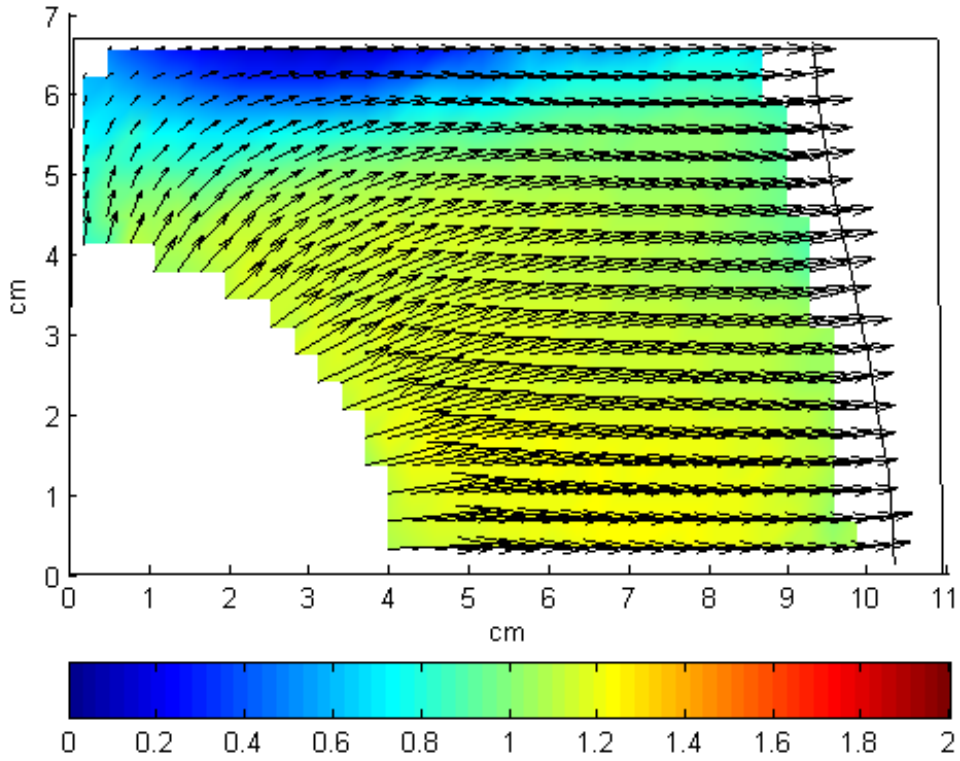

Figure 5.39: Pseudocolor overlay represents the ratio of magnitude of the PIV vectors to the simulation vectors. The median ratio is 0.998 with a standard deviation of 0.25.

near the walls, particularly in the corner. This is likely due to a combination of two factors. Near the walls the simulation is bound to have a higher velocity since the Hele-Shaw approximation does not impose the no-slip boundary condition. Second, near the corner the flow is transitioning from radial to channel flow. This means that the profile factor calculated from the purely channel-flow regime is probably not as applicable in this region.

The second method for comparing the Moldflow simulation to the PIV data is to use Moldflow itself to calculate midplane velocities. Moldflow allows the user to estimate midplane velocities by assuming a parabolic profile through the thickness of the part. The parabola is modified near the walls due to the presence of a frozen

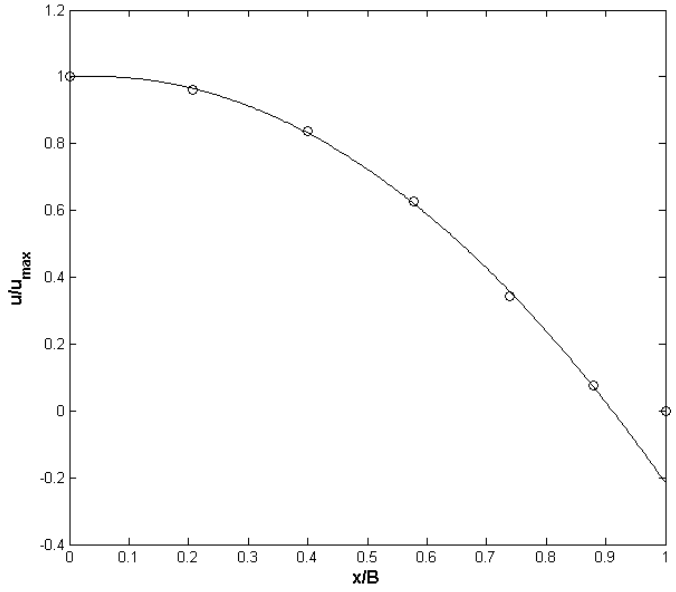

Figure 5.40: Moldflow uses a parabolic profile assumption in calculating the midplane velocity from the average velocity. Near the walls the flow is slower due to solidification effects. This further sharpens the profile at the midplane. The profile factor for this profile is 0.589

layer. An example of this profile is shown in Figure 5.40. Calculating the average value of this profile results in a profile factor $F = 0.589$. A pure parabola would have a profile factor $F = 0.667$.

Figure 5.41 shows the comparison of Moldflow's prediction of midplane velocity vectors superposed by the scaled continuity equation. Obviously, plotting a field of midplane velocity vectors is pushing Moldflow outside of its normal operating parameters. The continuity equation shows large errors compared to Moldflow's prediction of average velocities. Taking the final step, these midplane velocities are compared to the PIV vectors in Figure 5.42. Again the ratio of the PIV vectors to the simulated vectors is overlaid on the simulated vector field. The mean ratio is 0.89 with a standard deviation of 0.37. This means that the simulated midplane vectors consistently overestimate the PIV vector magnitudes. This is due to the fact

that Moldflow's assumed velocity profile through the cavity thickness is parabolic. Moldflow assumes a Newtonian profile instead of a non-Newtonian profile. The ratio of the PIV vectors to the simulation vectors should be equal to the inverse ratio of profile factors since the average flow rates are equal. For example, take a sample area dA spanning the mold cavity and perpendicular to the cavity walls:

$$dQ_{PIV} = F_{PIV} u_{PIV} dA \tag{5.18}$$

$$dQ_{MF} = F_{MF} u_{MF} dA \tag{5.19}$$

$$dQ_{PIV} = dQ_{MF} \tag{5.20}$$

$$F_{PIV} u_{PIV} dA = F_{MF} u_{MF} dA \tag{5.21}$$

$$\frac{u_{PIV}}{u_{MF}} = \frac{F_{MF}}{F_{PIV}} \tag{5.22}$$

where Q_{PIV} and Q_{MF} are the flow rates through the area dA based on the PIV vectors and the Moldflow midplane vectors. u_{PIV} and u_{MF} are the PIV and Moldflow midplane velocities and F_{PIV} and F_{MF} are the profile factors for the PIV field and the Moldflow field. Using the measured estimates of $F_{PIV} = 0.7$ and $F_{MF} = 0.589$ gives a predicted midplane velocity ratio of $u_{PIV}/u_{MF} = 0.86$, comparing favorably with the measured ratio of 0.89.

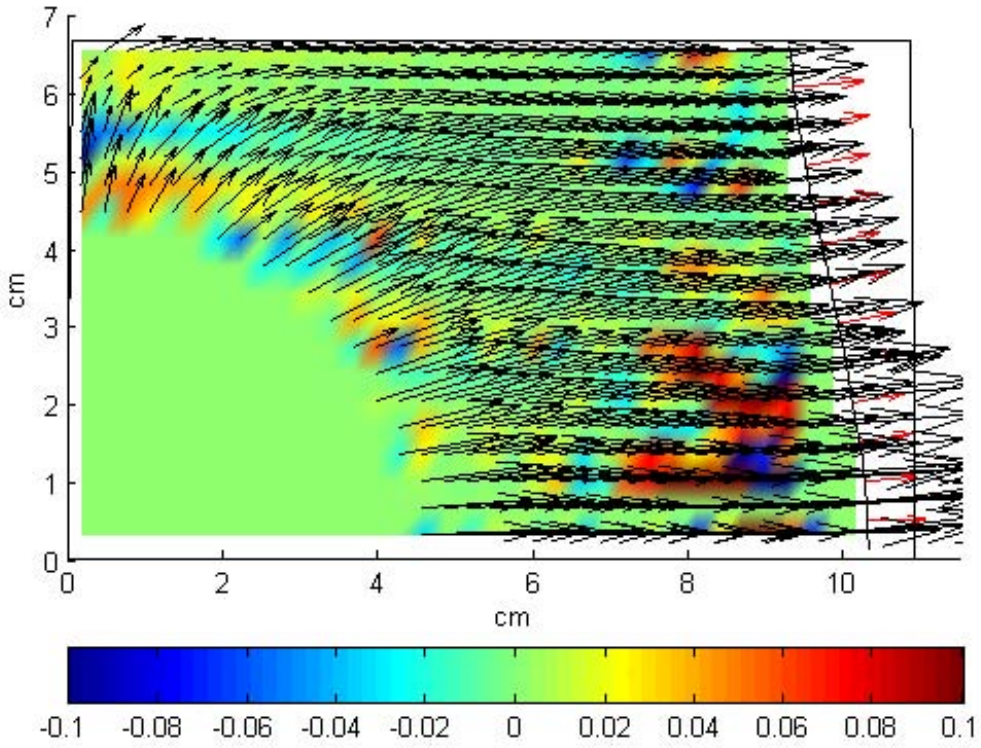

Figure 5.41: Moldflow prediction of midplane velocities superposed by the scaled continuity equation.

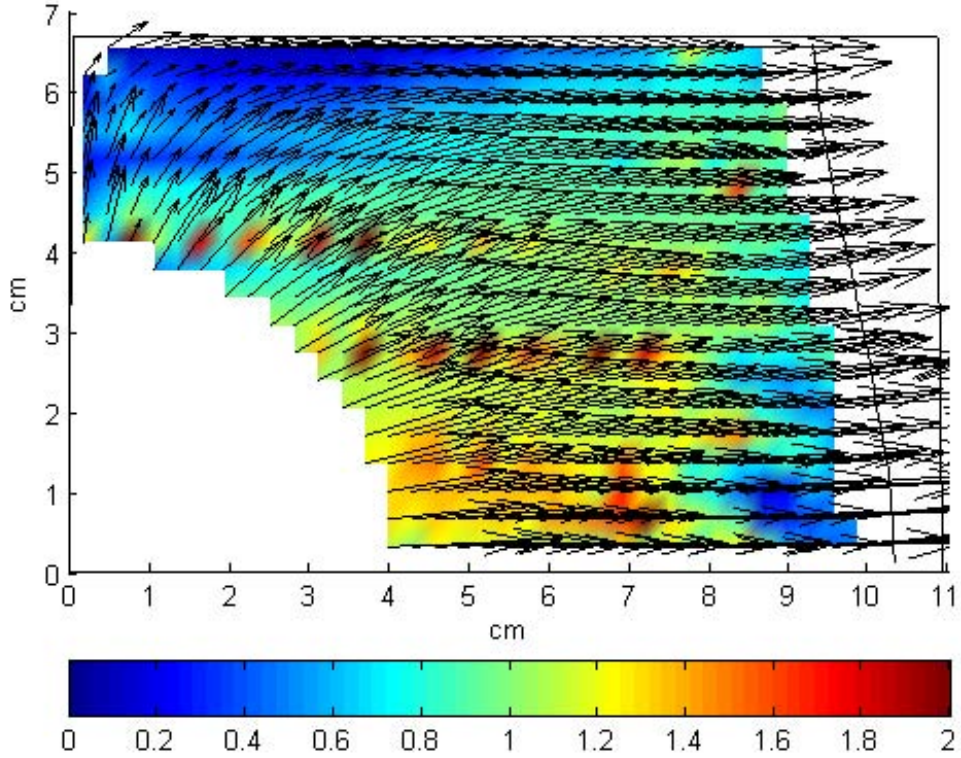

Figure 5.42: Ratio of the PIV data magnitudes to the Moldflow prediction of mid-plane velocity magnitudes. The predicted ratio based on the ratio of profile factors is 0.85. The measured mean ratio is 0.89 with a standard deviation of 0.37.

CHAPTER 6

Estimation of the Power Law Parameters of Polystyrene Using the Optical Access Mold

The direct outputs of the optical access mold experiment are the digital images, from which PIV and flow front data may be extracted, and the in-mold pressure traces. The gate pressure data corresponding to the PIV data presented in Chapter 5 will be presented here along with Moldflow simulations. An analytical model of the pressure rise during the radial flow portion and channel flow portion of the mold filling process will also be presented. The model will be used to estimate the power-law coefficient and exponent of STYRON 615 APR.

6.1 Gate Pressure During the Filling Phase

The pressure at the gate of the optical access mold was measured by a mold pressure sensor as described in Section 2.7. The pressure traces reflect three flow regimes as illustrated in Figure 6.1. The initial portion of the pressure trace is due to the radial flow of the polymer as it fills the mold and is described in Section 6.3.1. When the melt contacts the wall opposite the gate it transitions into a channel flow, characterized by a linear pressure rise as described in Section 6.3.2. When the melt contacts the last wall it rises sharply, with the pressure reaching a maximum as the

melt fills the final corner of the mold.

The gate pressure curves corresponding to the molding conditions found in Table 5.1 are shown in Figure 6.2 and Figure 6.3. The pressure traces were averaged over each set of molding conditions.

As described in Section 2.7, the mold pressure sensor proved inaccurate at the relatively low pressures seen during the filling phase. The calibration curve shown in Figure 2.25 was applied to the pressure data. The plateau value of the correction factor seen in Figure 2.26 was extended to cover pressures up to 1.5 MPa, the range of pressures seen during the filling stage.

The pressure sensor problems are most evident in the 11.5cm^3/s data sets. These data sets have "dead zones" at the beginning of the shot where the pressure does not begin to increase until at least 0.25 seconds into the shot. These runs were at the lowest gate pressures, and apparently the pressures were too low during the beginning of the mold filling to register on the pressure sensor. The sensor seems to exhibit a threshold stress when it is in the mold and the mold is closed. The sensor did not exhibit this behavior when calibrated outside of the mold, suggesting a friction problem with the mold pin that the sensor is seated beneath.

6.2 Moldflow Simulation of the Gate Pressure During the Filling Phase

The Moldflow simulations described in Chapter 5 produce gate predictions as well as velocity fields. The same mesh shown in Figure 5.23 and described in Table 5.4 was used to generate gate pressure traces.

Two sets of Moldflow simulations were performed. The first set used the entry for STYRON 615APR found in the Moldflow material database. The viscosity

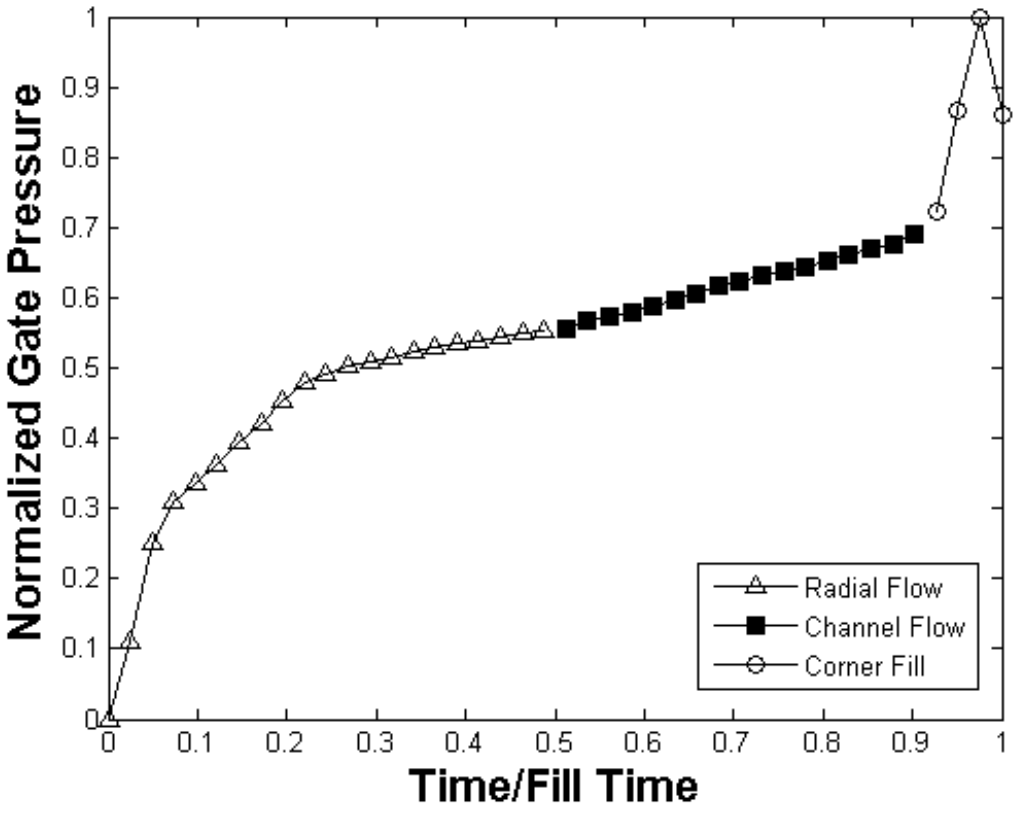

Figure 6.1: Typical gate pressure curve for the filling of the optical access mold. The curve reflects three different flow regimes: radial flow for the first half of the shot, channel flow for the second half of the shot, and a peak due to the flow contacting the far wall and filling the last corner of the mold.

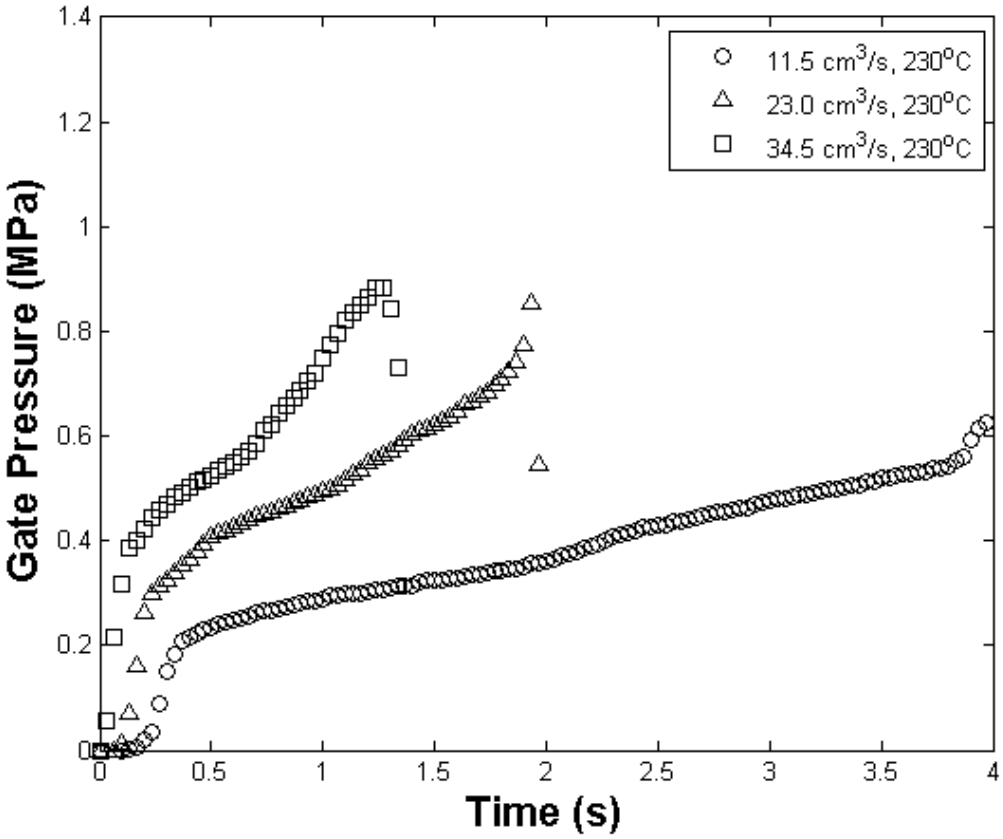

Figure 6.2: Averaged gate pressure traces for specimens molded at 230°C.

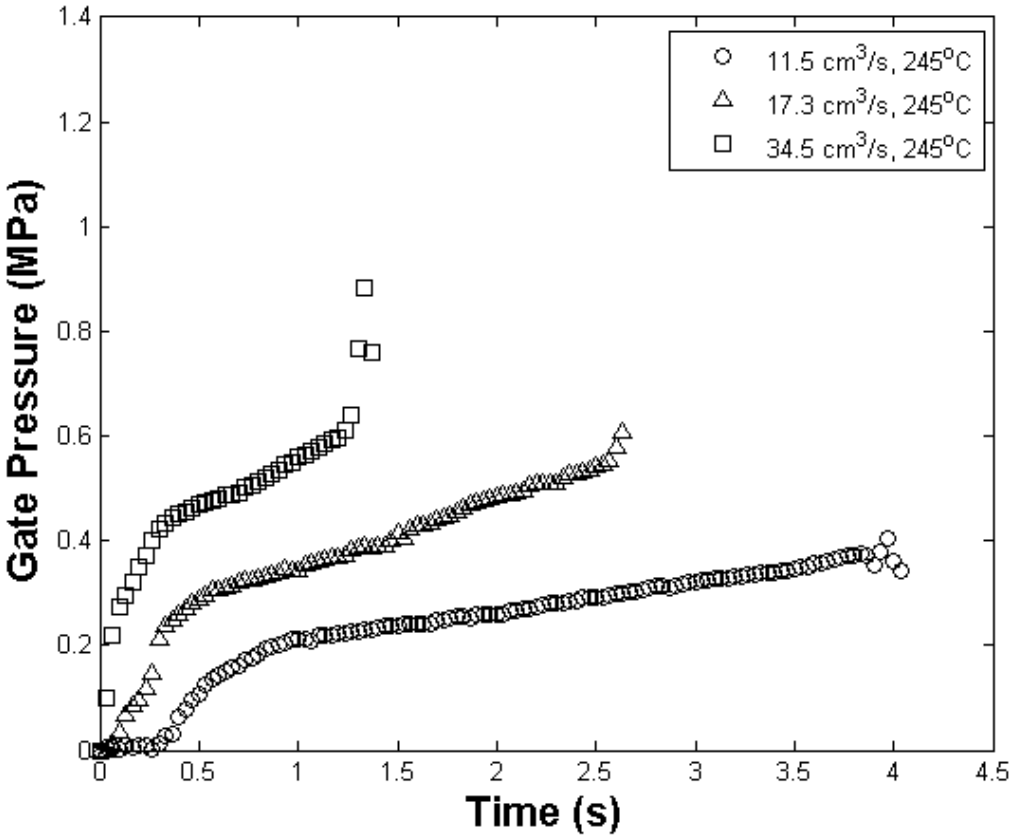

Figure 6.3: Averaged gate pressure traces for specimens molded at 245°C.

curves in this database were generated by a capillary rheometer. A second set of simulations was performed using data generated by an injection molding rheometer. Tseng [104] and Amano [105] have used injection molding machines to force polymer melts through capillary rheometers. The goal of this type of measurement is to ensure that the polymer melt undergoes a shear history typical of injection molding before its viscosity is measured.

Moldflow Plastics Labs (MPL) measured the viscosity of the polymer and particle mixture used in the present work using an injection molding rheometer. Their full report can be found in Appendix A. MPL also provided a Moldflow-compatible material database file that contained the Cross-WLF and Carreau model parameters that best fit the injection molding rheometer data.

Viscosity curves calculated from the Cross-WLF models for both the standard capillary rheometer data and the injection molding rheometer data are shown in Figure 6.4. The Cross-WLF model is given by:

$$\eta = \frac{\eta_0}{1 + (\eta_0 \dot{\gamma}/\tau^*)^{1-n}} \tag{6.1}$$

where

$$\eta_0 = D_1 \exp\left[\frac{-A_1(T - T^*)}{A_2 + (T - T^*)}\right] \tag{6.2}$$

$$T^* = D_2 + D_3 P \tag{6.3}$$

$$A_2 = \tilde{A}_2 + D_3 P \tag{6.4}$$

$$\tag{6.5}$$

where P is the melt pressure in Pascals and T is the melt temperature in degrees Kelvin.

The viscosity as measured by the injection molding rheometer tends to be lower than that measured by the standard capillary rheometer at identical melt temper-

Table 6.1: Comparison of the Cross-WLF model parameters for STYRON 615 APR from two different types of viscosity measurement. The Moldflow database values were extracted from capillary rheometer data, and these are compared with parameters extracted from data taken on an injection molding rheometer.

.

Cross-WLF Parameter	Moldflow database value	Injection molding rheometer value
n	0.3775	0.3720
τ^* (Pa)	12726	21765.5
D_1 (Pa·s)	7.44×10^{10}	4.32561×10^{10}
D_2 (K)	373.15	373.15
D_3 (K/Pa)	0	0
A_1	25.391	25.245
$\tilde{A}_2$ (K)	51.6	51.6

atures and shear rates. The lower viscosity leads to lower predicted gate pressures as seen in Figure 6.5 and Figure 6.6. The differences between the simulations are slight, but are more pronounced at the lower injection rates.

The Moldflow simulations using the injection molding rheometer data are compared with the experimental results in Figure 6.7 and Figure 6.8. The correspondence between the simulation and the data is best during the radial flow portion of the pressure traces, although allowance has to be made for the poor sensor sensitivity in the slower injection rate data. Both the data and the simulations evince a linear channel flow regime, but the data shows a smaller slope than the simulation in every case. Both the data and the simulation show a sharp pressure peak during the corner filling regime, but the peak in the simulation is significantly higher than that seen in the data in every case.

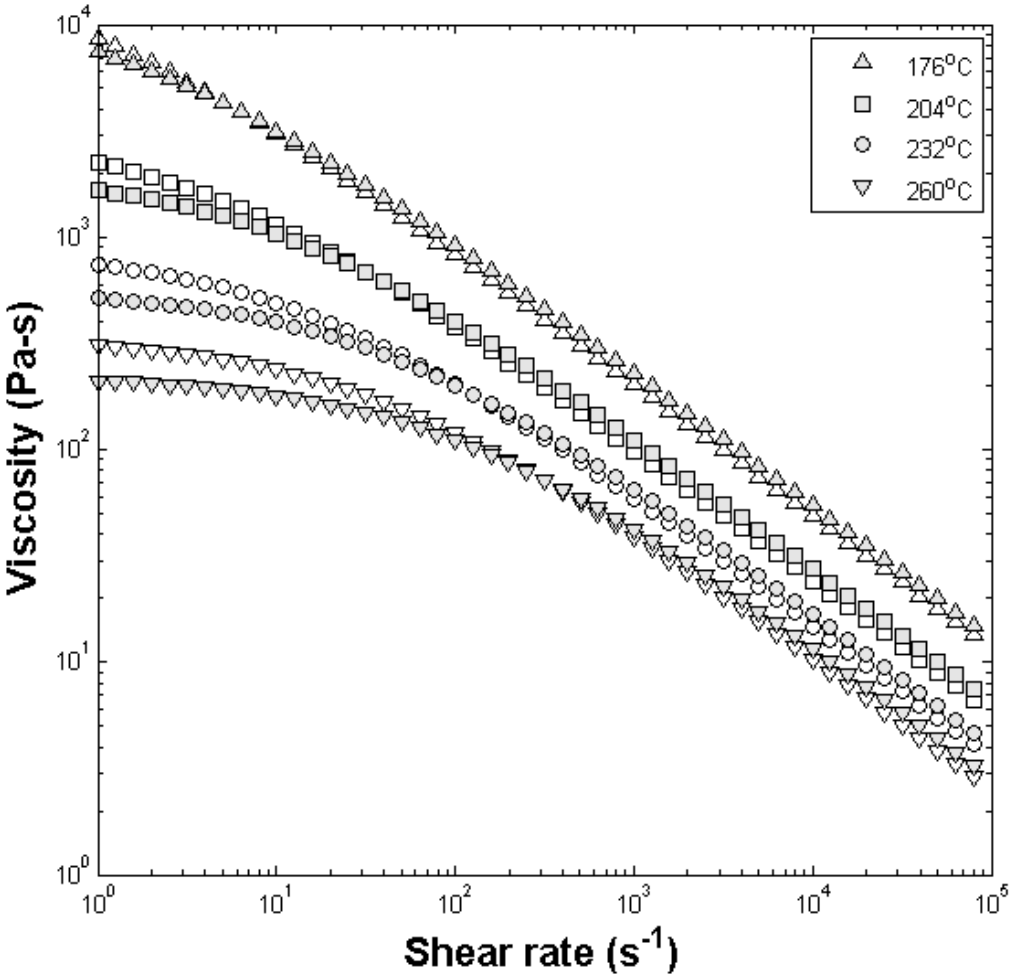

Figure 6.4: Comparison of the viscosity curves of STYRON 615 APR measured on two different types of rheometer. The open symbols represent the viscosity as found in the Moldflow database, measured by capillary rheometer. The filled symbols represent the viscosity as measured by an injection molding rheometer.

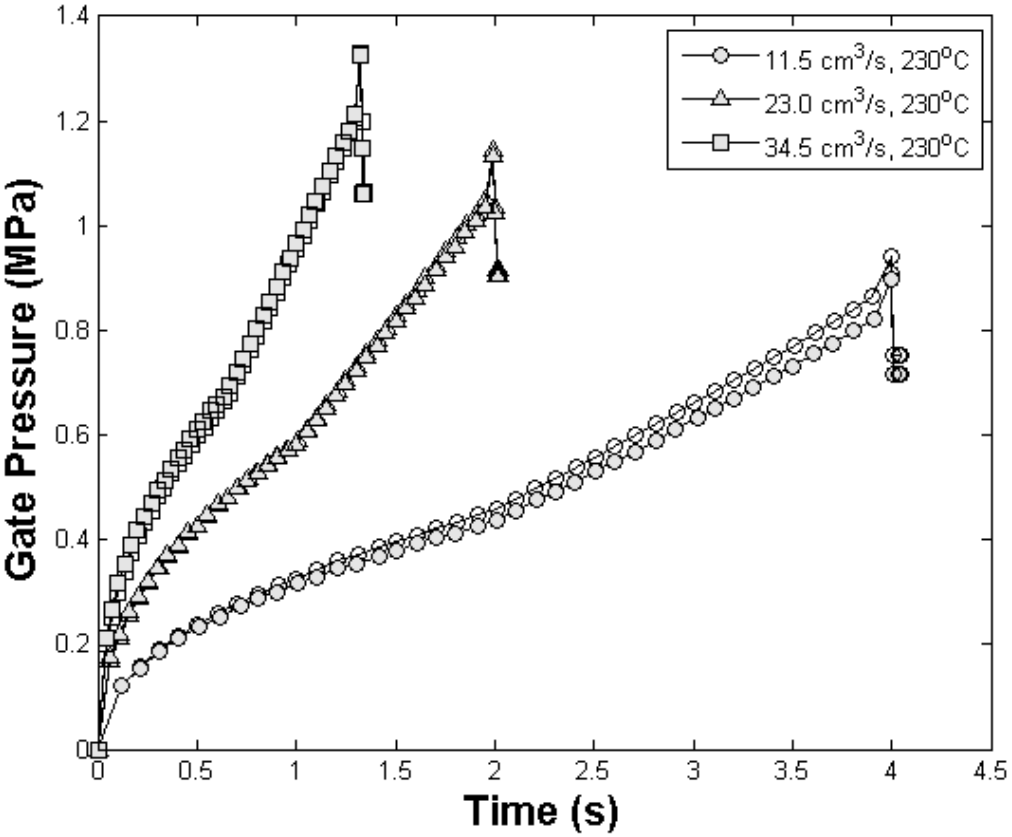

Figure 6.5: Moldflow gate pressure simulations for specimens molded at 230°C. The open symbols represent simulations using the standard viscosity data for STYRON 615 APR. The filled symbols represent simulations using the viscosity measured by an injection molding rheometer.

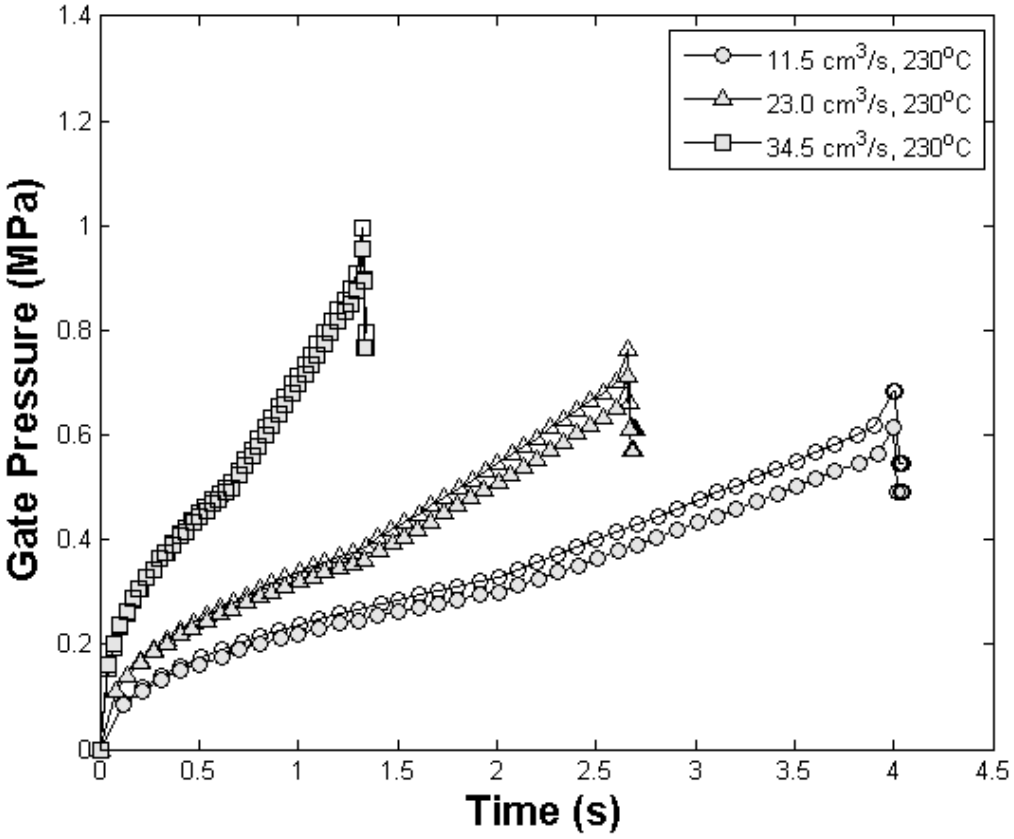

Figure 6.6: Moldflow gate pressure simulations for specimens molded at 245°C. The open symbols represent simulations using the standard viscosity data for STYRON 615 APR. The filled symbols represent simulations using the viscosity measured by an injection molding rheometer.

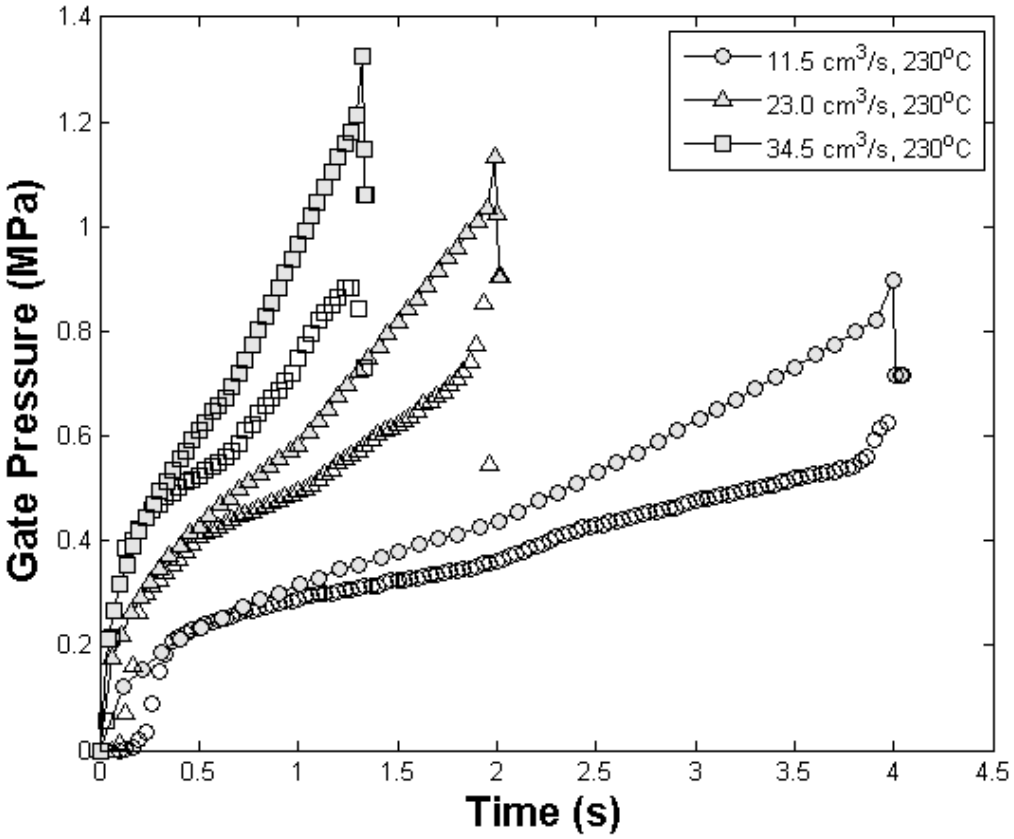

Figure 6.7: Comparison of measured gate pressures with Moldflow simulations using viscosity data from the injection molding rheometer. The data is for a melt temperature of 230°C.

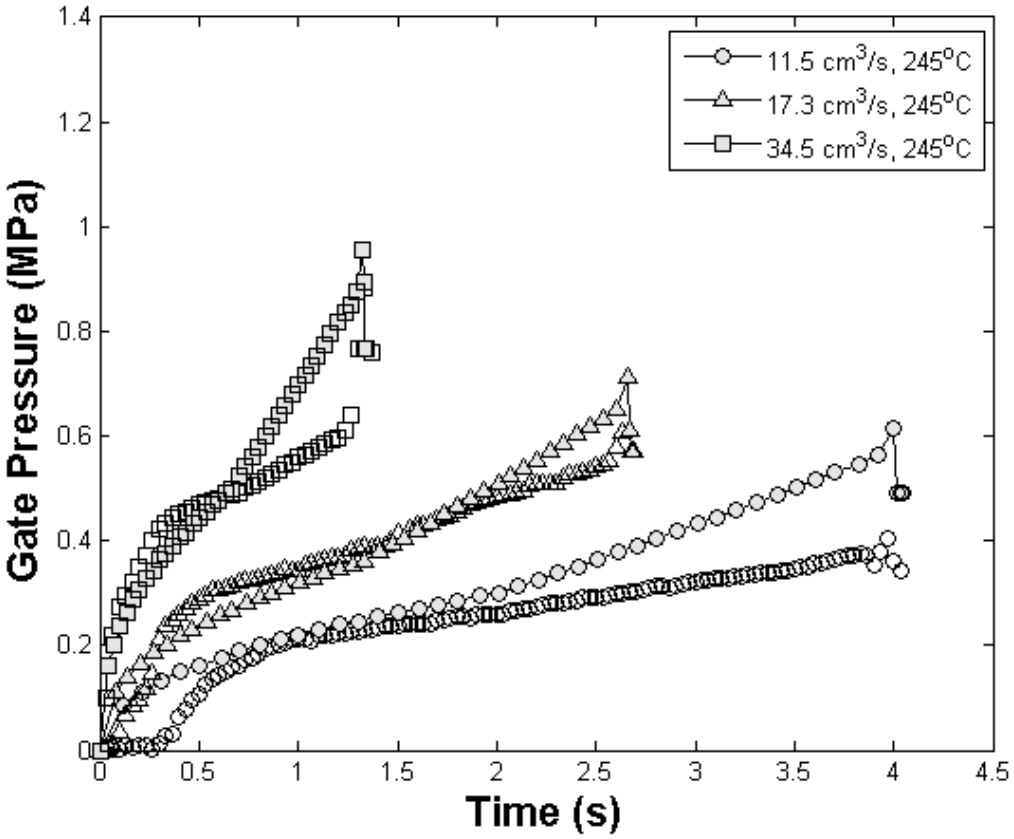

Figure 6.8: Comparison of measured gate pressures with Moldflow simulations using viscosity data from the injection molding rheometer. The data is for a melt temperature of 245°C.

6.3 Power Law Model of the Gate Pressure During the Filling Phase

Following Bird's [63] formulation, the constitutive relationship between shear stress and strain rate for a power law fluid is given in tensor form by:

$$\tau_{ij} = m\dot{\gamma}^{n-1}\dot{\gamma}_{ij} \tag{6.6}$$

where $\dot{\gamma}_{ij}$ is the rate-of-strain tensor

$$\dot{\gamma}_{ij} = \frac{\partial u_i}{\partial x_j} + \frac{\partial u_j}{\partial x_i} \tag{6.7}$$

The scalar $\dot{\gamma}$ is a function of the second invariant of $\dot{\gamma}_{ij}$:

$$\dot{\gamma} = \sqrt{\frac{1}{2}\dot{\gamma}_{ij}\dot{\gamma}_{ji}} \tag{6.8}$$

The constants m and n are the power law coefficient and exponent respectively.

The power law model has the virtue of simplicity and accuracy at high shear rates. It is not a good model for low shear rates, but this is typically not a problem for polymer processing since most relevant molding processes occur at a high rate of shear.

The power law's greatest benefit is that it can be used to provide an analytical solution to many flow problems in simple geometries. Many of these solutions can be found in Bird [63].

6.3.1 Modeling the Radial Flow Portion of the Mold Filling Process

In order to model the flow of polystyrene in the mold it is first necessary to restrict our attention to the radial flow portion of the mold filling process. By doing this we can take advantage of the solution of a standard problem, that of the radial flow of a power law fluid between parallel plates. The solution to this problem is given in

Bird [63], but the analysis is left to the reader. The basic approach to the problem is to first solve the simpler problem of the one-dimensional pressure-driven flow of a power law fluid between parallel plates. Then the lubrication approximation is made to apply this solution locally to radial flow between parallel plates. The velocity profile is then integrated to relate the flow rate to the pressure drop, power law parameters and mold geometry. The steps in this analysis are detailed in Appendix C. The final result of the analysis, Equation C.21, is the following:

$$Q_\circ = \frac{4\pi B^2}{(1/n)+2}\left[\frac{(P_1-P_2)B(1-n)}{m(R_2^{1-n}-R_1^{1-n})}\right]^{1/n} \tag{6.9}$$

where m and n are the power law coefficient and exponent respectively and B is the half-height of the cavity. The subscripts 1 and 2 refer to two different points of interest in the cavity, with P the pressure at these points and R the radial distance from the origin of the flow. The circle subscript on the flow rate Q is a reminder that the radial flow occurs in a full 360° arc around the source.

Let us choose point 1 to be at the origin of the radial flow. Point 2 will be used to represent the location of the flow front at a particular point in time. We can then set $R_1 = 0$, and $R_2 = R_{front}$. P_1 is equal to the pressure at the gate. The atmospheric pressure acting on the flow front is equal to P_2. This gives $P_1 - P_2 = P_{sensor}$, where P_{sensor} is the gage pressure read by the melt pressure sensor at the gate. These substitutions lead to:

$$Q_\circ = \frac{4\pi B^2}{(1/n)+2}\left[\frac{P_{sensor}B(1-n)}{mR_{front}^{1-n}}\right]^{1/n} \tag{6.10}$$

In the present work the radial flow of the polymer covers a 90° arc, so the injection rate Q is related to $Q_\circ$ by the relation $Q = Q_\circ/4$. If the injection molding machine is set to a constant volume flow rate Q and if the shot starts at time $t = 0$, mass

conservation leads to:

$$Qt \approx \frac{\pi}{4} R_{front}^2 (2B) \tag{6.11}$$

This is an approximation that assumes a flat velocity profile perpendicular to the mold with radius R_{front}. The velocity profile in reality is not flat, thus the approximation. It is good approximation, though, since the actual flow front for a power law fluid has a very broad and flat central region, minimizing the error of approximation.

Solving Equation 6.11 for R_{front} as a function of time and taking the approximation as an equality gives:

$$R_{front} = \sqrt{\frac{2Qt}{\pi B}} \tag{6.12}$$

It must be kept in mind that the flow into the corner-gated rectangular cavity is one quarter of the full radial flow assumed in Equation 6.10. This gives:

$$Q = \frac{Q_\circ}{4} = \frac{\pi B^2}{(1/n)+2} \left[\frac{P_{sensor} B(1-n)}{m R_{front}^{1-n}} \right]^{1/n} \tag{6.13}$$

Substituting the expression for R_{front} from Equation 6.12 into Equation 6.13 gives

$$Q = \frac{\pi B^2}{1/n+2} \left[\frac{P_{sensor} B(1-n)}{m} \left(\frac{\pi B}{2Qt} \right)^{\frac{1-n}{2}} \right]^{1/n} \tag{6.14}$$

Solving this equation for P_{sensor} gives

$$P_{sensor} = \frac{m}{B(1-n)} \left[\frac{Q(1/n+2)}{\pi B^2} \right]^n \left[\frac{2Qt}{\pi B} \right]^{\frac{1-n}{2}} \tag{6.15}$$

Since m, n, B, and Q are constant for any given shot we have:

$$P_{sensor} \propto t^{\frac{1-n}{2}} \tag{6.16}$$

If a plot is made of $\log P_{sensor}$ vs $\log t$, the result should be a straight line with slope of $(1-n)/2$. Equation 6.15 can also be used to calculate the power law coefficient. According to this equation the intercept of the $\log P_{sensor}$ vs $\log t$ plot would be:

$$\log \left\{ \frac{m}{B(1-n)} \left[\frac{Q(1/n+2)}{\pi B^2} \right]^n \left[\frac{2Q}{\pi B} \right]^{\frac{1-n}{2}} \right\} \tag{6.17}$$

Since Q and B are known and since n can be calculated from Equation 6.16 the only remaining unknown in the above expression is m.

Another way to calculate m and n from the pressure data is to fit Equation 6.15 directly to the data. This approach was taken using MATLAB to perform an unconstrained nonlinear optimization using the function `fminsearch`. The pressure data from the two 34.5cm^3/sruns were used. These runs had the highest recorded gate pressures and showed the least ill-effects from the pressure sensor low-pressure sensitivity issue. In particular, these runs had little or no "dead zone" at the beginning of the run. Equation 6.15 makes no allowance for a dead zone, the pressure begins to rise immediately. The presence of a dead zone in the data makes it impossible to fit the data to Equation 6.15.

Even without the dead zone, though, the data points at the very beginning of the 34.5cm^3/s runs are still suspect since they have the lowest pressure values and hence the highest errors. To avoid biasing the nonlinear optimization the first four points of the two data sets were removed from consideration. The data points in the radial flow regime were used for the optimization up to the point t^*=0.5, a time of

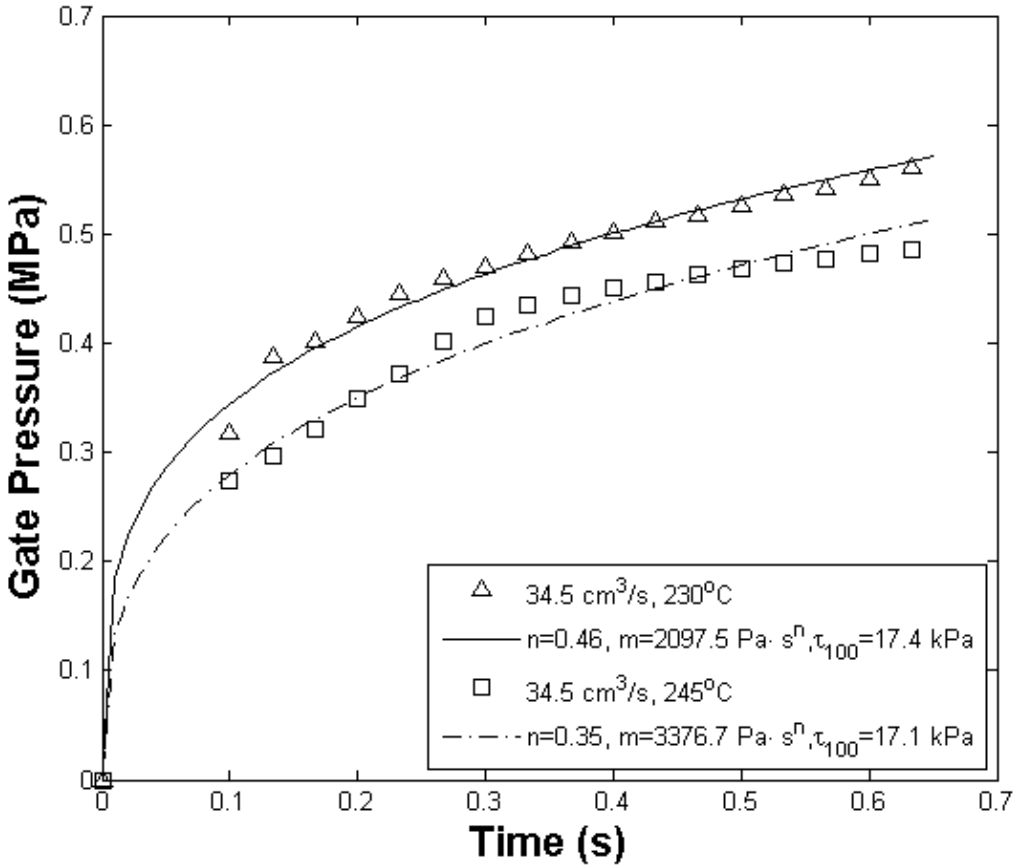

Figure 6.9: Averaged gate pressures as a function of time for the radial portion of the filling flow for specimens molded at the highest flow rate. The best fit curves using Equation 6.15 are also shown. The best-fit values of n and m for each curve are noted in the legend.

0.65 seconds for these two runs. The data points used and the resulting curve fits are shown in Figure 6.9.

The extracted power-law parameters for the two data sets, as well as for the capillary rheometer data presented in Chapter 2, are shown in Table 6.2. The mean value of the shear-thinning exponent n was 0.4063, within 0.4% of $n = 0.4079$ measured from the rheometer data. The mean reference stress was 17.25 kPa, within 14%

While it is natural to compare values of n computed from different data sets, comparing values of m is more problematic. Reiner [106] points out that since the

Table 6.2: Values of n, m, and τ_{100} extracted from the 34.5 cm^3/s gate pressure data. The reference stress τ_{100} is the stress calculated from the given power-law parameters at a reference strain rate of 100 s^{-1}. The "mean" value of m is the reference value m_{100} defined in Equation 6.18. The row labeled "Rheometer" contains the constants extracted from the capillary rheometer data shown in Figure 2.3.

.

	n	m (Pa·s^n)	τ_{100} (kPa)
230°	0.4600	2097.5	17.4
245°	0.3526	3376.7	17.1
Mean	0.4063	2659.4	17.25
Rheometer	0.4079	2940.6	20.14

units of m depend on n the values of m for different shear thinning exponents cannot be compared directly. It also means that since the value of n extracted from the pressure data has error attached to it, the dimensions of m become uncertain. Direct comparison of values of m is senseless. A way around this difficulty is to choose a reference shear rate. For each data set a value of n may be extracted and then the shear stress at that reference shear rate can be calculated. The values of the shear stresses at the reference shear rate can then be compared. Observed differences in the shear stress will be due in part to differences in m.

For the purposes of the present work a reference shear rate of 100 s^{-1} was chosen, a shear rate typical of injection molding processes. Using this shear rate and the values of n and m shown in Table 6.2 the reference shear stress τ_{100} was calculated. This stress had a mean of 17.25 kPa for the two 34.5cm^3/s runs, within 14% of the 20.1 kPa calculated using the values of n and m extracted from rheometer data.

Given the reference strain rate $\dot{\gamma}_{100} = 100\ s^{-1}$ and the mean values of n and τ_{100}, a reference value of m can be calculated:

$$m_{100} = \frac{\tau_{100}}{\dot{\gamma}_{100}^{n}} \tag{6.18}$$

This results in m_{100}=2659.4 Pa·s , a value within 9.5% of the value of m calculated from the rheometer data.

6.3.2 Modeling the Channel Flow Portion of the Mold Filling Process

The radial flow portion of the mold filling process ends when the flow front contacts the wall opposite the gate. After a short transition period the flow front shape becomes fairly constant and the front moves across the mold at a constant rate. The rate of pressure increase during this channel flow portion of the mold filling is linear as shown in Figure 6.1.

This linear rise can be explained as follows. For comparison, consider a duct flow of a generalized Newtonian liquid. A generalized Newtonian liquid is one for which $\eta = f(\dot{\gamma})$. For a steady flow with constant flow rate Q the pressure gradient must also be constant.

The channel flow portion of the mold filling is very similar to the duct flow. The flow rate Q is held constant by the injection molding machine controller. The main difference in the mold filling is the presence of the flow front. But since the front shape is fairly constant and moves at constant rate the flow can be treated as quasi-steady. In order to maintain the constant flow rate the pressure gradient must also be constant.

The pressure gradient can be estimated as follows:

$$\frac{dp}{dx} \approx \frac{\Delta P}{\Delta x} \approx \frac{P_{front} - P_{gate}}{x_{front} - x_{gate}} = K \tag{6.19}$$

where K is a constant. Taking the pressure at the front to be zero and the position of the gate to be zero gives

$$\frac{dp}{dx} \approx -\frac{P_{gate}}{x_{front}} = K \tag{6.20}$$

But during the channel flow the front moves at an average speed of $Q/2BW$, where Q is the injection flow rate and $2BW$ is the cross-sectional area of the cavity. Thus

$$x_{front} = \frac{Q}{2BW}t + c \tag{6.21}$$

where c is a constant. So:

$$P_{gate} = -Kx_{front} = -K\left(\frac{Q}{2BW}t + c\right) \tag{6.22}$$

where W is the width of the channel in the z direction and B is the channel half-thickness. This equation predicts that the the pressure will rise linearly with time during the channel filling process.

Up to this point the argument has been applicable to any generalized Newtonian fluid. To estimate the rate of pressure rise the constant K must be determined, and this depends on the type of fluid used. Appendix C gives the derivation of the volume flow rate of a power-law fluid in a channel:

$$Q = \frac{2WB^2}{\frac{1}{n}+2}\left[-\frac{B}{m}\frac{dP}{dx}\right]^{1/n} \tag{6.23}$$

Thus the constant K is determined as

$$\frac{dp}{dx} = K = -\frac{m}{B}\left[\frac{Q\left(\frac{1}{n}+2\right)}{2WB^2}\right]^n \tag{6.24}$$

Using Equation 6.22, the estimated rate of pressure rise during the channel flow portion of the mold filling of a power-law fluid is given by

$$\frac{dP_{gate}}{dt} = \frac{Qm}{2WB^2}\left[\frac{Q\left(\frac{1}{n}+2\right)}{2WB^2}\right]^n \tag{6.25}$$

Equation 6.25 was used on the 230°C pressure traces in conjunction with the values of $n = .41$ and $m = 2941$ extracted from Figure 2.3. Since the data in Figure 2.3 was taken at 230°C, and since the value of m is a function of temperature,

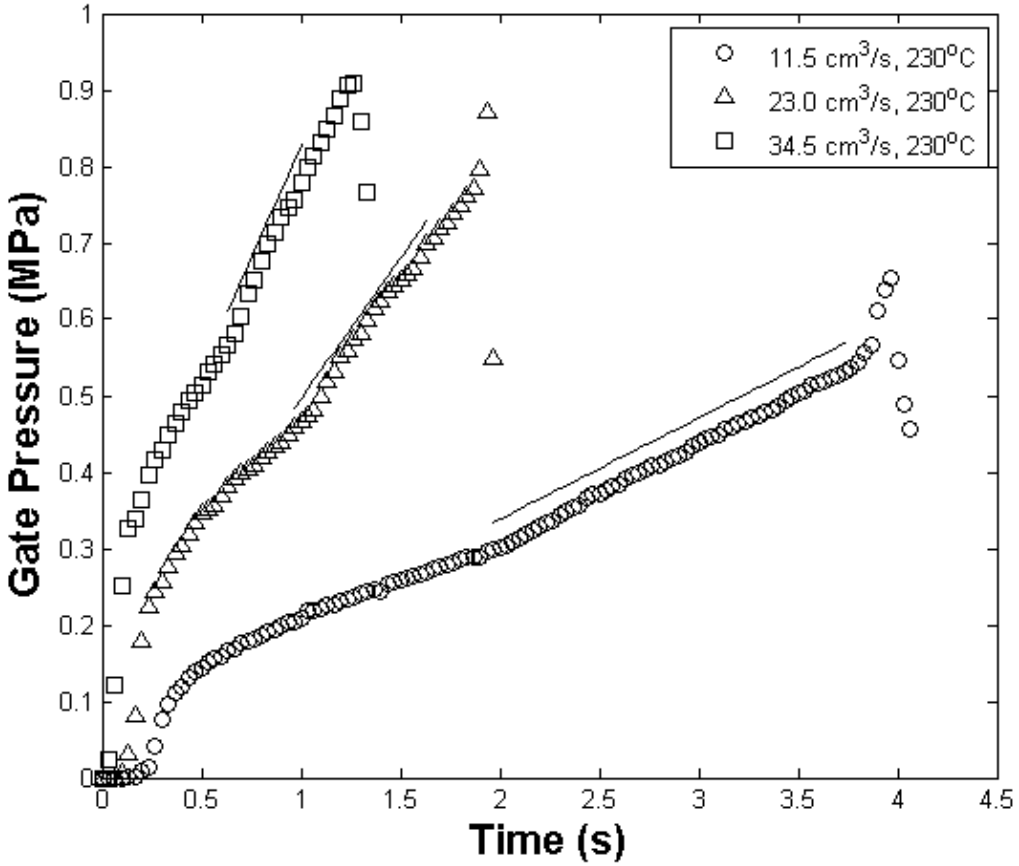

Figure 6.10: Predicted slopes of the 230°C pressure traces in the channel flow regime. The slopes were predicted using Equation 6.25 and the values of $n = .41$ and $m = 2941$ Pa·s^n extracted from Figure 2.3.

only the 230°C pressure traces were analyzed. The result of this analysis is shown in Figure 6.10. The predicted and actual slopes from this figure are summarized in Table 6.3. The comparison between predicted and actual slopes is quite good. Since the channel flow regime has a higher gate pressure than the radial flow regime the pressure sensor issues do not come into play.

Table 6.3: Slopes of the pressure traces during the channel flow portion of the filling phase. The slopes were predicted using Equation 6.25 and the values of $n = .41$ and $m = 2941$ Pa·s^n extracted from Figure 2.3.
.

Flow rate (cm^3/s)	Predicted slope (MPa/s)	Actual slope (MPa/s)	Deviation
11.5	0.0990	0.1104	12%
23.0	0.2610	0.2927	12%
34.5	0.5047	0.5176	3%

6.4 On the Non-Newtonian Fluid Dynamics of the Polymer Melt

The results of Chapter 5 showed that the polymer melt flow in the optical access mold scaled linearly with injection rate. No interesting non-Newtonian flow artifacts were observed. It could therefore be said that the fluid kinematics of the melt flow behaved in a Newtonian fashion.

However, the results of Section 6.3.1 and Section 6.3.2 show that the behavior of the pressure at the gate can be convincingly modeled as that of a shear-thinning power-law fluid. Both the radial flow and channel flow regimes of the mold filling process show shear-thinning power-law behavior. It could therefore be said that the fluid dynamics of the melt flow behaved in a non-Newtonian fashion.

This pattern of Newtonian kinematics paired with non-Newtonian dynamics is not uncommon in non-Newtonian fluid mechanics [63], particularly for second-order fluids. A second-order fluid is one whose constitutive relation relies upon only the rate of strain tensor $\dot{\gamma}_{ij}$ and its first contravariant convected derivative [63]. At small Deborah numbers the model recovers Newtonian behavior.

The three-dimensional flow theorem of Giesekus [107] states that a velocity field that satisfies the equations for creeping flow of an incompressible Newtonian fluid will also satisfy the equations for the creeping flow of a second-order fluid but with

a different pressure field. The plane-flow theorem of Tanner and Pipkin [73] is similar and applies to the creeping plane flow of an incompressible second-order fluid. Tanner [108] later examined the extension of these Giesekus-like theorems to other non-Newtonian flows.

The polymer melt studied in the present work cannot be modeled as a second-order fluid since second-order fluids have constant viscosity [63] and polystyrene shows marked shear-thinning. But the fact that in this study the polystyrene melt exhibits Newtonian fluid kinematics and non-Newtonian dynamics is not unprecedented.

6.5 A Proposal for the Quality Control of Polymers

Rheology in a laboratory and rheology on the plant floor are two different beasts entirely. A good comparison of these two methodologies is given by Dealy and Wissbrun [62]. They point out that laboratory-based rheology is typically aimed at measuring well-defined physical properties or material functions, such as the viscosity curve and the storage and loss moduli. The goal is to make measurements that are independent of the testing equipment, measurements of properties that are particular to the material itself.

Industrial rheology is mainly concerned with tests that simulate the molding process. The two goals of industrial rheology are quality control and the determination of processability. Industrial tests do not typically measure properties of the polymers tested, but rather give an indication of how the polymer will perform in a given mold. Repeatability of the results of these tests using different batches of a polymer indicate that the polymer is consistent from batch to batch. Comparison of the results of the same test with two different polymers may indicate which polymer would fill a given

mold on the plant floor more readily. By their very nature such tests are equipment- and process-dependent. Two of the most popular industrial rheology tests are the melt flow index test and the moldability test. Dealy [109] describes other empirical tests, such as testing the melt strength during fiber drawing, measurement of extrudate swell, generating squeezing flows in a parallel plate plastometer, and mixing tests using torque rheometers. These tests are most often used in processes that have a considerable extensional flow component. Since the melt flow index and the moldability test are two of the most prevalent tests for injection molding applications these tests will be considered in detail.

6.5.1 The Melt Flow Index

The melt flow index is a quantity described and regulated by ASTM D1238-04c [110]. A melt flow indexer is basically a primitive capillary rheometer. A polymer sample is forced through a capillary tube by a weight-driven piston. The flow rate of the polymer through the capillary is the melt flow index.

Obviously the melt flow index is related to the viscosity of the polymer. The problem is that the melt flow index itself is not sufficient for measuring the true viscosity, only an apparent viscosity. The quantities measured are not sufficient for calculating the end correction or the Rabinowitsch correction necessary for determining the true viscosity [62]. The Rabinowitsch correction needs the rate of change of the psuedo-shear rate with respect to the wall shear stress, as pointed out by Brodkey [64]. End effects are even harder to correct. As Brodkey [64] points out, end effects are best eliminated by using capillaries with large L/d ratios. The viscosity of polymers is so high, though, that the only way to pump them through a capillary with a reasonably low pressure gradient is to use capillaries with small L/d ratios.

So end effects cannot be eliminated from the measurement of the melt flow index.

Another serious limitation of the melt flow index is that it is a single point test. Even if the test could measure the true viscosity, it would only make the measurement at one particular rate of shear. Even worse, that rate of shear is orders of magnitude smaller than the shear rates experienced by the polymer during injection molding.

6.5.2 The Moldability Test

The moldability test is an empirical test of a polymer's ability to fill a mold. The polymer is placed in an injection molding machine and is injected into a mold with a long flow path typically in the form of a spiral [62]. Other popular geometries include disks, snakes and bars. The result of the test, the moldability index, is simply the distance the polymer travelled before solidifying. The further the travel, the more easily flowing the polymer. ASTM D3123-98(2004) [111] describes a spiral mold test for thermosets at low injection pressures, but there is no universal standard for thermoplastics.

Again, the viscosity is obviously related to the moldability index. But in this test the relationship between the true polymer viscosity and the result of the test is even murkier than for the melt flow index. The result is highly dependent on the molding parameters and mold geometry as well as the viscosity of the polymer.

6.5.3 A Proposal

The viscosity of a polymer is the dominant factor in determining its moldability. The melt flow index gives an approximation of the viscosity, but it is difficult to apply the result to a real mold on the factory floor. The moldability index is more applicable to real situations, but is a complex function of material parameters, molding conditions, and mold geometry. Perhaps there is a middle way that combines

the appealing qualities of both tests: measurement of the viscosity in a way that is applicable to actual injection molding conditions.

The analysis given in this chapter can be used as this middle way. Use of an optical access mold with a laser to measure Carreau model parameters is not recommended for industrial purposes, but this chapter has demonstrated that a measurement of the power law parameters of a polymer can be carried out with a radial flow mold and a pressure sensor if the test is carried out under the right conditions.

Consider a mold designed to produce radial flow from the gate. There are a number of possible geometries that could be used. For example the mold cavity could be a disk with a centrally located sprue. The problem with this is that the cavity would be larger than it needs to be since a full 360° radial flow is not necessary. The cavity could be rectangular with the gate near the corner as described in Chapter 2. This results in a smaller cavity. The problem with a rectangular cavity is that the flow is only radial for a portion of the filling process. A third possibility would be to make the cavity a sector of a circle with the gate near the corner as shown in Figure 6.11. This would combine the benefits of both a circular cavity and a rectangular cavity, giving a radial flow field over the entirety of the flow and minimizing the amount of polymer consumed in each shot. The hatched circle in the figure represents the location of the pressure sensor. The sensor is directly below the injection location, with the polymer entering the cavity perpendicular to the plane of flow. The cavity could also be constructed in such a way that the polymer entered parallel to the plane of flow, as shown in Figure 6.12. This design is not recommended, though, as the polymer would be prone to jetting across the cavity. Placing the gate perpendicular to the cavity causes the polymer to contact the opposite wall quickly and leads to a smoother fill of the mold.

Consider Equation 6.9. For the radial flow of a power law fluid in which the lubrication approximation is valid the flow rate is a function of the pressure gradient, the power law parameters and the geometry of the cavity. Keeping the flow rate constant results in Equation 6.16. Thus the pressure trace alone can be used to estimate the power law exponent and coefficient.

Of the two parameters, the power law exponent is more robust. The power law coefficient is more sensitive to temperature and is thus sensitive to shear rate as well, since higher shear rates lead to higher temperatures in the melt. It is interesting to note that if the power law exponent is the only desired quantity, then the measurement itself is very robust. Note that Equation 6.16 is independent of the flow rate and the cavity thickness. This measurement is even independent of the calibration of the pressure sensor. If we assume that the pressure sensor is properly zeroed and that it produces a voltage proportional to the pressure then we have:

$$V_{sensor} \propto P_{sensor} \propto t^{\frac{1-n}{2}} \tag{6.26}$$

A log-log plot of the voltage trace vs. time will have the same slope as the log-log plot of the pressure vs. time and can thus be used to determine n. The measurement of the power law coefficient, though, requires knowledge of the flow rate, the cavity thickness and the pressure sensor calibration constant.

So, a radial flow mold with a pressure sensor at the origin of flow is sufficient for determining the power law representation of the polymer for a given melt temperature. This gives it the appealing virtue of being directly related to the viscosity, much like the melt flow index.

As stated in Section 6.5.2, disk cavities are a popular choice for moldability tests. If the cavity radius in this proposed test is larger than the expected radial travel of the

polymer before solidifying, then the test could also be used to judge the moldability of the polymer. The outcomes of the test would be the pressure trace (from which the power law parameters would be extracted) and the radius of the solidified part. This would combine the best aspects of both the melt flow index and the moldability tests into a single test, all for a cost comparable to that of a standard moldability test.

This test does not appear in the literature and is claimed to be original to this work. A review of periodical databases and ASTM standards turned up no references to this kind of test. Furches [112] considered rheological quality control tests for ABS resins in 1989 but did not mention anything like this proposal. More convincingly, Dealy [109] published a book on rheology and its role in plastics quality control in 2000. The entire book deals with the subject of rheology in the lab and on the plant floor as used for quality control. No mention of this kind of test was found in this work.

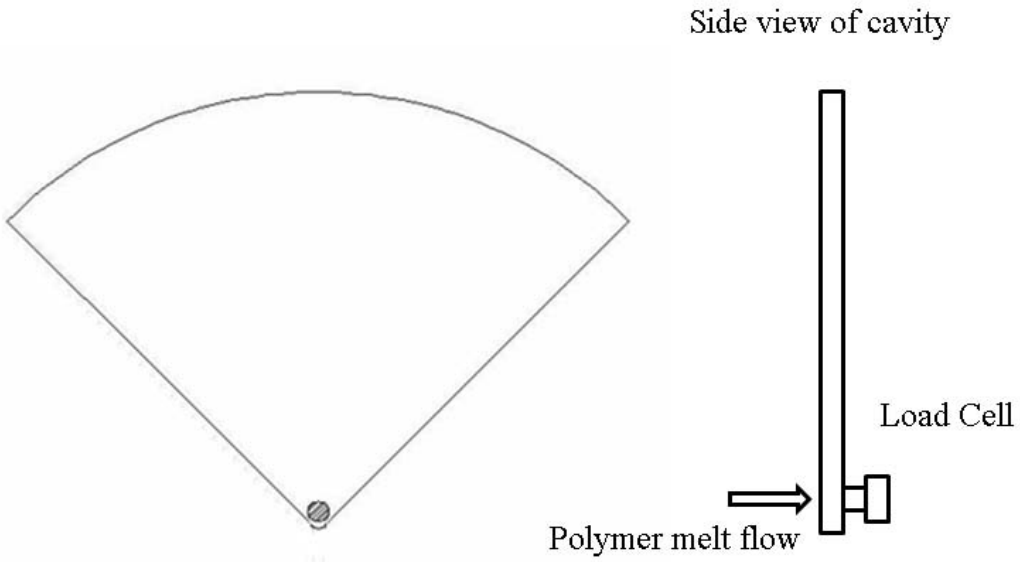

Figure 6.11: Proposed cavity geometry for polymer quality control. The hatched circle indicates the location of the pressure sensor. The gate is at the corner of the 90° arc with the plastic entering the cavity perpendicular to the pressure sensor, as shown in the side view. The radius is large enough to ensure that the mold will not fill during the test.

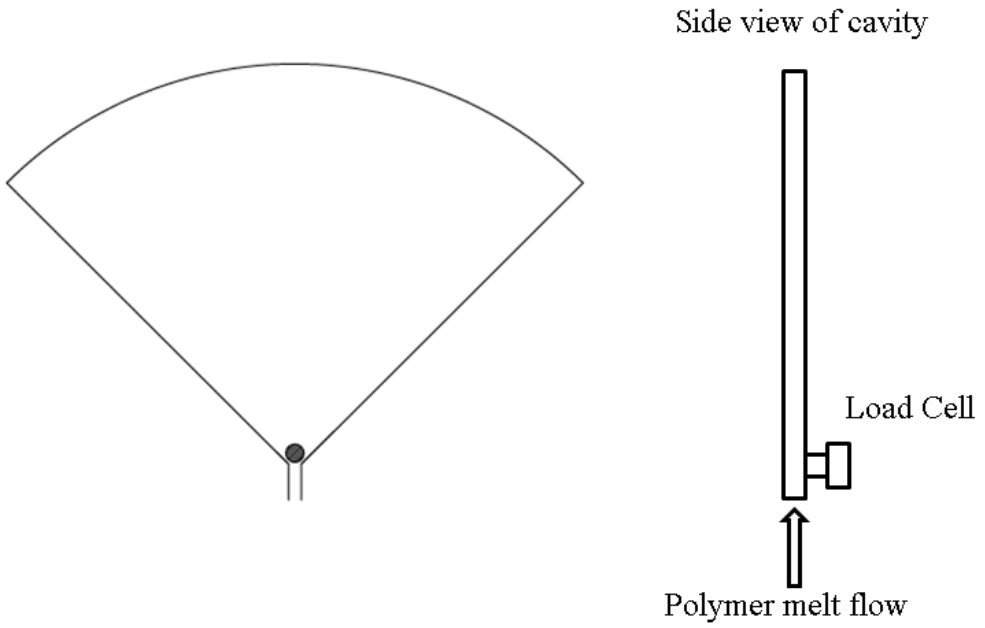

Figure 6.12: Proposed cavity geometry for polymer quality control. The hatched circle indicates the location of the pressure sensor. The gate is at the corner of the 90° arc with the plastic entering the cavity parallel to the pressure sensor, as shown in the side view. The radius is large enough to ensure that the mold will not fill during the test.

CHAPTER 7

Polymer Melt Flow During Packing

Molten polymers shrink during solidification, defeating the goal of making parts that match the mold cavity shape. This phenomena is known as *shrinkage*. To combat shrinkage liquid plastic is packed into the mold after the filling phase is complete. The pressure in the mold rises rapidly during the packing stage. This high pressure is maintained in the holding phase. Fluid enters the mold slowly during this phase until the gate solidifies, isolating the mold cavity from the pressure being applied to the melt by the screw in the barrel of the injection molding machine.

The goal of this portion of the present work is to study the flow during the packing phase. In some ways this flow is easier to study than the flow during the filling phase:

- The flow is slower. This effectively increases the time resolution of the PIV analysis since the ratio of the time scale of the flow to the frame rate of the camera is increased. This also ameliorates the problem of resolving PIV vectors near the gate. A slower flow rate leads to a smaller dead zone around the gate.

- There is no flow front. This simplifies the analysis greatly. Image masks are no longer necessary for the PIV analysis as described in Section 4.3. Calculation of the velocity gradients, as described in Section 4.5.1, is also easier without a flow front. The digital images of the flow are also improved because the

absence of a front leads to a more uniform illumination of the flow, eliminating the "searchlight" problem described in Section 3.1.4.

In other ways the packing flow is harder to study:

- The melt pressure is much higher. This puts more stress on the glass windows in the optical access mold and can lead to glass breakage. Even if the glass does not break, higher pressures can cause polymer leakage out of the mold, known as *flash*.

- The flow is no longer two-dimensional. Unlike the filling process, there is no theoretical reason for the flow at the midplane to stay at the midplane.

7.1 Molding Conditions

The specimens used in this study were all molded with an injection rate of 11.5 cm^3/s and a melt temperature of 245° C. The specimens had nominal packing pressures of 11.0 MPa, 16.5 MPa and 27.6 MPa. The packing pressure applied for five seconds, followed by an identical holding pressure for five seconds. The actual pressure at the gate of the mold cavity as a function of time was beyond the control of the operator. Only the nominal packing pressure could be specified. The actual pressure trace was a function of the injection molding machine's internal hydraulic control system. Solidification at the gate also influenced the pressure measured at the gate.

Five specimens were made sequentially at each condition and the results averaged for the pressure traces and PIV data presented in this chapter. The averaged gate pressure traces for the three different packing levels are shown in Figure 7.1.

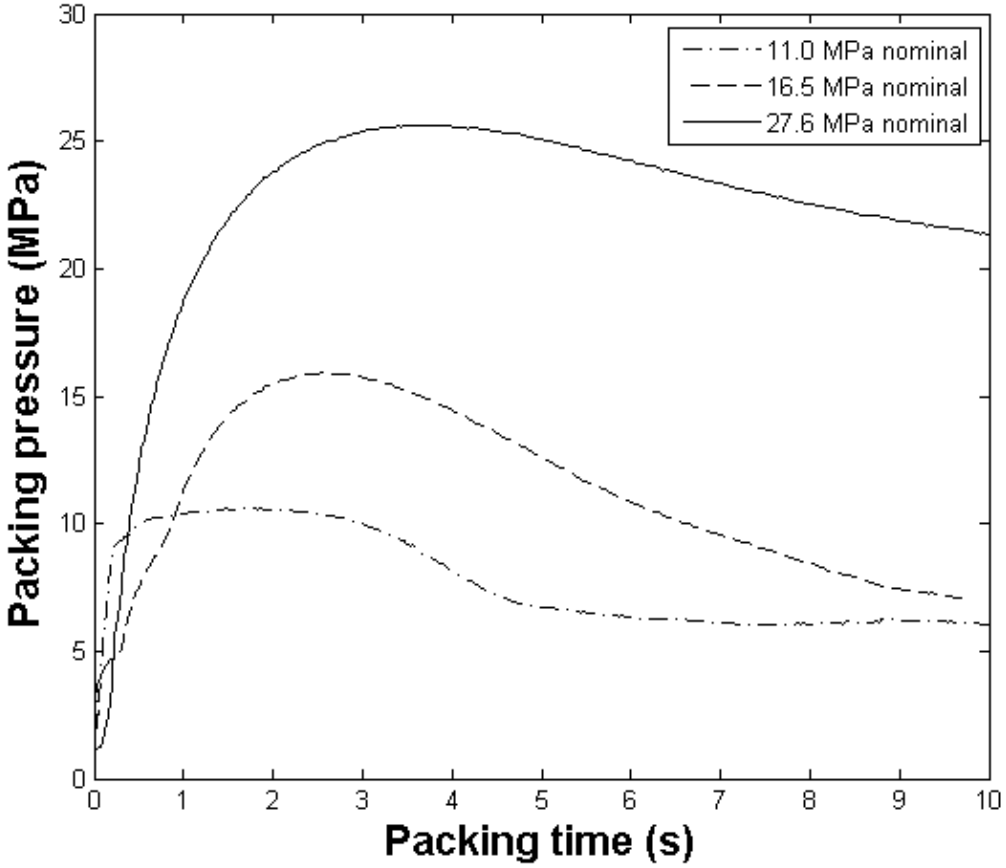

Figure 7.1: Measured gate pressure as a function of time for nominal constant packing pressures of 11.0 MPa, 16.5 MPa, and 27.6 MPa.

7.2 PIV Results for Flow During the Packing Phase

PIV measurements of the packing flow were produced with the same experimental setup described in Chapter 2. The image processing followed the same steps outlined in Chapter 4 with the following exceptions. Since there was no flow front present during the packing phase all steps related to the manual extraction of flow fronts and calculation of flow front propagation velocity vectors were omitted. The binary image masks were created solely from the cavity outlines.

The PIV processing was identical to the that described in Chapter 2. It was found that the PIV vector fields were much more complete than those of the filling study. This was possibly due to the fact that the illumination was more even due to the lack of a flow front, and to the fact that the flow was much slower than that of the filling phase. The character of the flow was more constant than that of the filling phase as well. In the filling phase the character of the flow changed as the flow front contacted the cavity walls. This was not an issue for the packing flow.

Since the PIV vector fields did not have the vector dropout problems shown in Figure 4.10 no median filtering was performed. The fields were averaged, however, to present the mean flow fields observed during the packing phase.

7.2.1 Estimating the Volume Flow Rate During Packing Flow

In the filling phase the flow is driven by the injection rate Q set by the operator. In the packing phase the flow rate is not set directly by the operator, but indirectly through the packing pressure. Since the packing flow rate is not known directly a different metric was required.

The packed specimens were weighed after they had solidified. The average masses of the packed specimens are given in Table 7.1. The difference between the mass of the

Table 7.1: Average mass of specimens molded at different packing pressures. The overall packing flow rates are also listed, calculated using Equation 7.5.

Packing pressure (MPa)	Specimen mass (g)	ΔM (g)	Packing flow rate (cm^3/s)
Unpacked	50.2	-	-
11.0	51.0	0.8	0.16
16.5	51.3	1.1	0.22
27.6	53.9	3.7	0.74

packed specimens and mass of the unpacked specimens is an indicator of the amount of flow that took place during the packing phase. As the specimens solidified in the mold a volume change took place. The freed volume was then taken up by polymer melt entering the gate at the nominal melt temperature and packing pressure. If the melt density were known it could be used in conjunction with the specimen mass differentials to calculate the overall melt volume flow rate during the packing phase.

The Tait equation is often used as an equation of state for polymer melt calculations [113] and it was used to calculate the melt density during packing. Using the implementation of the Tait model found in Moldflow:

$$v(T,p) = v_0(T)\left(1 - 0.894\ln\left((1 + \frac{p}{B(T)}\right)\right) \tag{7.1}$$

where v is the specific volume of the melt. The functions $v_0(T)$ and $B(T)$ are given by

$$v_0 = b_1 + b_2\bar{T} \tag{7.2}$$

$$B = b_3\exp(-b_4\bar{T}) \tag{7.3}$$

$$\bar{T} = T - b_5 \tag{7.4}$$

The constants b_1 through b_5 for STYRON 615 APR as found in the Moldflow material database are given in Table 7.2.

Table 7.2: Material specific constants for the Tait model. The following values are taken from the Moldflow database for a STYRON 615 APR melt.

b_1	0.000972 m^3/kg
b_2	6.042e-7 m^3/kg-K
b_3	1.85917e8 Pa
b_4	0.004927 1/K
b_5	376.81 K

The Tait model was used to calculate the melt density ρ_m as a function of packing pressure and melt temperature. The duration of the packing phase, t_p, was set at five seconds The magnitude of the packing flow was close to zero by this time, as will be shown in Section 7.2.4. Using the mass differential ΔM, the melt density ρ_m and the packing phase duration t_p a packing flow rate Q_p was calculated:

$$Q_p = \frac{\Delta M}{\rho_m t_p} \tag{7.5}$$

7.2.2 Scaling the Velocity Divergence For Packing Flow

In the packing flow the melt is compressible and solidifying, so in general $\nabla \cdot \vec{v} \neq 0$. The divergence at each point of the velocity field can still be calculated, but it is now not purely an error term as it was during the filling flow. Non-zero residuals are to be expected, but it is impossible to separate the legitimate residual due to compressibility and solidification from numerical error.

The packing flow rate Q_p can be used to scale the divergence residual ε described in Equation 4.7

$$\varepsilon^* = \frac{V_I \varepsilon}{Q_p} = \frac{V_I \rho_m t_p \varepsilon}{\Delta M} \tag{7.6}$$

where V_I is the interrogation volume. Just as in Figures 5.1-5.12 this scaled divergence residual was overlaid as a pseudocolor plot on the PIV vector fields.

7.2.3 Polymer Melt Velocity Fields During Packing Flow

The PIV vector plots for the packing flow are presented here. Since the duration of the packing flow is not known ahead of time, the fields will not be presented in terms of a nondimensional time t^* as in Figures 5.1-5.12. Here the results are presented at half-second increments of time during the packing phase. Two other plotting conventions are different as well. The scale on the colorbars is much larger to match the larger velocity divergences seen during the packing flow. The vectors themselves are also presented at full scale. This makes them look large in comparison to the filling vector fields, where the vectors were scaled down by a factor of ten for clarity in plotting. The packing velocity vectors are much smaller in magnitude and do not need to be scaled down for ease of plotting.

The PIV vector fields paint an interesting picture of the packing flow. The flow decays rapidly and shows a shrinking radius of effect as the packing time increases. There is also a high amount of variability as shown by the velocity divergence. Alternating blocks of positive and negative divergence dominate the lower edge of the cavity. Since these are averaged fields, the lower edge hot spots are likely the result high variability among the individual fields in those areas. This is supported by Figure 7.11. In this figure the pseudocolor overlay represents the sums of the variances of the u and v components of the five velocity fields the average field is drawn from. The variance of the velocity vectors is very high along the bottom wall.

One possible explanation for this is that the bottom wall is the wall with the gate. The flow along this wall stays parallel to the wall for the entire filling process and represents the area of the flow field with the most consistent shear history. The molecular orientation is likely highest along this wall, as is evidenced by the birefringence photos in Figures 8.2-8.9. As pointed out in Chapter 8, the orientation

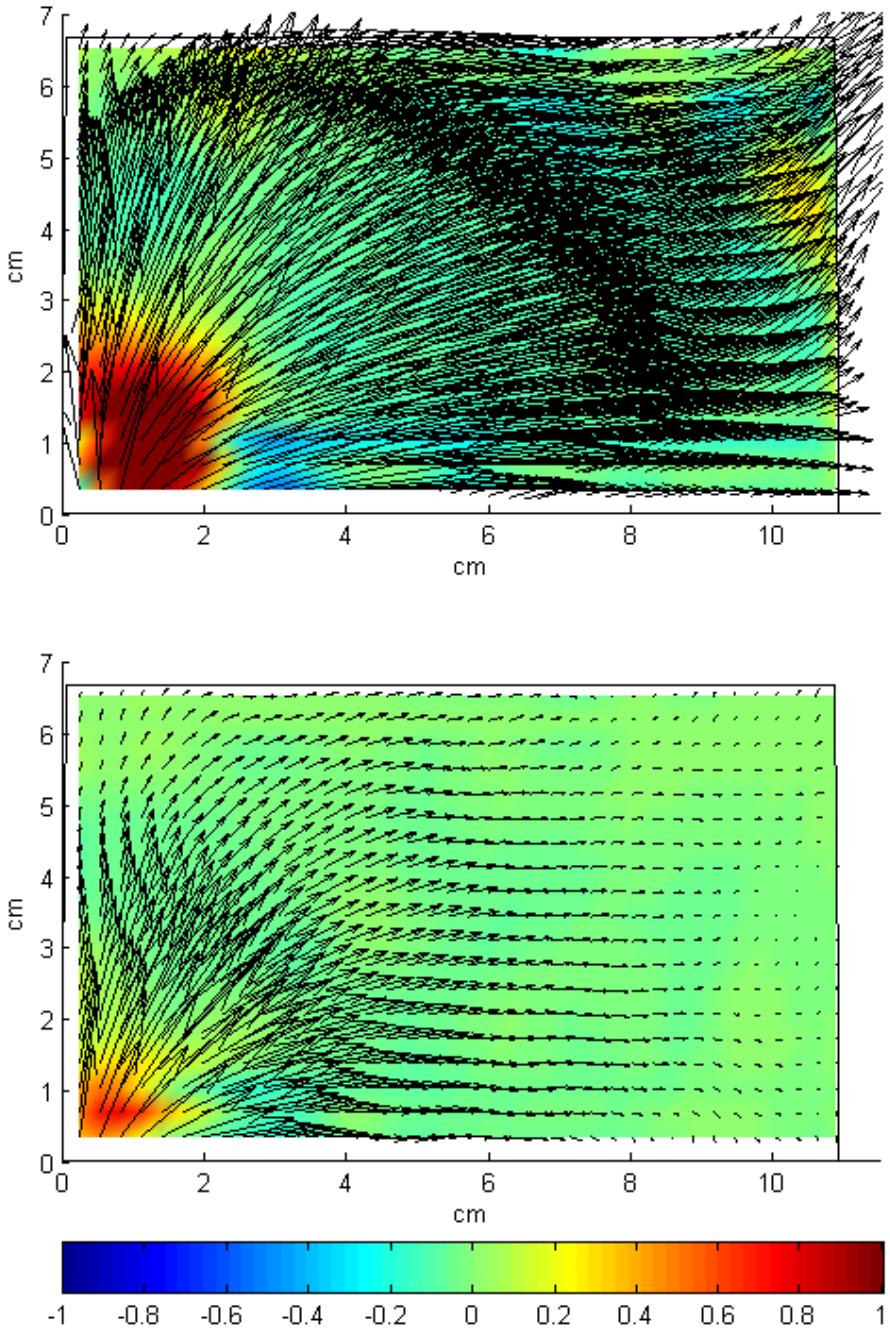

Figure 7.2: Initial packing flow (top) and flow at 0.5 seconds (bottom) for the 27.6 MPa packing pressure, 245°C data sets.

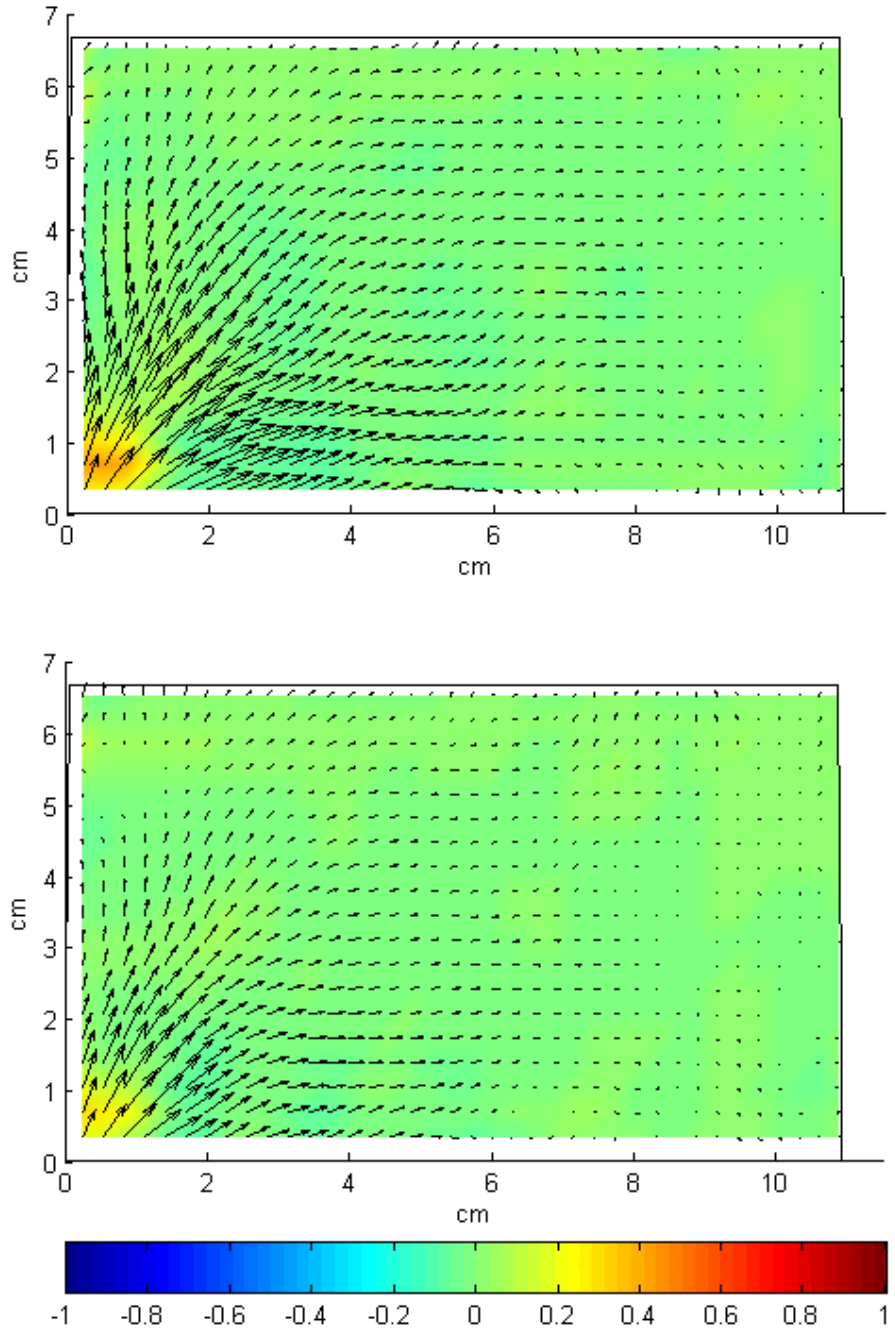

Figure 7.3: Packing flow at 1.0 seconds (top) and for 1.5 seconds (bottom) for the 27.6 MPa packing pressure, 245°C data sets.

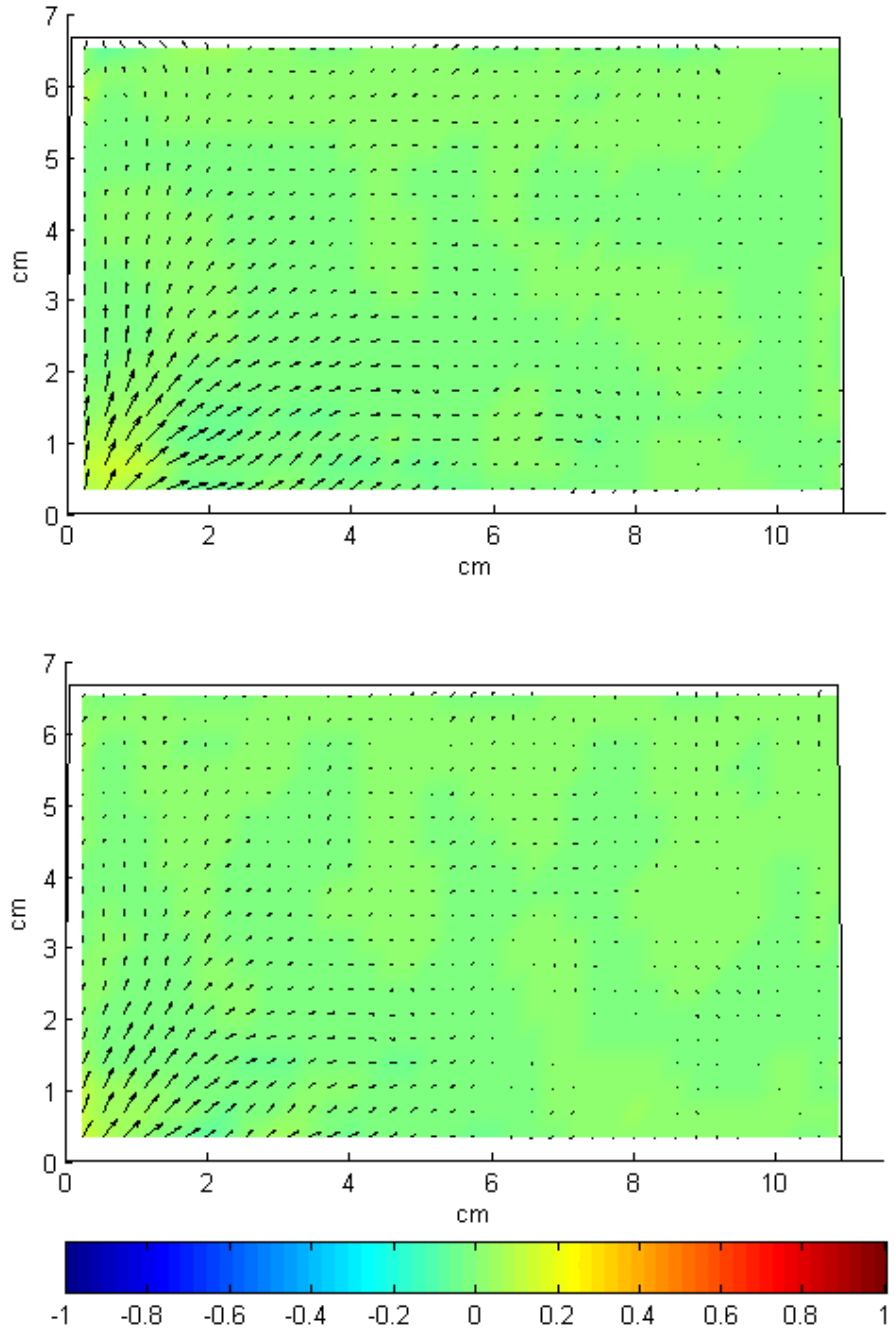

Figure 7.4: Packing flow at 2.0 seconds (top) and for 2.5 seconds (bottom) for the 27.6 MPa packing pressure, 245°C data sets.

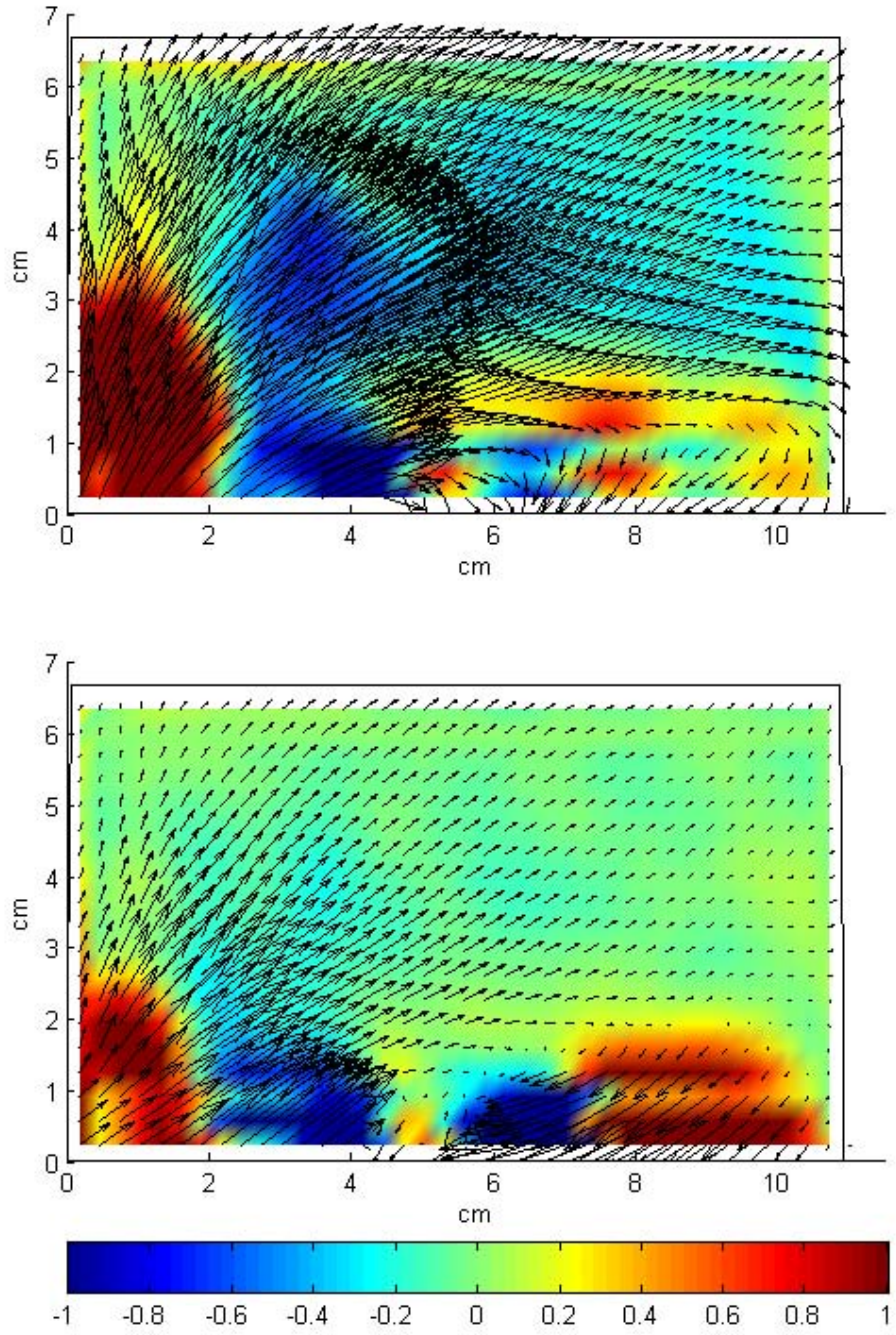

Figure 7.5: Initial packing flow (top) and flow at 0.5 seconds (bottom) for the 16.5 MPa packing pressure, 245°C data sets.

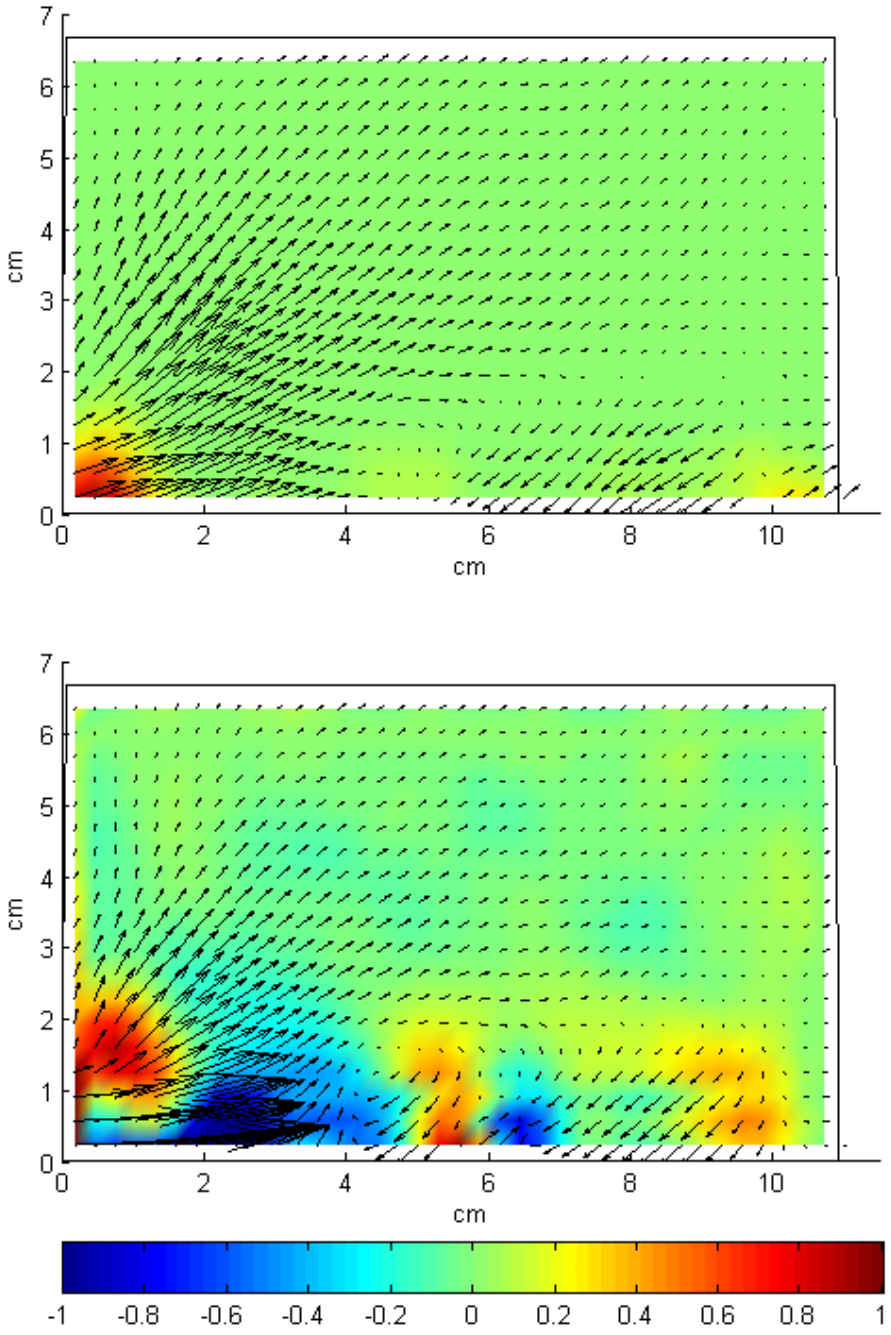

Figure 7.6: Packing flow at 1.0 seconds (top) and for 1.5 seconds (bottom) for the 16.5 MPa packing pressure, 245°C data sets.

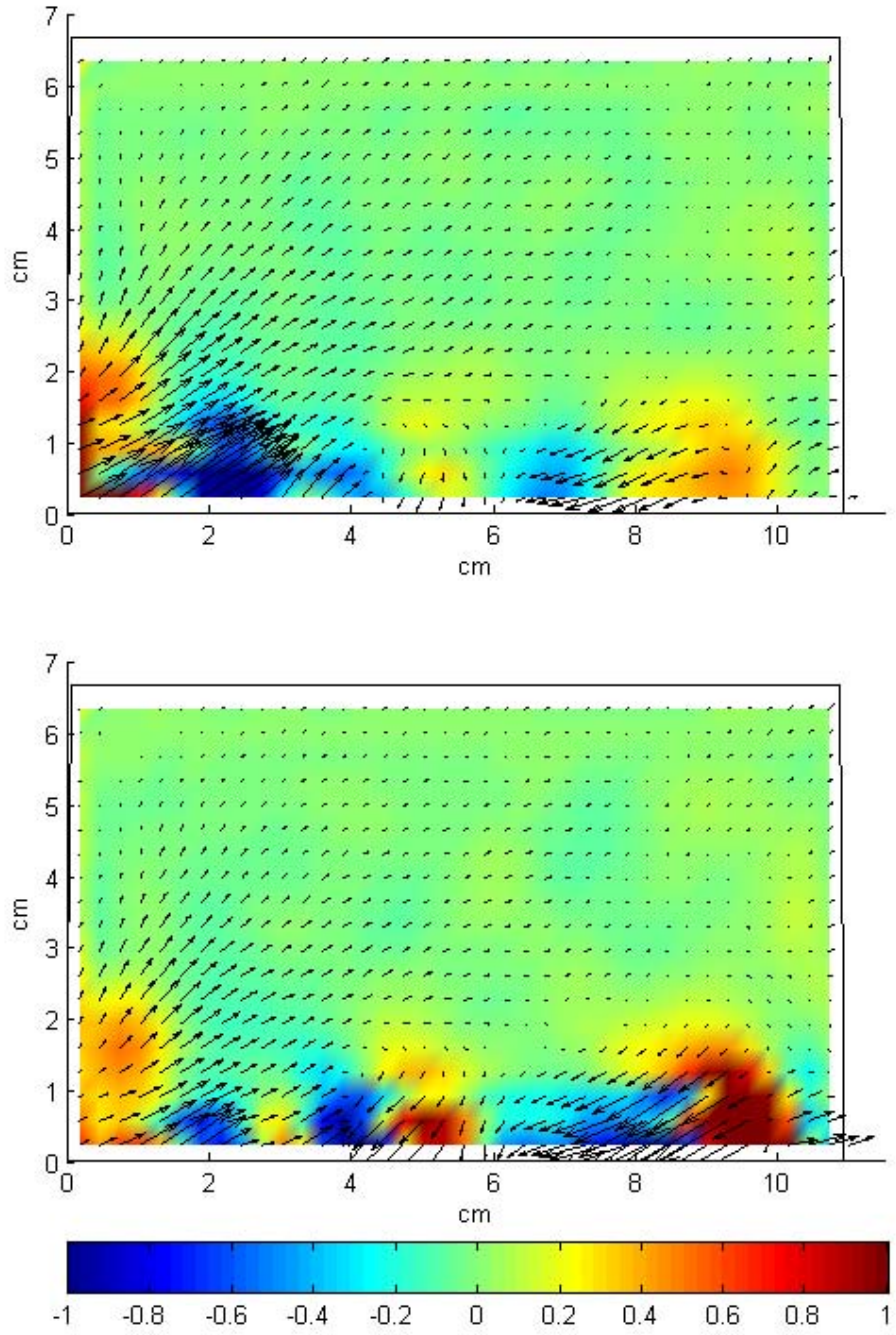

Figure 7.7: Packing flow at 2.0 seconds (top) and for 2.5 seconds (bottom) for the 16.5 MPa packing pressure, 245°C data sets.

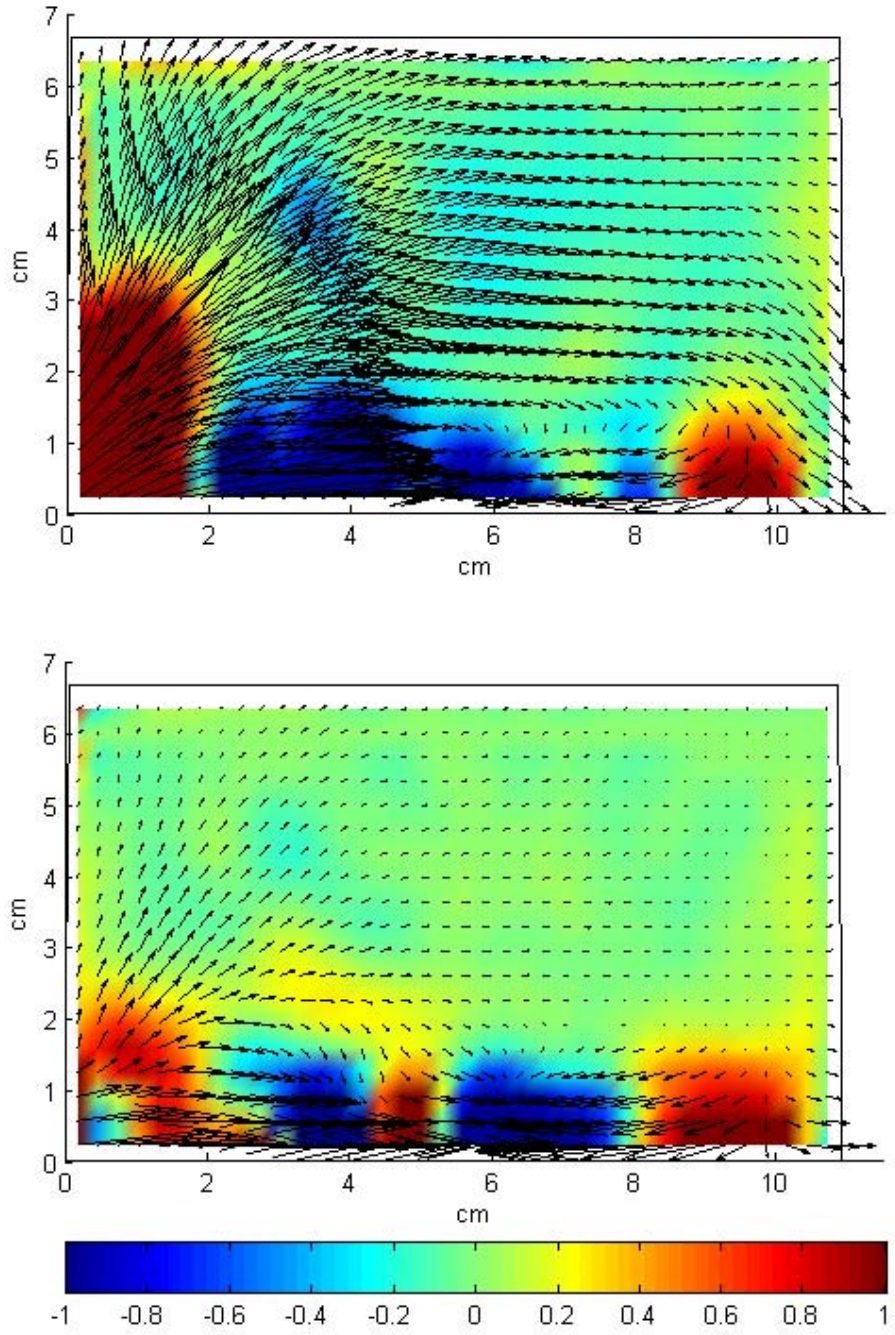

Figure 7.8: Initial packing flow (top) and flow at 0.5 seconds (bottom) for the 11.0 MPa packing pressure, 245°C data sets.

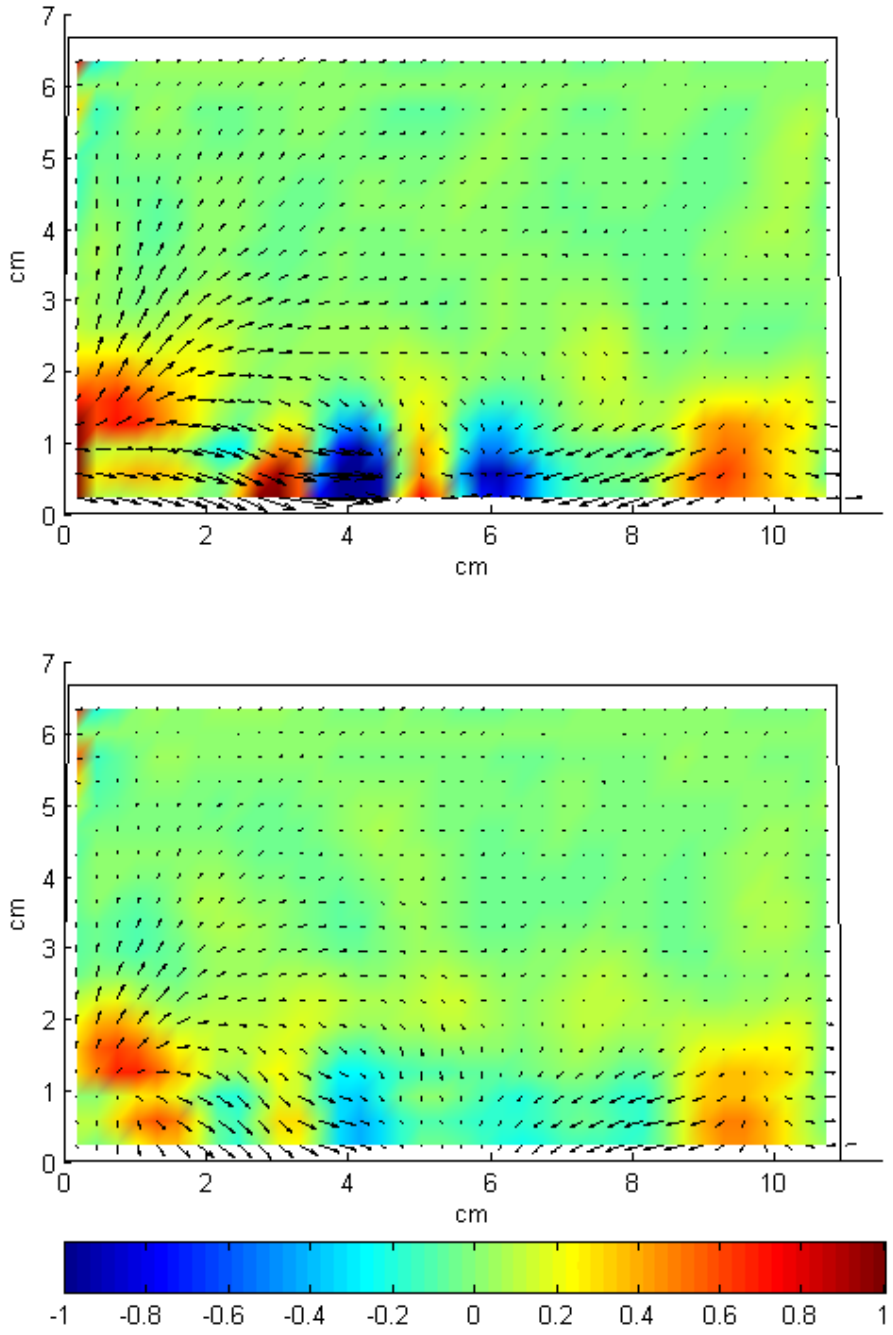

Figure 7.9: Packing flow at 1.0 seconds (top) and for 1.5 seconds (bottom) for the 11.0 MPa packing pressure, 245°C data sets.

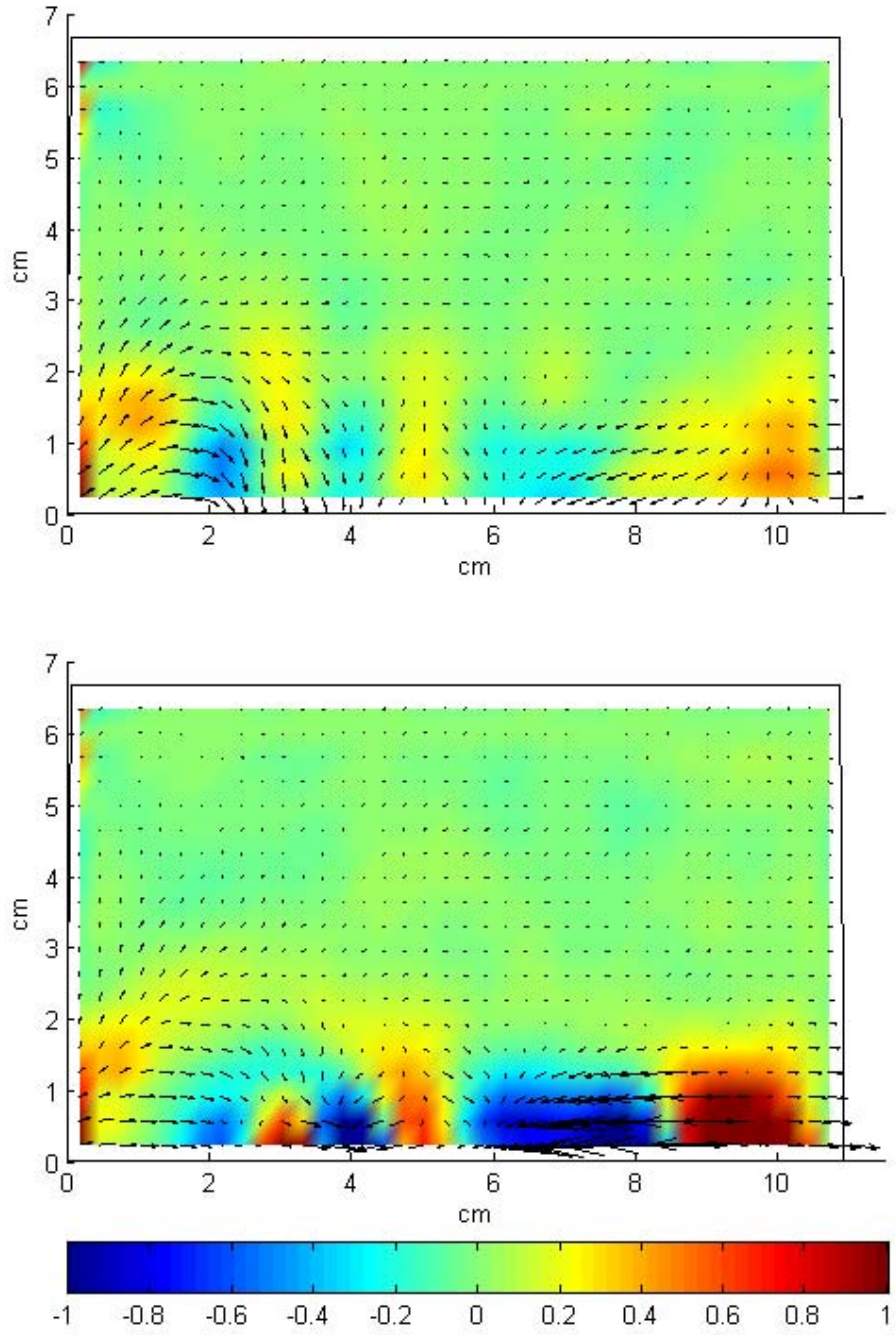

Figure 7.10: Packing flow at 2.0 seconds (top) and for 2.5 seconds (bottom) for the 11.0 MPa packing pressure, 245°C data sets.

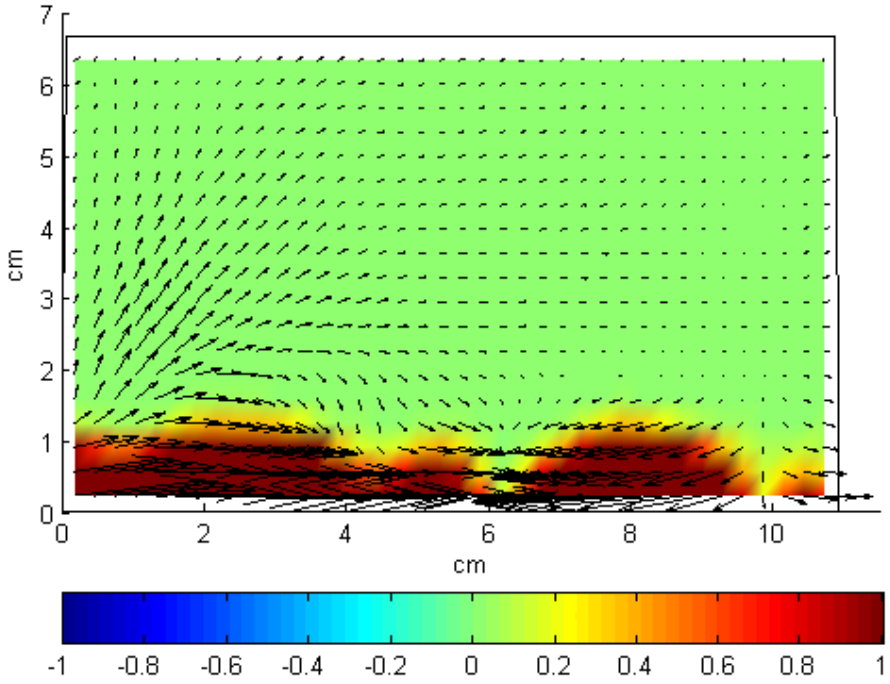

Figure 7.11: Packing flow at 2.0 seconds (top) and for 2.5 seconds (bottom) for the 11.0 MPa packing pressure, 245°C data sets. The pseudocolor overlay represents the sum of the variances of the u and v components of the velocity vector field. The greatest velocity variance is found on the wall with the gate.

is so uniform near the specimen edges that the residual stress field is two-dimensional in this region. The depth of penetration of the fringes along the bottom wall is as high or higher than any other region of the part, indicating that the principle stress difference is also high in this region.

It is possible that there is a correlation between the high molecular orientation along this wall and the high variance in the packing flow along this wall. High orientation could lead to a higher rate of stress relaxation during the packing flow, which could be reflected by the higher variance of the packing flow in this region.

7.2.4 Calculating the Magnitude of the Packing Flow

The magnitudes of the PIV results were then analyzed. The first PIV vector field in the packing phase, $\vec{u}_0$, was used as a baseline. The following PIV vector fields $\vec{u}_i$ were calculated for each sequential pair of movie frames and were compared with the baseline field. A best-fit scaling factor ϕ was then calculated by comparing each velocity field with the baseline by minimizing the following residual:

$$r_i = \|\vec{u}_i - \phi\vec{u}_0\| \tag{7.7}$$

The scaling factor curves were then averaged over six runs to obtain a mean scaling factor curve. The curves were quite repeatable. Figure 7.12 shows a superposition of the scaling factor curves from six runs at a nominal packing pressure of 16.5 MPa.

The best-fit scaling factors ϕ for the three packing pressures studied are shown in Figure 7.13. The three curves indicate that the evolution of the flow is very similar for all three pressures. The scaling factors decay exponentially, as evidenced by the fact that the plots are linear on semilogarithmic axes.

7.2.5 Calculating the Variability of the Packing Flow

A residual metric similar to that defined in Equation 5.11 can be defined to examine the variability of the packing PIV fields. In Equation 5.11 two vector fields were compared with each other. The magnitude of the residual vector was calculated at each point in the field, and then the entire field of residual magnitudes was summed together. This was divided by the sum of the magnitudes of the vectors of one of the two fields. This idea can be extended to compare multiple fields.

The mean velocity vector components are computed at each point. The variances of each component are then computed at each point and summed to get a total

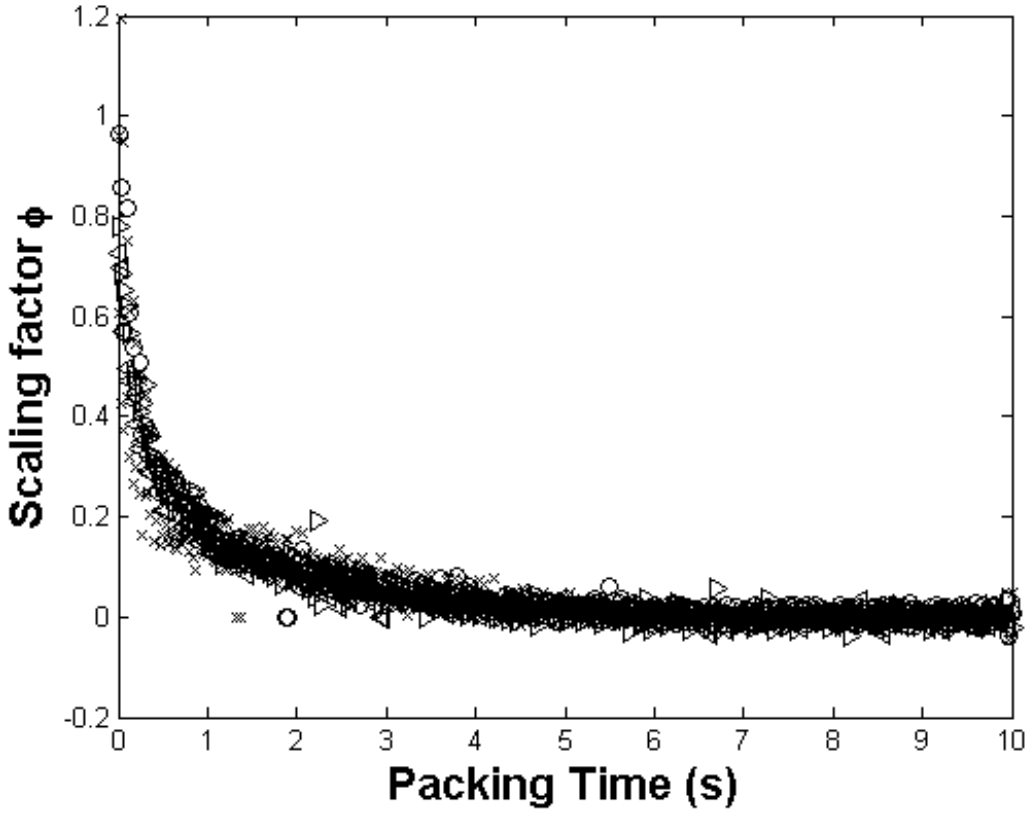

Figure 7.12: Superposition of the scaling factor curves for six runs at a nominal packing pressure of 16.5 MPa.

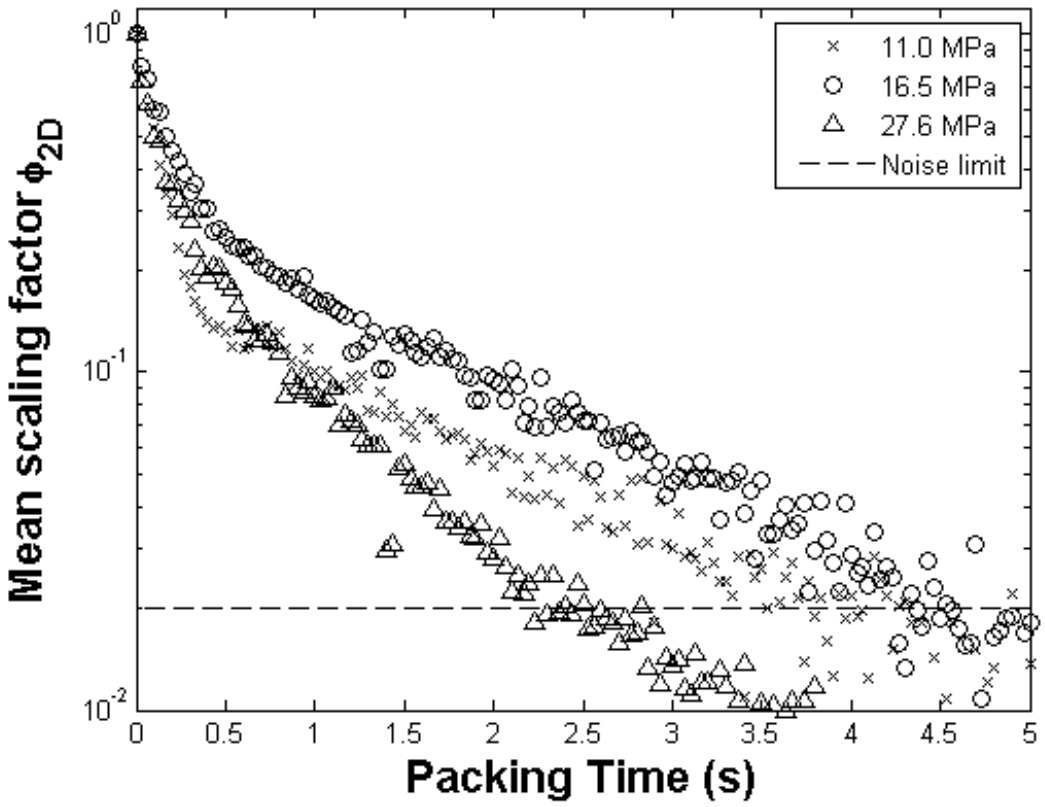

Figure 7.13: Calculated scaling factors showing the evolution of the packing flow in time compared to the first velocity vector field computed during the packing phase.

variance of both vector components at each point. The total variances can be thought of as the square of the magnitude of a "standard deviation vector" at each point. This magnitude is then summed over the entire field and is then divided by the sum of the squares of the magnitudes of the mean velocity vectors.

Letting $s_u(i,j)$ and $s_v(i,j)$ represent the standard deviation of the u and v velocity components at a point and $\bar{u}(i,j)$ and $\bar{v}(i,j)$ represent the mean velocity components at a point the packing residual metric ε_p is given by:

$$\varepsilon_p = \frac{\sum_{i,j}[s_u^2(i,j) + s_v^2(i,j)]}{\sum_{i,j}[\bar{u}^2 + \bar{v}^2]} \tag{7.8}$$

The packing residual metric was calculated for each of the PIV plots shown in Figures 7.8-7.4. The residual metrics are plotted as a function of packing time in Figure 7.14. A number of conclusions may be drawn from this figure:

1. The residuals are quite high. Even at the beginning of the packing phase the residual magnitudes are between 10-20%. After 2.5 seconds they range from 40-80%. There is a strong random component to the packing flow.

2. The residuals tend to increase with time for all cases. The random element of the packing flow becomes stronger with time.

3. The curves do not intersect. The residual magnitudes increase as the packing pressure decreases.

The combination of the last two points is interesting. In Section 7.3 it is shown that the flow during packing can be convincingly modeled as a combination of flow due to melt compressibility and flow due to solidification. The influence of the flow due to compressibility is greater at the beginning of packing. After the packing pressure stabilizes the packing flow is due to solidification.

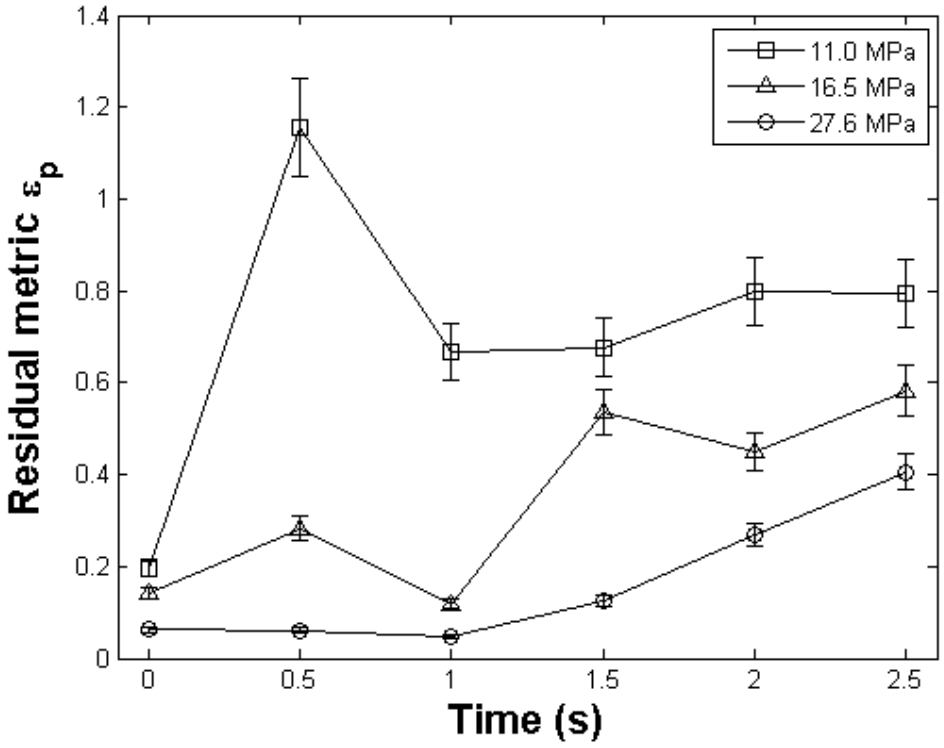

Figure 7.14: The residual metric ε_p as a function of time for the packing PIV vector fields.

It would seem that the packing pressure has a large impact on moderating the random element of the packing flow. As noted above, the residual metric decreases as the packing pressure increases independent of time. Second, the flow due to compressibility is strongest at the beginning of packing and decays rapidly as the packing pressure stabilizes. As the packing time increases the flow due to compressibility decreases and the flow due to heat transfer increases. So there is a negative correlation between the magnitude of packing flow due to the application of packing pressure and the residual metric. There is a positive correlation between the magnitude of the flow due to heat transfer and the residual metric.

7.3 Calculating the Mass Flow During the Packing Phase

Unlike the filling phase, the flow rate during the packing phase is not imposed directly by the injection molding machine. Flow into the mold during packing is a function of a number of factors, including packing pressure, melt compressibility, and melt solidification. Melt solidification is a function of the overall heat transfer coefficient between the melt and the mold and mold geometry and will be dealt with in a later section.

The curves shown in Figure 7.13 can be thought of as representing the ratio of the two-dimensional volume flow rate at any given time during the packing flow to that of the initial two-dimensional flow at the start of the packing phase. By making the assumption that the calculated scaling factors apply to the three-dimensional flow as well, the volume flow rate during the packing phase can be written as

$$Q = Q_0 \phi(t) \tag{7.9}$$

where Q_0 is the unknown initial volume flow rate at the onset of packing.

The mass flow into the cavity during packing can then be calculated. The injection pressure during the packing phase changes with time so the density of the melt entering the cavity also changes with time. The density can be calculated from the packing pressure and melt temperature using the Tait equation, Equation 7.1. Using Equations 7.9 and 7.1 with the packing pressure trace and the melt temperature, the mass flow rate into the cavity can be calculated:

$$\dot{m} = Q_0 \phi(t) \rho(t) \tag{7.10}$$

where $\rho(t)$ is the time-varying density calculated from the Tait equation. At this point the initial volume flow rate during packing, Q_0, is still unknown. In order to calculate it, Equation 7.10 can be integrated to produce the total mass influx to the cavity during packing:

$$m(t) = \int_0^t \dot{m} dt = Q_0 \int_0^t \phi(t) \rho(t) dt \tag{7.11}$$

This integral can be carried out numerically since $\phi(t)$ and $\rho(t)$ are known. By integrating the curve until the end of the packing phase, the final part mass can be calculated. This mass can then be compared with the measured specimen mass to solve for the the unknown Q_0. Letting the duration of the packing time be denoted as t_p and letting the measured difference in mass between a packed specimen and an unpacked specimen be denoted by ΔM:

$$Q_0 = \frac{\Delta M}{\int_0^{t_p} \phi(t) \rho(t) dt} \tag{7.12}$$

Substituting this into Equation 7.11 gives

$$m(t) = \Delta M \frac{\int_0^t \phi(t) \rho(t) dt}{\int_0^{t_p} \phi(t) \rho(t) dt} \tag{7.13}$$

Equation 7.11 was then applied to the 11.0 MPa, 16.5 MPa, and 27.6 MPa data sets. The PIV scaling factor curves of Figure 7.13, the packing pressure traces of

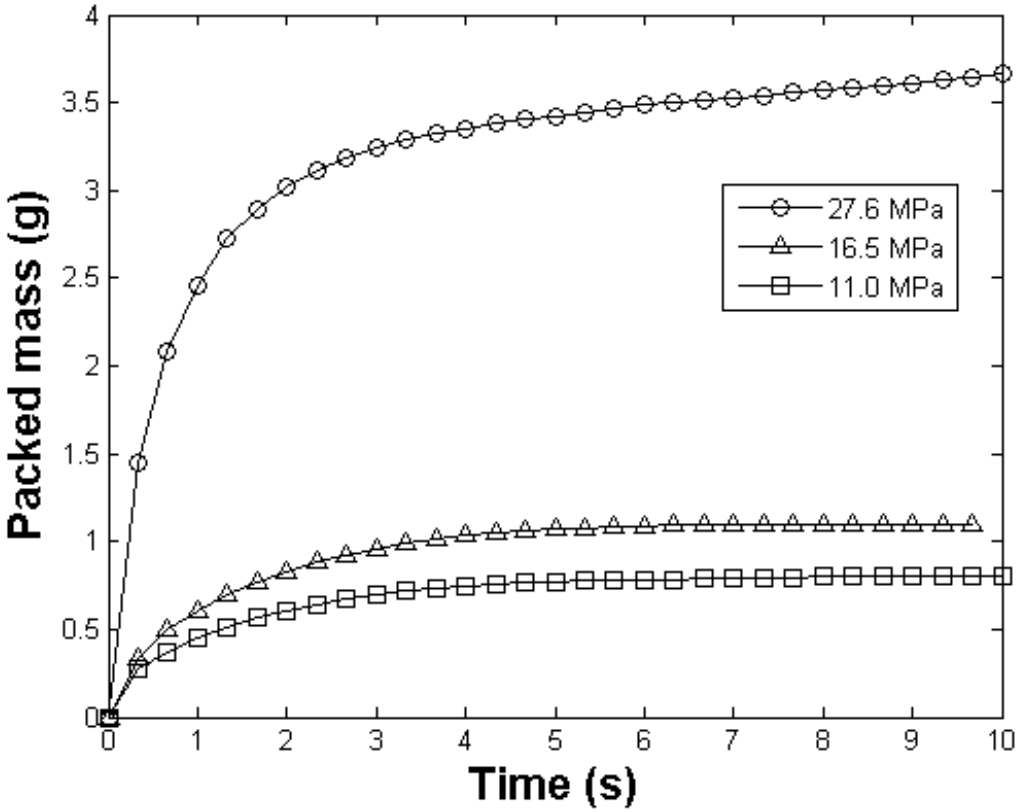

Figure 7.15: Increase in mass of the filled part as a function of time at three packing pressures.

Figure 7.1 and the specimen averaged masses shown in Table 7.1 were combined with Equation 7.11 to produce Figure 7.15.

One striking feature of Figure 7.15 is that the 27.6 MPa packing masses seem disproportionately large compared with the 16.5 MPa data and the 11.0 MPa data. Estimates of packing mass using the Tait equation could only account for approximately half of the 27.6 MPa packed mass curve shown in Figure 7.15. No reasonable adjustment of the model parameters described in Section 7.4 could produce results matching this curve.

Further investigation revealed that the solid specimens produced at the 27.6 MPa packing pressure had thicknesses larger than the nominal cavity thickness including

Table 7.3: Evidence of mold window deflection at the 27.6 MPa packing pressure level. Specimen thicknesses were measured for eight parts at six locations shown in Figure 8.10. The measurements are tabulated in Table E.15. The specimen thicknesses exceed the nominal cavity thickness including draft.

Measurement location	Nominal cavity thickness (mm)	Mean specimen thickness (mm)	Specimen thickness standard deviation (mm)
1	6.49	6.76	0.06
2	6.64	6.95	0.04
3	6.79	7.00	0.06
4	6.49	6.79	0.06
5	6.64	6.96	0.04
6	6.79	7.06	0.04

draft. A micrometer was used to measure the thickness of eight 27.6 MPa specimens at the six locations shown in Figure 8.10. These measurements are tabulated in Table E.15 and are summarized in Table 7.3. It is evident that the high packing pressure pushed the window approximately a quarter millimeter away from the mold cavity. This also explains why the maximum pressure for the 27.6 MPa trace shown in Figure 7.1 is only 25 MPa. The packing pressure was relieved as the window moved away from the cavity. Unfortunately the window deflection as a function of time is unknown, so it is impossible to account for it in the analytical model that follows. Therefore the model will only be compared with the 16.5 MPa and 11.0 MPa data sets. Investigation of the specimen thicknesses for these packing pressures shows no evidence of window deflection. All thicknesses, found in Table E.7 and Table E.11, are less than the nominal cavity thicknesses shown in Table 7.3.

7.4 Analytical Model of Flow Rate During the Packing Phase

The polymer melt solidifies as it cools. Since the density of the solid is higher than the density of the melt, this creates volume in the mold cavity as the polymer

cools. This effect is known as *shrinkage*. The purpose of the packing phase is to force molten polymer into the mold to compensate for shrinkage and to ensure that the final part matches the mold dimensions.

In order to force polymer melt into the cavity to combat shrinkage the melt pressure must increase considerably. In the present work the packing pressure climbed as high as 25 MPa. The hydraulic system of the injection molding machine cannot impose such a dramatic pressure increase instantaneously, so the melt pressure increases as a function of time. Melt compressibility becomes another mechanism for mass influx during the packing stage.

Analytical models for flow due to heat transfer and for flow due to melt compressibility were developed and are presented below. Since the compressibility model depends on the results of the heat transfer model, the heat transfer model will be presented first.

7.4.1 Single-Sided Model of Flow Due to Heat Transfer Effects

Shrinkage is a thermal effect, and a heat transfer model was created to estimate the volume flow rate of polymer melt into the cavity as a function of time. The mold cavity is essentially a rectangular slab with length and width much greater than the cavity thickness. In addition, polymer melts are poor conductors of heat. These two factors suggest that the heat transfer from the melt to the mold will primarily be through the thickness direction and that the mold cavity can be satisfactorily modeled as a one-dimensional slab as shown in Figure 7.16. Note that in this model the glass face of the mold is considered to be insulated to take into consideration that the thermal conductivity of glass is much less than that of steel. Since heat will only leave the polymer melt through the steel side of the mold this model is called

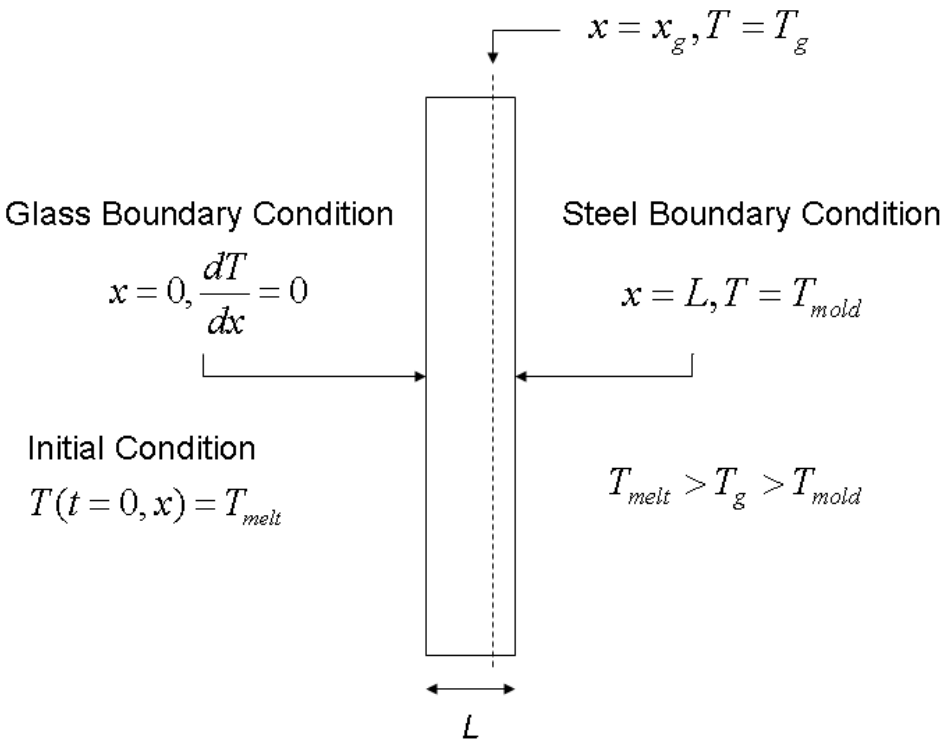

Figure 7.16: Illustration of the single-sided one-dimensional heat transfer model with boundary and initial conditions used to predict the volume flow rate of polymer during the packing phase. The glass boundary is treated as an insulated surface. The dashed line shows a possible location of the glass transition temperature plane.

the single-sided heat transfer model.

Amorphous polymers such as polystyrene do not have a sharp phase transition from liquid to solid as they cool and solidify. They pass through a rubbery or leathery stage over a range of temperatures rather than having a well-defined melting point. Yet it is common to choose a temperature known as the glass transition temperature T_g to mark the boundary between solid-like and liquid-like behavior of a polymer. For the purposes of this model is is assumed that the density change of the polymer as it transitions from liquid to solid occurs at the glass transition temperature.

In this one-dimensional heat transfer model the temperature varies with x and

all points on a plane perpendicular to the x-axis share the same temperature. That means we can imagine a plane at a location x_g whose points are all at the glass transition temperature T_g. This plane is guaranteed to exist since $T_m > T_g > T_\infty$, where T_m is the initial melt temperature and T_∞ is the mold temperature. As time progresses the T_g plane moves in the negative x direction from the steel face of the mold toward the glass face. As the T_g plane moves it frees up an incremental volume ΔV as the polymer melt changes density.

$$\Delta V = -\left(1 - \frac{\rho_m}{\rho_s}\right) A \frac{dx_g}{dt} \Delta t \tag{7.14}$$

where A is the cross-sectional area of the mold perpendicular to the thickness direction, ρ_m is the melt density, and ρ_s is the solid density. The negative sign is due to the fact that the T_g plane is moving in the negative x direction. The volume flow rate of polymer into the cavity Q is then:

$$Q = \frac{\Delta V}{\Delta t} = -\left(1 - \frac{\rho_m}{\rho_s}\right) A \frac{dx_g}{dt} \tag{7.15}$$

In order to get the mass influx into the cavity, integrate Equation 7.15 and recognize that the incoming mass is at the melt density:

$$M(t) = \rho_m \int_0^t Q dt = \rho_m \left(1 - \frac{\rho_m}{\rho_s}\right) A \Delta x_g(t) \tag{7.16}$$

where $\Delta x_g(t)$ is the distance traveled by the the x_g plane from the beginning of the packing phase until the desired time t.

In order to estimate the distance travelled by the x_g plane the one-dimensional heat transfer model shown in Figure 7.16 must be used. Following the derivation in Lienhard [115], the nondimensionalized one-dimensional heat equation is given by:

$$\frac{\partial^2 \Theta}{\partial X^2} = \frac{\partial \Theta}{\partial Fo} \tag{7.17}$$

Table 7.4: Parameters used in the analytical model of flow rate during the packing phase.

Dimensional Parameters	
$T_m = 245°\text{C}$	Melt temperature
$T_g = 100°\text{C}$	Glass transition temperature
$T_\infty = 30°\text{C}$	Mold temperature
$L = 6$ mm	Cavity thickness (single-sided model)
$L = 3$ mm	Cavity half-thickness (double-sided model)
$\alpha = 0.82\times10^{-7}\text{m}^2/\text{s}$[114]	Thermal diffusivity of the melt

Dimensionless Parameters	
$\Theta = (T - T_\infty)/(T_m - T_\infty)$	Temperature difference
$\Theta_g = (T_g - T_\infty)/(T_m - T_\infty)$	T_g
$X = x/L$	Length
$X_g = x(T_g)/L$	Location of the T_g plane
$Fo = \alpha t/L^2$	Fourier number

with nondimensionalized parameters as shown in Table 7.4. The initial condition is that the entire melt is at the specified melt temperature:

$$\Theta(X, Fo = 0) = 1 \tag{7.18}$$

The face of the slab at $x = 0$ is formed by the glass window of the optical access mold while the face at $x = L$ is formed by the steel face of the mold. Since glass is a poor conductor of heat compared to steel, an insulated boundary condition is imposed at $x = 0$:

$$\left.\frac{\partial\Theta}{\partial X}\right|_{X=0} = 0 \tag{7.19}$$

Since the thermal capacity of the steel mold is very high and the heat transfer from the poorly conducting polymer is slow the mold temperature remains nearly constant during the packing phase. Thus a constant mold temperature boundary condition is imposed at $x = L$.

$$\Theta(X = 1, Fo) = 0 \tag{7.20}$$

Lienhard [115] give the exact solution of the one-dimensional heat transfer equation with the specified boundary conditions as:

$$\Theta = \frac{4}{\pi} \sum_{n,\text{odd}}^{\infty} \frac{1}{n} \exp\left[-\left(\frac{n\pi}{2}\right)^2 Fo\right] \sin\left[\frac{n\pi}{2}(X+1)\right] \tag{7.21}$$

Using the values given in Table 7.4, the nondimensionalized glass transition temperature $\Theta_g = 0.326$. Therefore the location of the T_g plane as a function of time can be calculated using Equation 7.21

$$0.326 = \frac{4}{\pi} \sum_{n,\text{odd}}^{\infty} \frac{1}{n} \exp\left[-\left(\frac{n\pi}{2}\right)^2 Fo\right] \sin\left[\frac{n\pi}{2}(X_g+1)\right] \tag{7.22}$$

In order to use Equation 7.22, the number of terms in the summation must be specified. MATLAB was used to solve Equation 7.22 using 1 to 40 terms in the summation. The solutions were computed at a discrete set of Fourier numbers Fo_i ranging from 0-0.025, representing a 10 second packing and holding time. The residuals between successive approximations of $X_g(Fo)$ were computed using the following formula:

$$\varepsilon^{j+1} = \left(\sum_i \left[X_g^{j+1}(Fo_i) - X_g^j(Fo_i) \right]^2 \right)^{1/2} \tag{7.23}$$

where the superscripts refer to the number of terms kept in the summation. The resulting residuals are plotted as a function of the number of terms retained in the summation in Figure 7.17. It can be seen from the figure that the residuals plateau at a value of approximately 10^{-3} after 25 terms retained. The resulting position of the T_g plane as a function of Fourier number when retaining 25 terms in the summation is shown in Figure 7.18.

7.4.2 Double-Sided Model of Flow Due to Heat Transfer Effects

A second heat transfer model can be developed similar to the one described above. The single-sided model treated the glass as an insulated surface. The double-sided

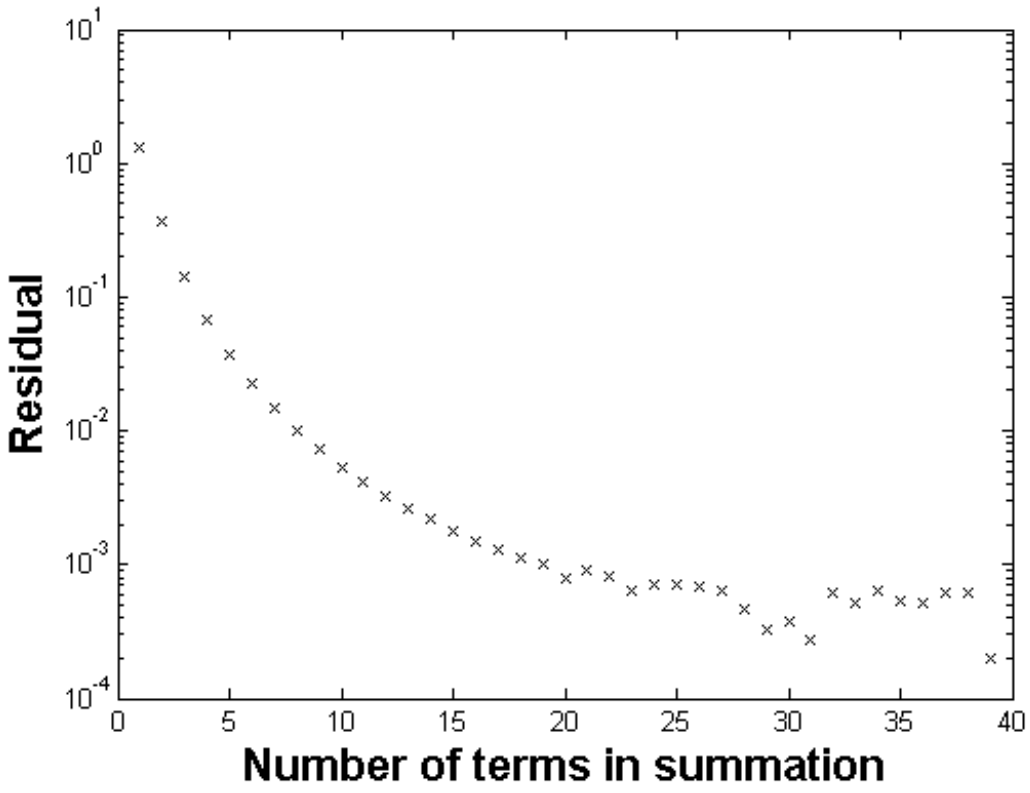

Figure 7.17: Residual of comparing successive solutions of $X_g(Fo)$ using Equation 7.22. The x axis shows the number of terms retained in the summation in Equation 7.22.

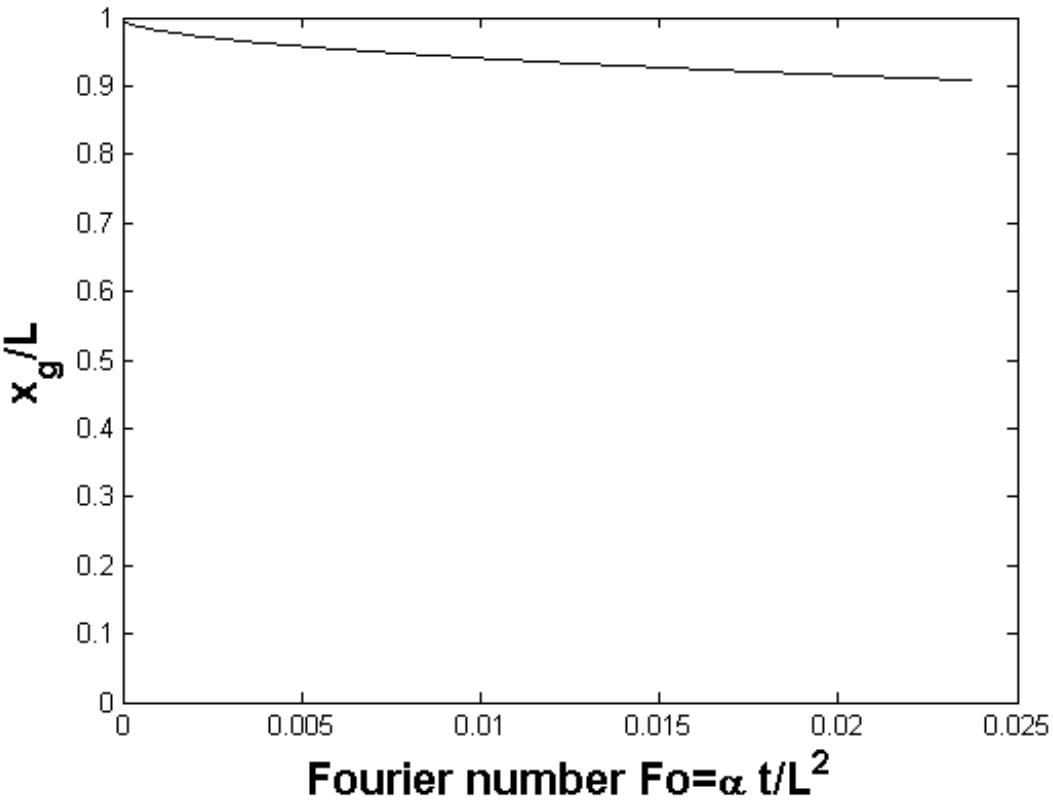

Figure 7.18: Plot of the nondimensionalized location of the T_g plane as a function of Fourier number for the single-sided model. This result was generated by solving Equation 7.22 and retaining 25 terms in the summmation.

heat transfer model, shown in Figure 7.19, treats the glass as a constant temperature surface at $T = T_{mold}$. This model treats the glass as if it were no different from the steel on the opposite face. The heat transfer equations for this model are exactly the same as in the single-sided model. The only difference is that the length L is now the cavity half-thickness instead of the cavity thickness. The effect of this change is that the Fourier numbers are increased. There are now two T_g planes spaced symmetrically about the cavity midplane. The planes move faster than in the single sided model and cause the melt to solidify more quickly.

The single-sided and double-sided models represent two extreme ways to model the glass. In the single-sided model the glass conducts no heat at all, and in the double-sided model it conducts heat as well as the mold steel.

7.4.3 Model of Flow Due to Melt Compressibility

The Tait equation (Equation 7.1) can be used to predict the flow due to melt compressibility. Given a measured packing pressure trace $P(t)$ and a melt temperature T_m, the melt density as a function of time can be calculated using Equation 7.1. The mass flow rate into the cavity due to the compressibility can then be given by

$$\dot{m} = \frac{d\rho}{dt} V \tag{7.24}$$

where V is the cavity volume.

Two refinements can be made to this model. The first refinement is to recognize that the volume of the cavity filled by polymer melt decreases with time due to the increasing presence of solidified melt near the wall. Using the T_g plane as the demarcation line between liquid and solid polymer in the cavity and denoting the distance of travel of the T_g plane from the beginning of packing to time t as $\Delta x_g(t)$

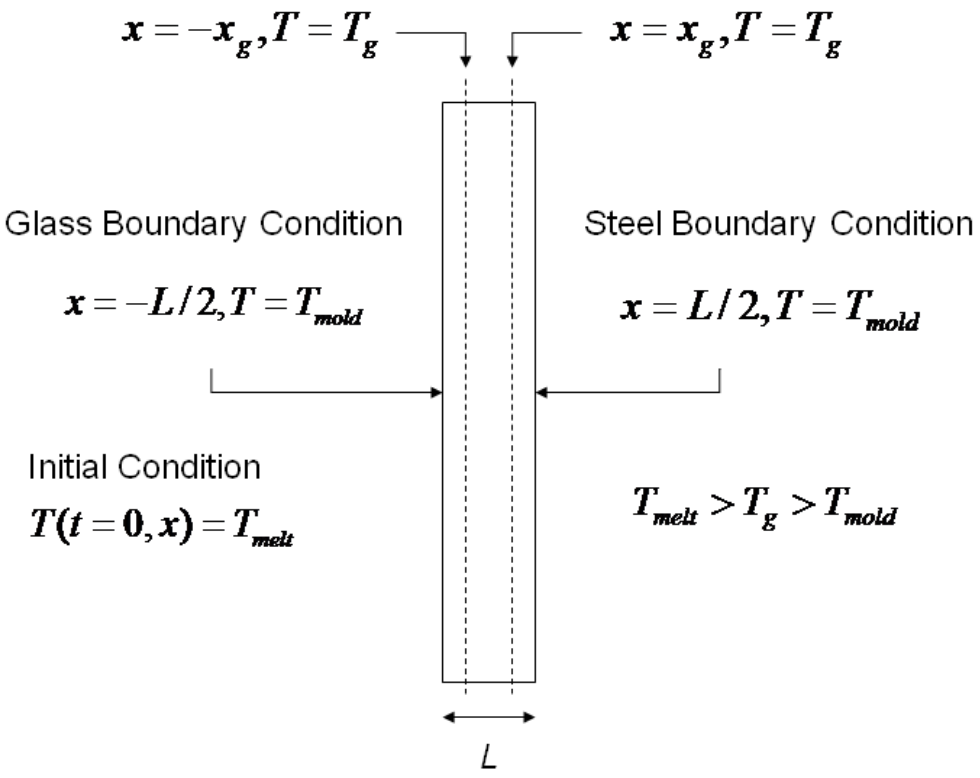

Figure 7.19: Illustration of the double-sided one-dimensional heat transfer model with boundary and initial conditions used to predict the volume flow rate of polymer during the packing phase. The glass boundary is treated as a constant temperature surface with $T = T_{mold}$. The dashed line shows a possible location of the pair of glass transition temperature planes.

gives

$$\dot{m} = \frac{d\rho}{dt}(V - A\Delta x_g(t)) \tag{7.25}$$

where A is the cross-sectional area of the cavity perpendicular to the cavity thickness.

The second refinement of this model is to recognize that the PIV results show no evidence of flow toward the gate during packing. Equation 7.25 can give negative mass flow rates if $d\rho/dt < 0$. In fact, the packing pressure curves do show negative slopes after the packing peak. Using the Tait equation, this would predict density curves that also have negative slopes after the packing peak. This would cause the compressibility model to predict negative mass flow rates that were not observed in the experiment. In order to avoid this, the compressibility model can be adjusted to "turn off" the packing flow if the rate of change of the density becomes negative.

$$M_\rho = \int_0^{\Delta t} \dot{m} = \int_0^{\Delta t} \max(\frac{d\rho}{dt}, 0)(V - A\Delta x_g(t))dt \tag{7.26}$$

where M_ρ is the mass influx into the cavity due to compressibility and Δt is the packing duration.

7.4.4 The Combined Compressibility and Heat Transfer Model

The compressibility model and the single and double-sided heat transfer models were applied to the 11.0 MPa and the 16.5 MPa data. The 27.6 MPa data was not treated due to the evidence of window deflection presented in Table 7.3.

Figure 7.20 shows the results of the compressibility model and the two heat transfer models when applied to the 11.0 MPa data. Figure 7.21 shows the results of applying the three models to the 16.5 MPa data. The mass influx due to compressibility is 63.8% of the total packing mass for the 11.0 MPa case, and is 63.5% of the total for the 16.5 MPa case. The mass influx due to compressibility enters rapidly during the first two seconds of packing. The mass influx due to heat transfer

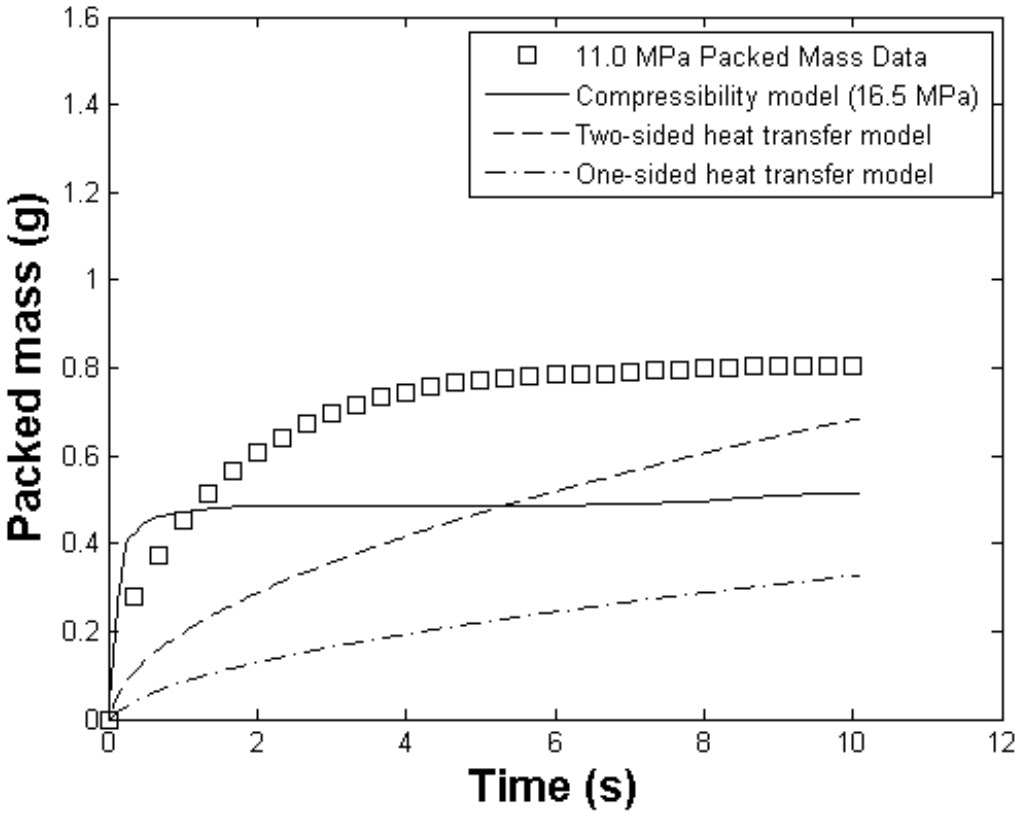

Figure 7.20: Components of the compressibility model, the single-sided heat transfer model and the double-sided heat transfer model compared with the 11.0 MPa packed mass data.

enters more slowly but at near-constant rate. This supports the conclusion drawn in Section 7.2.5 about the variability of of the PIV vector fields during packing. The residual metric is low during the portion of the flow dominated by the packing pressure. The residual metric increases as the flow due to heat transfer increases.

The compressibility and heat transfer models are combined and compared with the 11.0 MPa data in Figure 7.22. The models are again combined and compared with the 16.5 MPa data in Figure 7.23. In both figures the experimental data is bracked closely by the combined compressibility and single-sided heat transfer model and the combined compressibility and double-sided heat transfer model. This suggests that the actual behavior of the glass boundary lies between the two extremes posited by

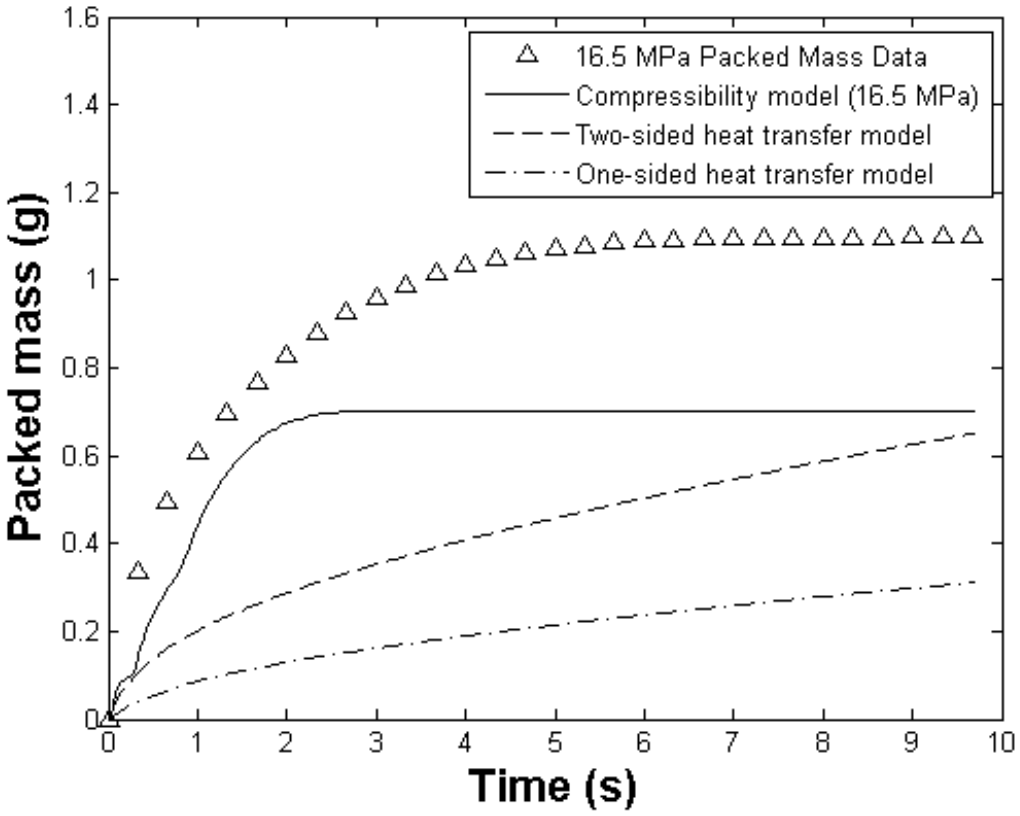

Figure 7.21: Components of the compressibility model, the single-sided heat transfer model and the double-sided heat transfer model compared with the 16.5 MPa packed mass data.

the heat transfer models. The glass is neither an insulated boundary nor a constant mold temperature boundary, but is somewhere in between. To pursue this further a heat transfer coefficient for the glass-polymer melt boundary would need to be measured and a Biot number Bi calculated. The heat transfer model boundary condition at $x = 0$ would need to be modified to [116]:

$$\left.\frac{\partial \Theta}{\partial X}\right|_{X=0} = -Bi\Theta(0, Fo) \tag{7.27}$$

This is beyond the scope of the present work. The analytical models have served their purpose by bracketing the experimental data. The models show that the magnitudes of the packing flow PIV vector fields are reasonable. The models also show that the evolution of the PIV fields with time is physically realistic and is consistent with the packing pressure data and the observed masses of the solid parts.

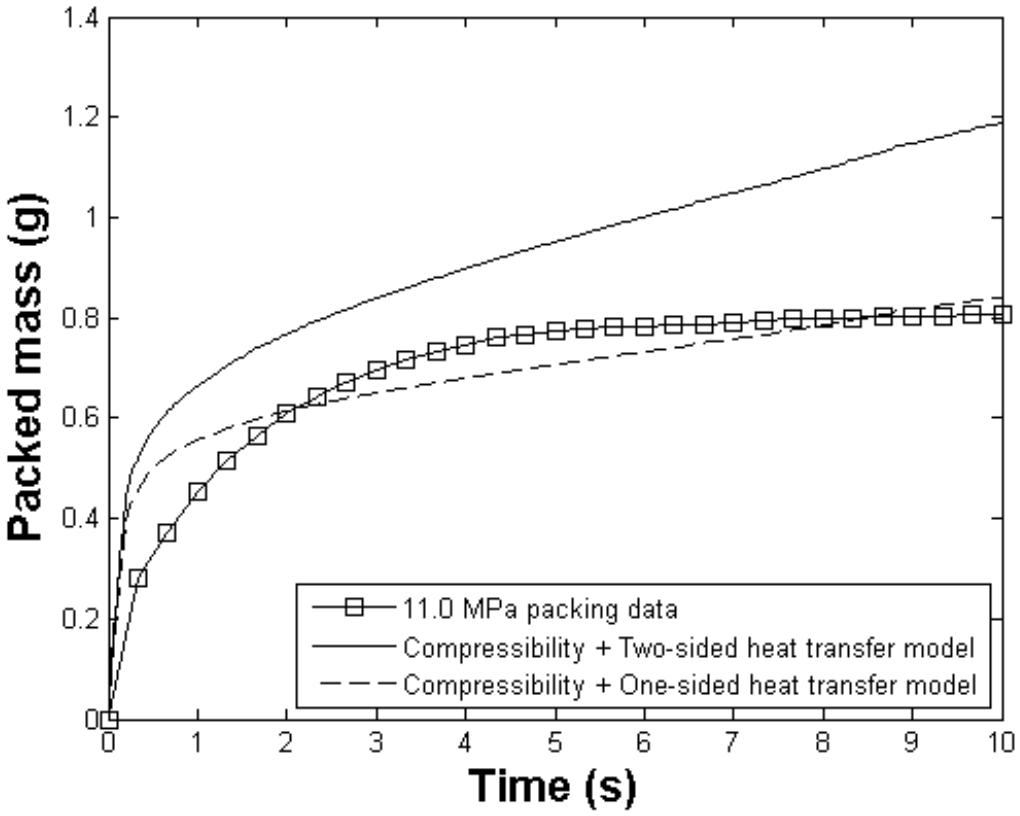

Figure 7.22: Comparison of the 11.0 MPa packed mass curve extracted from the PIV data, gate pressure traces, and specimen weight with the analytical model. The single-sided and double-sided heat transfer models bracket the packed mass curve.

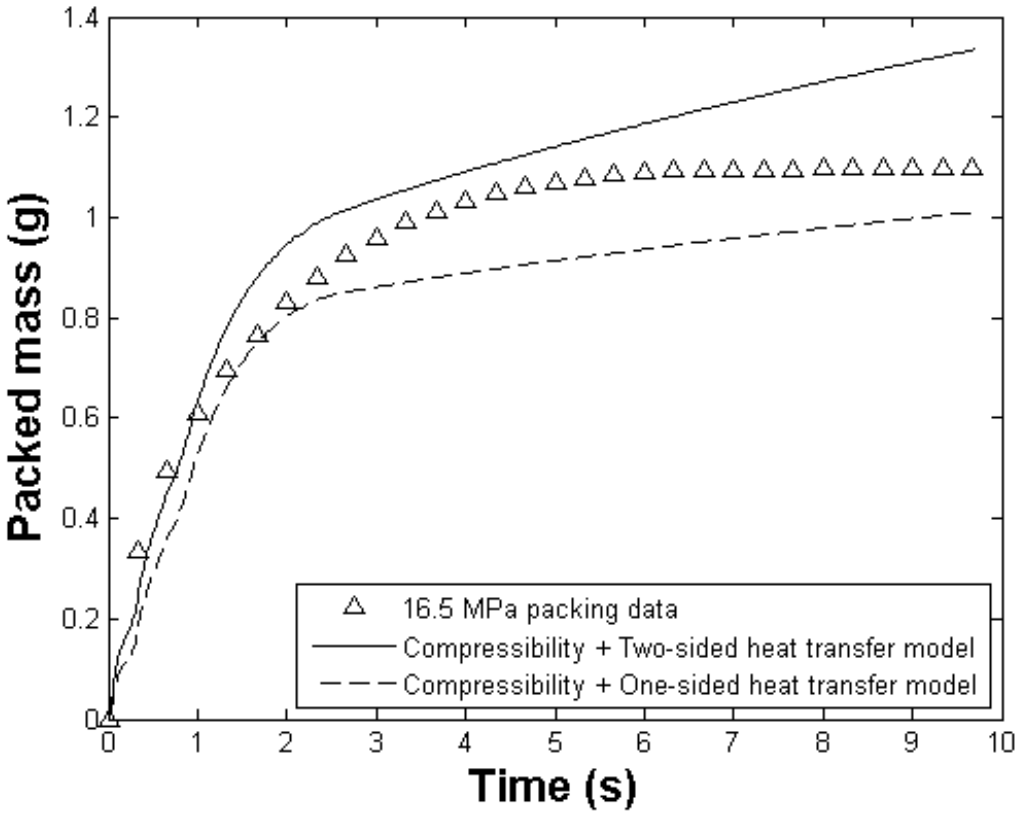

Figure 7.23: Comparison of the 16.5 MPa packed mass curve extracted from the PIV data, gate pressure traces, and specimen weight with the analytical model. The single-sided and double-sided heat transfer models bracket the packed mass curve.

CHAPTER 8

Effect of Fluid Flow on the Residual Stain of Solid Parts

The photoelastic effect has long been used to study strain [45, 46] in mechanical components. Typically a model is made of the component using a transparent, homogeneous photoelastic material. The model is constructed in such a way that when it is unstrained it produces no fringes when placed in a polarimeter. When a load is applied, fringes appear due to the photoelastic effect. This method can also be used to study residual strains in transparent polymers. In this case, the specimen produces fringes in a polarimeter even when no external stresses are applied due to the presence of residual strains in the interior of the specimen.

For the most part studies have been done on specimens specially prepared to have a two-dimensional strain field, with the principal strain directions and differences remaining constant throughout the thickness of the part. Most reference books on the subject devote the bulk of their pages to the study of two-dimensional birefringent plates known as linear retarders. A brief introduction to two-dimensional photoelasticity will aid in the discussion of three-dimensional photoelasticity.

8.1 Two-Dimensional Photoelasticity

When polarized light impinges on a two-dimensional birefringent material in a state of plane strain it is split into two components, each one parallel to a principal strain axis. These waves propagate through the material at different speeds due to the different indices of refraction along those two directions. This speed difference causes a relative phase retardation between the two waves as they exit the specimen. As shown by Dally [47] this relative retardation δ (in radians) is given by:

$$\delta = \frac{2\pi hc}{\lambda}(\sigma_1 - \sigma_2) \tag{8.1}$$

where h is the thickness of the specimen at the point of interest, c is the stress-optic coefficient for the polymer, λ is the wavelength of light used in the polarimeter, and σ_1 and σ_2 are the principle stresses at the point of interest. This result is known as Wertheim's law [117]. Note that even though it is the residual strains that produce this effect, it is typical in the literature to refer to the residual stresses. This convention will be followed in this chapter when standard photoelasticity equations are cited.

The retardation can also be expressed as a length δ_l:

$$\delta_l = \frac{\delta}{2\pi}\lambda = hc(\sigma_1 - \sigma_2) \tag{8.2}$$

where the last equality was obtained using Equation 8.1.

Another way to think about linear retarders is to consider them as transformers of polarization. In general, when light of any polarization is passed through a linear retarder it will emerge with an elliptical polarization different than the initial state. It can be shown that for any two-dimensional linear retarder there are two orthogonal principal directions with unique properties. When plane polarized light enters the

retarder oriented in one of the principal directions it will emerge as a plane polarized beam. In addition, the orientation of the emerging light will be the same as that of the incoming plane polarized light. For any other entrance angle the light loses its plane polarization and emerges as an elliptically polarized beam.

8.1.1 Using a Polarimeter to Determine Principal Directions

A plane polariscope can be used to find the principal directions of the residual strain tensor at a given point. The plane polariscope consists of a light source, a plane polarizer (the "polarizer"), and a second plane polarizer (the "analyzer"). The polarization axes of the polarizer and analyzer are perpendicular to each other. When no model is present, the transmitted light is blocked and the polarimeter field appears dark.

When a two-dimension linear retarder is placed between the polarizer and the analyzer a fringe pattern emerges. At any point in the retarder where the local principal directions are aligned with the polarizer and analyzer axes light is extinguished. These fringes are called *isoclinics*, meaning "same inclination", because they occur when the inclination of the principal axes matches that of the polarimeter axes. These fringes are a function of principal axis orientation only and are not functions of the wavelength of light used. Isoclinic fringes extinguish all light, causing black fringes even in a white light polariscope.

The polarizer and analyzer can be rotated as a unit until a black isoclinic fringe moves over a given point of interest. When that occurs the orientation of the polarizer and analyzer axes match the orientation of the principal axes at that point.

8.1.2 Measuring Relative Retardation

Isoclinic fringes are caused solely by the orientation of the principal axes relative to the polarimeter axes. There are other fringes, called *isochromatics*, that are produced by the phase retardation introduced by the linear retarder independent of the principal axis orientation.

Dally [47] shows that the transmitted light intensity in a polariscope is modulated by $\sin^2(\delta/2)$, where δ is the retardation at the point of interest. Whenever the phase retardation is a multiple of 2π light is extinguished. In a monochromatic polariscope the isochromatic fringes will be black. But this modulating factor depends on δ, which is a function of wavelength. In a white light polariscope, the only frequencies of light extinguished are those with a period that is a multiple of the retardation at that point. Since only certain wavelengths of light are extinguished at any given point the fringe pattern is in color. Hence an isochromatic fringe (meaning "same color") is a fringe along which the retardation is constant.

The relative retardation is typically measured using a null-balance compensator to subtract known amounts of birefringence at the point of interest along the principal direction corresponding to the higher strain. As the compensator is adjusted the fringe changes color. When the fringe goes to black at the point of interest the output of the null-balance compensator can be used to calculate the relative retardation at that point. Typically the results are given in terms of fringe order N rather than δ, with

$$N = \frac{\delta}{2\pi} = \frac{\delta_l}{\lambda_1} \tag{8.3}$$

where δ_l is defined in Equation 8.2 and λ_1 is the reference wavelength of the polarimeter. Table 8.1 shows the correspondence between observed color and fringe order for

Table 8.1: Isochromatic fringe characteristics for a polariscope with $\lambda_1 = 575$ nm

Color	Approximate Relative Retardation (nm)	Fringe Order N
Black	0	0.00
Gray	160	0.28
White	260	0.45
Pale Yellow	345	0.60
Orange	460	0.80
Dull Red	520	0.90
Purple (Tint-of-Passage)	575	1.00
Deep Blue	620	1.08
Blue-Green	700	1.22
Green-Yellow	800	1.39
Orange	935	1.63
Rose Red	1050	1.82
Purple (Tint-of-Passage)	1150	2.00
Green	1350	2.35
Green-Yellow	1440	2.50
Red	1520	2.65
Red/Green Transition	1730	3.00
Green	1800	3.10
Pink	2100	3.65
Pink/Green Transition	2300	4.00
Green	2400	4.15

a reference wavelength of 575 nm, the design wavelength of the quarter-wave plates used in the Vishay 080 Teaching Polariscope.

The measured retardation can then be used to calculate the principal strain difference at that point using either Equation 8.1 or Equation 8.2.

This procedure can also be used for the special three-dimensional case where the retardation varies through the thickness of the part but the orientation of the principal axes remain constant. In this case there is only one set of principal directions and the resulting retardation is determined by the integral of the incremental retardations through the thickness of the part. This result is known as the integral

Wertheim law [117]:

$$\delta_l = \int_0^h c(\sigma_1 - \sigma_2)dz \tag{8.4}$$

where δ_l is the retardation length from Equation 8.2. The integral Wertheim law can be used to show that if two birefringent plates with the same principal axes are stacked the resulting retardation is equal to the sum of the individual retardations. This is the reason why the compensator principal axis must match the local principal axis. It makes no difference whether the compensator is inserted between the polarizer and the specimen or between the specimen and the analyzer.

8.2 Three-Dimensional Photoelasticity

In a two-dimensional state of strain the principal strain difference, the orientation of the principal strain axes, and the stress-optic coefficient are constant throughout the thickness of the part.

These conditions do not generally apply to the residual strain distribution found in plastic parts made by injection molding. The fountain flow effect produces highly oriented layers near the walls of the cavity with a more randomly oriented layer at the center. The wall layers also solidify much more quickly than the center. Since the molecular orientation is affected by the fluid flow and since the flow patterns change between the time that the walls and the center solidify the orientation changes as well. It is unreasonable to expect that the result would be a purely two-dimensional state of residual strain. For example, Wimberger [118] has studied the injection molding of polycarbonate compact disks and shows that the magnitude of retardation and principal axis orientation are functions of position through the thickness of the compact disk.

Three-dimensional states of residual strain in birefringent materials have a more

complicated effect on polarized light than do two-dimensional states of strain, but there are some similarities. A birefringent material in a three-dimensional state of strain can still be thought of as a transformer of polarization. There are still two orthogonal principal directions, and plane polarized light oriented along either of these directions emerges as plane polarized light. There the similarity ends. In the three-dimensional case the orientation of the emerging plane polarized light need not be the same as that of the entering plane polarized light.

8.2.1 Poincaré's Equivalence Theorem

The fundamental principal of three-dimensional photoelasticity is known as Poincaré's equivalence theorem [119]. A recent treatment of this theorem has been published by Hammer [120]. Poincaré's equivalence theorem states that any non-absorbing passive optical element can be replaced by an optically equivalent model consisting of one linear retarder and one rotator. A rotator is an optical element that introduces no retardation, but rotates the electric vector by a specified amount. Figure 8.1 gives a schematic of the optically equivalent model.

The optically equivalent model has the same effect on polarized light as the three-dimension birefringent plate. If plane polarized light enters the linear retarder along either of the principal axes it emerges as a plane polarized beam with the same orientation. The rotator then rotates the beam and the beam exits the model plane polarized but with a different orientation than it had originally.

A consequence of Poincaré's equivalence theorem is that the integrated effect of any three-dimensional residual strain field on polarized light travelling through the field can be characterized by three parameters. These three parameters are the characteristic elements of the optically equivalent model: the principal axis orientation

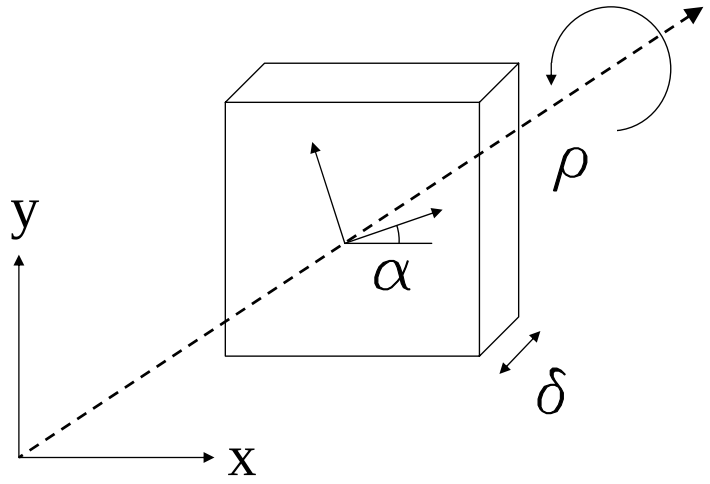

Figure 8.1: Schematic of Poincaré's optically equivalent model of a three-dimensional strain field at a point. The model consists of a linear retarder in series with a rotator. The linear retarder has principal axes oriented at angle α to the reference axes and angular retardation δ. The the amount of angular rotation due to the rotator is ρ. The orientation angle of the secondary axis β (not shown) is given by $\beta = \alpha + \rho$.

α of the linear retarder with respect to a given zero axis, the retardation δ of the linear retarder, and the rotation angle ρ of the rotator. The secondary principal axis orientation β with respect to the same zero axis could also be specified, with $\beta = \alpha + \rho$. Then δ and any two of α, β or ρ completely specify the optically equivalent model at the point of interest. Unfortunately, unlike the two-dimensional case, these parameters are not easily related to the underlying strain field.

8.2.2 Using a Plane Polarimeter to Determine Primary and Secondary Principal Directions in a Three-Dimensional Residual Strain Field

The presence of the rotator in the optically equivalent model causes difficulties when using a polariscope. Consider a two-dimensional birefringent plate. If a plane polarized beam of light is oriented with either of the principal directions it exits the specimen as a plane polarized beam with the same orientation. The principal axes

can be found by crossing the polarizer and analyzer and rotating them as a unit because it is known in advance that the plane polarized light entering and leaving the part will have the same orientation. Finding the principal directions requires a one-parameter search space.

For a three-dimensional birefringent plate there exist two orthogonal primary principal directions and two orthogonal secondary principal directions. If a plane polarized beam is oriented at one of the principal directions it exits the part as a plane polarized beam, but it will now be oriented in the corresponding secondary principal direction. The light can still be extinguished by properly orienting the analyzer with respect to the polarizer, but the required angle is not known *a priori*. The polarizer and analyzer must be rotated independently of each other to cause extinction of the transmitted light. This is a two-parameter search space.

Srinath and Keshavan [121] and Srinath and Sarma [122] have described a fast iterative procedure to determine these characteristic directions with a standard polariscope. The key to their approach is to decouple the polarizer and analyzer. First the polarizer is rotated until the transmitted light intensity is minimized. Then the analyzer is rotated to reduce this intensity even further if possible. Then the polarizer and analyzer are alternately rotated until the transmitted intensity cannot be minimized further. When this occurs the polarizer will be oriented along one of the primary principal directions and the analyzer will be oriented along one of the secondary principal directions. Srinath and Keshavan [121] show that the transmitted light intensity is reduced each iteration by a factor of $\cos^2 \delta$ and they claim that the primary and secondary directions can usually be found within three iterations.

8.2.3 Measuring Relative Retardation in a Three-Dimensional Residual Strain Field

The compensator can also be used to measure relative retardation in the three-dimensional case, although it is not obvious how to go about it. Srinath [121, 122] states that it is possible to use a circular polarimeter in the standard configuration to measure retardation, but does not go into detail. The presence of the rotator in the optically equivalent model is the issue. Should the analyzer be crossed with the polarizer (the primary axis), or should it be crossed to the secondary axis? Should the second quarter-wave plate be crossed with the first quarter-wave plate, or should it be adjusted to account for the rotator as well?

Physically, it would seem that the rotator can be ignored in the case of a circular polarimeter. The light entering the rotator is already circularly polarized, adding an extra rotation should be irrelevant. This seems to be what Srinath was suggesting when he spoke of a circular polarimeter in a standard configuration.

In order to test this hypothesis an analysis was made of the effect of a three-dimensional birefringent specimen on polarized light in a circular polarimeter. The analysis was done using the Mueller calculus.

Mueller [123] proposed a vector representation of polarized light in the late 1940's. Instead of trying to represent the polarization state of the light directly, Mueller used a collection of four experimentally measured parameters called the Stokes parameters. The parameters are all real and are collected into a vector called the Stokes vector S.

A good explanation of the significance of the Stokes parameters may be found in Huard [53]. The parameters are all related to the intensity of the polarized light. The first parameter, I, is the overall intensity of the light and can be measured

with a photocell. The remaining parameters can also be measured experimentally by passing the light through various linear and circular polarizers and measuring the intensity of the transmitted light, as discussed by Gerrard [54].

The Mueller representation of polarized light is linear. An optical element can be represented by a 4× 4 real matrix known as the Mueller matrix, M. The effect of the element on polarized light is given by:

$$S_{out} = MS_{in} \tag{8.5}$$

For a series of n optical elements with Mueller matrices M_i the output polarization is given by:

$$S_{out} = M_n M_{n-1} \cdots M_2 M_1 S_{in} \tag{8.6}$$

In Appendix D Equation 8.6 is used to calculate the intensity of light transmitted through an optically equivalent model of a three-dimensional birefringent specimen in a circular polariscope in a standard configuration. Assuming without loss of generality a horizontally oriented polarizer, that configuration is as follows:

1. Ideal linear polarizer (the "polarizer") with $\theta = 0°$
2. Ideal quarter-wave linear retarder with $\theta = 45°$
3. Ideal linear retarder with retardation δ and fast axis at angle α
4. Ideal rotator of strength ρ
5. Ideal quarter-wave linear retarder with $\theta = 135°$
6. Ideal linear polarizer (the "analyzer") with $\theta = 90°$ (dark-field circular polarimeter) or with $\theta = 0°$ (light-field circular polarimeter)

The final result of the calculation in Appendix D is that the intensity of the transmitted light as it exits the dark-field circular polariscope is

$$I \propto \sin^2 \frac{\delta}{2}, \quad I = 0 \text{ for } \delta = 2n\pi \tag{8.7}$$

The intensity as it exits the light-field circular polariscope is

$$I \propto \cos^2 \frac{\delta}{2}, \quad I = 0 \text{ for } \delta = (2n+1)\pi \tag{8.8}$$

The final intensity is a function of the retardation only and is independent of the primary axis orientation and the rotator strength. The final intensity is identical to that produced by a two- dimensional birefringent specimen of the same retardation placed in a circular polarimeter, as shown by Dally [47]. Therefore a compensator can be used to measure the birefringence of a three-dimensional specimen using the same procedure as for a two-dimensional specimen.

As shown in Section 8.1.2, in the two-dimensional case the compensator must be aligned with the principal axes and the compensator can be inserted on either side of the part. The three-dimensional procedure is similar. If the compensator is inserted between the polarizer and the part it must be aligned with the primary principal direction with the larger principal strain. If the compensator is inserted between the part and the analyzer then it must be oriented along the corresponding secondary principal direction.

When the compensator is aligned in this way the retardation introduced by it will be additive with the retardation in the part at that point. The compensator is then adjusted until a black fringe moves over the point of interest. The reading on the compensator equals the amount of retardation in the part at that point.

8.3 The Effect of the Flow Field and Packing Pressure on Residual Strain

The residual strain fields of the solidified specimens produced by the optical access mold were measured using the Vishay 080 Teaching Polariscope and accessories described in Section 2.9. All specimens were made at flow rates of 11.5 cm^3/s and melt temperatures of 245° C. Eight specimens were made at each of the following nominal packing pressures: 11.0 MPa, 16.5 MPa and 27.6 MPa. The parts were packed at the specified pressures for ten seconds, the maximum allowed by the VS-33 injection molding machine.

8.3.1 Residual Strain Near the Cavity Walls

The specimens were first examined in a circular polariscope to compare their isochromatic fringe patterns. These fringes were functions of the retardation only as described in Section 8.2.3. A representative image of the fringe patterns for an unpacked specimen in both the dark-field and light-field polarimeters is shown in Figure 8.2. A representative image of the fringe pattern for a packed specimen in both the dark-field and the light-field polarimeters is shown in Figure 8.3.

The specimens themselves are larger than the aperture of the Vishay 080 Teaching Polariscope, so a series of three images were taken with a digital camera on a tripod, moving the specimen as needed to get full coverage of the specimen in the three photos. In all of the photos the polariscope was set with the polarizer and analyzer parallel to the specimen edges. The photos were then undistorted using the MATLAB package described in Section 2.6.2. The images were then cropped to show only the specimen itself, and these images were merged using the Adobe Photoshop Elements 2.0 Photomerge function. Since the Photomerge function is automatic the

user cannot control the output to ensure the correct aspect ratio of the part. The photos are therefore not suitable for data extraction, but are provided as a visual reference.

A series of photos was also taken of specimens in a larger plane polariscope, the same polariscope as shown in Figure 2.29. The plane polariscope aperture was large enough to allow an entire specimen to be photographed. Digital photographs were taken of the specimens in the plane polariscope with the polariscope axes aligned with the specimen edges (0° polariscope orientation) and at 45° to the specimen edges. The specimens were photographed with a millimeter scale to allow measurements to be made. The photographs were then undistorted using the MATLAB package described in Section 2.6.2. The undistorted images were then cropped. The images are shown in Figures 8.6 through 8.9.

The circular polariscope photos (Figures 8.2- 8.5) show isochromatic fringes, fringes that are due to retardation only. The dark-field photos show the ordinal fringes ($n = 0, 1, 2 \ldots$) while the light-field photos show half-order fringes ($n = 0.5, 1.5, 2.5 \ldots$). The striking feature of these photos is that fringes are parallel to the edges of the specimens. The number of fringes and their penetration toward the center of the part both increase as the packing pressure increases.

The plane polariscope photos (Figures 8.6- 8.9 show a superposition of isochromatic fringes due to retardation and isoclinic fringes due to orientation of the residual strain axes in the specimens. The images taken at 0° polarimeter orientation with respect to the specimen edges are particularly interesting. The regions near the wall are dark, almost black. Polarimeter measurements taken in the near-wall regions gave two interesting results:

- The rotator angle for points near a wall was zero.

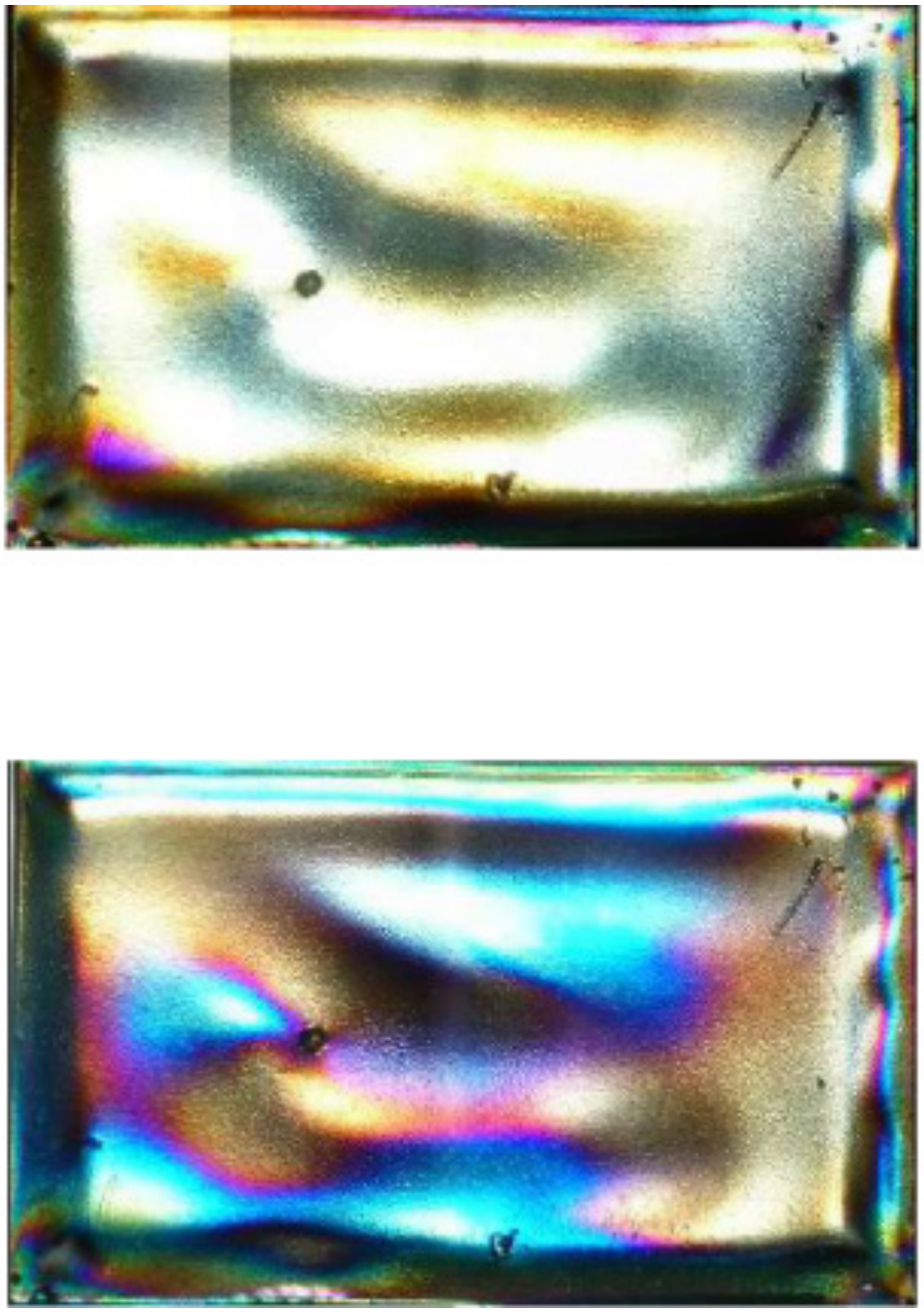

Figure 8.2: Unpacked sample viewed in a dark-field circular polarimeter (top) and a light-field polarimeter (bottom). The gate is in the lower left corner.

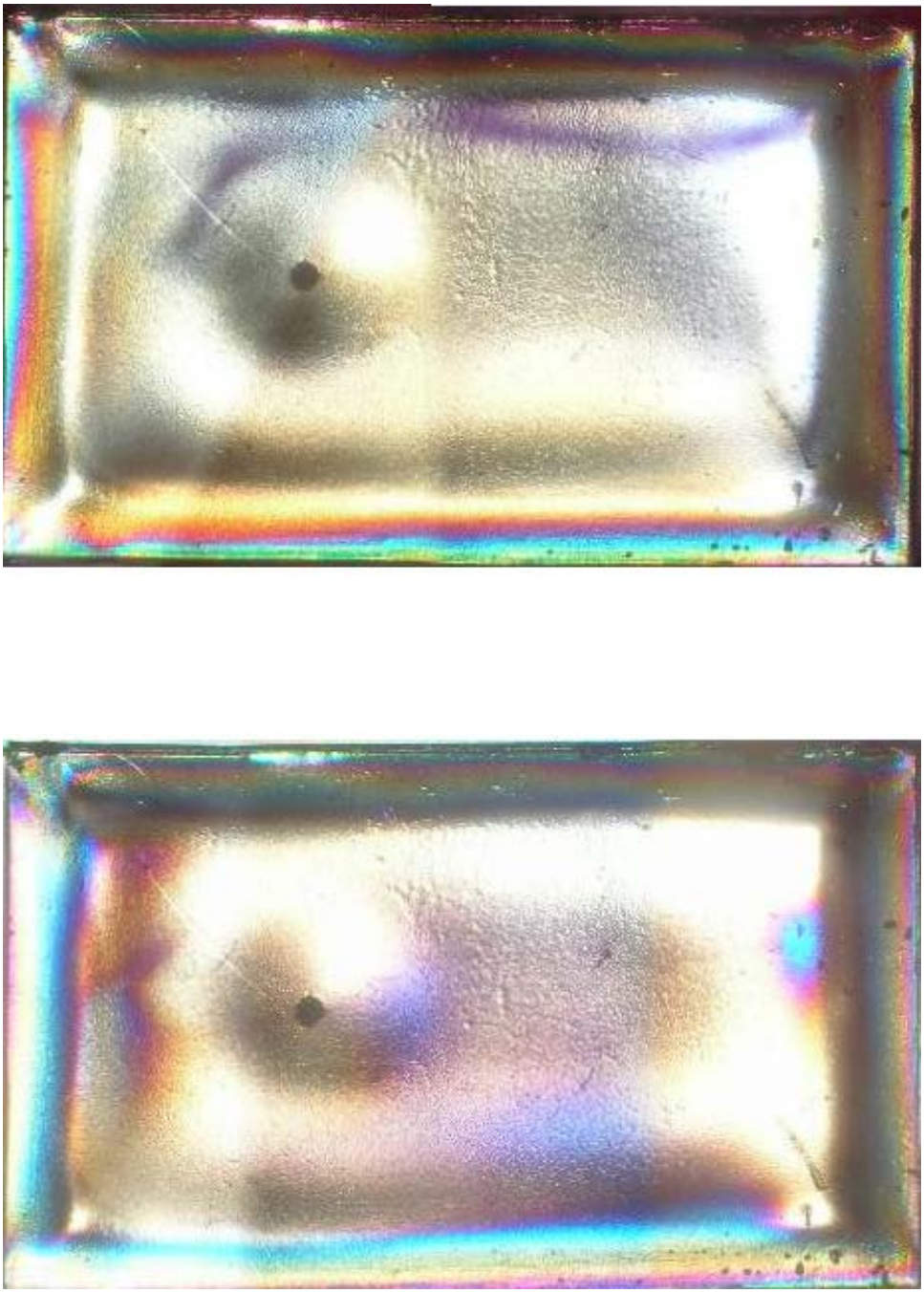

Figure 8.3: Sample packed at 11.0 MPa viewed in a dark-field circular polarimeter (top) and a light-field polarimeter (bottom). The gate is in the lower left corner.

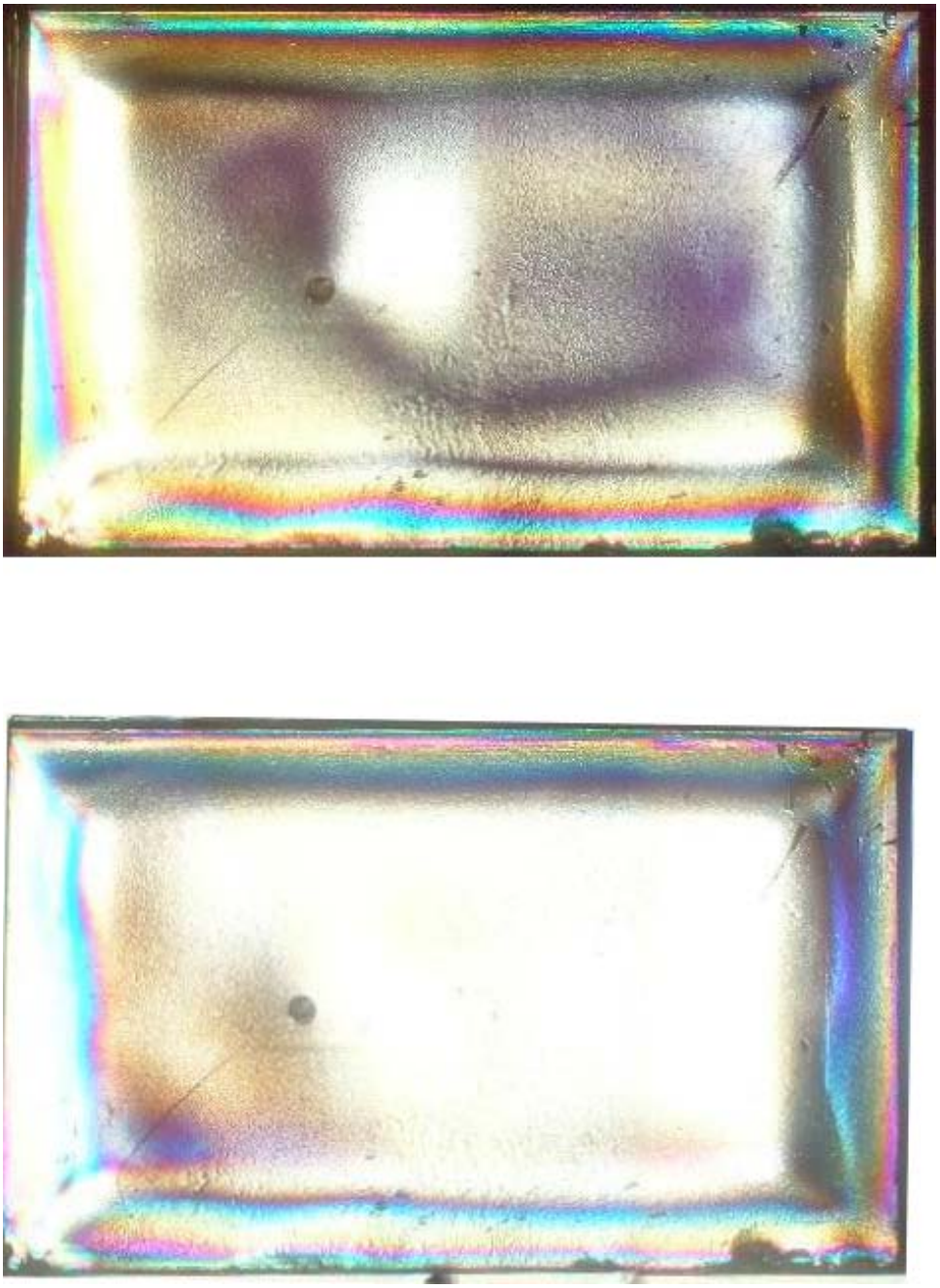

Figure 8.4: Sample packed at 16.5 MPa viewed in a dark-field circular polarimeter (top) and a light-field polarimeter (bottom). The gate is in the lower left corner.

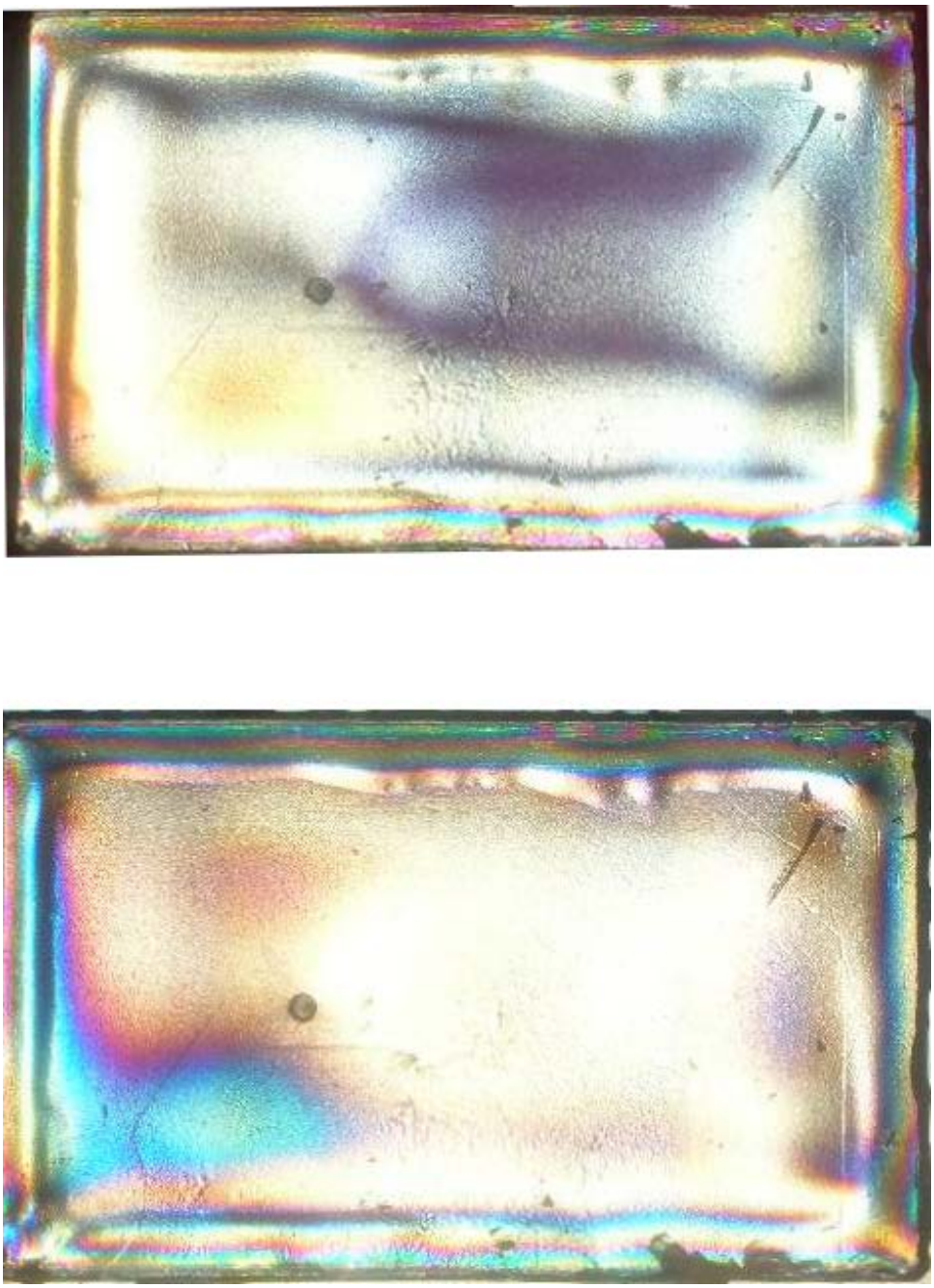

Figure 8.5: Sample packed at 27.6 MPa viewed in a dark-field circular polarimeter (top) and a light-field polarimeter (bottom). The gate is in the lower left corner.

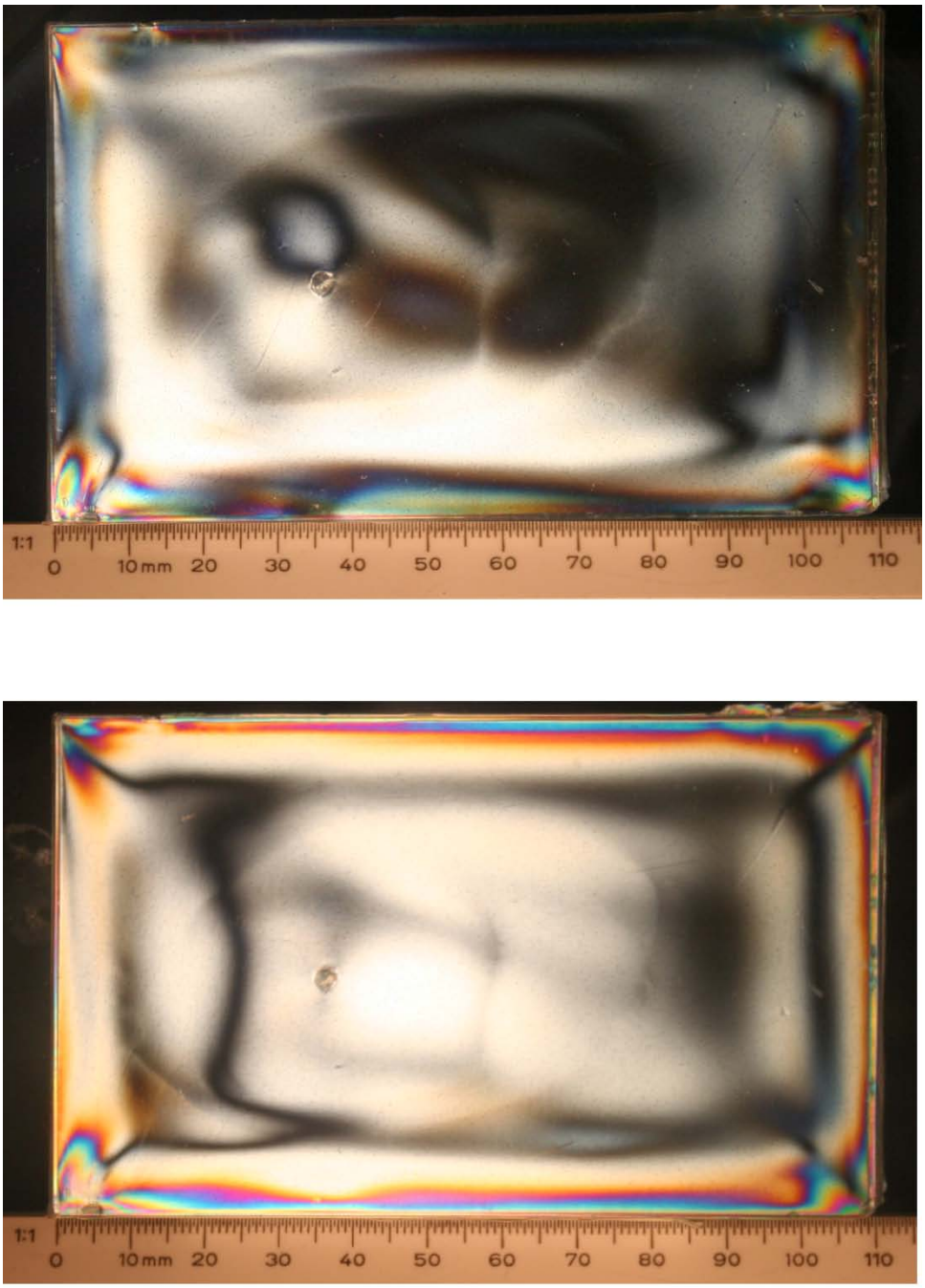

Figure 8.6: Unpacked sample viewed in a plane polarimeter with primary axes oriented parallel to the specimen edges (top) and at 45° to the specimen edges (bottom). The gate is in the lower left corner and the scale is in millimeters.

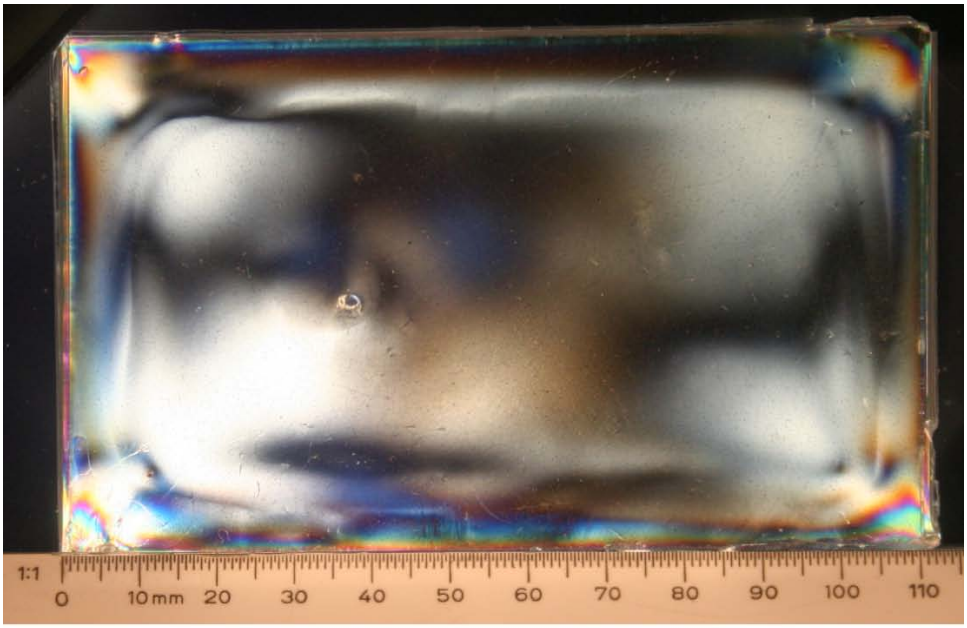

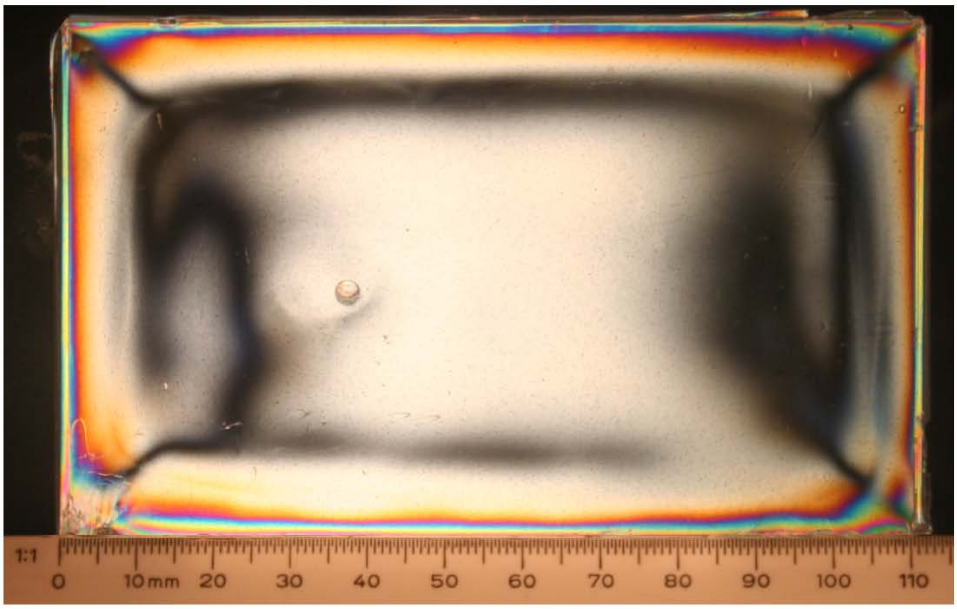

Figure 8.7: Sample packed at 11.0 MPa viewed in a plane polarimeter with primary axes oriented parallel to the specimen edges (top) and at 45° to the specimen edges (bottom). The gate is in the lower left corner and the scale is in millimeters.

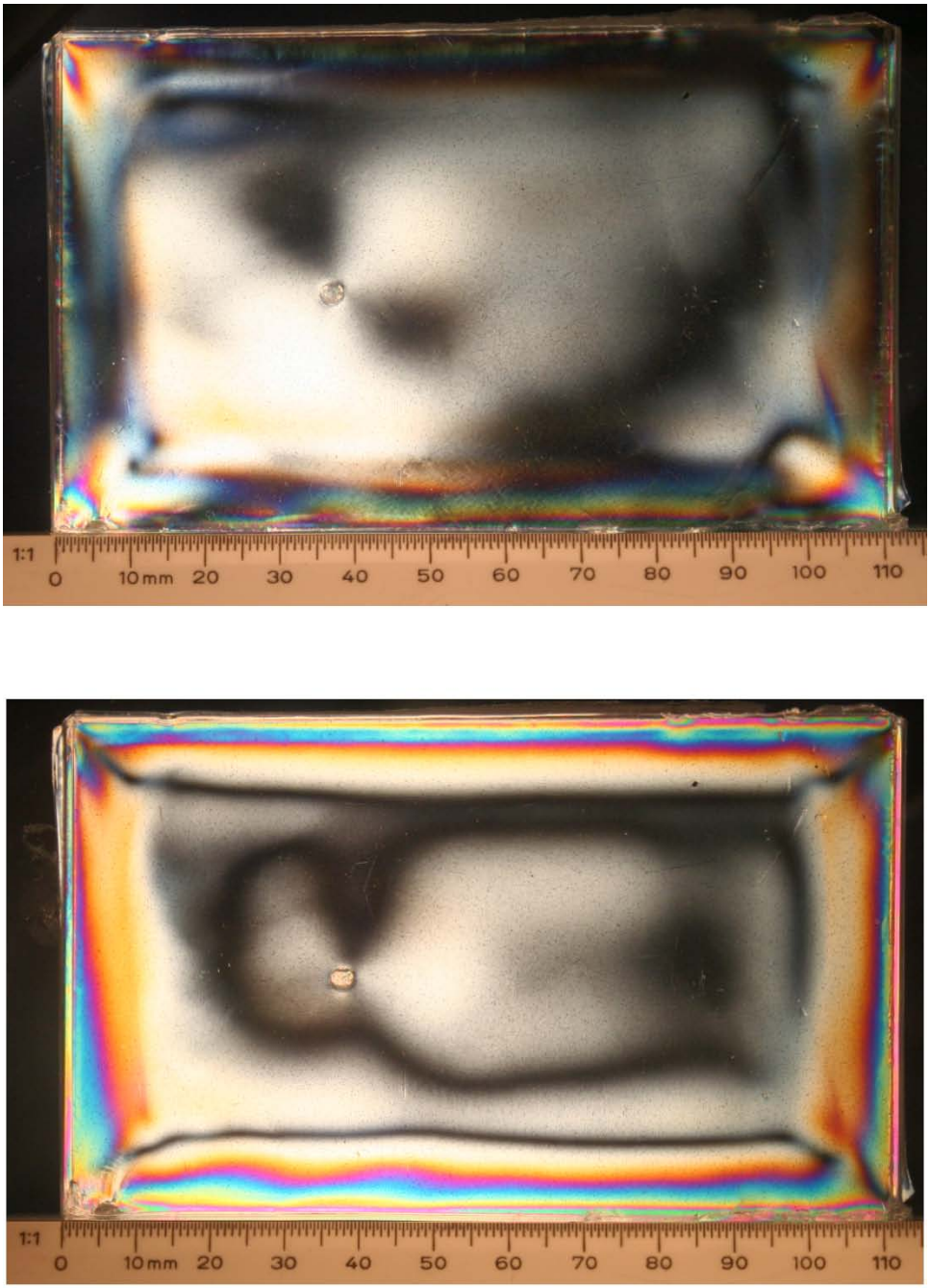

Figure 8.8: Sample packed at 16.5 MPa viewed in a plane polarimeter with primary axes oriented parallel to the specimen edges (top) and at 45° to the specimen edges (bottom). The gate is in the lower left corner and the scale is in millimeters.

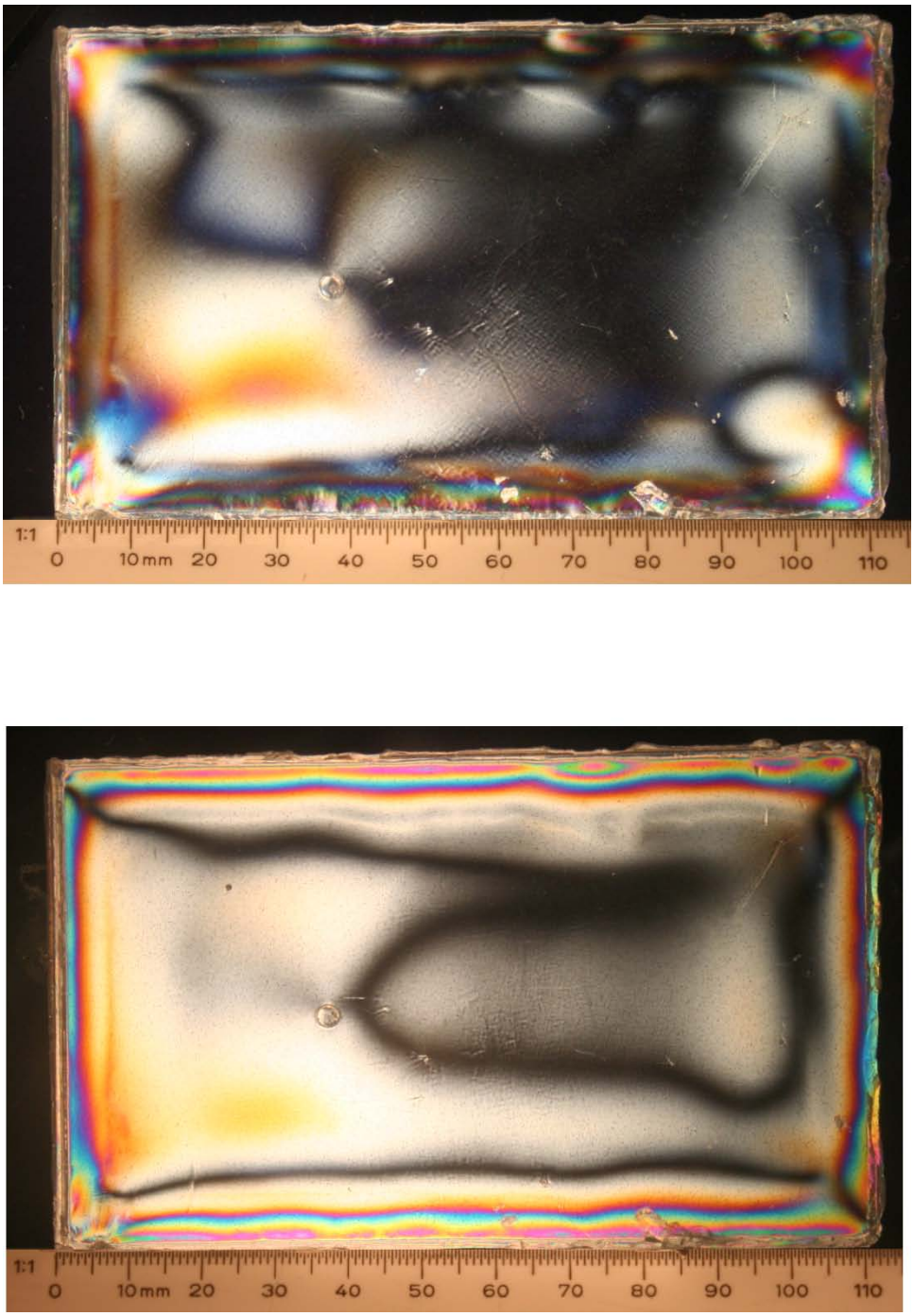

Figure 8.9: Sample packed at 27.6 MPa viewed in a plane polarimeter with primary axes oriented parallel to the specimen edges (top) and at 45° to the specimen edges (bottom). The gate is in the lower left corner and the scale is in millimeters.

- The primary axes for points near a wall were parallel and perpendicular to the wall

The images taken at 45° polarimeter orientation to the specimen edges are also interesting. The color fringes near the walls are isochromatic fringes, fringes of constant retardation. The black fringes are isoclinics, showing areas in the specimen whose primary axis orientation is at 45° to the specimen edges. Polarimeter measurements taken near the corners gave two interesting results:

- The rotator angle for points near the corner was zero.
- The primary axes for points on the corner angle bisectors were parallel to the angle bisectors (at 45° to the edges)

These observations lead to an interesting set of conclusions:

- The residual strain field near the edges of the specimen is two-dimensional
- The primary axes of the residual strain tensor near the edges of the specimen are parallel and perpendicular to the edges of the specimen, and parallel to the corner-angle bisector near the corners.
- The retardation near the specimen edges is constant along planes parallel to the edge

The conclusion about the two-dimensionality of the residual strain field near the edges of the specimen follows directly from the observation that the rotator strength is zero in these regions. The three-dimensional, three-parameter Poincaré model degenerates into the two-dimensional, two-parameter model for a linear retarder. The conclusion about primary axis orientation comes from the near-wall measurements

made with a plane polarimeter at 0° orientation to the specimen edges, and is also evidenced by the black regions near the wall in Figures 8.6- 8.9. The conclusion about the retardation comes from near-wall measurements made with a circular polarimeter and is also evidenced by the color fringes in Figures 8.2- 8.5.

These conclusions deal with the two-dimensionality of the residual strain field near the edges of the part and are primarily based on measurements of the the primary angle and rotator strength. Since the field does appear to be constant through the thickness of the specimen in these regions, thickness variations due to draft have no effect on the measurements.

The two-dimensionality of the residual strain field near the walls can be explained by examining the fluid flow of the polymer during the filling stage. The region near the walls of the cavity are the regions of the highest shear stress and shear stress gradients during the filling phase. The orientation of the flow in these regions is also very uniform throughout the entire shot, as shown in Figures 5.1- 5.12. The high shear stress and shear stress gradient would be expected to give a very uniform molecular orientation near the walls, with the long-chain polymer molecules oriented parallel to the walls. The uniformity of the flow orientation throughout the entire shot would lead to uniformity of molecular orientation through the thickness since the flow orientation in the quickly solidified skin would be same as in the more slowly solidifying core, leading to a two-dimensional residual strain field.

8.3.2 Residual Strain in the Interior Region

Six points in the interior of the specimens far from the cavity walls were then examined in the Vishay 080 Teaching Polariscope, see Figure 8.10. The three constants of the optically equivalent model were measured: the primary axis orientation, the

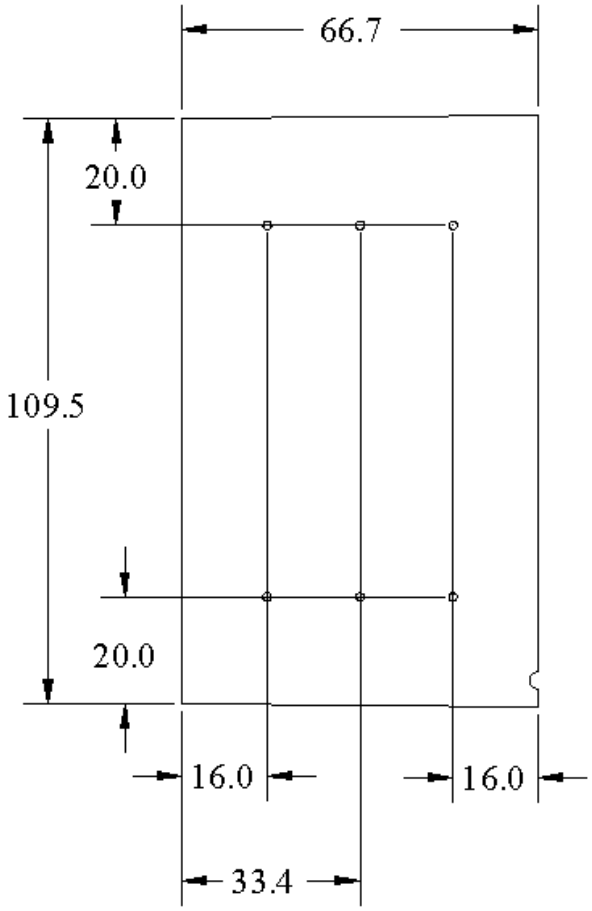

Figure 8.10: Locations of the birefringence measurements. The gate is in the lower right corner. All dimensions are in millimeters.

retardation, and the rotator strength. These quantities were measured following the procedures outlined in Section 8.2.2 and Section 8.2.3.

In the case of a two-dimensional residual strain field the measured angular retardation is linearly proportional to the specimen thickness at a given point (see Equation 8.1. A nondimensional retardation can be defined that takes thickness variations into account using Equation 8.2:

$$\delta^* = \frac{\delta_l}{h} = N\frac{\lambda}{h} \tag{8.9}$$

where N and h are the fringe order and thickness at a given point, and λ is the design wavelength of the polarimeter.

In a three-dimensional residual strain field the retardation is no longer directly proportional to specimen thickness, yet it is reasonable to account for thickness variations in the same way. Due to the draft present in the optical access mold the specimen thickness is not constant even in highly packed parts. In lightly packed or unpacked parts there is a further thickness variation due to uneven shrinkage of the part away from the mold surfaces. For each specimen in the present work the thickness was measured at each of the six measurement locations using a micrometer with conical tips. These measurements were then used to calculate the values of δ^*.

The measurement data for the primary axis orientation α, rotator strength ρ, and nondimensional retardation δ^* can be found in Appendix E.

In contrast to the near-wall region, the rotator strength in this region was not zero. The residual field in the interior region was three-dimensional, not two-dimensional.

A major difference between the interior region and the wall region is that the flow velocity orientation does not remain constant in the interior region. The velocity orientation at the beginning of the shot determines the molecular orientation in the frozen layers at the top and bottom of the part. The orientation at the end of the shot determines the molecular orientation in the core of the part. Since these orientations are different in the interior region of the part the resulting residual strain field is three-dimensional.

8.3.3 The Influence of the Flow History and Packing Pressure on the Residual Strain Field

In order to investigate the influence of packing pressure and flow history on the residual strain field two-way ANOVA analyses [100] were performed on the primary axis orientation, the retardation and the rotator strength data. The ANOVA factors considered were position and packing pressure, where the position factor can be thought of as a flow history factor. The goal of the analyses was to see if these factors had a statistically significant effect on the optically equivalent model parameters.

The two-way ANOVA analysis was carried out with the null hypotheses that packing pressure and position had no effect on the measured values of primary axis orientation, rotator strength, and retardation. The tests were carried out at the 5% significance level using the MATLAB `anova2` function. The statistical significance as a function of p-value used follows that described by Koopmans [100] and is shown in Table 5.3.

Both position and packing pressure have significant effects on the retardation and rotator strength, but their interactions are not significant factors. The packing pressure is only a mildly significant factor in determining primary axis orientation. Position is a significant factor, and the interaction of position and packing pressure is significant, but the packing pressure itself is not significant.

A physical explanation of this can be made by equating the position factor with flow history. Each different position in the solid part experienced a different flow history. The flow history has a significant effect on the orientation of the long-chain polymer molecules in the molten state and in the solid state. Thus it is reasonable to expect that position (and thus flow history) have a significant impact on the primary axis orientation, the rotator strength and retardation.

Table 8.2: Resulting p-values from the two-way ANOVA analyses examining the effect of position and packing pressure on primary axis orientation α, retardation δ, and rotator strength ρ.

Significance of Position

Factor	p-value	Significance
α	6.60×10^{-6}	Highly significant
δ^*	2.26×10^{-6}	Highly significant
ρ	0.0256	Significant

Significance of Packing Pressure

Factor	p-value	Significance
α	0.0669	Mildly Significant
δ^*	1.86×10^{-4}	Highly significant
ρ	0.0158	Significant

Significance of Position and Packing Pressure Interaction

Factor	p-value	Significance
α	4.00×10^{-3}	Highly significant
δ^*	2.49×10^{-4}	Highly significant
ρ	0.3843	Not significant

Figures 8.2 through 8.5 demonstrate that packing pressure has an obvious effect on the polarimeter fringe pattern, and thus on the retardation. It is less obvious why packing pressure should be significant for rotator strength and less significant for primary axis orientation. One possible way of explaining this result would be to assume that the primary axis orientation is determined by by the highly oriented skin of the specimen and that the rotator strength is determined by the more amorphous core of the specimen.

The fountain flow effect causes the frozen molecular orientation of the top and bottom surface of the part to be set during the filling stage of the flow. The orientation of the top and bottom layers should be equal due to the symmetry of the flow. The orientation of the core of the specimen is set during the later phase of the flow, including the packing phase since the core is molten during the packing phase. The application of packing pressure will effect the orientation of the core since the core is still solidifying, but it will have little effect on the orientation of the frozen layer at the top and bottom of the part.

Therefore the solid part can be thought of as a stacked series of three plates: two highly oriented plates with equal primary axes sandwiching a third, less oriented plate with a possibly different primary axis orientation. If this third plate has roughly the same orientation as the other two plates the rotator strength would be zero, as shown by the integral Wertheim law in Equation 8.4. The rotator strength will grow larger as the difference in orientation between the core and the skin grows larger.

Since the packing pressure only affects the core of the specimen it would have a strong effect on rotator strength but only a second order effect on the primary axis orientation. This shows up in the ANOVA analysis as a mildly significant effect of the packing pressure on primary axis orientation but a significant effect on rotator

strength.

The p-value of the effect of packing pressure on the primary axis orientation was found to be mildly significant at the 5% significance level. Further statistical testing was performed to investigate the validity of this finding. The ANOVA procedure assumes that the data being studied has a normal distribution. A Lilliefors test [124] was used to test the normality of the birefringence data.

The normality of the data was tested by examining sets of data taken from specimens molded under the same conditions. As mentioned above, there were four different packing pressures used, and birefringence measurements were made at six points on each plaque. Eight specimens were measured from each packing pressure. This leads to 24 combinations of packing pressure and position, with eight replications at each combination. Three different birefringence measurements were made at each point (primary axis orientation, rotator angle, and retardation). This gives a total of 72 data sets, with each set having a unique combination of measured quantity, position, and packing pressure. These 72 data sets all had eight measurements. The Lilliefors test was performed for each of these 72 data sets to test their normality.

The Lilliefors test uses the Kolmogorov-Smirnov statistic to perform a two-sided goodness-of-fit test to determine if a given distribution comes from a normal distribution. The Lilliefors tests in the present work were performed with the null hypothesis that the birefringence data were drawn from normal distributions. The tests were performed at the the 5% significance level. The MATLAB `lillietest` function was used to perform the calculations. The results of these tests are tabulated with the raw data in Appendix E. A total of 19 of the 72 distributions (26.4%) failed the Lilliefors test for normality, indicating that the distributions did not wholly meet the assumption of normality made by the ANOVA analysis.

A Friedman analysis [125] was then performed to further investigate the significance of packing pressure and position on the measured residual strain field parameters. A Friedman analysis is similar to an ANOVA analysis except that it relaxes the assumption that the data is drawn from a population with a normal distribution [125]. In a Friedman analysis it is assumed that the data is drawn from a population with a continuous, but not necessarily normal, distribution. The Friedman analysis treats each factor separately and does not test for interactions.

The Friedman tests were carried out with the null hypotheses that packing pressure and position had no effect on the primary axis orientation, rotator strength, and retardation measurements. The tests were carried out at the 5% significance level using the MATLAB function `friedman`.

The results of the Friedman analyses are shown in Table 8.3. The resulting p-values are different from those of the two-way ANOVA tests shown in Table 8.2, but the conclusions are similar. Position and packing pressure are both highly significant factors for rotator strength and retardation. Position is also a highly significant factor for primary axis orientation. Packing pressure in not a significant factor for primary axis orientation ($p = 0.3339$). This is a stronger result than the corresponding ANOVA analysis, which showed that packing pressure was a mildly significant factor for primary axis orientation ($p = .0669$). But the two tests are in basic agreement. The packing pressure and position are significant factors affecting the retardation strength and rotator strength. The position is also a significant factor on primary axis orientation. The packing pressure is a much less significant factor on primary axis orientation.

In conclusion, the flow history has a number of important effects on the residual strain:

Table 8.3: Resulting p-values from the Friedman analyses examining the effect of position and packing pressure on primary axis orientation α, retardation δ, and rotator strength ρ.

Significance of Position

Factor	p-value	Significance
α	1.16×10^{-5}	Highly significant
δ^*	3.35×10^{-5}	Highly significant
ρ	3.22×10^{-3}	Highly significant

Significance of Packing Pressure

Factor	p-value	Significance
α	0.3339	Not Significant
δ^*	9.60×10^{-4}	Highly significant
ρ	1.26×10^{-3}	Highly significant

- Near the walls the residual strain field is two-dimensional and the primary strain axes parallel the walls. This is a flow artifact independent of packing pressure.
- Packing pressure increases the observed number of fringes near the walls.
- In the interior of the cavity the strain field is three-dimensional.
- The primary axis orientation of the equivalent optical model is a function of position with packing pressure a second order effect.
- Position and packing pressure are both significant factors for retardation and rotator strength in the interior of the cavity.

CHAPTER 9

Summary and Conclusions

9.1 Summary

Flowing polymer melts have been studied using a variety of optically accessible molds since the 1950s. Much of this early work was qualitative rather than quantitative. Flow front tracings and mold pressure measurements provided some quantitative data, but melt velocity fields were beyond the reach of the experimental methods available at the time.

Experimental methods in non-Newtonian fluid mechanics have advanced rapidly, although the adoption of techniques such as Particle Image Velocimetry (PIV) has been slower than in Newtonian fluid experiments. The use of PIV in non-Newtonian flows has grown in the last ten years, but due to the wide variety of non-Newtonian effects these experiments have been on model fluids in simplified geometries at standard temperatures and pressures.

For this thesis a series of PIV experiments has been performed using an industrial polymer in an optical access mold in an industrial injection molding machine. Studies of the filling phase have been performed under different injection rates and melt temperatures. The velocity vector fields have been measured, analyzed and evaluated. The vector fields were checked for consistency with the imposed flow rates and

a scaled version of the continuity equation was employed to evaluate the resulting vector fields.

The PIV vector fields were then compared to Moldflow simulations of the same flows. The Moldflow data was formatted and displayed on the same grid as the PIV data and the same analyses were performed. The accuracy of the Moldflow vector magnitudes and orientations was measured. The Moldflow simulation velocity vectors were, for the most part, within $\pm 1.7^{\circ}$ of the experimentally measured velocity vectors. The magnitudes of the cavity-thickness averaged velocities were also found to be accurate for the bulk of the flow, but significant deviations were found near the walls and flow front. These deviations are caused by Moldflow's use of the Hele-Shaw model and the inability of the Hele-Shaw model to impose no-slip boundary conditions at the cavity walls.

The vector fields during the filling phase were found to scale linearly with the flow rate, leading to the conclusion that the flow kinematics were Newtonian in nature for this weakly elastic polymer in this simple geometry. The measured gate pressures, however, showed strong evidence of shear-thinning behavior. An analytical power-law model was proposed that accurately predicted the shape of the pressure curve in both the radial and channel flow regimes of the mold filling phase. The model of the radial flow pressure rise was used to successfully calculate the power-law exponent. The power-law coefficient was also predicted from the pressure traces, but with somewhat less success when compared with results from standard rheological tests.

The packing flow of the polymer melt was also studied. PIV vector fields were measured for the influx of polymer melt during the packing phase. These fields showed a high level of variability that increased with time and decreased with packing pressure magnitude. The velocity fields, gate pressure traces and final part masses

were used to estimate the mass flow rate into the mold during packing as a function of time. An analytical model was then constructed to predict the mass flow rate into the mold during packing. The model included melt compressibility and solidification effects. The model predictions were then compared with the mass flow rate curves generated from the experimental data.

The residual stress fields of the solidified parts were then studied using a polariscope. The polariscope was capable of generating plane polarized or circularly polarized light, but it was intended to measure two-dimensional residual stress fields. Injection molded parts may be expected, in general, to have three-dimensional residual stress fields. Detailed measurements of the internal residual stress fields were not possible, but it was possible to measure the three components of the Poincaré optically equivalent model of the three-dimensional field. These three parameters include a primary axis orientation, a retardation, and a rotator strength.

It was found that the residual stress field near the edges of the part were two-dimensional in character since the measured rotator strength was zero. The fringes were parallel to the edges as well, with higher order fringes appearing at higher packing pressures. The two-dimensionality of the field along the edges was likely due to the fact that the polymer melt experiences the highest shear stresses near the walls of the cavity, and that these stresses are uniform through the thickness of the part. These high, uniform shear stresses cause the molecular orientation to align with the cavity walls causing the primary stress axes to be parallel to the walls and the rotator strength to be zero.

Far from the walls, however, the residual stress field was found to be three-dimensional. This was indicated by the measurement of non-zero rotator strengths at points far from the walls. An analysis of variance (ANOVA) was performed to see

if the position (or flow history) and packing pressure levels were significant factors in explaining the observed variance in primary axis orientation, retardation, and rotator strength.

9.2 Conclusions

This work led to the following conclusions. These results are new and unique to the present work except as noted below.

1. PIV is possible in a polymer melt in an injection molding machine.

Chapter 3 explores the theoretical and practical consequences of attempting PIV in an injection molding machine. The relevant issues are summarized in Table 3.2. The extremely low Reynolds number and the blunt velocity profile through the cavity thickness produced by the shear-thinning polymer are positive factors in performing a PIV experiment and help to minimize velocity bias errors (Figure 3.2. The moving flow front and fountain flow effect make PIV difficult near the front. The strong radial flow at the gate produces a dead zone in which the PIV analysis fails (Equations 3.16 and 3.17). This dead zone is a function of camera frame rate and decreases with increasing frame rate. The high temperatures and pressures call for a robust optical window design. The high shear rates present in the barrel of the injection molding machine mandated the use of metal particles. These particles needed to be mixed in the solid state with the plastic pellets. The high viscosity of the polymer was sufficient to drag the particles at the local fluid velocity despite their weight, enabling their use in PIV (Equations 3.27 and 3.28).

2. The flow kinematics in the optical access mold scale linearly with injection rate.

Figures 5.1-5.12 show the PIV vector fields for specimen made at the conditions listed in Table 5.1. A control surface analysis was employed to examine the consistency of the PIV results with each other. Figure 5.14 shows that the calculated volume flow rates are consistent with each other when normalized by the calculated volume flux of the 11.5 cm^3/s run. Best fit scaling factors were found between the vector fields from different tests. These scaling factors were found to deviate from the ratio of injection rates by less than 5% on average. The portions of the fields that remained after accounting for this scaling factor were also examined. These residual fields were found to be small in all cases as shown in Figure 5.19. The residual fields were then correlated with each other to see if there were any flow structures that persisted from one set of molding conditions to another. The distribution of the correlations were statistically indistinguishable from that of a uniform distribution as shown in Figure 5.21 and Figure 5.22. Thus, the flow kinematics in the optical access mold scale linearly with injection rate.

3. Moldflow accurately predicts velocity orientation and average velocity magnitude in the bulk of the flow. Moldflow does not accurately predict the velocity field near the cavity walls and flow front.

The Moldflow simulation results were plotted on the same grid as the PIV vectors and were plotted and analyzed in the same fashion as the PIV vectors. The velocity vector fields resulting from the Moldflow simulation are shown in Figure 5.27 and Figure 5.28. The Moldflow simulations also scaled linearly with injection rate. The best-fit scaling factor between any two flows deviated from the ratio of injection rates by an average of 0.2%.

However, Moldflow's predictions of flow front shapes are not realistic, as seen in Figure 5.35. The differences between the simulated fronts and actual fronts are shown in Figure 5.36 and Figure 5.37.

Moldflow does a much better job simulating the melt-flow velocity vectors. The simulations were compared to the PIV data. Figure 5.38 shows the difference between the simulated vector orientations and the PIV vector orientations. The mean angular difference over the whole field was 1.7°, although larger deviations were seen near the cavity wall and corner opposite the gate.

Two different methods were used to assess the accuracy of Moldflow's velocity vector magnitudes. This was necessary since Moldflow reports thickness-averaged velocities, not midplane velocities. The first method was to use the PIV vectors to estimate the thickness-averaged velocities. This was done using a profile factor of 0.7 calculated from Figure 5.15. The ratio of the PIV estimated average velocities to the Moldflow average velocities is shown in Figure 5.39. The mean of this ratio for the entire field was 0.998 with a standard deviation of 0.25. Regions near the walls and flow front fared worse than regions near the center of the field.

A second method of comparing the magnitude of the simulation to the magnitude of the PIV data was to have Moldflow calculate midplane vectors. This did not produce a good comparison. Moldflow uses the Hele-Shaw approximation, and this approximation does not conserve mass except in an average sense as shown in Equation 5.17 and illustrated in Figure 5.41. Another problem lies in the fact that Moldflow assumes a parabolic velocity profile with a profile factor of 0.6 through the cavity thickness even though it has access to models of the material viscosity as shown in Figure 5.40.

The ratio of the PIV midplane vectors to the Moldflow prediction of midplane

vectors is shown in Figure 5.42. The mean ratio across the entire field is 0.87 with a standard deviation of 0.37. The sub-unity mean ratio is due to difference in profile factors between the simulation and the real flow, which has a profile factor of approximately 0.7. The ratio of these two profile factors is 0.86.

4. The flow dynamics in the optical access mold exhibit shear-thinning behavior. The gate pressure can be used to measure the shear-thinning exponent of the polymer melt.

An analytical model of the gate pressure during the radial flow portion of the mold filling is given in Equation 6.15. This model is an extension of a power-law exercise presented by Bird [63]. The power-law coefficient and exponent are decoupled in this equation, and a best-fit curve to this equation has been used to estimate the power-law parameters. The best-fit curves of Equation 6.15 are shown in Figure 6.9 for the two data sets at 34.5 cm^3/s. The power-law exponent was predicted successfully to within 0.4% of the value measured by a capillary rheometer, with the predicted n=0.4063 and the value extracted from the rheometer data being n=0.4079. A reference stress based on the extracted values of n and m at $\dot{\gamma}$= 100 s^{-1} was within 14% of the value calculated from the rheometer power-law parameters. The mean value of m based on the reference stress was defined in Equation 6.18 and was equal to 2660 $Pa{\cdot}s^n$, a value within 9.5% of the value of m=2940 $Pa{\cdot}s^n$ calculated from the rheometer data. The results are tabulated in Table 6.2.

An analytical model of the gate pressure was also made for the channel flow regime of the mold filling process. Equation 6.25 predicts a linear rise of the gate pressure during the channel flow regime and provides an estimate of the slope. Figure 6.10 compares these predicted slopes to the actual pressure data, and the results of this comparison are tabulated in Table 6.3. The predicted slope was within 3% of the

actual slope for the 34.5 cm^3/s, 230° C run and was with in 12% for the 11.5 cm^3/s, 230° C run and for the 23.0 cm^3/s, 230° C run.

5. The flow during packing is highly variable. The variability increases as packing progresses and decreases with higher packing pressures. The variability is particularly intense along the wall region that has the highest residual stresses in the solidified specimens.

The packing PIV velocity fields are shown in Figures 7.2-7.10. A residual metric was defined in Equation 7.8 to gauge the level of variability of the packing flow. A plot of the residual metric versus time for all three packing pressure levels is found in Figure 7.14. The random component of the packing flow at the beginning of packing was between 10-20% of the mean flow and grew to be between 60-80% of the mean flow after five seconds of packing. Figure 7.14 shows that the variability of the flow increased with time for all packing pressures and decreased with packing pressure level for all times.

Figure 7.11 shows a packing PIV field with a pseudocolor overlay representing the sum of the variances of the u and v components of the velocity field. This figure shows that the variance is highest on the wall with the gate. This wall also happens to be the region of the flow with the most uniform flow history and is a region of high stress as evidenced by Figures 8.6-8.9. It is possible that the high variability in this region is due to a higher rate of stress relaxation during the packing flow.

6. The flow into the mold during packing can be accounted for using a melt compressibility model and a one-dimensional solidification model.

The mass flow into the cavity during packing was estimated from the evolution of the PIV vector fields, the packing pressure trace, and the mass of the final part using Equation 7.13. The results of this calculation are plotted in Figure 7.15. An analytical model was constructed to predict the mass flow into the mold during packing.

The model was composed of two components, mass flow due to melt compressibility and mass flow due to solidification. The compressibility model used the Tait model as an equation of state and resulted in Equation 7.11. The solidification model was based on two one-dimensional heat transfer models illustrated in Figure 7.16 and Figure 7.19. In one model the glass window is treated as an insulated surface and in the other it is treated as a constant temperature surface. The model equation is given by Equation 7.16.

The comparison of the model components with the experimental data is shown in Figures 7.20 and 7.21. The model predicts that the packed mass due to compressibility is 63.8% of the total packing mass for the 11.0 MPa case, and is 63.5% of the total for the 16.5 MPa case. The comparison of the total model with the data is shown in Figures 7.22 and 7.23. The data lies between the two model formulations, suggesting that some heat transfer to the glass window does occur, but that it is less than the amount of heat transferred to the opposite steel mold surface.

7. The three-dimensional residual stress field of a polymer specimen may be explored with a two-dimensional polarimeter using the Poincaré optical equivalence theorem

The optical equivalence theorem is described in Section 8.2.1 and is illustrated in Figure 8.1. This theorem provides three experimentally measured parameters that describe the integrated effect of the specimen on polarized light. These three parameters are a primary axis orientation, a retardation, and a rotator strength. This conclusion is not unique to this work, although a search of the literature provided scant details on how to use a two-dimensional polarimeter to measure these parameters. In particular, details about how to use a compensator to measure the retardation in a three-dimensional field were scarce. Section 8.2.3 describes a method

for doing so in detail. The method is confirmed mathematically in Appendix D where a Mueller matrix calculation is carried out to show that the polarimeter and compensator configuration described does indeed measure the retardation accurately.

8. The residual strain field in the solid parts produced by the optical access mold are two-dimensional near the cavity walls. The primary axes of the residual strain field are parallel the specimen edges in the two-dimensional region. The residual strain field is three-dimensional in the central region of the solid specimens.

Figures 8.6-8.9 show the specimens in a plane polarimeter with the polarimeter primary axes aligned with the specimen edges. The dark fringes along the edges show that the primary axis of the residual strain field is also aligned with the specimen edges. The rotator strength was found to be zero in this region, showing that the field was two-dimensional.

In the central portion of the specimens six points were selected for study, the locations of which are shown in Figure 8.10. The rotator strength was found to be non-zero at these points, indicating a three-dimensional residual strain field.

9. Position (flow history) has a significant to highly significant impact on the parameters of the Poincaré equivalent model of the solid specimens. Packing pressure is also significant, but plays less of a role in determining the primary axis orientation.

A two-way ANOVA analysis was performed with the null hypothesis that position (also considered as flow history) and packing pressure were not significant factors in predicting the values of the Poincaré parameters. Twenty-four specimens were sampled, eight specimens at each of three packing pressure levels. Six positions on each specimen measured using a polariscope and compensator. The results of this study are found in Table 8.2. Position was found to significant for rotator strength and highly significant for primary axis orientation and retardation. Packing

pressure was found to be significant to rotator strength and highly significant for retardation, but only mildly significant for primary axis orientation. This suggests that primary axis orientation is "locked in" by the flow history and is influenced by packing pressure magnitude only to a lesser extent.

9.3 Possible Future Work

The work presented here is fundamental in the sense that it presents, for the first time, a full-bodied PIV study in an industrial polymer in an industrial injection molding machine. Since this had not been done before the selection of polymer and mold cavity geometry were primarily driven by applicability and simplicity. There are a number of possible future projects that could be done to extend the research presented here.

1. Choose a mold design and polymer combination that will exhibit viscoelastic behavior.

The polymer used in the present work was shear-thinning but not strongly viscoelastic. Also, the mold cavity was a simple plaque gated at the corner. This combination did not produce any distinctly non-Newtonian behavior in the velocity fields. One possibility for a future project would be to design the experiment to specifically produce non-Newtonian behavior in the velocity fields. This would be challenging for a number of reasons. A more aggressive polymer would probably require the installation of cooling lines in the mold, complicating the design, manufacture and operation of the mold.

A more severe challenge lies in designing the mold to produce viscoelastic effects. These are typically produced in experiments by forcing the non-Newtonian fluid to flow around a corner or through a contraction. This could be done by introducing flow

obstructions into the mold cavity. In order to do this in a mold cavity perpendicular to the parting plane, as in the current work, complex coring mechanisms would have to be introduced into the mold cavity to retract the obstructing features and allow ejection of the solid part. It would be far easier to introduce obstructions into the mold if the cavity were parallel to the parting plane as would typically be done in industry. However, this would require a complete redesign of the optical access routes to the mold cavity. Mirrors would have to be introduced into the mold to allow the cavity to be visualized. In either case, the flow obstructions would have to be made of a transparent material to allow passage of the laser sheet.

2. Build and test the quality control mold proposed in Figure 6.11 and Figure 6.12

The analytic model of the gate pressure presented in Equation 6.15 successfully predicted the shear thinning exponent of the polystyrene used in the present work and proposal was made in Section 6.5.3 to build a quality control mold based on this model. It would be interesting to actually build this mold in conjunction with a turn-key data acquisition and analysis system to see if it could successfully detect variations in the shear thinning exponent between different grades of the same polymer, or between filled and unfilled versions of the same polymer. How robust would such a system be? How sensitive would it be to mold temperature or other environmental factors? Would it be of any practical use to industrial molders?

3. Design a stereo-PIV experiment to investigate particle migration across streamlines in rectangular channels

In Chapter 3 experiments were cited [93, 94] that studied particle migration across streamlines in the tubular Couette and Poiseuille flow of shear-thinning and viscoelastic liquids. The tubular geometry is not generally applicable to PIV in

injection molding. A channel geometry would be far more useful in establishing whether or not particle migration across streamlines is an issue for non-Newtonian PIV researchers. A stereo-PIV experiment could be used to explore this question. A vertical channel with glass walls could be set up to ensure that gravity does not influence the results. A steady channel flow of a non-Newtonian liquid could be established in the channel and a laser sheet introduced at the cavity midplane. A stereo-PIV experiment could be designed to dectect out-of-plane motion of the PIV particles. Does the migration happen? If so, do the particles move toward or away from the midplane? The laser sheet could be indexed to different positions off the midplane to measure the growth or decay of the out-of-plane motions as a function of distance from the midplane. Various non-Newtonian fluids could be used to attempt to correlate out-of-plane velocities with fluid properties.

APPENDICES

APPENDIX A

STYRON-615APR Characterization

This appendix presents the Datapoint Lab results and the Moldflow Testing Lab results

This appendix presents the results of rheological testing done on the polymer-particle mixture used in the present work. Two laboratories were contracted with to perform testing on this material. DatapointLabs performed capillary rheometer testing at a single temperature and cone-and-plate steady and oscillatory tests at the same temperature. Moldflow Plastics Labs performed an injection molding capillary rheometer test on the material to see if the inclusion of a typical injection molding shear history would lead to significantly different viscosity results.

Test Report: Styron 615APR

Client	Thomas Bress
Company	University of Michigan
Address	1231 Beal Ave.
	Ann Arbor, MI
	United States
Sample Received	6/25/2007
Sample Source	Client
Report Prepared	7/2/2007
Prepared By	
Title	Engineer
Issued By	
Title	Operations Manager

DatapointLabs is accredited by the American Association for Laboratory Accreditation (A2LA Certificate # 1242.01), and maintains a quality system in accordance with ISO/IEC 17025. Any opinions or interpretations expressed in this report are outside the scope of the accreditation.

The results in this report relate only to the items tested. This report shall not be reproduced except in full without the written approval of DatapointLabs.

DatapointLabs cannot be held liable under any circumstances for damages arising out of the use of this information or for claims in excess of that originally paid for the testing. DatapointLabs disclaims all other warranties, either express or implied, including implied warranties of merchantability or fitness for a particular purpose.

http://www.datapointlabs.com

95 Brown Road, Ithaca, NY 14850
Phone: 607-266-0405 Fax: 607-266-0168
Toll-Free (U.S.): 1-888-328-2422

This data is available in True Digital format

Table of Contents

Viscosity

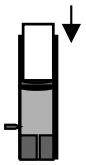

Method	ASTM D 3835 - 02 Determination of Properties of Polymeric Materials by Means of a Capillary Rheometer		
Instrument	Goettfert Rheograph 2003 Capillary Rheometer		
Specimen	type	pellets	
	drying	none	
	other preparation	none	
Parameters	initial pressure	0	MPa
	barrel diameter	12	mm
	die entry angle	180	°
	die inner diameter	1	mm
	die length	20	mm
	preheating time	6	min
Data Correction			
Precision	temperature	+/- 0.1	°C
	die inner diameter	+/- 0.0069	mm
	die length	+/- 0.025	mm
Uncertainty	per standard		

Polymer rheology characterizes the complex flow behavior of plastics. A capillary rheometer measures viscosity as a function of temperature and shear rate. The Goettfert rheometer utilizes direct measurement of melt pressures through a side mounted pressure transducer.

Viscosity Data

245 °C	
Shear Rate s^{-1}	**Viscosity Pa·s**
10	304.64
20	274.18
50	244.28
100	201.53
200	155.73
500	102.60
1000	69.61
2000	45.49
5000	25.16
10000	15.94

Tested By: *JA*
Certified By:
Test Date: *6/29/2007*

Viscosity Continued

Viscosity vs Shear Rate

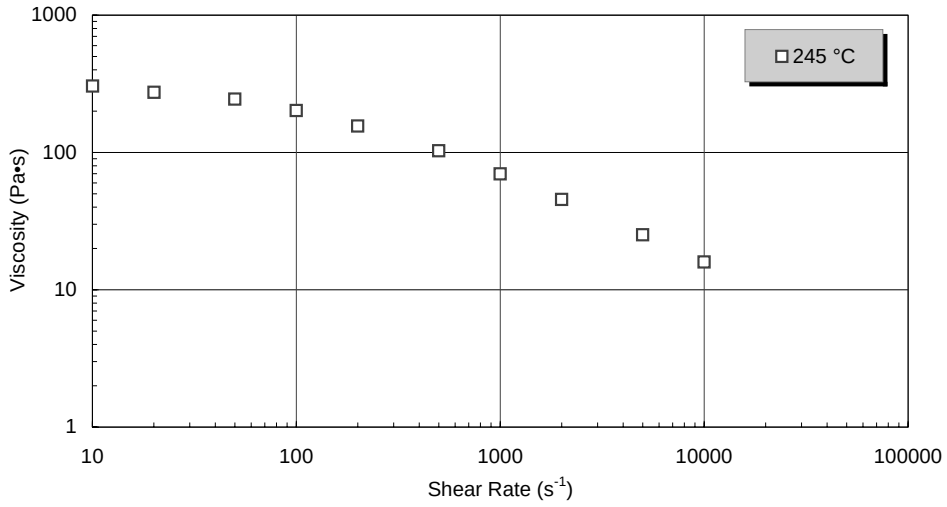

Cone & Plate Rheology

Method	ASTM D 4440 - 95a Rheological Measurement of Polymer Melts Using Dynamic Mechanical Procedures		
Instrument	Rheometrics ARES		
Specimen	type	disc	
	conditioning	none	
	other preparation	none	
Parameters	plate diameter	25	mm
	cone angle	0.1	radians
	gap	50	µm
	temperature	245	°C
	frequency range	0.1-500	rad/s
	strain	15	%
Precision	temperature	±2	°C

Polymer rheology characterizes the complex flow behavior of plastics. A dynamic mechanical rheometer measures complex viscosity as a function of temperature and frequency. Assuming the applicability of the Cox Merz relationship, the frequency bears a 1:1 relationship to the shear rate.

Strain Sweep

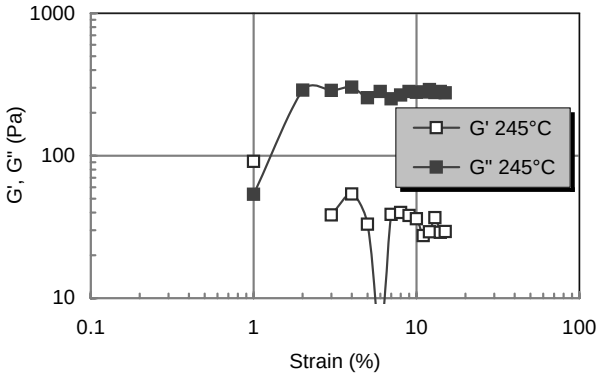

Tested By: *JA*
Certified By: *BC*
Test Date: *6/29/2007*

Cone and plate DMA measurements are not included in our current scope of accreditation.

Cone & Plate Rheology Continued

DMA Data

Temp °C	ω rad/s	η* Pa•s	G' Pa	G" Pa
245	0.1	366.1	-7.58	35.82
245	0.1	296.1	6.10	43.03
245	0.2	361.6	13.76	76.67
245	0.3	307.9	18.55	95.58
245	0.5	318.0	9.32	147.30
245	0.7	275.7	19.94	186.76
245	1.0	286.1	28.39	284.71
245	1.5	268.8	35.91	392.84
245	2.2	266.0	60.71	569.78
245	3.2	263.1	103.74	825.64
245	4.6	255.4	173.73	1172.51
245	6.8	247.3	298.35	1658.16
245	10.0	237.3	506.97	2317.95
245	14.7	225.1	844.25	3194.46
245	21.5	210.8	1368.77	4329.65
245	31.6	194.9	2164.10	5770.62
245	46.4	177.5	3312.83	7544.08
245	68.1	159.2	4923.81	9663.83
245	100.0	140.6	7107.37	12129.50
245	146.8	122.1	9956.72	14898.80
245	215.4	104.1	13544.40	17886.80
245	316.2	87.1	17858.20	20970.00
245	464.2	71.0	22768.60	23854.20

NOTE: Shaded cells denote torque below instrument limits.

Cone & Plate Rheology Continued

Complex Viscosity Plot

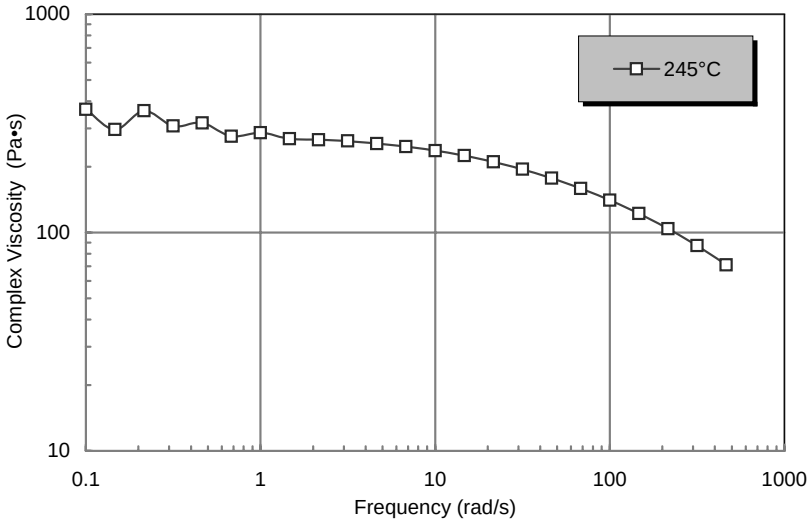

G'-G" Plot

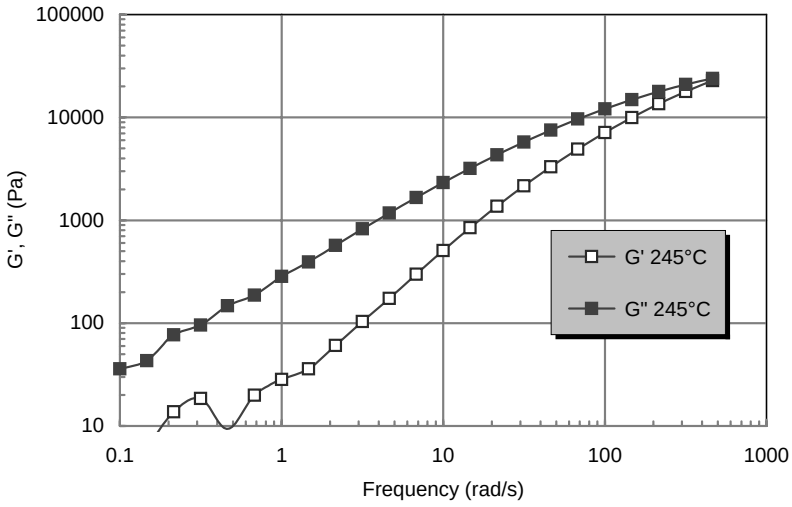

First Normal Stress Difference

Method	ASTM D 4440 - 95a Rheological Measurement of Polymer Melts Using Dynamic Mechanical Procedures		
Instrument	Rheometrics ARES		
Specimen	type	disc	
	conditioning	none	
	other preparation	none	
Parameters	plate diameter	25	mm
	cone angle	0.1	radians
	gap	50	µm
	temperature	245	°C
	scan time	1	s
	shear rate range	0.1-100	/s
Precision	temperature	±2	°C

Polymer rheology characterizes the complex flow behavior of plastics. A dynamic mechanical rheometer measures complex viscosity as a function of temperature and frequency. Assuming the applicability of the Cox Merz relationship, the frequency bears a 1:1 relationship to the shear rate.

Tested By: *JA*
Certified By: *BC*
Test Date: *6/29/2007*

Cone and plate DMA measurements are not included in our current scope of accreditation.

First Normal Stress Difference Continued

DMA Data

Temp °C	ω /s	η Pa•s	N1 Pa
245	1.0	246.4	246.44
245	1.6	236.5	374.90
245	2.5	228.2	573.22
245	4.0	220.4	877.57
245	6.3	212.7	1341.94
245	10.0	193.5	1935.05
245	15.8	133.9	2122.18
245	25.1	71.1	1786.35
245	39.8	26.3	1046.40
245	63.1	8.3	522.40
245	100.0	0.2	23.37

NOTE: Shaded cells denote material began to be forced out from between the cone and plate

First Normal Stress Difference v. Shear Rate

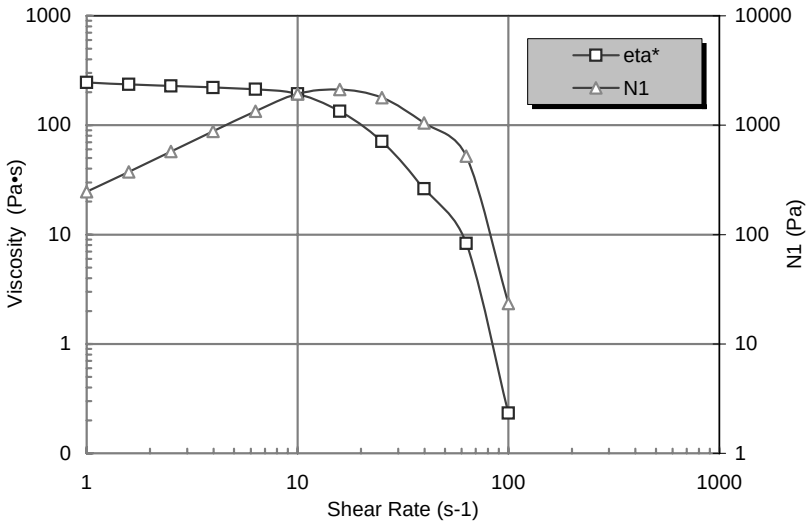

Moldflow Material Testing Report

S/N 5170

Styron 615 APR

Prepared for:

University of Michigan

1231 Beal Avenue

Ann Arbor, MI 48109

USA

Prepared by:

Moldflow Plastics Labs

2353 N. Triphammer Rd.

Ithaca, NY 14850

USA

Prepared on:

4 March, 2008

Report Authorized By:

Scott Grant

Laboratory Manager

4 March, 2008

Contents

Summary

Description

Family name	STYRENICS (PS, SAN, SBR, ...)
Trade name	Styron 615 APR
Manufacturer	Dow Chemical USA
Family abbreviation	GPPS
Material structure	Amorphous
Data source	Other : pvT-Supplemental : mech-Supplemental
Date last modified	04-MAR-08
Date tested	04-MAR-08
Data status	Non-Confidential
Material ID	
Grade code	SN5170
Supplier code	DOWUSA
Fibers/fillers	Unfilled

Recommended Processing

Mold surface temperature	35	°C
Melt temperature	218	°C

Mold temperature range (recommended)		
Minimum	21	°C
Maximum	48	°C

Melt temperature range (recommended)		
Minimum	176	°C
Maximum	260	°C

Absolute maximum melt temperature	300	°C

Ejection temperature	100	°C

Maximum shear stress	0.24	MPa
Maximum shear rate	40000	1/s

Maximum shear stress and maximum shear rate values have been supplemented with generic estimates.

Rheological Properties

Cross WLF Viscosity Model		
n	0.3720	
Tau	21765.5	Pa
D1	4.32561e+010	Pa-s
D2	373.15	K
D3	0	K/Pa
A1	25.245	
A2	51.600	K

Juncture loss method coefficients		
C1	0.03151	Pa^(1-c2)
C2	1.534	

Transition temperature		
Ttrans	105	°C

Moldflow Viscosity Index	VI(220)0072	

Melt mass-flow rate (MFR)		
Temperature		°C
Load		Kg
Measured MFR		g/10min

Thermal Properties

Specific heat data		
Temperature (T) °C	Specific heat (Cp) J/Kg-°C	Heating/Cooling rate °C/s
238	2100.0	-0.33

Thermal conductivity data		
Temperature (T) °C	Thermal conductivity (k) W/m-°C	Heating/Cooling rate °C/s
238	0.150	0.0

PVT Properties

Melt density	0.9608	g/cm^3
Solid density	1.0481	g/cm^3

2-domain Tait PVT model coefficients		
b5	376.81	K
b6	3.525e-007	K/Pa
b1m	0.000972	m^3/Kg
b2m	6.042e-007	m^3/Kg-K
b3m	1.85917e+008	Pa
b4m	0.004927	1/K
b1s	0.000972	m^3/Kg
b2s	2.234e-007	m^3/Kg-K
b3s	2.66301e+008	Pa
b4s	0.003474	1/K
b7	0.000e+000	m^3/Kg
b8	0.000e+000	1/K
b9	0.000e+000	1/Pa

pvT properties have not been tested for this material. The data has been supplemented with generic estimates for an unfilled GPPS.

Mechanical Properties

Mechanical properties data		
Elastic modulus, 1st principal direction [E1]	2700	MPa
Elastic modulus, 2nd principal direction [E2]	2700	MPa
Poissons ratio [v12]	0.3500	
Poissons ratio [v23]	0.3500	
Shear modulus [G12]	1000	MPa

Transversely isotropic coefficient of thermal expansion [CTE] data		
Alpha1	8.310e-005	1/C
Alpha2	8.310e-005	1/C

Shrinkage Properties

Corrected residual in-mold stress (CRIMS) model coefficients	
A1	
A2	
A3	
A4	
A5	
A6	

Residual strain model coefficients		
	Parallel	Perpendicular
A1		
A2		
A3		
A4		
A5		

Filler Properties

Filler data	
Description	Weight %

Viscosity

Method:
MPL Test Method

Instrument:
Arburg Allrounder 270S Injection Molding Machine

Test Specifications:

Sample Form:		Pellets
Pre-Processing:		Not required
Moisture Level:		Not measured
Capillary A:	Length:	31.9682 mm
	L/D:	15.9841
	Die Entry Angle:	180 degrees
Capillary B:	Length:	7.9004 mm
	L/D:	3.9502
	Die Entry Angle:	180 degrees
Barrel Diameter:		30 mm
Plastication Time:		20 sec
Dwell Time:		20 sec
Corrections:		Bagley, Rabinowitsch and shear heating
Date Received:		12-DEC-07
Date Tested:		30-JAN-08

Operator's Notes:
Testing was performed per standard testing procedures.
No anomalies were noted during the course of testing.

Apparent Viscosity Data

Temperature (°C)	Apparent Shear Rate (sec^{-1})	Apparent Viscosity (Pa-s)	Die Diameter (mm)	Die L/D
220.1	178	305.35	2	15.98
220.1	293	220.58	2	15.98
220.1	25401	15.59	2	15.98
220.2	63637	9.93	2	15.98
220.4	738	134.49	2	15.98
220.9	6430	34.81	2	15.98
221.1	1299	94.42	2	15.98
221.2	2559	62.34	2	15.98
221.2	12669	22.95	2	15.98
234	178	193.04	2	15.98
235	293	151.15	2	15.98
235	738	98.48	2	15.98
235	6443	27.87	2	15.98
235.1	12720	17.93	2	15.98
235.1	25439	11.68	2	15.98
235.1	63980	7.04	2	15.98
236	1311	71.32	2	15.98
236	2572	47.31	2	15.98
249	178	122.84	2	15.98
249	293	106.82	2	15.98
249	738	74.98	2	15.98
249.9	2559	38.01	2	15.98
249.9	6404	22.54	2	15.98
249.9	63649	5.53	2	15.98
250	1311	56.17	2	15.98
250	12720	14.79	2	15.98
251	25388	9.6	2	15.98
263.7	293	71.57	2	15.98
264.2	178	73.7	2	15.98
264.6	738	56.13	2	15.98
265.3	1299	44.8	2	15.98
265.6	6443	18.23	2	15.98
265.7	2559	30.5	2	15.98
265.7	12669	12.31	2	15.98
266.6	63586	4.62	2	15.98
266.7	25439	8.05	2	15.98
225.5	178	284.04	2	3.95
225.6	293	231.24	2	3.95
225.6	25401	28.18	2	3.95
225.7	2559	99.91	2	3.95
226.5	12669	43.61	2	3.95
226.5	63637	16.27	2	3.95
226.6	738	152.55	2	3.95
226.6	6430	66.73	2	3.95
228.6	1299	105.75	2	3.95
240.4	2572	69.88	2	3.95
241.4	178	188.17	2	3.95
241.4	293	157.76	2	3.95

Temperature (°C)	Apparent Shear Rate (sec^{-1})	Apparent Viscosity (Pa-s)	Die Diameter (mm)	Die L/D
241.4	738	108.84	2	3.95
241.6	6443	47.25	2	3.95
242.4	12720	34.08	2	3.95
242.4	25439	22.39	2	3.95
242.4	63980	13.18	2	3.95
242.8	1311	80.59	2	3.95
255.3	2559	52.92	2	3.95
256	293	127.51	2	3.95
256.3	738	84.84	2	3.95
256.4	178	156.22	2	3.95
256.4	6404	35.97	2	3.95
257.2	1311	64.67	2	3.95
257.3	63649	10.85	2	3.95
258.3	12720	26.37	2	3.95
258.3	25388	18.47	2	3.95
270.6	2559	41.55	2	3.95
270.8	293	103.73	2	3.95
271.3	178	134.92	2	3.95
271.3	738	69.42	2	3.95
271.3	1299	52.63	2	3.95
272.8	6443	27.7	2	3.95
273.3	25439	14.9	2	3.95
273.3	63586	9.12	2	3.95
273.4	12669	20.53	2	3.95

Calculated Viscosity Data

Temperature (°C)	Shear Rate (sec^{-1})	Calculated Viscosity (Pa-s)
220.1	178	202.94
220.1	25401	11.38
220.1	293	157.67
220.2	63637	6.42
220.4	738	94.86
220.9	6430	26.17
221.1	1299	67.76
221.2	2559	45.39
221.2	12669	17.18
225.5	178	180.04
225.6	25401	10.41
225.6	293	140.64
225.7	2559	41.99
226.5	12669	15.76
226.5	63637	5.8
226.6	6430	23.81
226.6	738	84.43
228.6	1299	59.3
234	178	150.18
235	6443	20.87
235	293	116.67
235	738	72.7
235.1	25439	9.01
235.1	12720	13.8
235.1	63980	5.09
236	2572	35.45
236	1311	52.12
240.4	2572	33.16
241.4	178	129.08
241.4	293	103.32
241.4	738	65.23
241.6	6443	18.98
242.4	63980	4.61
242.4	25439	8.15
242.4	12720	12.45
242.8	1311	46.8
249	178	111.14
249	293	89.91
249	738	57.68
249.9	6404	17.02
249.9	2559	29.01
249.9	63649	4.2
250	1311	41.98
250	12720	11.27
251	25388	7.31
255.3	2559	26.95
256	293	79.49
256.3	738	51.52
256.4	6404	15.67
256.4	178	96.59

Temperature (°C)	Shear Rate (sec^{-1})	Calculated Viscosity (Pa-s)
257.2	1311	37.85
257.3	63649	3.85
258.3	12720	10.18
258.3	25388	6.7
263.7	293	69.76
264.2	178	83.78
264.6	738	45.56
265.3	1299	34.03
265.6	6443	13.99
265.7	2559	23.58
265.7	12669	9.38
266.6	63586	3.48
266.7	25439	6.09
270.6	2559	22.2
270.8	293	62.12
271.3	178	73.96
271.3	1299	31.44
271.3	738	41.42
272.8	6443	12.9
273.3	63586	3.25
273.3	25439	5.69
273.4	12669	8.63

Rheological Data

Cross WLF Viscosity Model		
n	0.3720	
Tau	21765.5	Pa
D1	4.32561e+010	Pa-s
D2	373.15	K
D3	0	K/Pa
A1	25.245	
A2	51.600	K

Juncture loss method coefficients		
C1	0.03151	Pa^(1-c2)
C2	1.534	

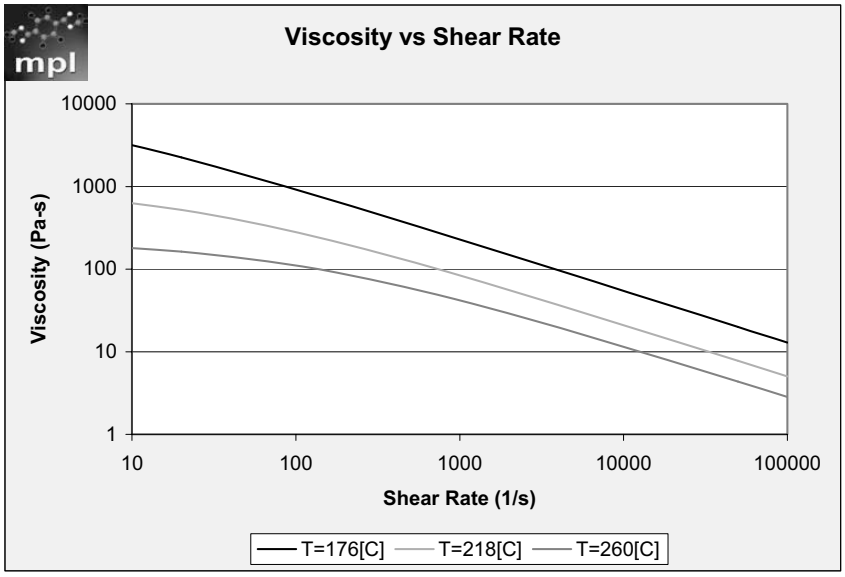

APPENDIX B

Detailed Drawings of the Optical Access Mold Components

Figure B.1 gives an exploded view of the optical access mold. This appendix will give a brief explanation of the functions of the mold components as well as detailed drawings. The drawings are not meant to enable the reader to duplicate the optical access mold in every detail, but the level of detail is hopefully sufficient to satisfy the the reader that wishes more specific information about the mold design.

The major mold components will be presented in isometric view. The machining details of the guide ring, top clamping plate, A plate, ejector plates and the rear clamping plate are specific to the problem of mounting this particular mold base in this particular injection molding machine. Therefore these details will be omitted. The machining details of the sprue bushing, B plate, cavity block and window brace are all relevant to the the polymer flow path geometry, the cavity geometry and the window performance and these components will be presented in more detail.

All dimensions are in inches. In this appendix the front view is considered to be the view you would see while facing the mold window. The side view is the view of the mold from the nozzle of the machine, and the top view is the view from above the machine.

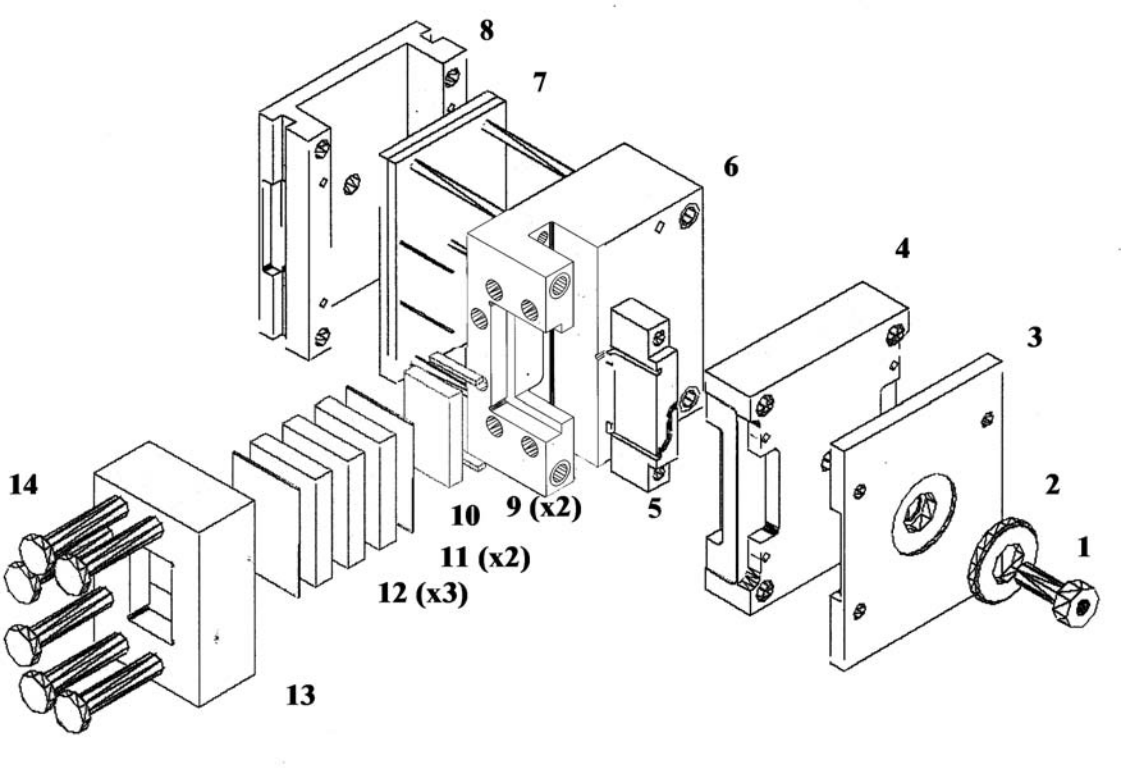

Figure B.1: Exploded view of the optical access mold. 1. Sprue bushing, 2. Guide ring, 3. Top clamping plate, 4. "A" plate, 5. Cavity block, 6. "B" plate, 7. Front and rear ejector plates with ejector pins and return pins, 8. Rear clamping plate, 9. Acrylic entrance and exit windows, 10. 0.75" thick quartz window, 11. 0.125" thick polycarbonate shields, 12. Three 1" thick glass plates, 13. Steel window brace, and 14. Six 1" diameter hardened steel bolts

Apologies must be made for the quality of some of the drawings in this appendix. The original CAD drawings were lost in a catastrophic hard drive crash. The images in this chapter were scanned in from hard copies of the original Autocad drawings.

B.1 Sprue Bushing and Guide Ring

The polymer first enters the mold through the sprue bushing. An isometric view of the sprue bushing can be found in Figure B.2. A section view can be seen in Figure B.3. The channel in the sprue bushing is tapered to facilitate the breakaway of the

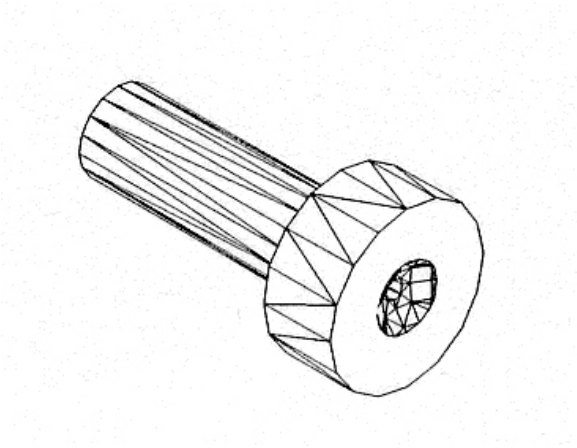

Figure B.2: Isometric view of the sprue bushing.

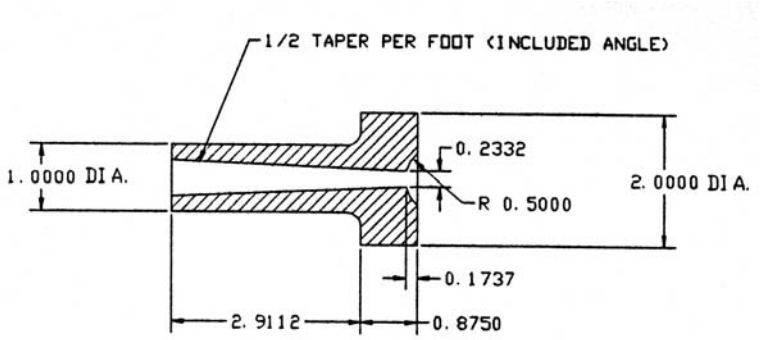

Figure B.3: Section view of the sprue bushing showing the taper of the sprue opening. All dimensions are in inches.

solidified sprue when the mold is opened. The dimensioned drawings of the sprue bushing, the B plate, and the cavity block (Figures B.3, B.9 and B.14 respectively) give all the geometric details necessary to model the polymer flow path from the nozzle of the injection molding machine to the cavity gate.

The guide ring serves as a locating device when seating the mold between the platens of the injection molding machine. It assures that the sprue bushing will line up with the nozzle of the injection molding machine. An isometric view of the guide ring is shown in Figure B.4.

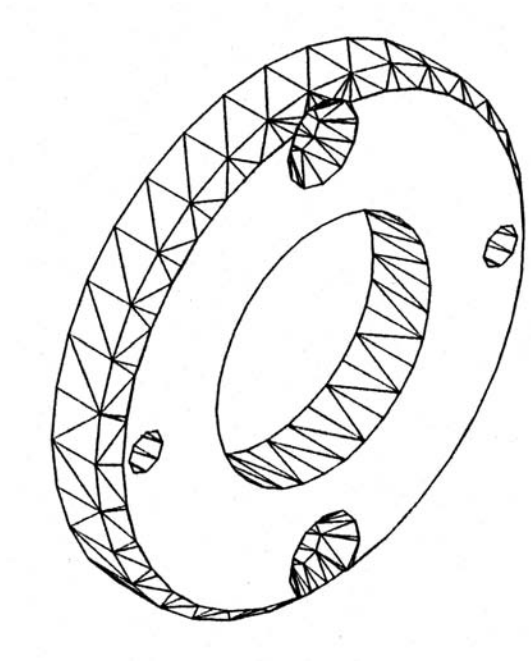

Figure B.4: Isometric view of the guide ring.

B.2 Top Clamping Plate and "A" Plate

The top clamping plate is the part of the mold that is bolted to the stationary platen of the injection molding machine. It houses the guide ring and part of the sprue bushing. An isometric view of the top clamping plate can be seen in Figure B.5.

The "A" plate houses the rest of the sprue bushing and is the mold component that forms the stationary half of the parting plane. An isometric view of the A plate can be seen in Figure B.6.

B.3 "B" Plate and Cavity Block

The B plate is the largest component of the mold. It houses the cavity block and forms the moving side of the parting plane. This plate also provides passage for the ejector pins and the return pins. The B plate also catches the first, cooler portion of

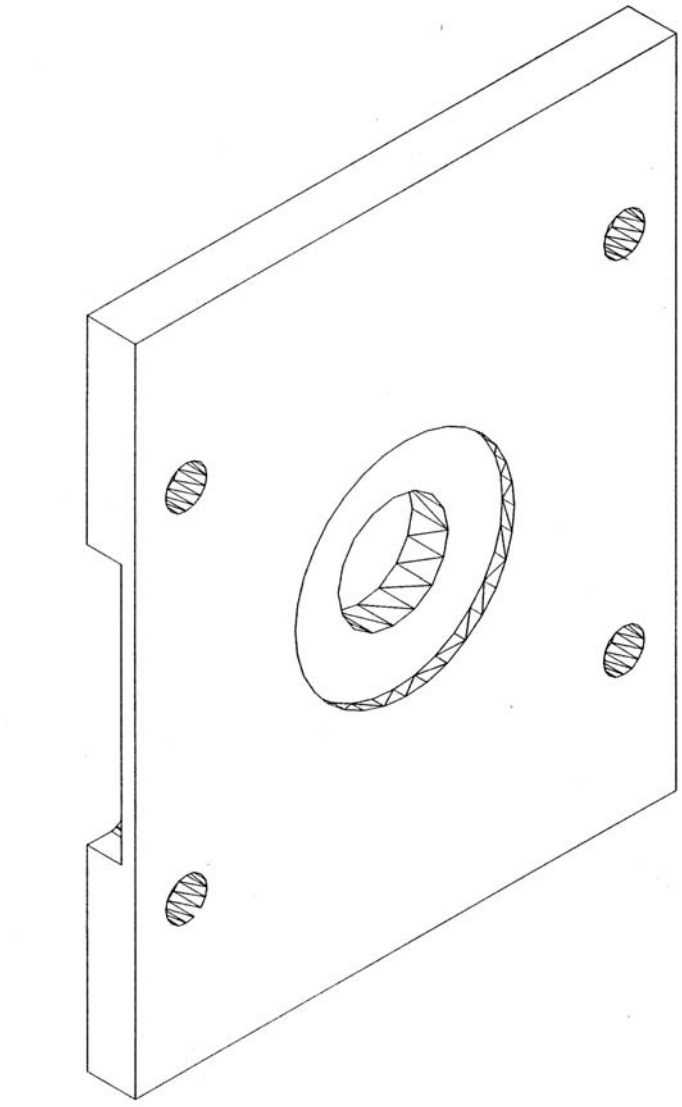

Figure B.5: Isometric view of the top clamping plate.

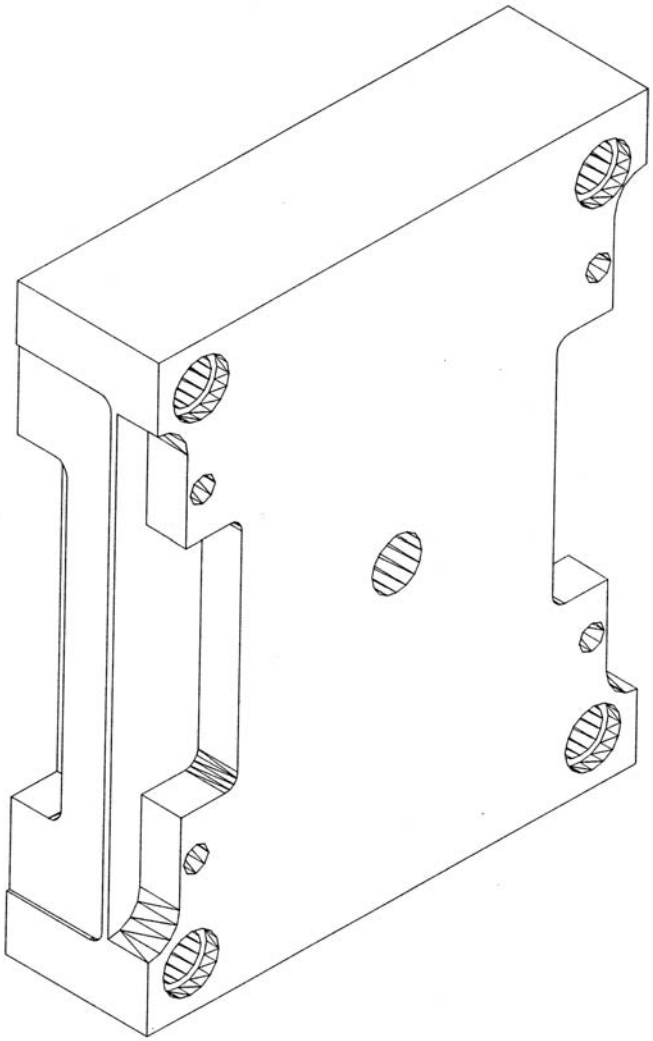

Figure B.6: Isometric view of the A plate.

the shot in the cold slug well and provides the portion of the runner from the sprue bushing to the cavity block. The B plate also contains the mounting holes for the bolts used to attach the window to the mold. An isometric view of the B plate can be seen in Figure B.7. The front view is in Figure B.8 and the side view is in Figure B.9 and the view from the clamp side of the mold is shown in Figure B.10.

The cavity block is the heart of the optical access mold. This block forms the cavity geometry. It also contains the portion of the runner not found in the B plate and also the gate. The cavity block houses the two acrylic entrance and exit windows for the passage of the laser sheet through the cavity. An isometric view of the cavity block can be seen in Figure B.11. The front view is in Figure B.12 and the side view is in Figure B.13. A detail of the runner and gate dimensions can be seen in Figure B.14.

B.4 Ejector Plates and Pins and the Rear Clamping Plate

The ejector pins push the part out of the mold after the mold has opened. The heads of the pins are sandwiched between two ejector plates. When this plate is pushed forward by the ejector of the injection molding machine the pins move forward and eject the part. These plates also contain the return pins. These longer pins contact the stationary half of the mold when it closes and push the ejector plates back into their home position. A detailed view of one of the ejector pins is shown in Figure B.15. Isometric views of the two ejector plates are shown in Figure B.16 and Figure B.17.

The ejector plates move back and forth in a space created by the rear clamping plate. The rear clamping plate is the portion of the mold that is clamped to the moving platen of the injection molding machine. It also provides a passage for the

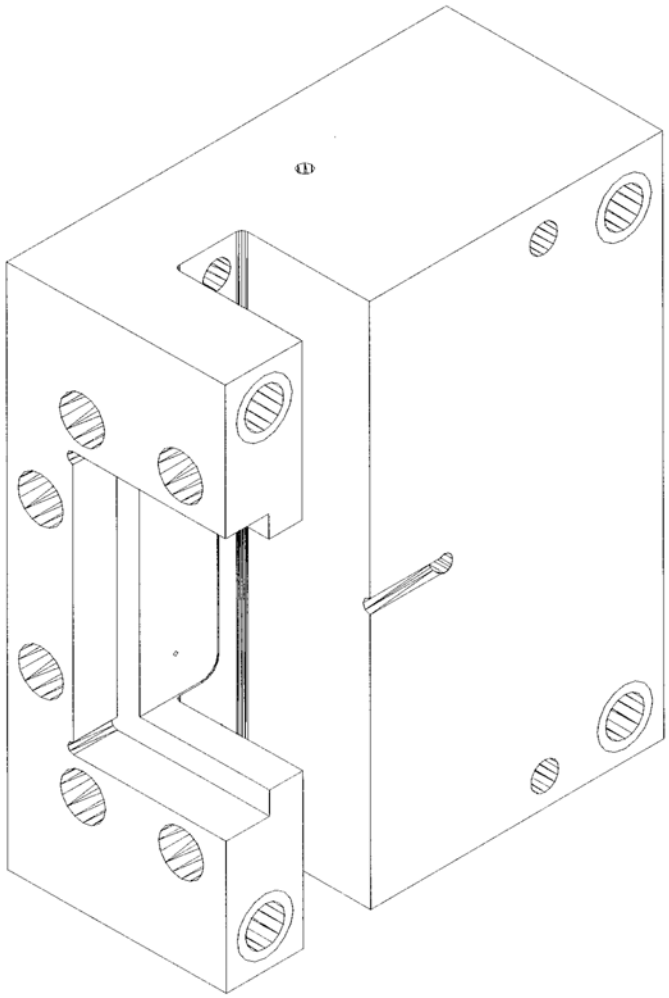

Figure B.7: Isometric view of the B plate.

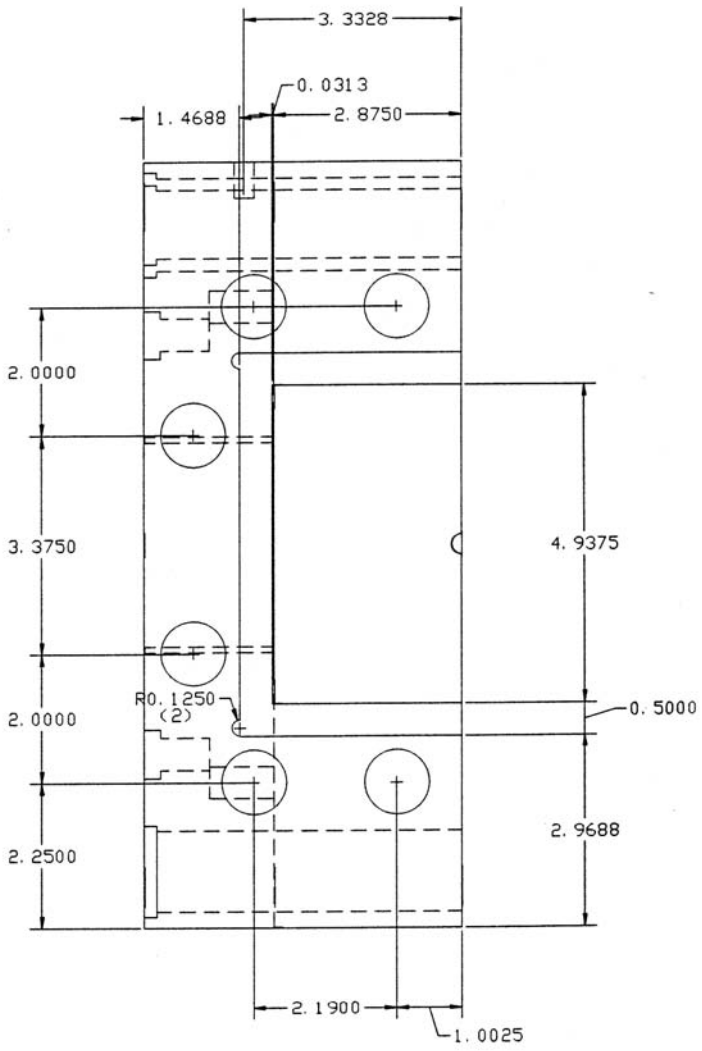

Figure B.8: Front view of the B plate. All dimensions are in inches.

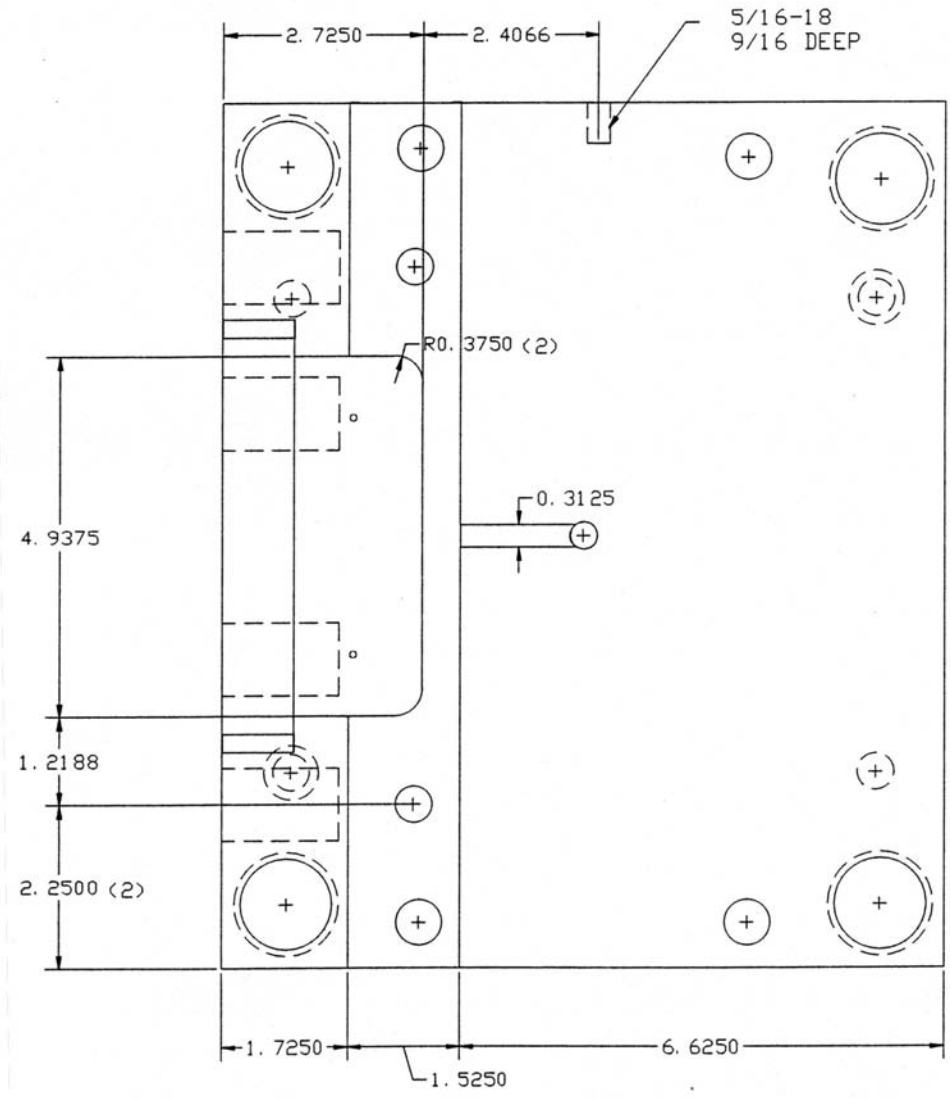

Figure B.9: Side view of the B plate from the nozzle direction. All dimensions are in inches.

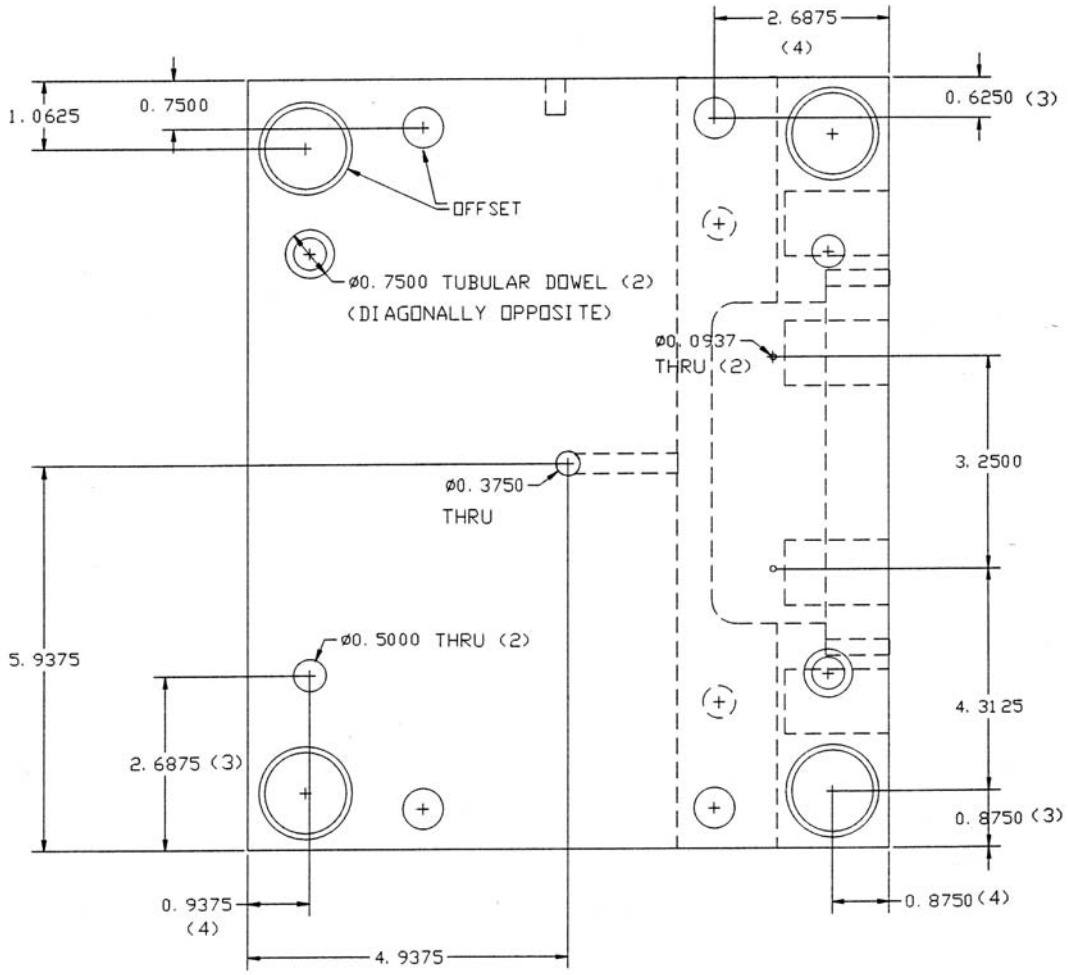

Figure B.10: Side view of the B plate from the clamp direction. All dimensions are in inches.

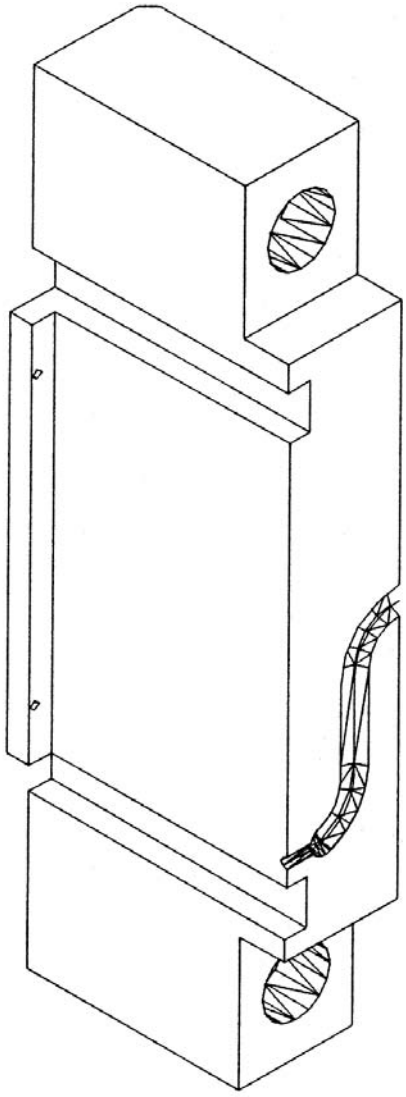

Figure B.11: Isometric view of the cavity block.

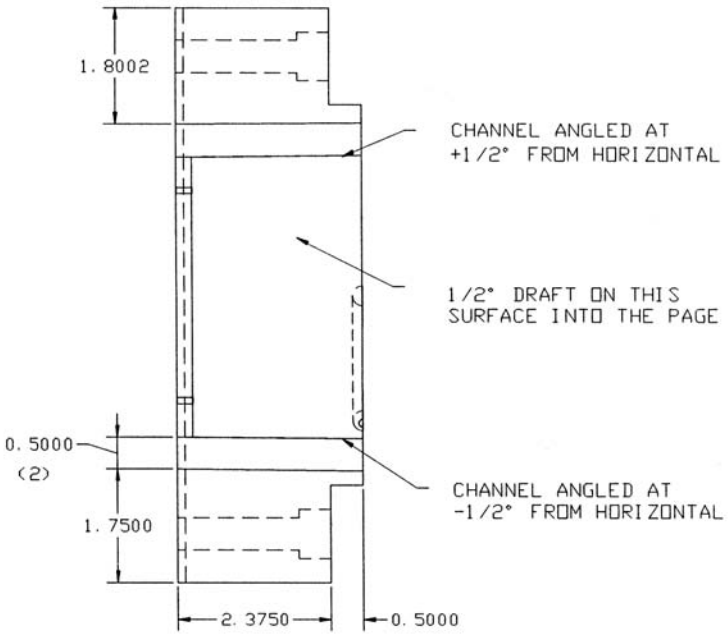

Figure B.12: Front view of the cavity block. All dimensions are in inches.

ejector ram of the injection molding machine. An isometric view of the rear clamping plate is shown in Figure B.18.

B.5 Window Components

If the cavity block is the heart of the optical access mold, the window components are its reason for being. The window components form three faces of the mold cavity. The two 6mm thick acrylic entrance and exit windows mentioned above form the top and bottom faces of the part. A 19mm thick quartz plate forms the front face of the cavity. Moving outward from the cavity the next component is a 3mm thick polycarbonate shield to protect the rest of the window and the user from broken glass should the quartz piece fail. This is followed by three 25mm thick pieces of plate glass and another polycarbonate shield.

The window elements are all paralellopipeds, so a list of their dimensions will

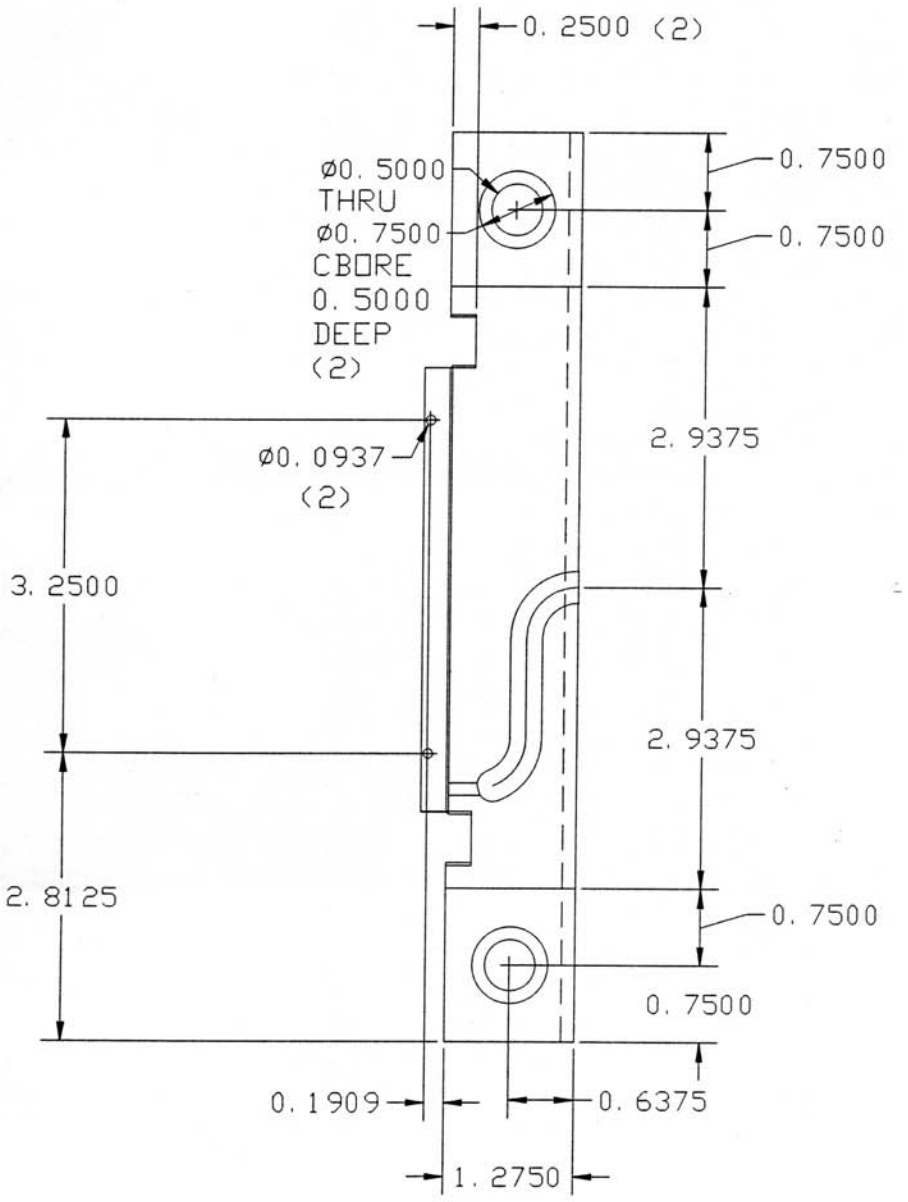

Figure B.13: Side view of the cavity block. All dimensions are in inches.

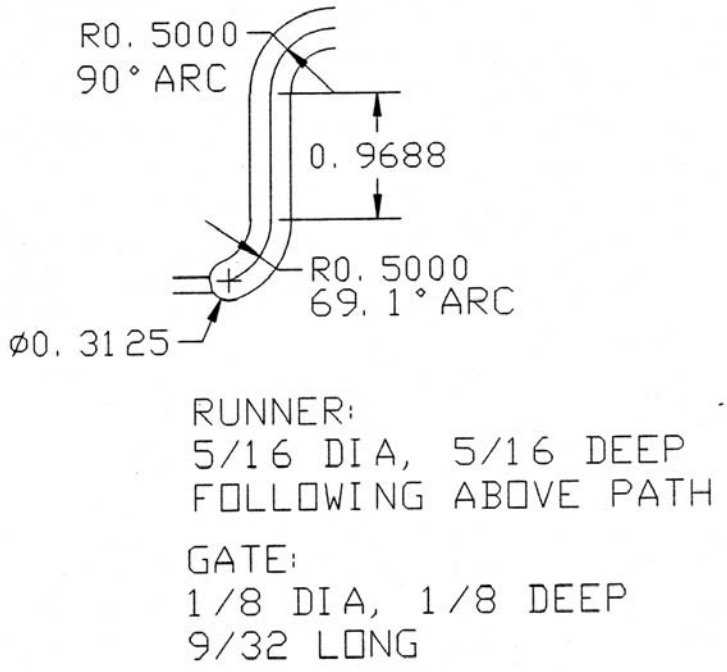

Figure B.14: Detail view of the runner and gate in the cavity block. All dimensions are in inches.

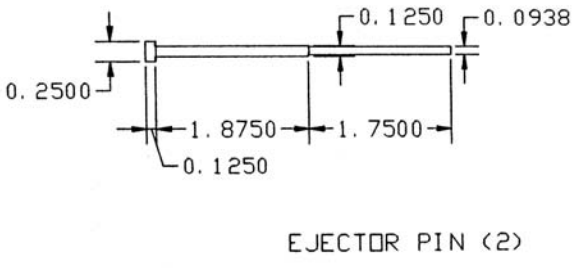

Figure B.15: Detail view of the ejector pin. All dimensions are in inches.

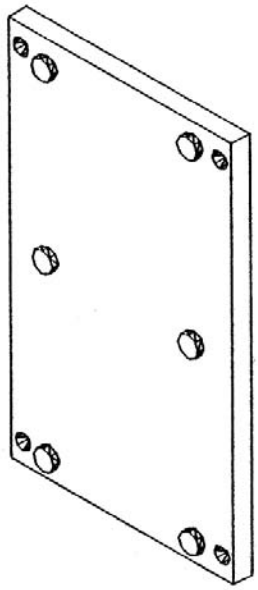

Figure B.16: Isometric view of the rear ejector plate from the clamp direction.

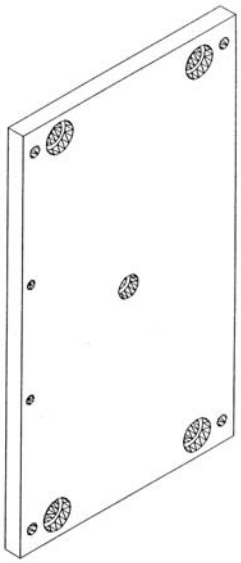

Figure B.17: Isometric view of the front ejector plate from the nozzle direction. The two small holes on the left edge are for the ejector pins.

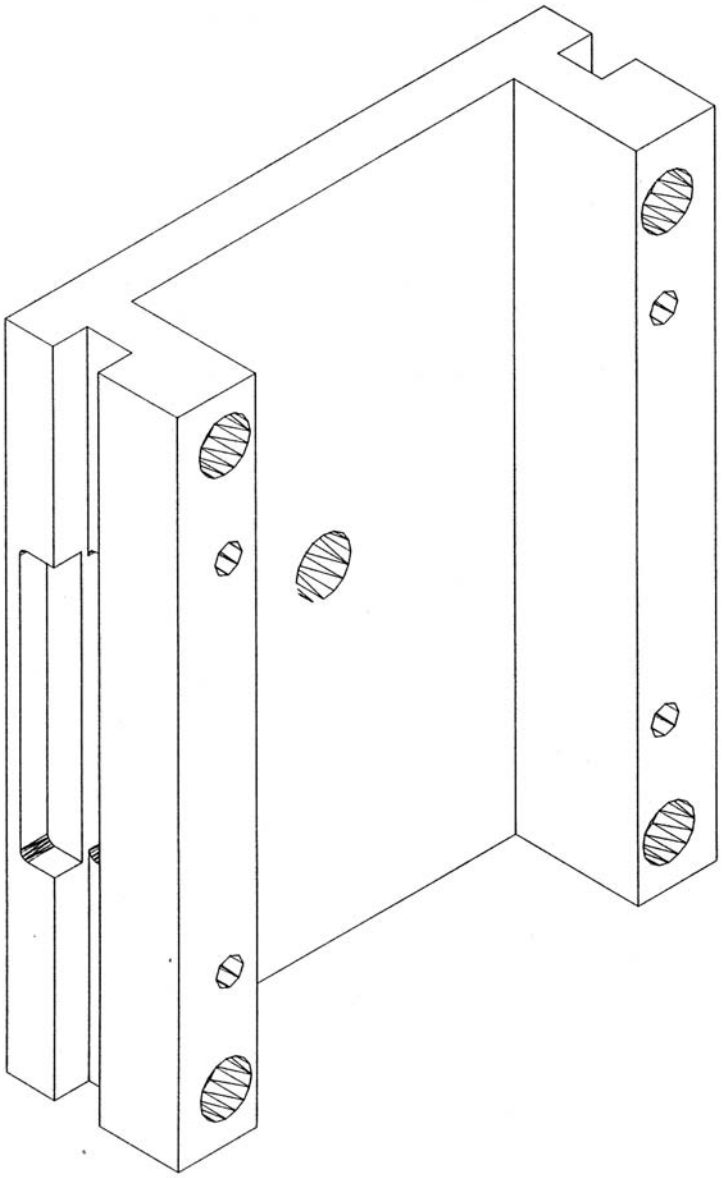

Figure B.18: Isometric view of the rear clamping plate plate.

suffice in lieu of dimensioned drawings. In keeping with the convention set by this appendix all dimensions will be given in inches.

The acrylic entrance and exit windows are the only elements with non-orthogonal sides. The cross-section of these windows is 0.25"× 0.25" and their length is 2.675". The two square faces of these windows are inclined 1/2°. This is because the windows themselves are placed in the block at an angle of 1/2° from horizontal to provide the draft on those faces of the cavity. The square faces of the windows need to be angled at 1/2° in order to be parallel to the parting plane of the mold.

The quartz window is 4.875"× 2.875"× 0.75". It sits on the acrylic windows and forms the large transparent face of the mold cavity. The three plates of glass are 5.875"× 4.25"× 1". The polycarbonate shields are 5.875"× 4.25"× 0.125".

B.6 Window Brace

The final portion of the mold is the steel brace that attaches the window to the mold. This brace must be strong enough to hold the window in place against the cavity block while resisting the high melt pressures exerted on the window. The clamping force is provided by six hardened steel bolts one inch in diameter. An isometric view of the window brace can be seen in Figure B.19. The front view is in Figure B.20 and the side view is in Figure B.21.

B.7 Reflections on the Engineering, Design and Fabrication of the Optical Access Mold

Learning to design even a simple mold is not an easy task. There are many details that must be addressed. How do you choose a gate? What clearances are necessary on the myriad pins and holes in the mold? How do you eject the part cleanly? The answers to these questions can be found in good books on mold design. Generally

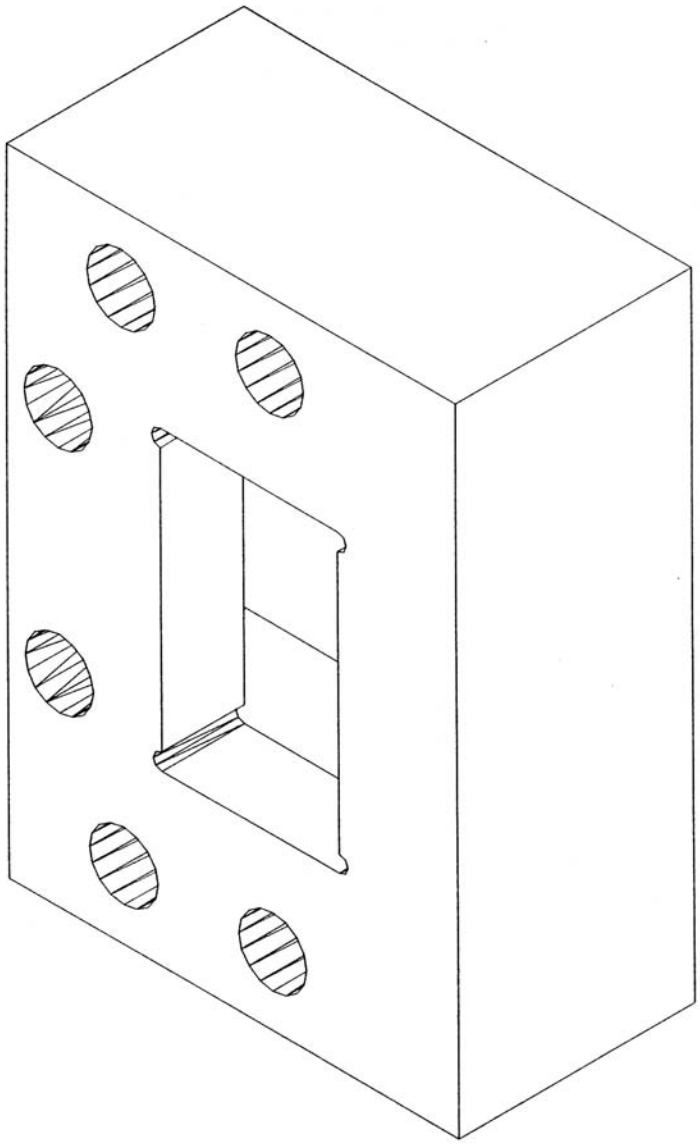

Figure B.19: Isometric view of the window brace.

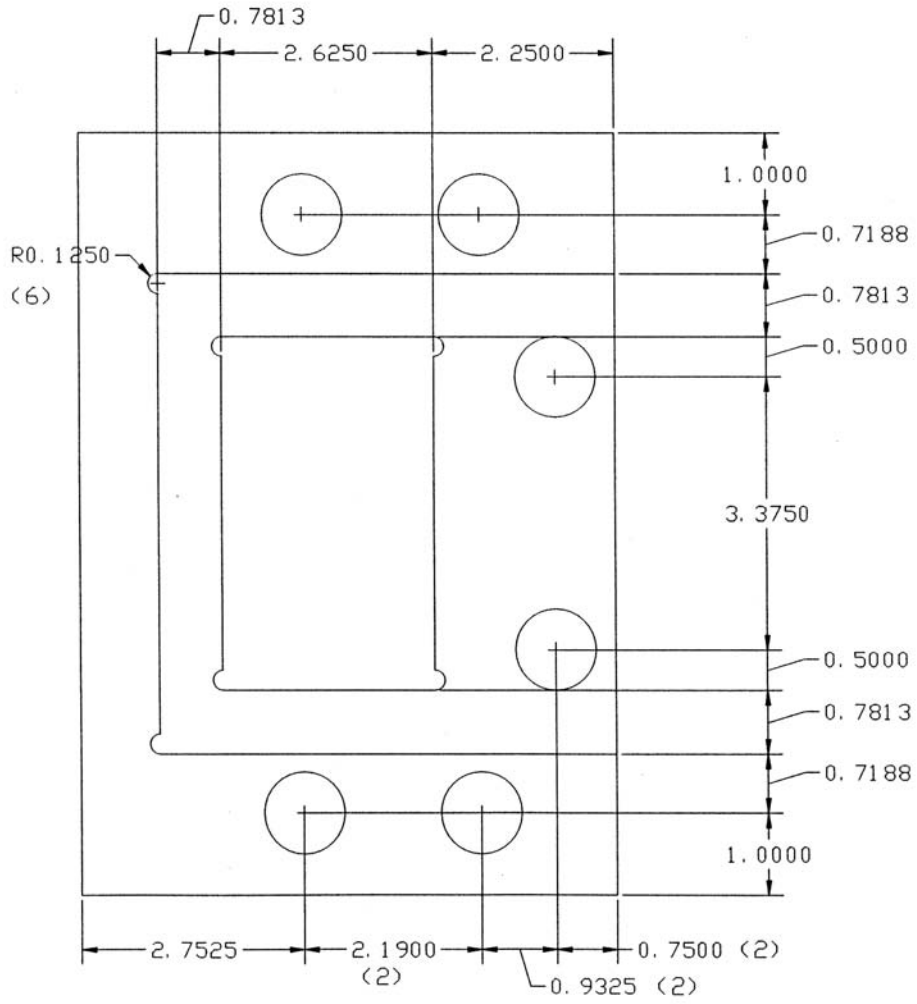

Figure B.20: Front view of the window brace. All dimensions are in inches.

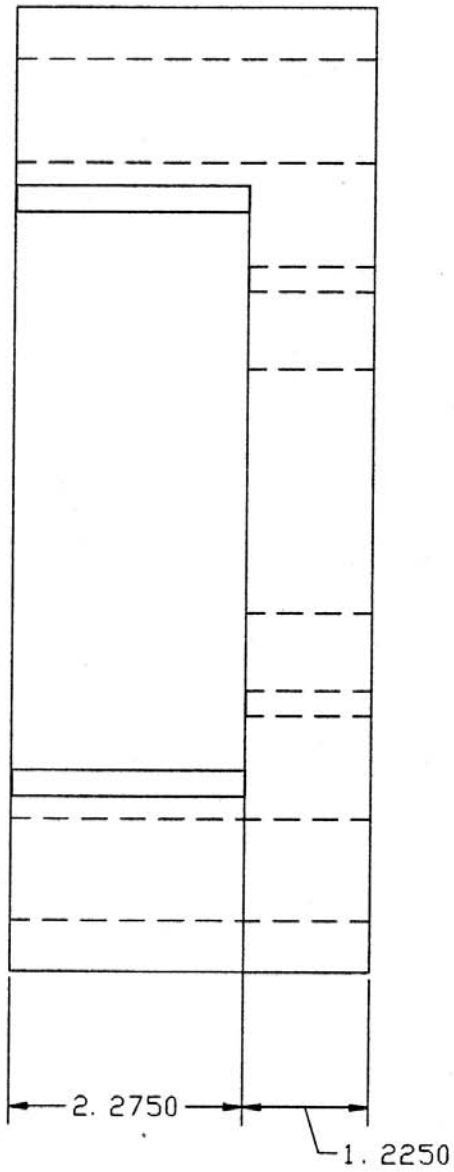

Figure B.21: Side view of the window brace. All dimensions are in inches.

speaking, the older the book the better the chance that you will find the answer to specific questions relating to the detailed design and machining of a mold. DuBois and Pribble [126] is an excellent resource. Stoeckhert [127] is a more recent work that is rich in the technical details of mold design.

The design of the optical access mold presented unique challenges. The design criterion for the window system was that it should be able to withstand a melt pressure of up to 10,000 psi. In order to do this a finite element model of the window design was made in Hypermesh, and a series of finite element analyses were run using Patran.

Many iterations of the design were required before the window passed the finite element test. The original design called for thinner windows, with some of the elements made of plexiglass. Two problems with this design were revealed by the finite element analysis. The first problem was that the stresses in the window were too high, which was corrected by using thicker glass. The second problem was that the plexiglass elements compressed significantly when the melt pressure was applied to the window. That would cause the window to move away from the cavity and would lead to flash. This problem was corrected by replacing the plexiglass elements with plate glass.

Once the window design was finalized the design of the mold itself was started. Solid models were made of each of the mold components using Autocad. This was time consuming, but it ensured that the mold components fit together without interference. It also allowed detailed prints to be made of each component for machining.

When the mold was machined and installed a series of materials were tested for sealing the mold cavity. Silicone RTV, Kapton tape, and other materials were tried. The best results were obtained by cutting strips from aluminum cans. These

aluminum strips acted as both gaskets and shims. They flattened when the bolts were torqued down and sealed the gaps between the glass surfaces. They were also strong enough to survive the pressures place on the edges exposed to the polymer melt.

APPENDIX C

Radial Flow of a Power Law Fluid Between Parallel Plates

The solution of the radial flow of a power law fluid between parallel plates is presented in Bird [63], but the analysis is left as an exercise to the reader. For convenience the analysis will be described here.

The first step in the solution of this problem is to solve the simpler but related problem of the pressure-driven channel flow of a power law fluid. This solution will then be applied locally to radial flow between parallel plates using the lubrication approximation.

C.1 Channel Flow of a Power Law Fluid

Assume a channel aligned with the x-axis with walls at $y = \pm B$, as shown in Figure C.1.

The relationship between stress and shear rate for a power law fluid is given by:

$$\tau = m|\dot{\gamma}|^n \tag{C.1}$$

where n is the power law exponent and m is the power law coefficient. This formulation, though standard, gives only positive shear stresses. To correct this defect the

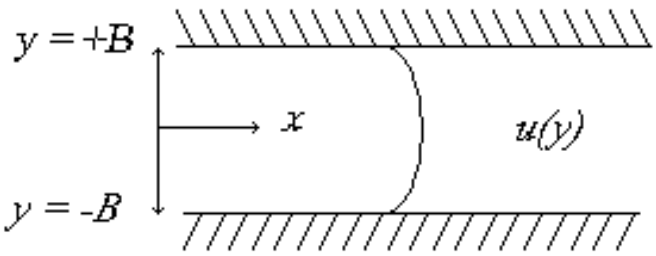

Figure C.1: Coordinate axes for the analysis of the channel flow of a power-law fluid.

equation can be rewritten as[64]:

$$\tau = m|\dot{\gamma}|^{n-1}\dot{\gamma} \tag{C.2}$$

For a two-dimensional channel flow with velocity $u(y)$:

$$\tau = m\left|\frac{du}{dy}\right|^{n-1}\frac{du}{dy} \tag{C.3}$$

For a steady, fully-developed flow:

$$0 = -\frac{dp}{dx} + \frac{d\tau}{dy} \tag{C.4}$$

Integrate in y to get:

$$\tau = y\frac{dp}{dx} + C \tag{C.5}$$

where C is a constant of integration. The shear stress $\tau = 0$ at the centerline of the channel so $C = 0$. Substituting for τ:

$$y\frac{dp}{dx} = m\left|\frac{du}{dy}\right|^{n-1}\frac{du}{dy} \tag{C.6}$$

Consider the top half of the channel only where $y > 0$ and $du/dy < 0$, then use symmetry to get the entire profile. Note also that since the pressure gradient

is negative, $y\frac{dp}{dx} < 0$ in this region. Rewriting Equation C.6 for the top half of the channel gives:

$$y\frac{dp}{dx} = -m\left(-\frac{du}{dy}\right)^n \tag{C.7}$$

Solving for the velocity gradient gives

$$\frac{du}{dy} = -\left[-\frac{y}{m}\frac{dp}{dx}\right]^{1/n} \tag{C.8}$$

Integrate to get the velocity:

$$u = -\frac{1}{1/n+1}\left[-\frac{1}{m}\frac{dp}{dx}\right]^{1/n} y^{\frac{1}{n}+1} + C \tag{C.9}$$

Since $u = 0$ at $y = B$:

$$u = -\frac{1}{1/n+1}\left[-\frac{1}{m}\frac{dp}{dx}\right]^{1/n}\left(y^{\frac{1}{n}+1} - B^{\frac{1}{n}+1}\right) \tag{C.10}$$

Rearranging this and generalizing it to make it applicable to the lower half of the channel as well leads to:

$$u = \frac{Bn}{n+1}\left[-\frac{B}{m}\frac{dp}{dx}\right]^{1/n}\left(1 - \left|\frac{y}{B}\right|^{\frac{n+1}{n}}\right) \tag{C.11}$$

Since $u = u_{max}$ at $y = 0$:

$$u_{max} = \frac{Bn}{n+1}\left[-\frac{B}{m}\frac{dp}{dx}\right]^{1/n} \tag{C.12}$$

$$u = u_{max}\left(1 - \left|\frac{y}{B}\right|^{\frac{n+1}{n}}\right) \tag{C.13}$$

The average velocity across the channel thickness can then be calculated:

$$\bar{u} = \frac{1}{B}\int_0^B u\, dy = \frac{n+1}{2n+1}u_{max} = Fu_{max} \tag{C.14}$$

where F is a profile factor. For a power-law fluid:

$$F = \frac{n+1}{2n+1} \tag{C.15}$$

The average velocity can be used to get the volume flow rate:

$$Q = 2WB\bar{u} = 2WB\frac{n+1}{2n+1}u_{max} = 2WBFu_{max} \tag{C.16}$$

where W is the width of the channel in the z direction and F is the profile factor defined in Equation C.15.

C.2 Radial Flow of a Power Law Fluid

To apply Equation 5.3 to the radial flow of a power law fluid between parallel plates use the lubrication approximation with $W = 2\pi r$ and $dP/dx = dP/dr$:

$$Q = \frac{4\pi r B^2}{\frac{1}{n}+2}\left[-\frac{B}{m}\frac{dP}{dr}\right]^{1/n} \tag{C.17}$$

Remembering that Q is not a function of r, solve for dp/dr and integrate to get an expression for P:

$$\frac{dP}{dr} = -\frac{m}{B}\left[\frac{Q(\frac{1}{n}+2)}{4\pi B^2}\right]^n r^{-n} \tag{C.18}$$

$$P = -\frac{m}{B(1-n)}\left[\frac{Q(\frac{1}{n}+2)}{4\pi B^2}\right]^n r^{1-n} + C \tag{C.19}$$

If we consider the pressure difference between two points in the flow at radial distances R_1 and R_2 the unknown constant can be eliminated:

$$P_1 - P_2 = -\frac{m}{B(1-n)}\left[\frac{Q(\frac{1}{n}+2)}{4\pi B^2}\right]^n (R_1^{1-n} - R_2^{1-n}) \tag{C.20}$$

Solving this equation for Q gives the result found in Bird [63]:

$$Q = \frac{4\pi B^2}{(1/n)+2}\left[\frac{(P_1-P_2)B(1-n)}{m(R_2^{1-n}-R_1^{1-n})}\right]^{1/n} \tag{C.21}$$

APPENDIX D

An Example Calculation Using Mueller Matrices

In Chapter 8 it was stated that a circular polarimeter in a standard configuration can be used to measure retardation of a three-dimensional birefringent specimen. That claim will be confirmed here using a Mueller matrix calculation.

Table D.1 shows the Mueller matrices for various ideal optical elements. In their most general forms these matrices allow the elements to be oriented at any desired angle, but without loss of generality the following calculation will assume that the polarimeter is configured with the fast axis of the first linear polarizer with $\theta = 0°$. With this assumption the standard configuration of the circular polarimeter and three-dimensional birefringent specimen is as follows:

1. Ideal linear polarizer with $\theta = 0°$ (the "polarizer")
2. Ideal quarter-wave linear retarder with $\theta = 45°$
3. Ideal linear retarder with retardation δ and fast axis at angle α
4. Ideal rotator of strength ρ
5. Ideal quarter-wave linear retarder with $\theta = 135°$
6. Ideal linear polarizer with $\theta = 90°$ (the "analyzer")

Table D.1: Mueller matrices for ideal optical elements. In the following arrays $S_{2\theta} = \sin 2\theta$, $C_{2\theta} = \cos 2\theta$, $S_\delta = \sin \delta$, and $C_\delta = \cos \delta$.

Ideal linear polarizer at angle θ

$$\frac{1}{2}\begin{bmatrix} 1 & C_{2\theta} & S_{2\theta} & 0 \\ C_{2\theta} & C_{2\theta}^2 & C_{2\theta}S_{2\theta} & 0 \\ S_{2\theta} & C_{2\theta}S_{2\theta} & S_{2\theta}^2 & 0 \\ 0 & 0 & 0 & 0 \end{bmatrix}$$

Quarter-wave linear retarder with fast axis at angle θ

$$\begin{bmatrix} 1 & 0 & 0 & 0 \\ 0 & C_{2\theta}^2 & C_{2\theta}S_{2\theta} & -S_{2\theta} \\ 0 & C_{2\theta}S_{2\theta} & S_{2\theta}^2 & C_{2\theta} \\ 0 & S_{2\theta} & -C_{2\theta} & 0 \end{bmatrix}$$

Ideal linear retarder with retardation δ and fast axis at angle θ

$$\begin{bmatrix} 1 & 0 & 0 & 0 \\ 0 & C_{2\theta} + S_{2\theta}^2 & C_{2\theta}S_{2\theta}(1 - C_\delta) & -S_{2\theta}S_\delta \\ 0 & C_{2\theta}S_{2\theta}(1 - C_\delta) & S_{2\theta}^2 + C_\delta C_{2\theta} & C_{2\theta}S_\delta \\ 0 & S_{2\theta}S_\delta & -C_{2\theta}S_\delta & C_\delta \end{bmatrix}$$

Rotator of strength θ

$$\begin{bmatrix} 1 & 0 & 0 & 0 \\ 0 & C_{2\theta} & -S_{2\theta} & 0 \\ 0 & S_{2\theta} & C_{2\theta} & 0 \\ 0 & 0 & 0 & 0 \end{bmatrix}$$

This configuration is commonly called a "dark-field" circular polarimeter since the field is black if no specimen is present.

The process starts with unpolarized light passing through the polarizer. The Stokes vector for unpolarized light of intensity I_0 is $S_0 = [\ I_0 \quad 0 \quad 0 \quad 0\ ]^T$. The Stokes vector of the light exiting the polarizer is given by

$$S_1 = \frac{1}{2}\begin{bmatrix} 1 & 1 & 0 & 0 \\ 1 & 1 & 0 & 0 \\ 0 & 0 & 0 & 0 \\ 0 & 0 & 0 & 0 \end{bmatrix}\begin{bmatrix} I_0 \\ 0 \\ 0 \\ 0 \end{bmatrix} = \frac{I_0}{2}\begin{bmatrix} 1 \\ 1 \\ 0 \\ 0 \end{bmatrix} \tag{D.1}$$

The light then passes through a quarter-wave plate with its fast axis at 45° to horizontal. The resulting Stokes vector is given by:

$$S_2 = \frac{I_0}{2}\begin{bmatrix} 1 & 0 & 0 & 0 \\ 0 & 0 & 0 & -1 \\ 0 & 0 & 1 & 0 \\ 0 & 1 & 0 & 0 \end{bmatrix}\begin{bmatrix} 1 \\ 1 \\ 0 \\ 0 \end{bmatrix} = \frac{I_0}{2}\begin{bmatrix} 1 \\ 0 \\ 0 \\ 1 \end{bmatrix} \tag{D.2}$$

Next the light passes through the three-dimensional birefringent plate. This plate is represented by the equivalent optical model of a linear retarder with retardation δ and principal axis at angle α followed by a rotator of strength ρ. First the linear retarder:

$$
\begin{aligned}
S_3 &= \frac{I_0}{2}\begin{bmatrix} 1 & 0 & 0 & 0 \\ 0 & C_{2\alpha}+S_{2\alpha}^2 C_\delta & C_{2\alpha}S_{2\alpha}(1-C_\delta) & -S_{2\alpha}S_\delta \\ 0 & C_{2\alpha}S_{2\alpha}(1-C_\delta) & S_{2\alpha}^2+C_\delta C_{2\alpha} & C_{2\alpha}S_\delta \\ 0 & S_{2\alpha}S_\delta & -C_{2\alpha}S_\delta & C_\delta \end{bmatrix}\begin{bmatrix} 1 \\ 0 \\ 0 \\ 1 \end{bmatrix} \\
&= \frac{I_0}{2}\begin{bmatrix} 1 \\ -S_{2\alpha}S_\delta \\ C_{2\alpha}S_\delta \\ C_\delta \end{bmatrix}
\end{aligned} \tag{D.3}
$$

Next the rotator of strength ρ:

$$
\begin{aligned}
S_4 &= \frac{I_0}{2}\begin{bmatrix} 1 & 0 & 0 & 0 \\ 0 & C_{2\rho} & -S_{2\rho} & 0 \\ 0 & S_{2\rho} & C_{2\rho} & 0 \\ 0 & 0 & 0 & 1 \end{bmatrix}\begin{bmatrix} 1 \\ -S_{2\alpha}S_\delta \\ C_{2\alpha}S_\delta \\ C_\delta \end{bmatrix} \\
&= \frac{I_0}{2}\begin{bmatrix} 1 \\ -C_{2\rho}S_{2\alpha}S_\delta - S_{2\rho}C_{2\alpha}S_\delta \\ -S_{2\rho}S_{2\alpha}S_\delta + C_{2\rho}C_{2\alpha}S_\delta \\ C_\delta \end{bmatrix}
\end{aligned} \tag{D.4}
$$

The light then passes through the second quarter-wave plate. The fast axis of this plate is at 135° to the horizontal:

$$
\begin{aligned}
S_5 &= \frac{I_0}{2}\begin{bmatrix} 1 & 0 & 0 & 0 \\ 0 & 0 & 0 & 1 \\ 0 & 0 & 1 & 0 \\ 0 & -1 & 0 & 0 \end{bmatrix}\begin{bmatrix} 1 \\ -C_{2\rho}S_{2\alpha}S_\delta - S_{2\rho}C_{2\alpha}S_\delta \\ -S_{2\rho}S_{2\alpha}S_\delta + C_{2\rho}C_{2\alpha}S_\delta \\ C_\delta \end{bmatrix} \\
&= \frac{I_0}{2}\begin{bmatrix} 1 \\ C_\delta \\ -S_{2\rho}S_{2\alpha}S_\delta + C_{2\rho}C_{2\alpha}S_\delta \\ C_{2\rho}S_{2\alpha}S_\delta + S_{2\rho}C_{2\alpha}S_\delta \end{bmatrix}
\end{aligned} \tag{D.5}
$$

Finally the light passes through a linear polarizer with a vertical axis:

$$
\begin{aligned}
S_6 &= \frac{I_0}{4}\begin{bmatrix} 1 & -1 & 0 & 0 \\ -1 & 1 & 0 & 0 \\ 0 & 0 & 0 & 0 \\ 0 & 0 & 0 & 0 \end{bmatrix}\begin{bmatrix} 1 \\ C_\delta \\ -S_{2\rho}S_{2\alpha}S_\delta + C_{2\rho}C_{2\alpha}S_\delta \\ C_{2\rho}S_{2\alpha}S_\delta + S_{2\rho}C_{2\alpha}S_\delta \end{bmatrix} \\
&= \frac{I_0}{4}\begin{bmatrix} 1 - C_\delta \\ -1 + C_\delta \\ 0 \\ 0 \end{bmatrix}
\end{aligned} \tag{D.6}
$$

The intensity of the light exiting the polarimeter, I_6, is the first element of the Stokes vector S_6:

$$
I_6 = \frac{I_0}{4}(1 - \cos\delta) = \frac{I_0}{2}\sin^2\frac{\delta}{2} \tag{D.7}
$$

This intensity is a function of the retardation only and is independent of the orientation of the principal axis α and the rotation strength ρ. Therefore the retar-

dation can be measured with a compensator with the same procedure that would be used for a two-dimensional birefringent specimen in a circular polarimeter.

Equation D.7 shows that light is extinguished when the retardation $\delta = 2n\pi$. A common technique in examining fringe patterns in two-dimensional specimens involves rotating the analyzer 90° putting the fast axes of the polarizer and analyzer in parallel. This configuration is commonly called a "light-field" polarimeter because the field is light if a specimen is not present. This configuration causes the fringes to appear when the retardation $\delta = (2n + 1)\pi$.

The light-field polarimeter follows the same analysis until the final step where the polarized light enters a horizontal analyzer rather than a vertical one:

$$\begin{aligned} S_6 &= \frac{I_0}{4} \begin{bmatrix} 1 & 1 & 0 & 0 \\ 1 & 1 & 0 & 0 \\ 0 & 0 & 0 & 0 \\ 0 & 0 & 0 & 0 \end{bmatrix} \begin{bmatrix} 1 \\ C_\delta \\ -S_{2\rho}S_{2\alpha}S_\delta + C_{2\rho}C_{2\alpha}S_\delta \\ C_{2\rho}S_{2\alpha}S_\delta + S_{2\rho}C_{2\alpha}S_\delta \end{bmatrix} \\ &= \frac{I_0}{4} \begin{bmatrix} 1 + C_\delta \\ 1 + C_\delta \\ 0 \\ 0 \end{bmatrix} \end{aligned} \tag{D.8}$$

The intensity of the light exiting the light-field polarimeter is given by the first Stokes parameter:

$$I_6 = \frac{I_0}{4}(1 + \cos\delta) = \frac{I_0}{2}\cos^2\frac{\delta}{2} \tag{D.9}$$

This confirms that even for a three-dimensional specimen a light-field polarimeter produces fringes that are functions only of the retardation. The fringes appear for $\delta = (2n + 1)\pi$.

APPENDIX E

Birefringence Measurements on Packed and Unpacked Specimens

This appendix contains a tabulation of the birefringence data analyzed in Chapter 8. The location and labels of the data points can be found in Figure E.1.

Each table summarizes all the data taken of a single birefringence parameter over eight specimens molded at the same packing pressure. The columns of the data tables in this chapters represent measurements taken at a single position over all eight specimens. The rows represent data at all six locations from a single specimen. The last row of each table is an indication of whether the data sets taken at each position passed the Lilliefors test for normality as described in Chapter 8. A "Y" indicates that the data passed the test at the 5% significance level and is considered normally distributed. An "N" indicates that the data did not pass the test at the 5% significance level and in not considered normally distributed.

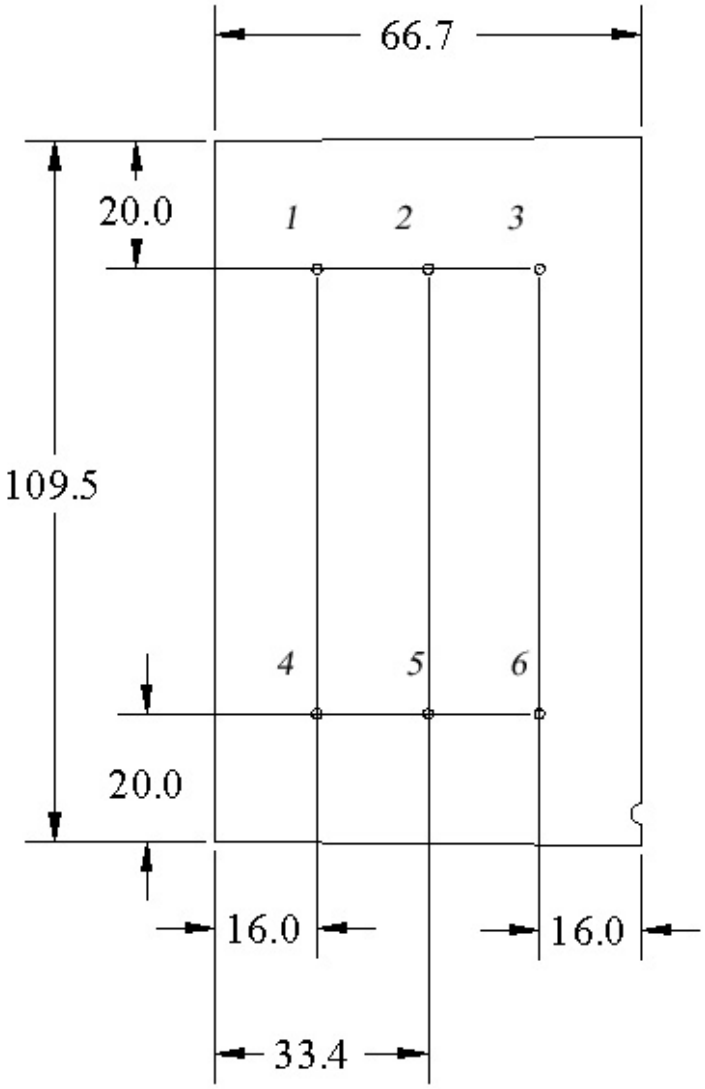

Figure E.1: The primary axis, rotator strength, specimen thickness and retardation were measured and the six locations shown. The gate is in the lower right corner. All dimensions are in millimeters. The italic numbers are the labels used in the data tables in this appendix.

Table E.1: Principal axis orientation measurements in degrees on unpacked specimens. The error is ±2°
.

Specimen	Position					
	1	2	3	4	5	6
1	56	60	80	43	14	36
2	79	78	65	47	26	39
3	70	39	40	41	45	51
4	62	8	12	45	10	25
5	52	78	89	48	2	52
6	63	85	84	51	82	2
7	65	66	33	43	11	38
8	66	64	39	45	9	30
Normal?	Y	Y	Y	Y	Y	Y

Table E.2: Rotator strength measurements in degrees on unpacked specimens. The error is ±0.9°
.

Specimen	Position					
	1	2	3	4	5	6
1	19.8	5.4	-3.6	10.8	5.4	-16.2
2	0.0	0.0	0.0	7.2	3.6	9.0
3	1.8	-5.4	-12.6	0.0	-3.6	5.4
4	12.6	-10.8	-10.8	3.6	3.6	19.8
5	14.4	3.6	-1.8	5.4	19.8	-39.6
6	5.4	3.6	-10.8	1.8	59.4	68.4
7	10.8	1.8	3.6	0.0	1.8	3.6
8	25.2	0.0	7.2	5.4	12.6	3.6
Normal?	Y	Y	Y	Y	Y	Y

Table E.3: Specimen thickness measurements in millimeters on unpacked specimens. The error is ±.0254 mm
.

Specimen	Position					
	1	2	3	4	5	6
1	6.1722	6.4516	6.6294	6.3500	6.4262	6.6294
2	6.0452	6.4008	6.4516	6.4008	6.3754	6.6802
3	6.1468	6.4516	6.5278	6.4516	6.4262	6.7310
4	6.2484	6.3754	6.4516	6.4008	6.4262	6.6294
5	6.1976	6.4516	6.8580	6.3754	6.5786	6.7564
6	6.0452	6.3754	6.4770	6.4008	6.3500	6.6802
7	6.0960	6.3754	6.5532	6.3246	6.4516	6.5786
8	6.1722	6.4008	6.4770	6.3246	6.4770	6.6294
Normal?	Y	Y	Y	Y	Y	Y

Table E.4: Measurements of the ratio of retardation length in nanometers to local specimen thickness in millimeters on unpacked specimens. The error is ±3.4%
.

Specimen	Position					
	1	2	3	4	5	6
1	37.26	33.67	19.27	-24.15	-45.73	-73.24
2	16.91	5.99	5.94	13.97	-18.04	-26.78
3	35.34	11.88	-19.57	-13.86	-11.93	34.17
4	22.49	34.07	27.73	-15.97	-33.80	-46.26
5	47.42	35.65	11.18	20.04	-60.21	60.52
6	23.25	24.05	17.76	5.99	52.32	-32.52
7	16.77	14.03	-11.70	8.08	-19.81	-33.02
8	-33.12	-23.96	17.76	-4.04	-19.73	-34.69
Normal?	N	Y	Y	Y	Y	N

Table E.5: Principal axis orientation measurements in degrees on 11.0 MPa packed specimens. The error is ±2°
.

Specimen	Position					
	1	2	3	4	5	6
1	81	80	33	20	38	12
2	65	87	88	53	27	20
3	87	79	40	15	80	49
4	56	15	36	44	3	42
5	5	83	56	28	21	19
6	68	5	37	38	19	41
7	70	86	39	43	10	41
8	55	82	45	40	16	50
Normal?	Y	N	N	Y	Y	N

Table E.6: Rotator strength measurements in degrees on 11.0 MPa packed specimens. The error is ±0.9°
.

Specimen	Position					
	1	2	3	4	5	6
1	-5.4	0.0	-3.6	-5.4	7.2	1.8
2	19.8	3.6	-1.8	-5.4	7.2	-5.4
3	7.2	3.6	9.0	-3.6	3.6	5.4
4	0.0	-3.6	1.8	-3.6	3.6	-3.6
5	19.8	3.6	-5.4	-9.0	1.8	-10.8
6	5.4	0.0	5.4	1.8	-3.6	9.0
7	5.4	1.8	3.6	3.6	1.8	-3.6
8	-1.8	-1.8	-1.8	1.8	1.8	5.4
Normal?	Y	Y	Y	Y	Y	Y

Table E.7: Specimen thickness measurements in millimeters on 11.0 MPa packed specimens. The error is ±.0254 mm
.

Specimen	Position					
	1	2	3	4	5	6
1	6.1976	6.4008	6.3754	6.3246	6.4516	6.5278
2	6.2230	6.4516	6.5278	6.3246	6.4262	6.5024
3	6.2230	6.4770	6.5024	6.2992	6.4770	6.5278
4	6.2230	6.4516	6.5024	6.3246	6.5024	6.5024
5	6.2230	6.4008	6.4008	6.2484	6.4770	6.5024
6	6.1976	6.4262	6.4770	6.2992	6.4770	6.4770
7	6.1976	6.4770	6.3754	6.3246	6.4516	6.4770
8	6.1722	6.4262	6.4516	6.2484	6.4770	6.5024
Normal?	N	Y	Y	Y	Y	Y

Table E.8: Measurements of the ratio of retardation length in nanometers to local specimen thickness in millimeters in 11.0 MPa packed specimens. The error is ±3.4%
.

Specimen	Position					
	1	2	3	4	5	6
1	18.6	24.0	14.0	14.1	17.8	-33.3
2	26.7	19.8	17.6	-26.3	-47.7	-43.2
3	12.3	7.9	9.8	0.0	-9.9	0.0
4	10.3	-17.8	33.4	26.3	-25.5	47.2
5	4.1	31.9	6.0	6.1	-7.9	-31.4
6	16.5	-2.0	-27.6	-20.3	11.8	13.8
7	24.7	3.9	24.1	24.2	-15.8	23.7
8	29.0	-11.9	-31.7	-20.4	11.8	23.6
Normal?	Y	Y	Y	Y	Y	Y

Table E.9: Principal axis orientation measurements in degrees on 16.5 MPa packed specimens. The error is ±2°
.

Specimen	Position					
	1	2	3	4	5	6
1	35	8	35	34	32	28
2	82	3	31	76	26	32
3	71	84	35	2	27	30
4	80	3	36	75	21	28
5	1	2	35	29	32	27
6	75	3	72	26	40	19
7	60	11	70	12	33	9
8	65	5	40	17	48	26
Normal?	Y	N	N	Y	Y	N

Table E.10: Rotator strength measurements in degrees on 16.5 MPa packed specimens. The error is ±0.9°
.

Specimen	Position					
	1	2	3	4	5	6
1	-12.6	19.8	-16.2	3.6	16.2	9.0
2	18.0	14.4	16.2	3.6	-1.8	1.8
3	-7.2	10.8	-3.6	1.8	-1.8	3.6
4	5.4	16.2	10.8	9.0	-3.6	0.0
5	7.2	12.6	-5.4	-3.6	12.6	9.0
6	5.4	3.6	12.6	1.8	19.8	21.6
7	5.4	3.6	9.0	3.6	-10.8	-32.4
8	3.6	9.0	7.2	-3.6	10.8	3.6
Normal?	Y	Y	Y	Y	Y	N

Table E.11: Specimen thickness measurements in millimeters on 16.5 MPa packed specimens. The error is ±.0254 mm
.

Specimen	Position					
	1	2	3	4	5	6
1	6.3246	6.5786	6.6040	6.3754	6.5786	6.7310
2	6.4008	6.6548	6.6548	6.3754	6.5024	6.6040
3	6.3246	6.6548	6.6548	6.4516	6.5786	6.7564
4	6.4008	6.6294	6.6548	6.3754	6.5532	6.6040
5	6.2992	6.5786	6.6040	6.3246	6.5278	6.5786
6	6.3754	6.5786	6.6040	6.3246	6.5278	6.5532
7	6.4008	6.6294	6.6040	6.3500	6.5532	6.5786
8	6.3246	6.5786	6.6040	6.3754	6.5532	6.6040
Normal?	Y	N	N	N	Y	N

Table E.12: Measurements of the ratio of retardation length in nanometers to local specimen thickness in millimeters in 16.5 MPa packed specimens. The error is ±3.4%
.

Specimen	Position					
	1	2	3	4	5	6
1	-10.1	9.7	-3.9	6.0	29.1	45.6
2	6.0	9.6	-17.3	-24.1	-3.9	-46.4
3	-18.2	-13.4	7.7	-9.9	-27.2	41.6
4	8.0	5.8	-5.8	-10.0	-9.7	-32.9
5	16.2	13.6	9.7	16.2	3.9	44.7
6	8.0	17.5	-38.7	26.3	7.8	56.5
7	14.0	7.7	-31.0	-18.1	9.7	40.8
8	12.1	9.7	-15.5	10.0	13.6	34.8
Normal?	N	N	Y	Y	Y	N

Table E.13: Principal axis orientation measurements in degrees on 27.6 MPa packed specimens. The error is ±2°
.

Specimen	Position					
	1	2	3	4	5	6
1	12	3	87	6	30	20
2	22	8	60	43	50	84
3	88	87	87	3	11	11
4	15	3	86	3	45	60
5	65	3	86	71	25	4
6	10	4	88	82	6	5
7	21	16	6	78	11	14
8	43	79	89	88	27	86
Normal?	N	N	N	Y	Y	N

Table E.14: Rotator strength measurements in degrees on 27.6 MPa packed specimens. The error is ±0.9°
.

Specimen	Position					
	1	2	3	4	5	6
1	0.0	5.4	-12.6	5.4	10.8	-14.4
2	5.4	0.0	0.0	-3.6	-3.6	-1.8
3	-3.6	-3.6	-9.0	7.2	10.8	-18.0
4	-5.4	0.0	-12.6	3.6	9.0	-25.2
5	-3.6	0.0	-7.2	3.6	-7.2	19.8
6	0.0	3.6	-16.2	-10.8	14.4	-5.4
7	-3.6	3.6	-9.0	-7.2	9.0	-7.2
8	7.2	-3.6	-10.8	1.8	0.0	28.8
Normal?	Y	Y	Y	Y	N	Y

Table E.15: Specimen thickness measurements in millimeters on 27.6 MPa packed specimens. The error is ±.0254 mm
.

Specimen	Position					
	1	2	3	4	5	6
1	6.6294	6.8580	6.8834	6.6802	6.8834	7.0104
2	6.7564	6.9342	6.9596	6.7564	6.9342	7.0612
3	6.7564	6.9596	6.9850	6.7310	6.9596	7.0358
4	6.7564	6.9342	7.0104	6.7818	6.9596	7.0612
5	6.7818	6.9850	7.0104	6.8326	7.0104	7.0358
6	6.7818	6.9850	7.0612	6.8326	7.0104	7.1374
7	6.8072	6.9596	7.0612	6.8326	6.9596	7.0612
8	6.8072	6.9850	7.0358	6.8326	6.9850	7.0866
Normal?	N	Y	Y	N	Y	Y

Table E.16: Measurements of the ratio of retardation length in nanometers to local specimen thickness in millimeters in 27.6 MPa packed specimens. The error is ±3.4%
.

Specimen	Position					
	1	2	3	4	5	6
1	7.7	35.4	-26.0	-13.4	-16.7	-34.6
2	9.5	-9.2	-14.7	5.7	-11.1	-32.6
3	-7.6	-27.5	-40.2	-24.7	-27.5	-49.0
4	9.5	27.6	-20.0	-24.5	-18.4	-29.0
5	15.1	34.8	-16.4	-22.4	-7.3	-40.0
6	5.7	20.1	-30.8	-28.1	-27.3	-60.9
7	9.4	20.2	-14.5	-33.7	-18.4	-57.9
8	5.6	27.4	-27.2	-13.1	-7.3	-32.5
Normal?	N	N	Y	Y	Y	Y

BIBLIOGRAPHY

BIBLIOGRAPHY

[1] Market Search, Inc. *Automotive Plastics Report*, 2001.

[2] R. Spencer and G. Gilmore. Residual strains in injection molded plastics. *Modern Plastics*, 28, December 1950.

[3] G. Gilmore and S. Spencer. Photographic study of the polymer cycle in injection molding. *Modern Plastics*, 28, April 1951.

[4] G. Gilmore and S. Spencer. Role of pressure, temperature and time in the injection molding process. *Modern Plastics*, 27, April 1950.

[5] R. Spencer and G. Gilmore. Some flow phenomena in the injection molding of polystyrene. *Journal of Colloid Science*, 6, 1951.

[6] M. Kamal and S. Kenig. The injection molding of thermoplastics Part I: Theoretical model. *Polymer Engineering and Science*, 12, 1972.

[7] M. Kamal and S. Kenig. The injection molding of thermoplastics Part II: Experimental test of the model. *Polymer Engineering and Science*, 12, 1972.

[8] J. Tordella. Capillary flow of molten polyethylene—a photographic study of melt fracture. *Transactions of the Society of Rheology*, 1, 1957.

[9] L. Schmidt. A special mold and tracer technique for studying shear and extensional flows in a mold cavity during injection molding. *Polymer Engineering and Science*, 14, 1974.

[10] J. White and H. Dee. Flow visualization for injection molding of polyethylene and polystyrene melts. *Polymer Engineering and Science*, 14, 1974.

[11] J. White. Fluid mechanical analysis of injection mold filling. *Polymer Engineering and Science*, 15, 1975.

[12] K. Oda, J. White, and E. Clark. Jetting phenomena in injection mold filling. *Polymer Engineering and Science*, 16, 1976.

[13] Y. Chan, J. White, and Y. Oyangi. Influence of glass fibers on the extrusion and injection molding characteristics of polyethylene and polystyrene melts. *Polymer Engineering and Science*, 18, 1978.

[14] W. Lee and H. George. Flow visualization of fiber suspensions. *Polymer Engineering and Science*, 18, 1978.

[15] J. White and W. Dietz. Some relationships between injection molding conditions and the characteristics of vitrified molded parts. *Polymer Engineering and Science*, 19, 1979.

[16] M. Anastas, R. Lynn, and R. Brodkey. A visual study of the dynamics of polymer extrusion. *Journal of Rheology*, 22, 1978.

[17] D. Coyle, J. Blake, and C. Macosko. The kinematics of fountain flow in mold filling. *American Institute of Chemical Engineering Journal*, 33, 1987.

[18] D. Boger. Viscoelastic flows through contractions. *Annual Review of Fluid Mechanics*, 19, 1987.

[19] S. Hobbs. Some observations on the morphology and fracture characteristics of knit lines. *Polymer Engineering and Science*, 14, 1974.

[20] S. Chen, K. Hsu, and W. Jung. Study of polymer melt flow during injection molding using co-injection molding technique. *SPE Technical Papers (ANTEC)*, 40, 1994.

[21] H. Yokoi, S. Kamata, and T. Kanematsu. Visual observation of three dimensional melt flow inside a mold cavity by gate-magnetization method. *SPE Technical Papers (ANTEC)*, 37, 1991.

[22] H. Yokoi and Y. Murata. Visual analysis of weld line vanishing process by glass inserted mold. *SPE Technical Papers (ANTEC)*, 37, 1991.

[23] M. Weissenberger, A. Giacomin, J. Reuscher, and C.M. Russell. Real time neutron radiography of injection mold filling. *International Polymer Processing*, 8, 1993.

[24] A. Özdemir, O. Uluer, and A. Güldaş. Flow front advancement of molten thermoplastic materials during filling stage of a mold cavity. *Polymer Testing*, 23, 2004.

[25] H. Yokoi, T. Hayashi, K. Toda, and N. Morikita. Direct observation of jetting phenomena under a high injection pressure using a prismatic glass inserted mold. *SPE Technical Papers (ANTEC)*, 34, 1988.

[26] H. Yokoi, S. Nagami, A. Kawasaki, and Y. Murata. Visual analyses of flow marks generation process using glass-inserted mold - Part I. Micro-grooved flow marks. *SPE Technical Papers (ANTEC)*, 40, 1994.

[27] H. Yokoi, Y. Deguchi, L. Sakamoto, and Y. Murata. Visual analyses of flow marks generation process using glass-inserted mold - Part II. Synchronous flow marks with same phases on both top and bottom surfaces of molded samples. *SPE Technical Papers (ANTEC)*, 40, 1994.

[28] S. Penner and T. Jerskey. Use of lasers for local measurement of velocity components, species densities, and temperatures. *Annual Review of Fluid Mechanics*, 5, 1973.

[29] A. Ramamurthy. Velocity descriptions in the die exit region for a polymer solution: Influence of die entry instabillities. *Transactions of the Society of Rheology*, 20, 1976.

[30] M. Mackley and I. Moore. Experimental velocity distribution measurements of high density polyethylene flowing into and within a slit. *Journal of Non-Newtonian Fluid Mechanics*, 21, 1986.

[31] R. Ahmed and M. Mackley. Experimental centerline planar extension of polyethylene melt flowing into a slit die. *Journal of Non-Newtonian Fluid Mechanics*, 56, 1995.

[32] R. Yalamanchili, A. Sirivat, and K. Rajagopal. An experimental investigation of the flow of dilute polymer solutions through corrugated channels. *Journal of Non-Newtonian Fluid Mechanics*, 58, 1995.

[33] B. Tremblay. Visualization of the flow of linear low density polyethylene/low density polyethylene blends through sudden contractions. *Journal of Non-Newtonian Fluid Mechanics*, 43, 1992.

[34] R. Kröger and H. Rath. Velocity and elongation rate distributions in stretched polymeric and Newtonian liquid bridges. *Journal of Non-Newtonian Fluid Mechanics*, 57, 1995.

[35] H. Yokoi and Y. Inagaki. Dynamic visualization of cavity filling process along thickness direction using a laser-light-sheet technique. *SPE Technical Papers (ANTEC)*, 38, 1992.

[36] M. Tehrani. An experimental study of particle migration in pipe flow of viscoelastic fluids. *Journal of Rheology*, 40, 1996.

[37] R. Binnington, G. Troup, and D. Boger. A low cost laser-speckle photographic technique for velocity measurement in slow flows. *Journal of Non-Newtonian Fluid Mechanics*, 12, 1983.

[38] R. Adrian. Particle-imaging techniques for experimental fluid mechanics. *Annual Review of Fluid Mechanics*, 23, 1991.

[39] M. Raffel, C. Willert, and J. Kompenhans. *Particle Image Velocimetry*. Springer-Verlag, 1998.

[40] P. Pakdel and G. McKinley. Digital particle image velocimetry of viscoelastic fluids. *American Institute of Chemical Engineering Journal*, 43, 1997.

[41] B. Baumert, D. Liepmann, and S. Muller. Digital particle image velocimetry in flows with nearly closed pathlines: the viscoelastic taylor-couette instability. *Journal of Non-Newtonian Fluid Mechanics*, 69, 1997.

[42] C. Willert and M. Gharib. Digital particle image velocimetry. *Experiments in Fluids*, 10, 1991.

[43] V. Kolli, S. Ogadhoh, S. Abel, F. Gadala-Maria, and T. Papathanasiou. Particle motion in the fountain flow region during filling of a tube with a viscoelastic fluid. *Polymer Engineering and Science*, 42, 2002.

[44] W. Michaeli and P. Blömer. Flat spiral dies - rheological design with network theory. *Journal of Polymer Engineering*, 24, 2004.

[45] D. Brewster. On the effects of simple pressure in producing that species of crystallization which forms two oppositely polarized images, and exhibits the complementary colors by polarized light. *Philosophical Transactions of the Royal Society of London*, 105, 1815.

[46] D. Brewster. On the communication of the structure of doubly-refracting crystals to glass, muriate of soda, fluor spar, and other substances, by mechanical compression and dilatation. *Philosophical Transactions of the Royal Society of London*, 106, 1816.

[47] J. Dally and W. Riley. *Experimental Stress Analysis*. McGraw-Hill Book Company, New York, 1955.

[48] A. Hendry. *Elements of Experimental Stress Analysis*. Pergamon Press, Oxford, 1977.

[49] M. Frocht. *Photoelasticity, vol. 1*. Wiley, London, 1941.

[50] M. Frocht. *Photoelasticity, vol. 2*. Wiley, London, 1948.

[51] H. Aben. Optical phenomena in photoelastic models by the rotation of principal axes. *Experimental Mechanics*, 6, 1966.

[52] K. Ramesh. *Digital Photoelasticity*. Springer, Berlin, 2000.

[53] S. Huard. *Polarization of Light*. John Wiley & Sons, Chichester, 1996.

[54] A. Gerrard and J. Burch. *Introduction to Matrix Methods in Optics*. John Wiley & Sons, London, 1975.

[55] P. Theocaris and E. Gdoutos. *Matrix Theory of Photoelasticity*. Springer-Verlag, Berlin, 1979.

[56] C. Han and C. Villamizar. Development of stress birefringence and flow patterns during mold filling and cooling. *Polymer Engineering and Science*, 18, 1978.

[57] S. White and D. Baird. Flow visualization and birefringence studies on planar entry flow behavior of polymer melts. *Journal of Non-Newtonian Fluid Mechanics*, 29, 1988.

[58] R. Subramanian, D. Wilson, and J. Picot. Flow birefringence in polymer rheoloogy. *Polymer Engineering and Science*, 32, 1992.

[59] T. Saito and I. Satoh. Visualization of polymer melt flow around an obstructive pin during the injection molding process. In *PSFVIP-2*. Pacific Symposia on Flow Visualization and Image Processing, 1999.

[60] Cincinnati Milacron. *Vista Sentry - VST User's Manual*, 1995.

[61] Dow Chemical. *STYRON 615APR General Purpose Polystyrene Resin*.

[62] J. Dealy and K. Wissbrun. *Melt Rheology and its Role in Plastics Processing*. Van Nostrand Reinhold, New York, 1990.

[63] R. Bird, R. Armstrong, and O. Hassager. *Dynamics of Polymeric Liquids*, volume 1. John Wiley and Sons, New York, 2 edition, 1987.

[64] R. Brodkey. *The Phenomena of Fluid Motions*. Dover Publications, Inc., New York, 1967.

[65] J. D. Ferry. *Viscoelastic Properties of Polymers*. J. Wiley and Sons, New York, 1980.

[66] J. Honerkamp and J. Weese. Using regularization methods for the determination of relaxation and retardation spectra of polymeric liquids. *Rheologica Acta*, 30, 1991.

[67] Freiburg Materials Research Center. *FTIKREG: A program for the solution of Fredholm integral equations of the first kind*.

[68] G. Schramm. *A Practical Approach to Rheology and Rheometry*. Gebrueder HAAKE GmbH, Karlsruhe, 1994.

[69] R. Tanner and K. Walters. *Rheology: An Historical Perspective*. Elsevier, Amsterdam, 1998.

[70] A. Shenoy and D. Saini. *Thermoplastic Melt Rheology and Processing*. Marcel Dekker, Inc., New York, 1996.

[71] T. Bress and D. Dowling. Visualization of injection molding. *Journal of Reinforced Plastics and Composites*, 17, 1998.

[72] J. Bouguet. Camera calibration toolbox for Matlab. `http://www.vision.caltech.edu/boughet/calib_doc/index.html#parameters`.

[73] R. Tanner and A. Pipkin. Intrinsic errors in pressure-hole measurements. *Transactions of the Society of Rheology*, 13, 1969.

[74] ASTM. *ASTM D 4093 Standard Test Method for Photoelastic Measurements of Birefringence and Residual Strains in Transparent or Translucent Plastic Materials*, 2001.

[75] G. Khanarian and Hoechst Celanese. Optical properties of cyclic olefin copolymers. *Optical Engineering*, 40, 2001.

[76] J. Bicerano. *Prediction of Polymer Properties*. Marcel Dekker, Inc., New York, 2002.

[77] R. Wimberger-Friedl. The assessment of orientation, stress and density distributions in injection-molded amorphous polymers by optical techniques. *Progress in Polymer Science*, 20, 1995.

[78] N. J. Mills. *Plastics: Microstructure and Engineering Applications*. Edward Arnold, London, 1993.

[79] E. Hecht. *Optics, 2nd Edition*. Addison-Wesley, Reading, 1990.

[80] R. Kean, R. Adrian, and Y. Zhang. Super-resolution particle image velocimetry. *Measurement Science and Technology*, 6, 1995.

[81] M. Kamal and A. Mutel. Rheological properties of suspensions of newtonian and non-newtonian fluids. *Journal of Polymer Engineering*, 5, 1986.

[82] A. Metzner. Rheology of suspensions in polymeric liquids. *Journal of Rheology*, 29, 1985.

[83] B. R. Jennings and K. Parslow. Particle size measurement: the equivalent spherical diameter. *Proceedings of the Royal Society of London. Series A, Mathematical and Physical Sciences*, 4192, 1988.

[84] C. Crowe, M. Sommerfeld, and Y. Tsuji. *Multiphase flows with Droplets and Particles*. CRC Press, Boca Raton, 1998.

[85] E. Avallone and T. Baumeister. *Marks' Standard Handbook for Mechanical Engineers, 9th Ed.* McGraw-Hill, New York, 1986.

[86] A. Melling. Tracer particles and seeding for particle image velocimetry. *Measurement Science and Technology*, 8, 1997.

[87] R. Chhabra. *Bubbles, Drops and Particles in Non-Newtonian Fluids*. CRC Press, Boca Raton, 1993.

[88] M. Bush and N. Phan-Thien. Drag force on a sphere in creeping motion through a carreau model fluid. *Journal of Non-Newtonian Fluid Mechanics*, 16, 1984.

[89] R. Chhabra and P. Uhlherr. Creeping motion of spheres through shearthinning elastic fluids described by the Carreau viscosity equation. *Rheologica Acta*, 19, 1980.

[90] A. Acharya, R. Mashelkar, and J. Ulbrecht. Flow of inelastic and viscoelastic fluids past a sphere. *Rheologica Acta*, 15, 1976.

[91] M. Solomon and S. Muller. Flow past a sphere in polystyrene-based Boger fluids: the effect on the drag coefficient of finite extensibility, solvent quality and polymer molecular weight. *Journal of Non-Newtonian Fluid Mechanics*, 62, 1995.

[92] C. Chmielewski, K. Nichols, and K. Jayaraman. A comparison of the drag coefficients of spheres translating in corn-syrup-based and polybutene-based Boger fluids. *Journal of Non-Newtonian Fluid Mechanics*, 35, 1990.

[93] F. Gauthier, H. L. Goldsmich, and Mason S. G. Particle motions in non-newtonian media. i. couette flow. *Rheologica Acta*, 10, 1971.

[94] F. Gauthier, H. L. Goldsmich, and Mason S. G. Particle motions in non-newtonian media. i. poiseuille flow. *Transactions of the Society of Rheology*, 15, 1971.

[95] S. Emerman. Prediction of polymer-filler redistribution in injection molding. *Polymer Engineering and Science*, 27, 1987.

[96] P. Brunn. The behavior of a sphere in non homogeneous flows of a viscoelastic fluid. *Rheologica Acta*, 15, 1976.

[97] P. C.-H. Chan and L. Leal. A note on the motion of a spherical particle in a general quadratic flow of a second order fluid. *Journal of Fluid Mechanics*, 82, 1977.

[98] P. Brunn. The motion of rigid particles in viscoelastic fluids. *Journal of Non-Newtonian Fluid Mechanics*, 7, 1980.

[99] C. Gerald and P. Wheatley. *Applied Numerical Analysis*. Addison-Wesley, Reading, 1985.

[100] L. Koopmans. *Introduction to Contemporary Statistical Methods*. Duxbury Press, Boston, 1987.

[101] R. McGill, J. Tukey, and W. Larsen. Variations of box plots. *The American Statistician*, 32, 1978.

[102] F. J. Massey. The kolmogorov-smirnov test for goodness of fit. *Journal of the American Statistical Association*, 46.

[103] J. Dantzig and C. Tucker. *Modeling in Materials Processing*. Cambridge University Press, Cambridge, 2001.

[104] H. Tseng. Analysis of rheological data from an automated-injection molding capillary rheometer. *SPE Technical Papers (ANTEC)*, 1985.

[105] O. Amano. Pressure dependent viscosity of polymer melts. *SPE Technical Papers (ANTEC)*, 2000.

[106] M. Reiner. *Deformation, Strain and Flow*. Interscience Publishers, Inc., New York, 1960.

[107] H. Giesekus. Die simultane Translation- und Rotationsbewegung einer Kugel in einer elastoviskosen Flüssigkeit. *Rheologica Acta*, 3, 1963.

[108] R. Tanner. Some extended giesekus-type theorems for non-newtonian flows. *Rheologica Acta*, 28, 1989.

[109] J. Dealy and P. Saucier. *Rheology in Plastics Quality Control*. Hanser Publishers, Munich, 2000.

[110] ASTM. *ASTM D 1238-04c Standard Test Method for Melt Flow Rates of Thermoplastics by Extrusion Plastometer*, 2005.

[111] ASTM. *ASTM D 3123-98(2004) Standard Test Method for Spiral Flow of Low-Pressure Thermosetting Molding Compounds*, 2005.

[112] B. Furches and G. Kachin. Comparison of simple rheology tests to predicted and measured flow properties of ABS resins. *SPE Technical Papers (ANTEC)*, 35, 1989.

[113] A. Kovarskii. *High-Pressure Chemistry and Physics of Polymers*. CRC Press, Boca Raton, 1994.

[114] Hendro-W. Fujii M. Imaishi N. Zhang, X. Measurements of the thermal conductivity and thermal diffusivity of polymer melts with the short-hot-wire method. *International Journal of Thermophysics*, 23, 2002.

[115] J. Lienhard. *A Heat Transfer Textbook*. Prentice-Hall, Englewood Cliffs, 1981.

[116] F. Incropera and D. DeWitt. *Introduction to Heat Transfer*. John Wiley and Sons, New York, 1990.

[117] H. Aben. *Integrated Photoelasticity*. Mc-Graw Hill, New York, 1979.

[118] R. Wimberger-Friedl. Analysis of the birefringence distributions in compact discs of polycarbonate. *Polymer Engineering and Science*, 30, 1990.

[119] H. Poincaré. *Theorie Mathématique de la Lumiere, vol. 2*. Gauthier-Villars, Paris, 1892.

[120] H. Hammer. Characteristic parameters in integrated photoelasticity: an application of Poincaré's equivalence theorem. *Journal of Modern Optics*, 10, 2004.

[121] L. Srinath and S. Keshavan. A fast iterative procedure to determine photoelastic characteristic parameters. *Mechanics Research Communications*, 5, 1978.

[122] L. Srinath and A. V. S. S. S. R.. Sarma. Determination of the optically equivalent model in three-dimensional photoelasticity. *Experimental Mechanics*, 14, 1974.

[123] H. Mueller. The foundations of optics. *Journal of the Optical Society of America*, 38, 1948.

[124] W. Conover. *Practical Nonparametric Statistics*. Wiley, New York, 1980.

[125] M. Hollander and D. A. Wolfe. *Nonparametric Statistical Methods*. Wiley, New York, 1973.

[126] J. DuBois and W. Pribble. *Plastics Mold Engineering*. American Technical Society, 1947.

[127] Klaus Stoeckhert, editor. *Mold-Making Handbook for the Plastics Engineer*. Hanser, 1983.